Title
Observation of the Crab Nebula in Soft Gamma Rays with the Nuclear Compton Telescope

Author
Bandstra, Mark ShenYu

Publication Date
2010

Peer reviewed|Thesis/dissertation

Observation of the Crab Nebula in Soft Gamma Rays with the Nuclear Compton Telescope

by

Mark ShenYu Bandstra

A dissertation submitted in partial satisfaction of the

requirements for the degree of

Doctor of Philosophy

in

Physics

in the

Graduate Division

of the

University of California, Berkeley

Committee in charge:

Professor Steven E. Boggs, Chair

Professor Robert P. Lin

Professor Joshua Bloom

Fall 2010

Observation of the Crab Nebula in Soft Gamma Rays
with the Nuclear Compton Telescope

Mark ShenYu Bandstra

Abstract

Observation of the Crab Nebula in Soft Gamma Rays
with the Nuclear Compton Telescope

by

Mark ShenYu Bandstra

Doctor of Philosophy in Physics

University of California, Berkeley

Professor Steven E. Boggs, Chair

Soft gamma rays (100 keV–10 MeV) are indispensable probes of the most violent and extreme processes in the cosmos. Gamma rays are produced by non-thermal processes in such disparate objects as neutron stars, X-ray binaries, and Active Galactic Nuclei (AGN), and they also result from the decays of many radioactive nuclei, such as certain isotopes produced in supernova explosions. The penetrating nature of gamma rays allows the astrophysicist to probe deep within these often obscured systems and make unique and complementary observations of their gravitational fields, magnetic fields, and nuclear reactions.

The challenges to soft gamma-ray measurements are numerous. First, the dominant interaction is Compton scattering, which necessitates careful imaging and simulation. Second, there is high background, predominantly from charged particle reactions and the activation of passive material in the instrument. Special care must be taken for background reduction, such as using active shielding and clever event selections. Third, atmospheric absorption of gamma rays necessitates being in space or at balloon altitudes to observe them.

Over the last four decades, various types of telescopes have been developed to detect and image soft gamma-rays. One promising technology is the Compton telescope, which exploits the Compton effect to perform direct imaging of gamma-ray photons. The current generation of Compton telescopes are compact Compton telescopes, which rely on both fine position and fine energy resolution of gamma-ray interactions within the detector volume in order to perform Compton imaging. The development of soft gamma-ray telescopes, and Compton telescopes in particular, is reviewed in Chapter 1.

The Nuclear Compton Telescope (NCT) is one such compact Compton telescope. NCT is a balloon-borne telescope designed to perform imaging, spectroscopy, and polarization analysis on soft gamma rays from astrophysical sources. NCT detects gamma rays using ten crossed-strip high-purity germanium detectors, each with a

2 mm strip pitch and a 15 mm thickness. This dissertation gives an overview of NCT's detectors, gondola systems, and data analysis pipeline (Chapter 3), as well as detailed descriptions of the detector calibrations – the depth calibration, energy calibration, cross-talk correction, and charge loss correction (Chapters 4–6).

The NCT instrument has flown twice, both times from the Columbia Scientific Balloon Facility in Fort Sumner, New Mexico. The first flight took place in 2005 with a prototype instrument housing only two germanium detectors. Due to the brief flight (6 hours), the only analysis that could be performed was a characterization of the gamma-ray background at float altitudes ($\approx$40 km). The second flight, on 17–18 May 2009, is detailed in this thesis (Chapter 7). The full ten-detector instrument was flown for a total of 37 hours. The primary goals of the flight were to observe the Crab Nebula and Cygnus X-1, both bright gamma-ray continuum sources (see Chapter 2 for a review of the Crab Nebula). The Crab Nebula was observed for 9.2 hours of the flight and was detected at a significance of 4σ (Chapter 8). This is the first detection of an astrophysical source by a compact Compton telescope. This work is an important step in establishing the viability of the compact Compton telescope design for future space-based wide-survey instruments.

To Belinda,
who helps me learn the more important things.

—

Where were you when I laid the earth's foundation?
Tell me, if you understand.
Have you comprehended the vast expanses of the earth?
Tell me, if you know all this.

Can you bind the beautiful Pleiades?
Can you loose the cords of Orion?
Can you bring forth the constellations in their seasons
or lead out the Bear with its cubs?
Do you know the laws of the heavens?
Can you set up God's dominion over the earth?

Who endowed the heart with wisdom
or gave understanding to the mind?

Job 38

Contents

List of Tables

Acknowledgments

The work contained in this dissertation was written by me but is not a product of myself alone. It reflects the contributions of a community of people around the world who have worked on NCT. There are many individuals I would particularly like to thank:

- I am grateful to Professor Steven Boggs, for his cultivation of me over the years and his commitment to my professional growth, from his support for me to go to several conferences, to his patient answers to my frequent questions. He has helped me achieve things that I did not know I could do, like running an entire balloon campaign, and he has infused good humor into every situation. I am so thankful for his personal and professional influence.
- Dr. Andreas Zoglauer deserves great thanks. He gets the credit for finding the first Crab image in the NCT data, which helped to focus our efforts. He has painstakingly read my entire thesis and helped me improve it significantly. I have probably run every step of analysis by him at some point. Without his MEGAlib code this research would not have been possible at all. He has had much patience in answering the multitude of questions and feature requests I have sent him.
- My dissertation and qualifying exam committee members: Professors Steven Boggs, Robert Lin, Joshua Bloom, and Jonathan Arons. Their support through this process, and particularly their encouragement to think about more than just data analysis, has been invaluable to me. Their comments have greatly improved the accuracy and clarity of this work.
- Jane Hoberman worked with me nearly daily for over a year to get the NCT detectors thoroughly tested. She has taught me so much about analog electronics and brought me from being afraid of bench electronics to actually being useful in the lab. She has also taught me a great deal about leadership and family as well.
- Steve McBride has been a fantastic source of practical physics knowledge — for example, thermal analysis (why do we paint the gondola white?). He was responsible for so many of the flight systems working as well as they did. I

am thankful for his leadership in the field, and for his many stories about past balloon campaigns that added a sense of history to our work.

- Thank you to our collaborators in Taiwan — Professors Hsiang-Kuang Chang and Yuan-Hann Chang, for their discussions about data analysis and science goals; Dr. C. H. Lin for his wonderful job on the electronics for NCT 2009, especially his ability to quickly troubleshoot the digital electronics; and Professor Alfred Huang for his work on the solar power system and helpful contributions in New Mexico.
- I have greatly enjoyed working with and getting to know the other NCT students. Special thanks to Eric Bellm for reading my thesis and for his very capable management of the project for the 2010 Australia campaign. I have thoroughly enjoyed our discussions of data analysis, GRBs, Python, and Gantt charts. Thanks to Alan Chiu, Zong-Kai Liu, Jau-Shian Liang, and Wei-Che Hung for the fun times of sharing an office at SSL, learning about each others' languages and cultures, and for their close collaboration on the different pieces of the NCT data analysis. Alan, Zong-Kai, and Justin were also wonderful hosts when I traveled to Taiwan. Thanks go to Alan for his great job taking over the GSE and for extracting data that I often requested. Daniel Perez-Becker needs to be thanked for his excellent calibration of the BGO shields, good humor in the field, and willingness to draw up CAD designs on the side. I could not have asked for a better group of colleagues.
- Thank you to the past members of the NCT team: Dr. Jason Bowen, for the many ways he helped me to get adjusted to our group, the discussions about relationships and science, and for his leading the analysis effort for the 2005 flight; Dr. Trixi Wunderer, for many fruitful suggestions, including the idea of how to evaluate different calibration models in Chapter 5, and for generally making me a better scientist; Dr. Wayne Coburn, for his work on the flight computer and good humor in spite of it; and Marsha Colby, for her work on the 2005 flight, and her warmth and kindness.
- NCT's success is largely due to the great development, fabrication, and testing of the detectors by Drs. Mark Amman and Paul Luke at LBL. I would also like to thank Mark in particular for many helpful discussions about the detectors.
- The rest of high-energy astrophysics group at SSL, including Drs. John Tomsick, Nicolas Barrière, Arash Bodaghee, and Philip von Doetinchem. I have had many helpful discussions with them about science, career, and family, and they gave me great comments on my thesis presentation. John helped me figure out how to do INTEGRAL analysis and guided me on a brief venture into X-ray binaries for my qualifying exam; I am thankful for his encouragements to keep good records and be precise, which have served me well.

- I and our entire team are hugely indebted to the wonderful engineers, machinists, and technicians at SSL. Bill Donakowski in particular handled many challenging engineering tasks that we set before him with great skill. Terry McDonald always did a great job welding and machining parts for us, even when we weren't exactly sure what we needed. Yvette Irwin made all of our cables not only perfect but elegant. Paul Turin, Greg Howe, Chris Cork, Jeremy McCauley, and Alec Plauche also deserve much thanks for their work. Extra thanks to Bill Donakowski, Terry McDonald, Paul Turin, and Steve McBride for pulling off the superhuman effort of mechanically testing and fixing our rotator in a single weekend, allowing us to be flight-ready on time.
- Anne Takizawa was a lifesaver throughout graduate school as I ran into various administrative issues. She is a real treasure to the physics department!
- Finally, a huge thank you to Bill Stepp and the rest of the crew of the Columbia Scientific Balloon Facility for their professional and capable balloon launching and support. What an adventure it was!

There are also a number of those who have not been directly involved in this work but whose influence on me has been just as important in its completion. I have been surrounded by so many loving people during my life. My deep personal gratitude goes to:

- Professors Alexander Barg and Masahiro Morii, who gave me research opportunities during college in coding theory and high-energy physics, respectively. Though I did not continue in their research, they taught me many things about working in the research world.
- My mentors in high school, especially Mr. Leon Varjian, who fostered my interest in math and teaching and gave me many opportunities for independent study. I do not think I would have dreamed of going this far in academia without his early influence.
- My spiritual mentors during graduate school, including Rev. Josh McPaul, Rev. Dr. Mark Labberton, Mrs. Carrie Bare, and Dr. and Mrs. David and Judy Newquist. They encouraged me to seek my calling and put graduate school in a larger perspective.
- My friends in the Veritas Graduate Christian Fellowship and First Presbyterian Church of Berkeley, who have come alongside me from the very beginning. There are too many to thank them all individually here!
- My family: my siblings — Christine and Rob, and Sharon and David — for their support and love throughout the years. My parents, John and Karen Bandstra, without whose prayers and support I would not have been able to get this far. Both of them fostered and modeled curiosity and hard work for me, gifts that

I am very thankful for. Also, I could have never guessed that I would end up using all the plumbing knowledge my father taught me. I also thank Drs. Simon and Betty Shen Yu, and Rev. Dr. Paul Shen, who love me as their own son and grandson.

- Lastly, my wife Belinda. She has taken care of so many things for me during my studies, from the logistical — bringing food to our team in New Mexico, testing analog boards, and bubble-wrapping gondola parts — to the non-logistical — her daily love, support, and friendship. I could not have done this without her.

May this work, and the work that I do going forward, be a testament of gratitude for the love I have received.

Part I

Introduction

Chapter 1

Soft Gamma-ray Astrophysics with Compton Telescopes

Soft gamma rays (100 keV−10 MeV) are indispensable probes of the most violent and extreme processes in the cosmos. Gamma rays are produced by non-thermal processes in such disparate objects as neutron stars, X-ray binaries, and Active Galactic Nuclei (AGN). The penetrating nature of gamma rays allows the astrophysicist to probe deep within these often obscured systems and make unique and complementary observations of them.

In addition, gamma rays are also probes of nuclear reactions occurring in outer space, since most nuclear gamma-ray lines are in this energy range. Detecting soft gamma rays allows us to access nuclear reactions and readily identify and quantify radioactive isotopes, such as those produced during supernova explosions. These measurements can give the astrophysicist insights into many other branches of astronomy and physics.

The challenges to soft gamma-ray measurements are numerous. First, the dominant interaction is Compton scattering, which necessitates careful imaging and simulation. Second, there is high background, predominantly from charged particle reactions in the atmosphere and the activation of passive material in the instrument. Special care must be taken for background reduction, such as using active shielding and clever event selections. Third, atmospheric absorption of gamma rays necessitates being in space or at balloon altitudes to observe them.

1.1 The soft gamma-ray sky

Gamma-ray sources can generally be divided into two classes — those that produce gamma-ray lines and those that produce a gamma-ray continuum. Here we will describe the various different science topics that can be addressed with each type of source and the current state of our understanding of them.

1.1.1 Gamma-ray line sources

Any source that produces a gamma-ray line does so as the result of a nuclear reaction that has occurred. These reactions include nuclear decay, positron production, neutron production and capture, and nuclear excitation.

1.1.1.1 Nucleosynthesis

All nuclei that were not created in the Big Bang are believed to form in a handful of ways: during nuclear burning inside a star on the main sequence, during nuclear burning in a nova on the surface of a white dwarf, during various nuclear reactions in a supernova explosion, and as a result of cosmic ray interactions in the interstellar medium [63]. Radioactive nuclei are created alongside stable nuclei in these reactions and can be tracers of the reactions, answering questions of how much, where, and when did certain types of nucleosynthesis occur. The answers to these questions help us understand the life cycle of the elements — how they are formed and how they are spread throughout the cosmos. Researchers have identified several radioactive isotopes that emit gamma-ray lines, and several have been detected. Because the production mechanisms and half-lives differ, each one offers slightly different information about supernovae and the galaxy.

For example, the isotopes ^{26}Al ($t_{1/2} = 7.5 \times 10^5$ yr; 1.809 MeV) and ^{60}Fe ($t_{1/2} = 2.0 \times 10^6$ yr; 1.173 and 1.333 MeV) are believed to be produced in the same regions of a massive star during main sequence burning and Type II (core-collapse) supernovae. Because of the short length of their half-lives relative to the age of most stars, these isotopes trace the recent history of nucleosynthesis in massive stars and their supernovae. The relative production of these two isotopes holds information about the type of stars that have produced them — ratios of ^{60}Fe to ^{26}Al that are less than one mean that the star's mass is $\gtrsim 25 M_\odot$, while equal ratios imply lower mass [63]. Both of these isotopes have been detected and even imaged. HEAO C first detected ^{26}Al [126], and COMPTEL produced an image of 1.8 MeV emission from the galactic plane (Fig. 1.1 and [139]). Recently, RHESSI measured the ratio of ^{26}Al to ^{60}Fe in the galaxy [154].

The isotope ^{44}Ti ($t_{1/2} = 89$ yr; 78.4, 67.9, and 1157 keV) is sensitive to the "mass-cut" of a core-collapse supernova — the division between the portion of the star that collapses into the compact object and the portion that is ejected. Modeling of core-collapse supernovae explosions produce dramatically different yields of ^{44}Ti depending on the details of the explosion mechanism [63]. Emission from ^{44}Ti was first observed by COMPTEL from Cas A [91], and because of its brief half-life many searches have been made for emission from SN 1987A without success.

The previous three isotopes are expected from core-collapse supernovae and massive stars, while ^{56}Ni and ^{57}Ni are expected from Type Ia supernovae. These isotopes are also expected in core-collapse supernovae, but the radiation will generally be

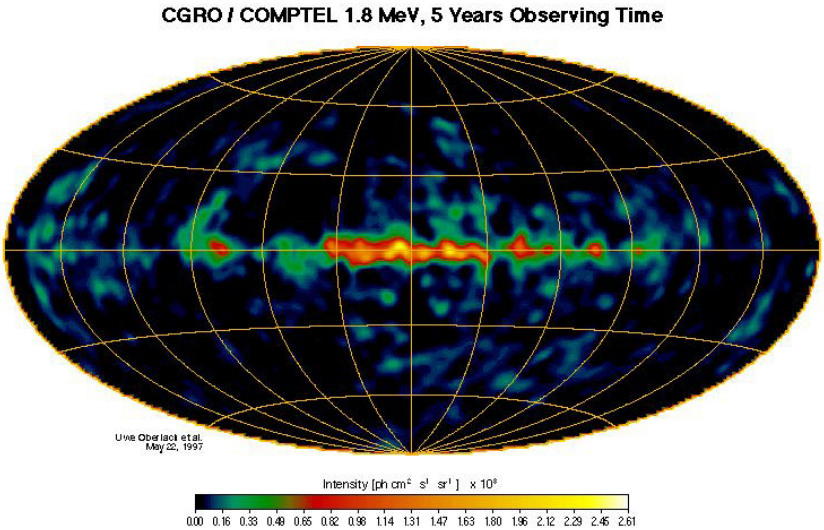

Figure 1.1: All-sky map of ^{26}Al 1.8 MeV emission from the galactic plane by COMPTEL. Image from `http://heasarc.gsfc.nasa.gov/docs/cgro/comptel/`. See also [139].

trapped by the ejecta in those supernovae. The way that the supernova ignites and burns determines ratio of these two isotopes and their lightcurves, so clear detection of both could constrain Type Ia models [63]. Emission from ^{57}Ni has been detected from SN 1987A by OSSE [111], while ^{56}Ni has also been observed in SN 1991T by COMPTEL [133].

1.1.1.2 Positron annihilation

Positrons are produced through inverse beta decay or pion decay. After a positron is created, it will annihilate with an electron in one of two ways: in the singlet state (spin-0), emitting two 511 keV photons in opposite directions, or in the triplet state (spin-1), where spin and momentum conservation requires the emission of three photons. A detection of the 511 keV line gives direct evidence for the presence of positrons in outer space. The line shape also gives evidence of the environment in which the annihilation took place, such as its temperature.

The most famous example of positron production in astrophysics is the annihilation emission from the galactic bulge and plane. Recent measurements by INTEGRAL/SPI show a strong bulge component and weak plane component, with a slight asymmetry (Fig. 1.2). It has been suggested that the slight asymmetry correlates with the distribution of galactic low-mass X-ray binaries, a possible positron production site, but the evidence is not yet conclusive [170].

Positrons may also be produced in supernovae or in the disks and pair plasma jets of accreting compact objects, but no evidence has yet been found for such sources.

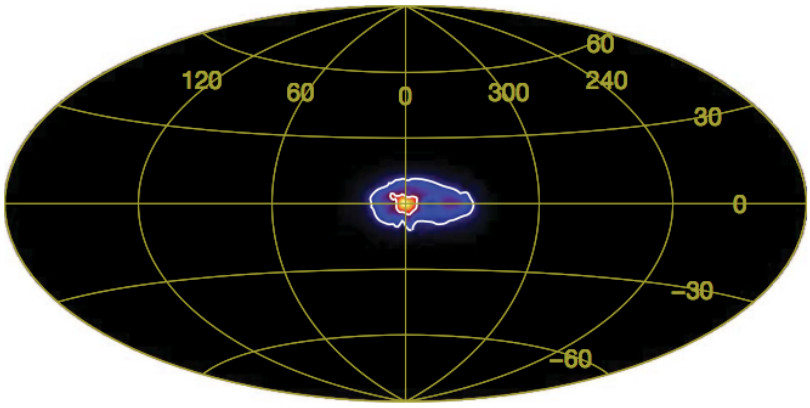

Figure 1.2: All-sky map of 511 keV emission from the galactic center region by INTEGRAL/SPI. Recent measurements have revealed a galactic disk component and asymmetry, perhaps correlated with the distribution of low-mass X-ray binaries. Figure 1 from [170].

1.1.1.3 Neutron-capture (2.223 MeV)

Another nuclear reaction of astrophysical importance is the capture of a neutron by a proton, which results in a deuteron and a 2.223 MeV gamma ray. The cross-section for this reaction is proportional to the inverse of the neutron's velocity, so the neutrons must first thermalize by undergoing many collisions in the ambient medium before they are captured. Therefore this line may be very narrow (FWHM $\lesssim 0.5\%$) if it occurs in a cool medium ($kT \lesssim 10$ keV). Also, because free neutrons decay on a timescale of $\approx$10 minutes, this reaction must occur near a source of neutrons.

Bildsten et al. have studied neutron production through the spallation of accreting helium nuclei onto a neutron star and their subsequent capture in the atmosphere of the neutron star [26]. The line should be gravitationally redshifted, with measured energy

$$E = E_0 \left(1 - \frac{2GM}{Rc^2}\right)^{1/2} \tag{1.1}$$

where E_0 is 2.223 MeV, G is the gravitational constant, M is the neutron star mass, and R the neutron star radius. This formula will hold because the neutron capture should take place in the outer atmosphere of the neutron star in a narrow range of radii ($\Delta R \ll R$). So any measurement of the redshift of this line would directly probe the mass-radius ratio M/R of a neutron star. This measurement would put a strong constraint on the equation of state of neutron stars when used together with other methods (see, e.g., [113]). To date, a few searches have been made, but none have yet found a redshifted neutron capture line [36, 45]. However, none of these searches have been done to the estimated narrow-line sensitivity requirement of $\sim 10^{-7}$ cm^{-2} s^{-1}

for the best neutron star candidates.

Another source of neutrons was studied by Jean and Guessoum [92]. They considered the production of neutrons from spallation of light elements in the accretion disk of the compact object of an X-ray binary. The neutrons would then have a probability of being captured in the atmosphere of the secondary star, leading to a narrow, unredshifted line. Only one potential source of an unredshifted 2.223 MeV line has been identified (by COMPTEL), though the source identification remains speculative and the origin of the line a mystery [131].

The only well-understood astrophysical detection of the neutron capture line (unredshifted) is from solar flares. The neutrons are products of the acceleration and spallation of ions in flares, and the neutrons are captured in the photosphere. A recent breakthrough in the understanding of solar flares came when the 2.2 MeV line was found to be spatially separated from hard X-ray electron brehmsstrahlung radiation by the RHESSI mission, indicating differences in the acceleration of ions and electrons during solar flares [118].

1.1.1.4 Nuclear de-excitation

The last nuclear line type that would be expected in the cosmos are gamma-ray lines from nuclear de-excitation. All nuclei have unstable excited states that are analogous to atomic excited states but with much higher energies ($\sim$MeV). For the relatively abundant nuclei ^{12}C and ^{16}O, these excitations have characteristic gamma-ray energies at 4.44 and 6.13 MeV, respectively. The excitations are generally triggered by cosmic ray collisions with the nuclei in the interstellar medium. These two lines have been seen by COMPTEL in the Orion region [27].

De-excitation lines could also be seen from the surface of a neutron star, where CNO nuclei are hit by other accreting nuclei, though the fluxes are probably too small for detection [25].

Lastly, it should be noted that these lines have been seen from the Sun during solar flares (e.g., [118]). In solar flares, ^{12}C and ^{16}O ions in the solar atmosphere are accelerated and collide with hydrogen and helium, placing them in their nuclear excited states. The de-excitation lines are then observed in areas where these ions have been accelerated.

1.1.2 Gamma-ray continuum sources

Sources that emit a continuum of gamma rays generally are "accelerators" with either extreme gravitational fields, extreme magnetic fields, or a combination of both. Gamma-ray emission results from non-thermal processes such as synchrotron radiation and inverse Compton radiation. Spectral measurements of these sources in the gamma-ray band are important to further understanding how their emission is

formed, but definitive measurements of gamma-ray polarization (with, e.g., a Compton telescope) would be crucial to distinguish between different models.

1.1.2.1 Active Galactic Nuclei

Active Galactic Nuclei (AGN) are believed to be accreting supermassive black holes at the center of galaxies. They produce broadband radiation, and some have a potential spectral break in the soft gamma-ray regime. The gamma rays are thought to be produced by inverse-Compton scattering of soft photons off of hot electrons in disks or in jets, and may have a high degree of polarization. Several AGN have been observed recently by INTEGRAL [106], though no gamma-ray polarization measurements have been made to date.

1.1.2.2 Stellar-mass compact objects

Stellar-mass neutron stars and black holes are other sources of soft gamma-ray continuum emission for various reasons. In some compact objects, such as the black hole candidate Cygnus X-1, accretion is the main source of energy, and gamma rays result from Comptonization, brehmsstrahlung, and annihilation in a hot, thin medium surrounding the disk [134]. In the Crab nebula and pulsar, energy comes from the spin-down of the pulsar, and gamma-ray emission comes from synchrotron emission in the magnetic field of the pulsar wind nebula (see Chapter 2). Other exotic sources of gamma rays include magnetars, which are highly magnetized neutron stars, and the energy for the system comes from the decay of the magnetic field (see [37] for detailed observations of a putative magnetar).

In all of these sources, gamma-ray polarization is key to understanding the detailed emission mechanism and emission region. In addition, gamma-ray polarization from the inner parts of an accretion disk around a black hole will provide important insights into General Relativity [55].

1.1.2.3 Gamma-ray bursts

Gamma-ray bursts (GRBs) were discovered in the late 1960s with the Vela satellites and made public a few years later [103]. They consist of brief, intense bursts of hard X-rays and soft gamma rays for $\sim 0.1-100$ seconds, and are often accompanied by an "afterglow" in lower wavebands, from X-ray to radio. There are two known classes based on duration: short GRBs ($\lesssim$1 s) and long GRBs ($\gtrsim$1 s), which are believed to be the results of compact object mergers and core-collapse supernovae, respectively. In both cases, the standard "fireball" model is that the central source produces polar jets of ultrarelativistic pair plasma, and the GRB emission results from a series of internal shocks in the plasma. The gamma-ray emission is blueshifted synchrotron radiation from the pair plasma. For a discussion of the standard GRB model, see [147].

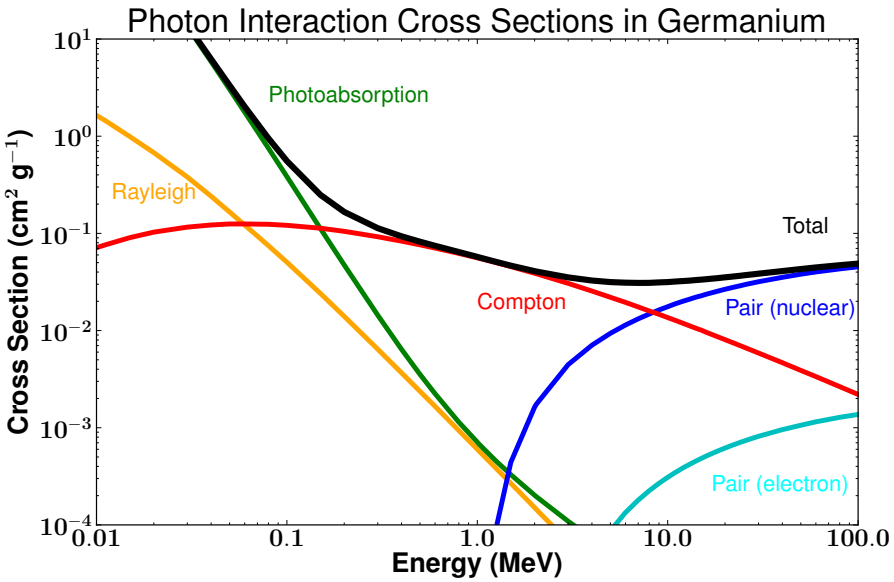

Figure 1.3: Photon interaction cross sections in germanium for the different processes discussed in the text (data from [24]).

Much is still unknown about GRBs, especially the prompt gamma-ray emission. The synchrotron emission of the standard fireball model requires a magnetic field and thus gamma rays could have a high degree of linear polarization. An attempt to measure the polarization of a GRB was made using RHESSI, and the result was 80%±20% polarization [52], though further analysis concluded that the result was not significant [172]. Gamma-ray telescopes, especially Compton telescopes and others that can measure polarization, are key to understanding the production of the prompt gamma-ray emission.

1.2 Gamma-ray interactions in matter

Before exploring gamma-ray detectors in detail, we will describe the dominant gamma-ray interactions that need to be dealt with. Gamma rays can undergo several different types of interactions as they pass through matter. Figure 1.3 shows a comparison of the cross sections for these different processes in germanium, a common detector material. Here we will explore each one.

1.2.1 Photoabsorption

At low gamma-ray energies, direct photoelectric absorption of the gamma ray by an atomic electron is the most important process. A schematic of this interaction is

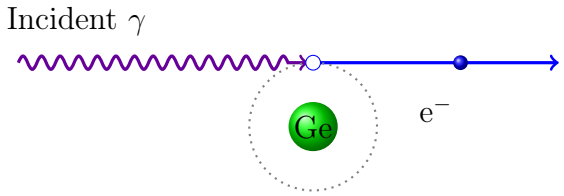

Figure 1.4: Schematic of photoelectric absorption with an atomic electron. The full photon energy is imparted to the electron, which usually leads to the ionization of the atom.

shown in Fig. 1.4. Since the entire energy of the photon is transferred to the electron, this usually results in the ionization of the atom and the liberation of the electron.

1.2.2 Rayleigh scattering

The next most important process at the lowest gamma-ray energies is Rayleigh scattering. Rayleigh scattering is coherent scattering with an atomic electron. Because of the high energy of the photon, only small angles are allowed so that energy-momentum conservation does not lead to ionization of the electron or cause its transition to another atomic orbital. The majority of Rayleigh scattering occurs at angles $< 20°$ at 100 keV and $< 3°$ at 1 MeV for most detector materials [65]. Since this type of scattering does not change the energy of the photon and the reaction cross section is very small, its effects are often ignored.

1.2.3 Compton scattering

The most important process in the soft gamma-ray regime is Compton scattering, which is incoherent scattering of the photon with an atomic electron. The photon imparts some of its energy to the electron and in most cases ionizes it. The basic diagram of a Compton scatter is shown in Fig. 1.5. Equating the four-momenta of the incoming and outgoing electrons and photons, we have:

$$\begin{pmatrix} E_{\gamma_0} \\ E_{\gamma_0} \\ 0 \end{pmatrix} + \begin{pmatrix} m_e c^2 \\ 0 \\ 0 \end{pmatrix} = \begin{pmatrix} E_{\gamma_1} \\ E_{\gamma_1} \cos\varphi \\ E_{\gamma_1} \sin\varphi \end{pmatrix} + \begin{pmatrix} \gamma_e m_e c^2 \\ \gamma_e \beta_e m_e c^2 \cos\varphi_e \\ -\gamma_e \beta_e m_e c^2 \sin\varphi_e \end{pmatrix} \tag{1.2}$$

The resulting solution for the energy of the outgoing photon E_{γ_1} in terms of the incident photon energy E_{γ_0} and the scatter angle φ is

$$E_{\gamma_1} = \frac{E_{\gamma_0}}{1 + \frac{E_{\gamma_0}}{m_e c^2}(1 - \cos\varphi)} \tag{1.3}$$

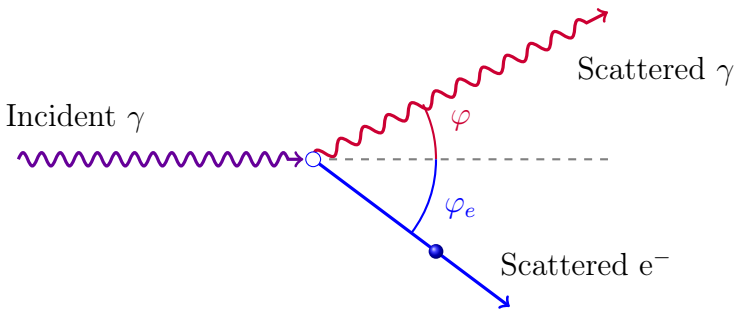

Figure 1.5: Basic setup for a photon undergoing a Compton scatter with a free electron at rest.

which is the famous Compton scatter formula. A detector cannot measure either photon energy directly, but it can measure the energy imparted to the electron:

$$E_e = E_{\gamma_0} - E_{\gamma_1} = E_{\gamma_0}\left[\frac{\frac{E_{\gamma_0}}{m_e c^2}(1-\cos\varphi)}{1+\frac{E_{\gamma_0}}{m_e c^2}(1-\cos\varphi)}\right]. \tag{1.4}$$

The differential cross section for Compton scattering is given by the Klein-Nishina cross section, shown here for a polarized gamma-ray source [104]:

$$\frac{d\sigma}{d\Omega} = \frac{3}{16\pi}\sigma_T\left(\frac{E_{\gamma_1}}{E_{\gamma_0}}\right)^2\left[\frac{E_{\gamma_0}}{E_{\gamma_1}} + \frac{E_{\gamma_1}}{E_{\gamma_0}} - 2\sin^2\varphi\cos^2\eta\right] \tag{1.5}$$

where φ is the Compton scatter angle, η is the angle between the initial polarization vector and the plane of the scattered photon, and σ_T is the Thomson cross section:

$$\sigma_T = \frac{8\pi}{3}\frac{e^4}{m_e^2 c^4}. \tag{1.6}$$

The cross section for an unpolarized photon can be found using by using $\frac{1}{2}$ as the average value of $\cos^2\eta$. Note that the cross section has a maximum when η is $\pm 90°$. The total cross section can be found in closed form:

$$\sigma = \frac{3}{4}\sigma_T\left\{\frac{1+x}{x^2}\left[\frac{2(1+x)}{1+2x} - \frac{1}{x}\ln(1+2x)\right] + \frac{1}{2x}\ln(1+2x) - \frac{1+3x}{(1+2x)^2}\right\} \tag{1.7}$$

where $x \equiv E_{\gamma_0}/m_e c^2$ [104]. The differential cross section is plotted in Fig. 1.6, revealing that as the incident photon energy increases, a forward scatter is more and more likely (if a scatter occurs at all). The total cross section is plotted in Fig. 1.7, where it is evident that the total probability of a scatter decreases rapidly with energy.

1.2.4 Pair production

As we proceed to the high-energy side of Fig. 1.3, we notice that two processes — pair production in the nuclear and electron fields — are activated above 1 MeV.

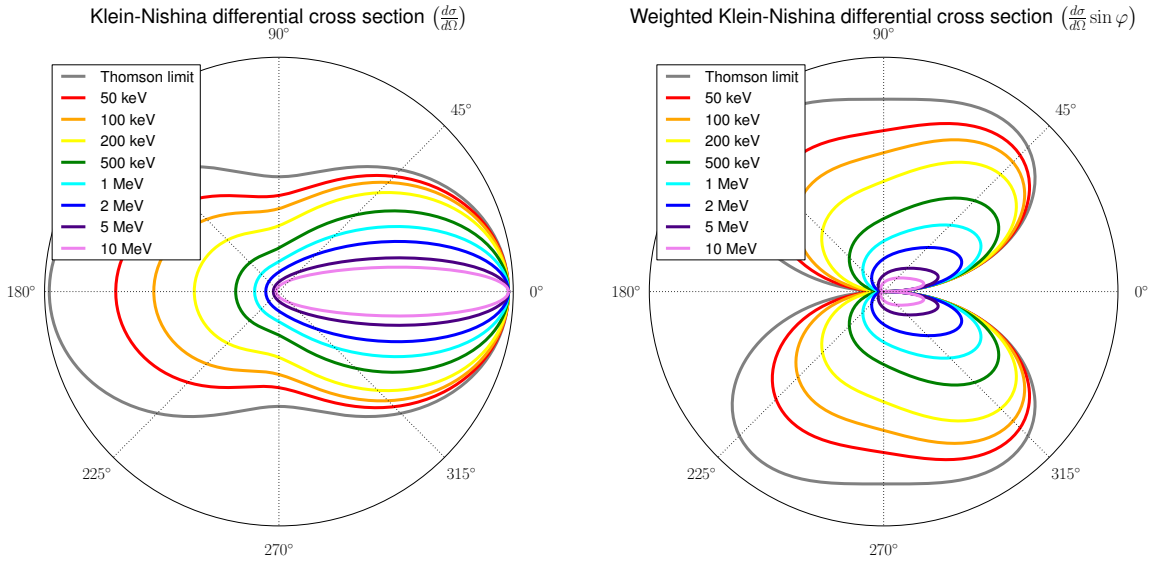

Figure 1.6: The Klein-Nishina differential cross section at different energies. The differential cross section $\frac{d\sigma}{d\Omega}$ is shown on the left, while the cross section weighted by $\sin\varphi$ (thus proportional to the probability for a given φ) is shown on the right. The maximum radius of each plot is the maximum classical value, $(3\sigma_T/8\pi)$. Note that at low energies, the differential cross section approaches the classical (Thomson) limit, while at large energies the differential cross section becomes strongly forward-peaked.

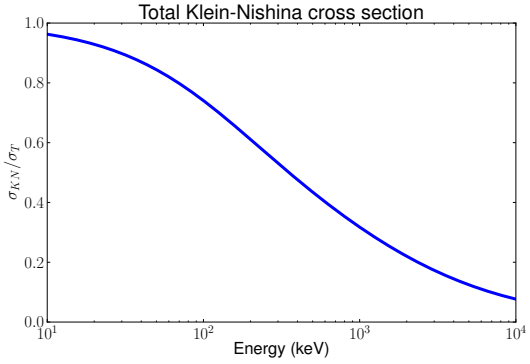

Figure 1.7: The ratio of the Klein-Nishina total cross section to the Thomson cross section at different energies. As expected, at low energies the cross section approaches the classical (Thomson) limit, while at large energies the cross section decreases.

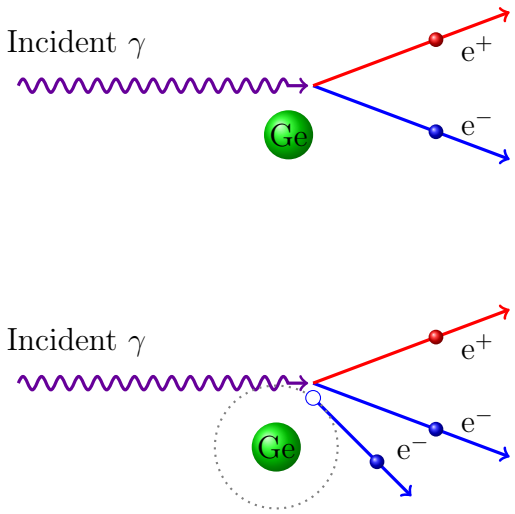

Figure 1.8: Pair production in the nuclear field (top) and electron field (bottom).

Using energy-momentum conservation, the threshold for pair production in the field of a charged particle of mass m is $E_\gamma \geq 2m_e c^2(1 + m_e/m)$, or $E_\gamma \gtrapprox 2m_e c^2 = 1.022$ MeV for nuclear pair production and $E_\gamma \geq 4m_e c^2 = 2.044$ MeV for electron pair production. The cross section is proportional to the square of the charge on the particle. So the cross section for an individual nucleus is larger than the cross section for an individual electron by a factor of Z^2, where Z is the atomic number. However, since there are Z electrons for every nucleus, the cross sections in bulk material only differ by a factor of $\sim Z$. This can be seen in Fig. 1.3, where the cross section for nuclear pair production is larger by a factor of 30 (for germanium, $Z = 32$).

1.2.5 Diffraction

Diffraction was not included in Fig. 1.3 because it is an interaction with the entire crystal lattice. Diffraction is coherent scattering, with "peaks" of scattering occurring at specific angles that are integral multiples of the ratio between the photon wavelength λ and the lattice spacing a. Because the wavelength of a gamma ray ($\lambda \sim 10^{-10}$ cm at 1 MeV) is much smaller than an atomic lattice spacing ($a \sim 10^{-8}$ cm), these diffraction angles are very small. The first-order Bragg diffraction angle is given by

$$\theta \approx \frac{\lambda}{2a} \tag{1.8}$$

$$\sim 20'' \tag{1.9}$$

for 1 MeV photons. This effect is exploited for gamma-ray astrophysics with so-called Laue lenses (e.g., CLAIRE [79]).

1.3 Soft gamma-ray telescopes

Given these different interaction processes for soft gamma rays, telescopes use a variety of different techniques to observe them. The techniques can be divided into three categories: non-imaging, indirect imaging, and direct imaging.

1.3.1 Types of telescopes: non-imaging, indirect-imaging, and direct-imaging

Non-imaging gamma-ray telescopes utilize large-volume detectors so that any photon that interacts has a high probability of being fully absorbed in the detector volume. The detectors are often surrounded by a collimator and anticoincidence shield to reduce the number of photons that interact and then escape the detectors. To detect astrophysical sources, these these instruments generally rely on on-source/off-source pointing. The source significance and spectrum is derived from the difference between the on-source and off-source datasets. An example of this category was HEAO C-1 [125].

Indirect imaging is done in two ways: coded-mask imaging and rotational modulation collimation (RMC). The telescope must have an array of different detectors that detect the "shadows" cast by the mask. On-source and off-source pointing may be used to measure the shadow pattern in the presence and absence of a source. This information is then deconvolved with the known mask pattern (or known rotation angle for RMC) and an image of the sky is produced. This method is indirect because an individual photon's direction cannot be inferred; images are built up through the accumulation of photon counts through the mask. An example of this category is INTEGRAL/SPI, which uses 19 high-volume germanium detectors to perform coded-mask imaging of gamma-ray sources with a hexagonal tungsten mask [168].

Direct imaging of gamma rays can be done in three distinct ways: through the Compton effect, though pair tracking, and with Laue lenses. Compton telescopes require at least one Compton scatter and one other interaction, and then they use the Compton scatter formula to infer the incoming photon direction. These instruments will be discussed in detail in Section 1.4.

Direct-imaging instruments that exploit pair production ("pair telescopes") use trackers and calorimeters to measure the electron and positron trajectories and energies. The direction of the incoming gamma ray is determined by the track directions, and its energy is the sum of the two measured energies. Examples of this kind of instrument are MEGA (a hybrid Compton-pair telescope) [98] and EGRET [99].

The final category of direct imaging uses a crystal "Laue lens" to diffract photons onto a focal plane detector. The photon detector itself may be one of the aforementioned kinds. This category is a nascent one — to date, only one balloon instrument has flown with a Laue lens (CLAIRE [79]). But there are currently several groups working on fabricating and testing crystal lenses, and there are plans for space missions, such as the Gamma-Ray Imager (GRI) [105]. Of the four categories, this one is unique in that the effective collection area is determined by the lens and not the detector material, so much higher sensitivities are expected. The tradeoff is that the field of view of such an instrument should be very small ($\sim$ arcminutes).

1.3.2 Major soft gamma-ray instruments

These different types of telescopes have been used in balloon- and space-based instruments over the last four decades. A selection of prominent instruments and results is discussed here and summarized in Table 1.1.

1.3.2.1 Early experiments: HEAO and GRIS

Gamma-ray astronomy began in the late 1960s and came of age in the late 1970s with the launches of HEAO-1 and HEAO-3. HEAO-1 carried the A-4 instrument, which consisted of seven NaI(Tl) and CsI(Na) scintillator detectors surrounded by CsI(Na) shields [129]. It was a non-imaging instrument with a field of view of 43° FWHM, and it covered the energy range 10 keV to 10 MeV. Its major contributions included a catalog of hard X-ray sources [115] and a measurement of the hard X-ray and soft gamma-ray cosmic background [77].

The HEAO-3 satellite carried the C-1 instrument, which consisted of four coaxial germanium detectors surrounded by a CsI scintillator shield [125]. HEAO C-1 was the first germanium spectrometer flown in space. Like A-4, it was non-imaging and so relied on on-source/off-source pointing. It was used to discover the first traces of 1.8 MeV emission from galactic ^{26}Al, a watershed result for nuclear astrophysics [124, 126].

The Gamma-Ray Imaging Spectrometer (GRIS) was a balloon-borne experiment using seven coaxial germanium detectors surrounded by a NaI shield [162]. The new feature of GRIS was an active coded mask of NaI, making it the first indirect-imaging gamma-ray telescope flown. Imaging was done over the energy range 20 keV to 10 MeV in the $9° \times 15°$ field of view, with a resolution of 4° and location accuracy of $\sim 0.2°$. It was used to confirm the observations of earlier missions, such as 511 keV emission from the Galactic center [71] and 1.8 MeV emission from galactic ^{26}Al [161].

1.3.2.2 The Compton Gamma Ray Observatory

A major step in gamma-ray telescopes came with the launch of the Compton Gamma Ray Observatory (CGRO), which carried several gamma-ray instruments (COMPTEL, BATSE, OSSE, and EGRET). CGRO was in orbit during the years 1991−2000.

The Oriented Scintillation Spectrometer Experiment (OSSE) and Burst and Transient Source Explorer (BATSE) were both non-imaging instruments on board CGRO. OSSE was a successor to HEAO A-4, using four NaI(Tl) and CsI(Na) scintillator detectors surrounded by a NaI(Tl) shield [94]. It succeeded in detecting the 511 keV emission from the galactic center and measuring the spectra of many gamma-ray sources.

BATSE used eight large-area scintillation detectors to detect GRBs and other gamma-ray transients [69]. It used brightness differences between its eight modules to perform crude ($\sim$ several degree) localization of GRBs. Besides measuring lightcurves and localizing sources, BATSE was also able to perform spectroscopic measurements of GRBs and other transient sources.

The EGRET instrument was a pair telescope sensitive in the range 20 MeV to 30 GeV [99]. It will not be discussed here in detail because of its higher energy range but is mentioned as an example of the complementarity of the pair telescope approach to the other types of telescopes used on CGRO.

COMPTEL was the first and only Compton telescope that has been flown in orbit, and it represents an important leap in gamma-ray telescopes [150]. The instrument consisted of two layers of scintillator material — a low-Z liquid scintillator in the top and the high-Z scintillator NaI(Tl) in the bottom — and gamma rays were required to Compton scatter between the two layers (see Fig. 1.9). Therefore, COMPTEL was the first direct-imaging gamma-ray instrument because it did not rely on on-source/off-source pointing or coded masks, but the direction of each individual gamma ray was determined to a circle on the sky. The energy range of COMPTEL was 1−30 MeV, and its angular resolution was 3−4° FWHM over its large ($\sim$1 steradian) field of view.

Many scientific achievements were made by COMPTEL, including an all-sky map of the galactic ^{26}Al emission ([139] and Fig. 1.1), the first astrophysical detection of ^{44}Ti (from the Cas A supernova remnant [91]), the detection of nuclear de-excitation lines from the Orion region [27], and a comprehensive soft gamma-ray source catalog [151].

1.3.2.3 RHESSI

The Reuven Ramaty High Energy Solar Spectroscopic Imager (RHESSI) was launched in 2002 primarily for hard X-ray and soft gamma-ray observations of the Sun [117]. It uses Rotational Modulation Collimation (RMC), in which photons are

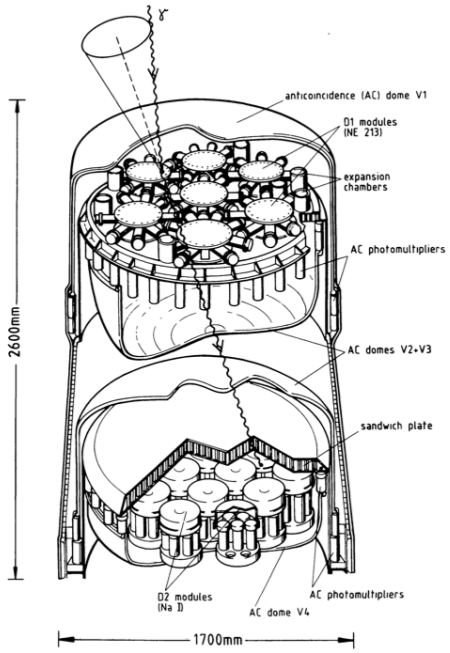

Figure 1.9: The COMPTEL instrument. There are two detector planes, and photons are required to Compton scatter in the top plane and be photoabsorbed in the bottom plane. Figure 2 from [150].

shielded by a series of tungsten slats, and imaging is done by deconvolving the rotation with the observed photon counts [90]. The detectors are nine coaxial germanium detectors segmented into two sections — the front segments are used in the hard X-ray regime, and the back segments are used for gamma rays.

Besides for many breakthroughs in our understanding of solar physics, RHESSI has also been used to explore other areas of gamma-ray astrophysics such as GRBs [23,52], neutron capture line searches [36], and galactic ^{26}Al and ^{60}Fe emission [154].

1.3.2.4 INTEGRAL

The International Gamma-Ray Astrophysics Laboratory (INTEGRAL) [175] was launched in 2002 into a highly elliptical orbit. It carries two primary instruments for gamma-ray imaging and spectroscopy, IBIS and SPI.

The Imager on Board Integral (IBIS) is optimized for fine-resolution imaging of gamma-ray sources [165]. It uses a tungsten coded mask and arrays of CdTe and CsI(Tl) detectors to perform coded-mask imaging from 15 keV to 10 MeV. Its fully-coded field of view is 9°, with 12′ angular resolution and 30″ source localization. In addition, its arrays of detectors can be operated in a "Compton mode," which has allowed researchers to measure the polarization of the Crab Nebula [70].

The Spectrometer aboard INTEGRAL (SPI) consists of nineteen coaxial germa-

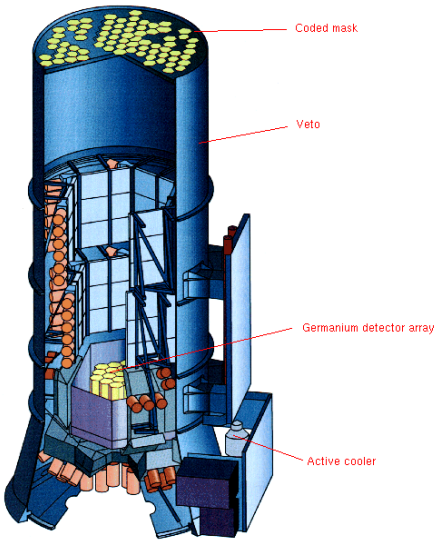

Figure 1.10: The SPI instrument on board INTEGRAL. The array of nineteen coaxial germanium detectors can be seen at the bottom of the diagram, and the tungsten mask is at the top of the diagram. The instrument is surrounded by anti-coincidence BGO shields. Image from `http://www.sciops.esa.int`.

nium detectors with a tungsten mask and anticoincidence BGO shields (see [168] and Fig. 1.10). The field of view of the instrument is $\approx 14°$, with 2.5° FWHM angular resolution and $\lesssim 1.3°$ point source localization. SPI has confirmed all earlier detections of gamma-ray lines, but it has not succeeded in discovering any new lines. The primary reason for this is that even though its germanium detectors have excellent spectral resolution, it has high instrumental background resulting from both large amounts of passive material and passages through radiation belts [93]. It has succeeded in providing higher resolution images of gamma-ray sources, such as the 511 keV emission from the Galactic center (see [170] and Fig. 1.2).

1.4 Compton telescopes

The development of Compton telescopes to this date has taken the form of two "generations" — the first generation of "classical" Compton telescopes like COMPTEL and the second generation of "compact" Compton telescopes like NCT. In this section we will examine the history and main features of each kind, and explore the advantages of Compton telescopes over other types of instrument.

Name	Years of operation	Telescope type	Detector Type(s)	Energy range (MeV)	Field of View	Angular resolution
HEAO A-4 [129]	1977−1979	non-imaging	NaI(Tl), CsI(Na)	0.010−10	43°	N/A
HEAO C-1 [125]	1979−1981	non-imaging	coaxial Ge	0.050−10	30°	N/A
GRIS [162]	1988−1995 (balloon)	coded-mask	coaxial Ge	0.020−10	9°×15°	4°
OSSE [94]	1991−2000	non-imaging	NaI(Tl), CsI(Na)	0.05−10	3.8°×11.4°	N/A
BATSE [68, 69]	1991−2000	non-imaging	NaI(Tl)	0.020−10	4π sr	N/A
COMPTEL [150]	1991−2000	Compton	liquid scintillator, NaI(Tl)	1−30	1 sr	3−4°
RHESSI [117]	2002−	RMC	coaxial Ge	0.003−17	1°	2−30″
IBIS [165]	2002−	coded-mask	CdTe, CsI(Tl)	0.015−10	9°	12′
SPI [168]	2002−	coded-mask	coaxial Ge	0.020−8	16°	2.5°

Table 1.1: A summary of soft gamma-ray telescopes, including their detector type and performance characteristics.

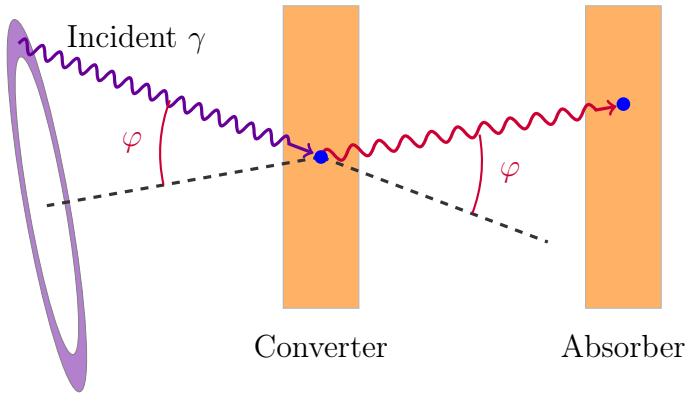

Figure 1.11: The classical Compton telescope design. The gamma ray scatters in the Converter detector and is absorbed in the Absorber detector, and time-of-flight information is used to accept or reject the event. The direction of the incoming photon is reduced to a Compton circle as shown. Compare to COMPTEL's design (Fig. 1.9).

1.4.1 Classical Compton telescopes

The idea for a gamma-ray telescope that would exploit the Compton scatter effect was first conceived in the early 1970s [60, 152]. The first instrument was built at the Max Planck Institute and flown on balloon flights in 1973, and it succeeded in measuring the spectrum of Cygnus X-2 between 1 and 10 MeV [116]. Other Compton telescopes soon followed, all of a similar design (e.g., at University of California Riverside [84] and the University of New Hampshire [120, 121]). This strand of research culminated in the COMPTEL instrument [150].

In this "classical" form (Fig. 1.11), a Compton telescope employs two sets of detectors: the Converter (**C**) and the Absorber (**A**). The gamma ray is assumed to Compton scatter in **C** and be photoabsorbed in **A**. The converter will generally be made of a low-Z detector material (e.g., liquid scintillator) to reduce the effect of Doppler broadening, and the absorber will be made of high-Z material (e.g., CsI) in order to stop the scattered photon. The telescope measures the interaction positions $\mathbf{r}_1$ and $\mathbf{r}_2$, and the energies deposited in the interactions E_1 and E_2. One can then use the two energies to reconstruct the Compton scatter angle of the incoming gamma ray. Using the direction of the scattered gamma-ray $(\mathbf{r}_1 - \mathbf{r}_2)$, the incoming gamma ray is constrained to a circle on the sky (the "Compton circle") as depicted in Fig. 1.11.

1.4.1.1 Event reconstruction in classical Compton telescopes

Time-of-flight information is generally used to reconstruct events in classical Compton telescopes. Using time-of-flight, one can tell whether the first scatter was indeed in **C** and the second was in **A**. (In many cases, the reverse ordering of a two-site

Compton event is kinematically allowed.) Assuming an average distance between **C** and **A** of 3 m (approximately the distance for COMPTEL), the time resolution needed is:

$$t_{res} \lesssim 10 \text{ ns } \left(\frac{d_{scatter}}{3\text{m}}\right) \tag{1.10}$$

which is achievable with many detector materials and signal processing electronics.

Compton kinematics can also be used to accept or reject events. If a photon of energy E undergoes a Compton scatter by angle φ in **C**, depositing energy E_1, and a photoabsorption in **A**, depositing energy $E_2 = E - E_1$, the Compton scatter formula requires that

$$E_1 = E\left(\frac{\frac{E}{m_e c^2}(1-\cos\varphi)}{1+\frac{E}{m_e c^2}(1-\cos\varphi)}\right) \quad , \quad E_2 = E\left(\frac{1}{1+\frac{E}{m_e c^2}(1-\cos\varphi)}\right). \tag{1.11}$$

Since the scatter angle is not immediately known, the energies can be in the ranges

$$0 \leq \quad E_1 \quad \leq E\left(\frac{E}{E+\frac{m_e c^2}{2}}\right) \tag{1.12}$$

$$E\left(\frac{\frac{m_e c^2}{2}}{E+\frac{m_e c^2}{2}}\right) \leq \quad E_2 \quad \leq E, \tag{1.13}$$

which imposes a kinematic constraint for $E < \frac{1}{2} m_e c^2$ but not for larger energies. Instead of all possible scatter angles φ, the range of scatter angles for observable events is determined by the detector thresholds ($\varphi_{min} \approx 15^\circ$ and $\varphi_{max} \approx 40^\circ$ at 1 MeV for COMPTEL), so these kinematic constraints will be tighter. Additional constraints can be placed on φ to reduce incorrectly reconstructed events. For example, COMPTEL used a maximum φ cut of 30° to further reduce detector background events [150].

1.4.1.2 Limitations to classical Compton telescopes

One limitation to the classical design is that there is a tradeoff between efficiency and having both reliable time-of-flight and good angular resolution. The larger the distance between **C** and **A**, the better the time-of-flight discrimination and angular resolution, but the worse the efficiency. For the COMPTEL design, the angular resolution was ≈4.7° FWHM at 1 MeV but the efficiency was only ∼0.1% [150].

Another limitation of the classical design is that besides time-of-flight and kinematic constraints, there are no tools available to reduce the number of background events. For example, if a gamma ray enters **C** and Compton scatters twice with a final photoabsorption in **A**, the observed event (interpreted as a two-site event) in

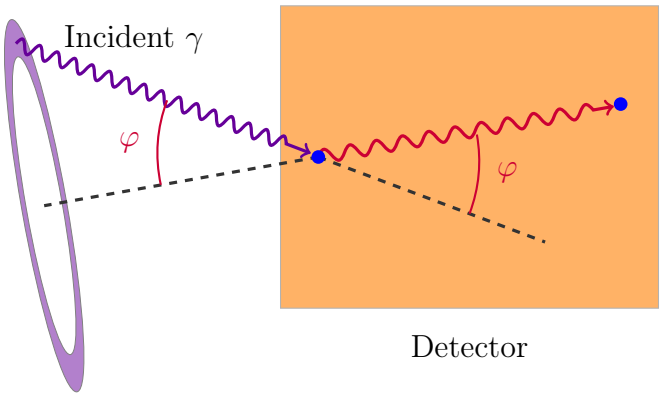

Figure 1.12: The compact Compton telescope design. The converter-absorber design has been abandoned in favor of only one 3D position-sensitive detector volume in which the photon interactions may occur. The efficiency of the compact design can be ∼2 orders of magnitude greater than the classical design.

many cases may be kinematically allowed as a two-site event. Then the reconstructed event can have a Compton circle that is very different from the original photon direction. This will limit the point source angular resolution achievable. Many types of instrumental radioactivity also cannot be rejected, such as delayed β-decay where the daughter releases a gamma ray, or many types of neutron interactions where there is a prompt gamma ray.

1.4.2 Compact Compton telescopes

In the late 1980s and early 1990s, several groups proposed a fundamental change in paradigm as new detector technologies became available. The new technologies were detectors with both high position sensitivity and high energy resolution that could further exploit the entanglement of position and energy inherent in Compton scattering (cf. equation (1.3)). The two detector planes of the classical design would be replaced by a single 3D position-sensitive detector volume (see Fig. 1.12). The detector would need to measure the 3D position and energy of single photon interactions with high spatial (∼1 mm) and energy ($\lesssim$10%) resolution. In principle, any photon whose interactions were spatially-resolved and above threshold could be reconstructed and imaged. This change in Compton telescope design greatly increases the achievable efficiencies, from ∼0.1% for a COMPTEL-like design to ∼10% [32]. The field of view would greatly increase, since a photon coming from nearly any direction has the possibility of being reconstructed.

Aprile et al. [13] proposed and built a Compton telescope using a single liquid xenon time projection chamber (TPC), instead of the two spatially-separated detector planes as had been proposed using liquid xenon in 1973 [60]. The TPC measures interaction positions with high spatial resolution (≈3 mm) and energy (≈10% at

1 MeV) resolution [12]. Soon others began testing the new technology of double-sided germanium strip detectors for use as a compact Compton telescope [107, 109]. Germanium's excellent energy resolution ($\lesssim$1% for soft gamma rays) was now combined with the fine spatial resolution, defined by the pitch of the strip electrodes (2 mm for NCT). Other instruments that are being developed include double-sided silicon strip detectors combined with scintillator calorimeters [28, 112, 141], double-sided silicon strip detectors combined with CdTe pixel detectors [160], and position-sensitive gaseous detectors combined with scintillator calorimeters [89, 166].

1.4.2.1 Event reconstruction in compact Compton telescopes

Event reconstruction becomes more challenging in compact Compton telescopes. The compactness of the detector makes it too difficult to implement time-of-flight information. Assuming an average distance between each photon scatter of $\sim$1 cm, the time resolution needed is:

$$t_{res} \lesssim 0.03 \text{ ns } \left(\frac{d_{scatter}}{1\text{cm}}\right), \tag{1.14}$$

which is not achievable by any current detector technology.

Since time-of-flight is essentially impossible, new methods have been developed to reconstruct the ordering of interactions in compact Compton telescopes [9, 31, 108, 140]. The basic idea of Compton Kinematic Discrimination (CKD) is to check each possible interaction ordering and determine the most likely ordering based on kinematic constraints. Let there be N interactions numbered from $i = 1$ to N with energy deposits E_i and positions $\mathbf{r}_i$ (see Fig. 1.13). The first $N-1$ interactions should be Compton scatters, and the last should be a photoabsorption. Using equation (1.3), the cosine of the Compton scatter angle at each interaction is determined via the energy deposits ($\cos\varphi_i$). Using the positions $\mathbf{r}_i$, the incoming and outgoing photon directions are calculated for $i = 2$ through $N-1$ ($i = 1$ is the initial scatter, so no incoming direction is known, and $i = N$ is a photoabsorption with no outgoing photon). Thus the cosine of the scatter angle at these locations can be inferred: $\cos\tilde{\varphi}_i$. The uncertainties of the cosine measurements can be calculated using the energy resolution of the detectors (to get $\sigma_{\cos\varphi_i}$) and the position resolution of the detectors (to get $\sigma_{\cos\tilde{\varphi}_i}$). A figure-of-merit is constructed that is the reduced χ^2 of the matching of energy and position measurements:

$$\chi^2_{CKD} = \frac{1}{N-2}\sum_{i=2}^{N-1}\frac{\left(\cos\varphi_i - \cos\tilde{\varphi}_i\right)^2}{\sigma^2_{\cos\varphi_i} + \sigma^2_{\cos\tilde{\varphi}_i}} \tag{1.15}$$

(cf. (13) from [31]). The value of this statistic should be ≈ 1 for a kinematically-allowed ordering and much greater for a non-physical ordering. Each of the $N!$ interaction orderings should be checked in order to find the best ordering. Once an

ordering is chosen, the axis of the Compton cone is calculated ($\mathbf{r}_2 - \mathbf{r}_1$) and the Compton scatter angle is calculated (φ_1).

Though this event reconstruction requires more computation than the classical method, and is "indirect" in the sense that no time-of-flight is used, a great benefit is achieved from the reconstruction of multiple-site events: χ^2_{CKD} is a powerful tool to reject background events. For example, if a multiple-site event has two Compton scatters that are very close and are resolved as only one interaction, there is a good chance that none of the $N!$ orderings will be kinematically allowed, leading to a large χ^2_{CKD}. Similarly, a neutron scattering event may also not be kinematically allowed. Cutting out events with large χ^2_{CKD} values will greatly improve the rejection of background events.

Because CKD requires internal Compton scatters (as can be seen in equation (1.15)), two-site events cannot be reconstructed using the method. Other techniques have been developed, such as using the simple two-site kinematic discrimination used in classical Compton telescopes. However, it has been found that as a consequence of the compactness of the detectors, the vast majority of two-site events over 500 keV have an initial backscatter (i.e., $E_1 > E_2$), so a simple rule can be used instead [31]. Efforts to improve on this method include choosing the ordering that maximizes the product of the Klein-Nishina differential cross section for the scatter and the probability of photoabsorption of the scattered photon, which has been used with NCT.

Lastly, other methods of event reconstruction have been implemented in compact Compton telescopes that exploit recent advances in computation. Neural networks have been tried with success on NCT [179], as well as Bayesian methods [182]. Both methods involve selecting an appropriate set of event parameters (e.g., photon energy, number of interactions), creating a large simulated dataset, applying the detector response to the simulated events, and then training the computer on the events. Preliminary results show better performance than the CKD method.

1.4.2.2 Further discussion

As the energy and position resolutions of detectors has greatly improved, compact Compton telescopes are finding themselves approaching the Doppler broadening limit of a Compton telescope. The Doppler broadening limit is a fundamental limit to Compton telescopes that is a result of using the idealized Compton scatter formula (1.3), which does not account for the energy and momentum of a bound atomic electron [3, 183]. Doppler broadening depends on the Z of the material; generally, higher Z leads to a higher Doppler broadening limit. Therefore, a tradeoff emerges between requiring high-Z detectors for gamma-ray stopping power but wanting low-Z detectors to reduce Doppler broadening.

Another reason to prefer low-Z materials is that in such materials, the Compton electron may be tracked. This is the principle of a few Compton telescopes, such

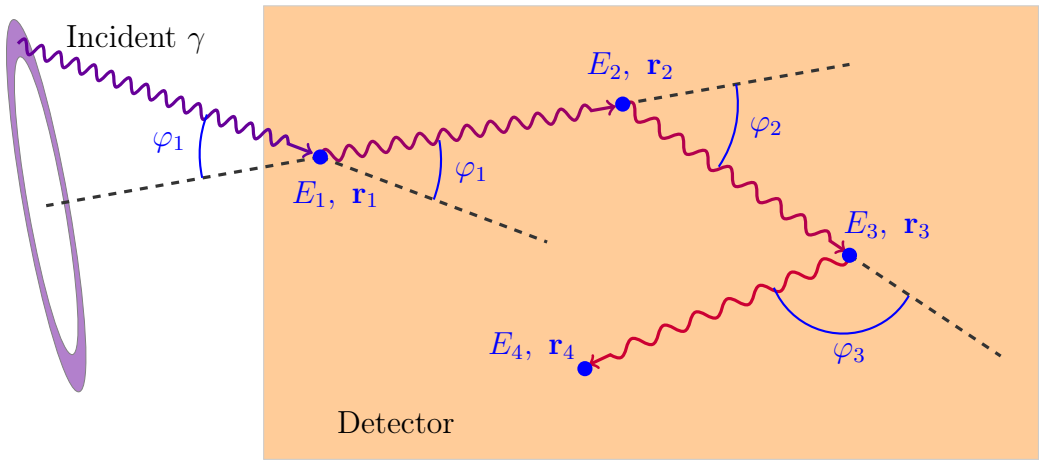

Figure 1.13: Compton event reconstruction using Compton Kinematic Discrimination (CKD). Here we have shown one possible ordering of four interaction sites. The figure-of-merit χ^2_{CKD} is constructed from this ordering by checking whether the energy-derived Compton scatter angles and the geometry-derived Compton scatter angles of the two internal scatters ($i = 2$ and 3) are consistent. This method allows the rejection of background events by cutting out events that are not kinematically allowed.

as MEGA [98] and TIGRE [185]. These two telescopes use silicon strip detectors surrounded by a calorimeter. The main advantage to measuring the direction of the Compton electron is that the photon can be traced to an arc on the sky, not a circle, which improves signal-to-noise. Another advantage to such detectors is that they can double as Compton telescopes and pair telescopes, extending their energy range well into the tens of MeV.

1.4.3 Comparison with other types of gamma-ray telescopes

Compton telescopes have distinct advantages over other kinds of instruments. By performing direct imaging, the sensitivity of a Compton telescope becomes source-limited instead of background-limited as in indirect imagers. Compact Compton designs, by improving the efficiency of Compton telescopes and in most cases the spectral resolution, greatly increase the number of counts from weak sources. Also, techniques like CKD are able to reject more background events than in classical telescopes. Both of these improvements lead to a great sensitivity leap over both classical Compton telescopes and indirect imagers. Figure 1.14 shows this sensitivity improvement for the Advanced Compton Telescope, a proposed space-borne compact Compton telescope (see Section (1.4.5)). The figure shows a plot of the expected sensitivity of ACT, along with the equivalent sensitivities of COMPTEL and SPI and estimated sensitivities needed to observe various line sources.

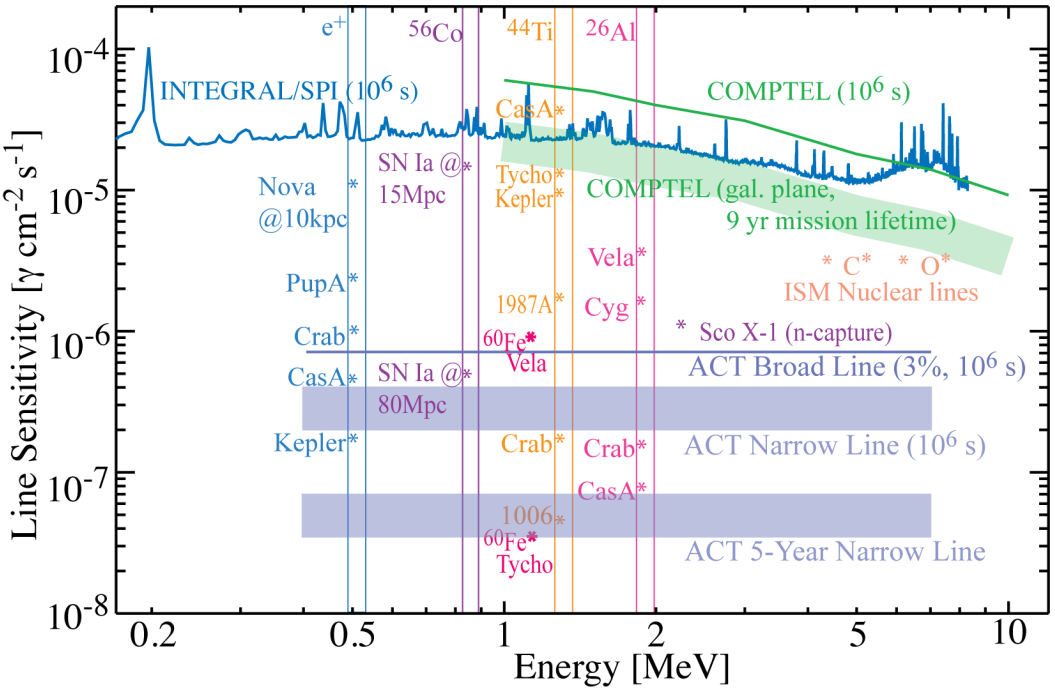

Figure 1.14: The expected sensitivity of the Advanced Compton Telescope, a proposed space-borne compact Compton telescope. Equivalent sensitivities of COMPTEL (for 10^6 seconds and the entire mission lifetime) and SPI (for 10^6 seconds) are shown for comparison. There is a large improvement in using compact Compton telescopes instead of classical Compton or indirect-imaging designs. Various line sources are labeled, suggesting many possible discoveries for ACT. Image from Fig. 1 of [34].

Compton telescopes have another great advantage over other kinds of telescopes — intrinsic sensitivity to polarization. Since the Klein-Nishina cross section depends on the polarization of the source (cf. (1.5)), any instrument that uses the Compton effect has the possibility of measuring polarization. As discussed earlier, gamma-ray polarization is a vital marker of the emission processes occurring in continuum sources and can probe the magnetic fields of AGN and GRBs.

1.4.4 Compact Compton balloon-borne telescopes

Over the last decade, compact Compton telescopes have been built, tested, and flown on high-altitude balloons by several groups. The five that have been extensively tested are listed in Table 1.2 with their performance characteristics. There have been six balloon flights to date of these projects, most of which have only succeeded in measuring the gamma-ray background (see Table 1.3). The discussion in this work will pertain to the most recent flight of NCT, which has detected the Crab nebula in

soft gamma-rays. This is the first detection of an astrophysical source by a compact Compton telescope.

1.4.5 The Advanced Compton Telescope

The current goal for all of the balloon-based compact Compton telescopes is to develop technologies for an eventual space-based Compton telescope. This telescope currently goes by the working title Advanced Compton Telescope (ACT) and is meant to be the next-generation equivalent of COMPTEL. The leap in technology from COMPTEL to the current instruments means that ACT may achieve an improvement of a factor of $\gtrsim$50 in sensitivity over COMPTEL. All compact Compton technologies are currently being investigated for use in ACT, though hybrids of germanium and silicon are among the most competitive designs [34].

1.5 Summary

An overview of the astrophysical topics available in the soft gamma-ray regime has been presented, along with a discussion of soft gamma-ray instruments. Compton telescopes, with their direct imaging capabilities and ability to perform background rejection, have a distinct advantage in sensitivity over other kinds of instruments to answer these key questions. NCT is one of the current generation of compact Compton telescopes, and NCT's germanium detectors are among the top competing technologies in the field.

Project	**Detector(s)**	**Energy Resolution (FWHM, keV)**	**Position Resolution (mm^3)**	**Angular Resolution (FWHM)**	**Effective Area @ 1 MeV (cm^2)**
LXeGRIT [11, 57]	liquid xenon TPC	83 @1 MeV	3×3×0.6	7° @1.8 MeV	29
TIGRE [185]	Tracker: double-sided Si strip Calorimeter: NaI(Tl) and CsI(Tl)	11 @122 keV 33 @662 keV	0.76×0.76×0.3 10×10×35	4.7° @1 MeV	80
MEGA [98, 184]	Tracker: double-sided Si strip Calorimeter: CsI	23 @122 keV 89 @662 keV	0.47×0.47×0.5 5×5×20	10° @2 MeV	46
ETCC (SMILE) [166]	Tracker: gaseous micro-TPC Calorimeter: GSO(Ce)	N/A 112 @662 keV	0.40×0.40 (2D) 6×6×13	12° @662 keV	10^{-4}
NCT [17, 18, 30]	Ge double-sided strip	2.5 @662 keV	2×2×0.6	6° @1 MeV	8

Table 1.2: A summary of balloon-borne compact Compton telescopes, including their detector type and performance characteristics.

Project	**Date**	**Location**	**Float Duration**	**Measurements**
LXeGRIT	7 May 1999	New Mexico	7 hr	Gamma-ray background spectrum and rates; compared to simulations [14]
LXeGRIT	4−5 October 2000	New Mexico	24 hr	Gamma-ray background; Crab would be at $\sim 2\sigma$ significance [10, 58]
NCT	1 June 2005	New Mexico	6 hr	Gamma-ray background spectrum; compared to simulations [41, 53]
ETCC (SMILE)	1 September 2006	Japan	4 hr	Gamma-ray background spectrum; compared to simulations [159]
TIGRE	2−3 June 2007	New Mexico	20 hr	Planned study of gamma-ray background and event cuts [186, 187]
NCT	17−18 May 2009	New Mexico	22 hr	Gamma-ray background spectrum [18] and 4σ detection of Crab (this thesis)
TIGRE	March 2010	Australia	52 hr	None reported to date.

Table 1.3: A summary of compact Compton telescope balloon flights to date.

Chapter 2

Soft Gamma-ray Emission from the Crab Nebula

2.1 Introduction

The Crab Nebula (Messier 1) was discovered by John Bevis in 1731 [85]. It was conclusively identified in the 1940s with the historical supernova recorded by Chinese and Japanese astronomers that occurred on July 4, 1054 [64,130]. Our understanding of the Crab has advanced considerably since the advent of radio and high-energy astronomy in the twentieth century. Today the Crab Nebula is known to be a cloud of expanding magnetized relativistic plasma housing a pulsar (the Crab Pulsar), which was formed as the result of a core-collapse supernova. The Crab, as it is often called, is one of the brightest radio, X-ray, and gamma-ray sources, and its spectrum has been measured in every photon waveband yet explored. Figure 2.1 shows a composite image of the Crab Nebula in optical, infrared, and X-rays.

2.2 Observational history

The Crab Nebula was first detected in radio by Bolton, Stanley, and Slee in 1949 [38, 39]. They and others [132, 155] refined the radio position and identified the radio source with the Crab Nebula optical source. It was immediately apparent to the discoverers that the implied effective blackbody temperature (2×10^6 K) was too high for the radio emission to be thermal emission, so a non-thermal source of emission was required [38, 39].

Emission from the nebula was subsequently detected in all photon bands from radio through optical. X-ray and gamma-ray emission has also been observed. Soft X-ray emission around 4 keV was first measured in 1964 by Bowyer et al. using a rocket-borne experiment [43, 44], and a power-law spectrum was seen to continue through the hard X-ray [49, 75, 145] and gamma-ray regimes [16, 59, 81]. Emission in

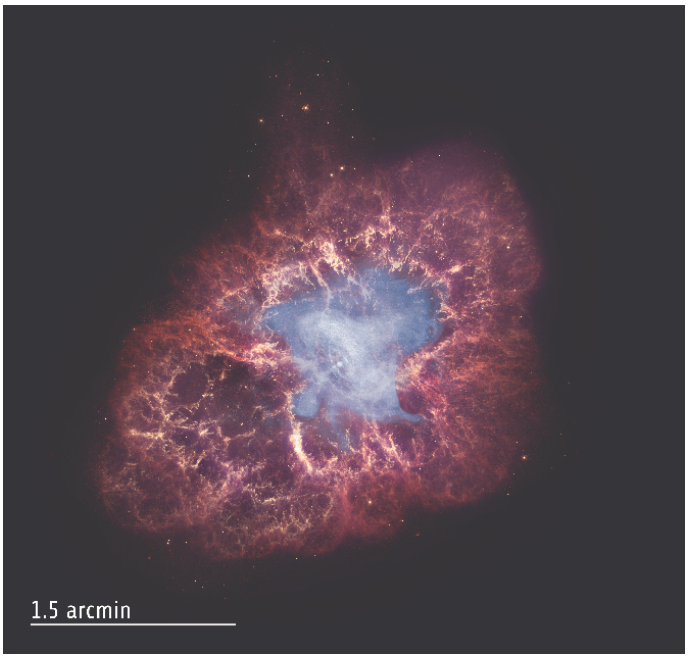

Figure 2.1: Image of the Crab Nebula in optical (red), infrared (purple), and X-rays (blue). Image credit: X-ray: NASA/CXC/SAO/F.Seward; Optical: NASA/ESA/ASU/J.Hester & A.Loll; Infrared: NASA/JPL-Caltech/Univ. Minn./R.Gehrz.

the TeV regime has also been observed by ground-based Cherenkov telescopes [169].

The brightness of the source, as well as its angular separation from other high-energy sources and its steady flux, make it a perfect candidate for an in-flight calibration source for X-ray and gamma-ray instruments [163]. As of this writing, the spectrum of the Crab in X-rays and gamma rays is so well-measured that it is used to cross-calibrate X-ray and gamma-ray telescopes (recently INTEGRAL and XMM-Newton [95, 102]).

The current celestial coordinates of the Crab pulsar and nebula are $\alpha = 05^h34^m31.9^s$, $\delta = +22°00'52.1''$, or $\ell = 184.5575°$, $b = -5.7843°$ in galactic coordinates [62].

2.3 Emission from the Crab nebula

The source of the Crab nebula's energy was found in 1968, when Staelin and Reifenstein detected a pulsar in the region of the Crab nebula [156]. This pulsar was among the first pulsars ever discovered, coming on the heels of the original discovery of pulsars by Hewish et al. [87]. It is also one of the few pulsars known to pulsate in the optical [137, 174]. Contemporaneously with these discoveries, it was suggested that pulsars could be rapidly rotating neutron stars, and that their emission would be

powered by the spin-down of the star, primarily through magnetic dipole radiation [73, 78, 143, 144]. The spin-down energy of the Crab pulsar was soon proposed as the source of the nebula's luminosity [67, 171], and the broad-band emission was explained as the result of relativistic electrons radiating in the nebula's magnetic field (i.e., synchrotron radiation) [153].

2.3.1 Spin-down luminosity

The standard theory is that the Crab pulsar is a rapidly-rotating magnetized neutron star. The pulsar is thought to be a typically-sized neutron star, with a radius of $R \approx 10$ km and mass $M \approx 1.4 M_\odot$ [85]. The Crab pulsar has an observed pulse period P of 33 ms, which is identified with the star's rotation period, and the period is observed to be increasing. This loss of rotational kinetic energy is the energy source powering the nebula emission.

The spin-down parameters for the Crab as of this writing are [123][1]:

$$\begin{aligned} \nu &= 29.7240976420 \text{ Hz} \\ \dot{\nu} &= -3.7128861 \cdot 10^{-10} \text{ s}^{-2} \end{aligned}$$

which can be used to calculate the current period and period derivative:

$$\begin{aligned} P &= 33.642737 \text{ ms} \\ \dot{P} &= 4.2023698 \cdot 10^{-13} \text{ s s}^{-1} \end{aligned}$$

The moment of inertia of the Crab can be estimated by assuming it is a hard sphere:

$$I \approx \frac{2}{5} M R^2 \sim 1.1 \times 10^{45} \text{ g cm}^2. \tag{2.1}$$

Some have argued that this value should be closer to 2 or 3×10^{45} g cm^2 [20]. Then the loss of rotational kinetic energy (the "spin-down luminosity") can be estimated:

$$L_{spin} = -I \Omega \dot{\Omega} = -(2\pi)^2 I \nu \dot{\nu} \sim 4.8 \times 10^{38} \text{ erg s}^{-1} \tag{2.2}$$

The total observed synchrotron luminosity is [85]

$$L_{sync} \approx 1.3 \times 10^{38} \text{ erg s}^{-1}, \tag{2.3}$$

which is approximately 25% of L_{spin} — so, somewhat surprisingly, the emission process is very efficient. Of the remaining energy, another 25% goes into thermodynamic work on the expanding shell and 50% is stored in the nebula [85].

[1] `http://www.jb.man.ac.uk/~pulsar/crab.html`

2.3.2 A simple model: Energy loss through magnetic dipole radiation

What is the mechanism for the loss of rotational energy by the pulsar? The classical model is that large magnetic fields ($\sim 10^{12}$ G) cause the rotating star to radiate at frequency Ω and thus lose energy. Following [78], the magnetic dipole radiation model says that the rate of energy loss should be

$$L_{dipole} = -\frac{2|\vec{m}|^2 \sin^2\theta \Omega^4}{3c^3} \tag{2.4}$$

where θ is the angle between the rotation axis and magnetic dipole and $\vec{m}$ is the magnetic dipole moment. The magnitude of the dipole moment can be estimated as

$$|\vec{m}| = \frac{1}{2} B_p R^3 \tag{2.5}$$

where B_p is the magnetic field on the surface of the star at the magnetic pole. The dipole radiation luminosity can be rewritten:

$$L_{dipole} = -\frac{B_p^2 R^6 \sin^2\theta \Omega^4}{6c^3} \tag{2.6}$$

Equating L_{dipole} with L_{sync} yields an estimate of the magnetic field at the pole of the Crab pulsar:

$$B_p \sim 8 \times 10^{12} (\sin\theta)^{-2} \text{ G}. \tag{2.7}$$

This field is in the range one would expect for the collapsed core of a main sequence star with a frozen-in magnetic field [176]. Magnetic fields of this magnitude allow the transfer of rotational kinetic energy into the surrounding nebula and beyond.

If energy loss were due to this mechanism alone, and the magnetic field were constant, then we could solve for the frequency derivative as a function of frequency:

$$L_{spin} = -I\Omega\dot{\Omega} = -\frac{B_p^2 R^6 \sin^2\theta}{6c^3}\Omega^4 \tag{2.8}$$

$$\Rightarrow \dot{\Omega} \propto \Omega^3. \tag{2.9}$$

But for the Crab pulsar, $\dot{\Omega} \propto \Omega^n$, where the "braking index" $n \approx 2.51$ [123]. So there must be a modification to this basic model.

2.3.3 Magnetohydrodynamic (MHD) models

In reality, the magnetic field of the neutron star is not isolated in a vacuum (as was assumed in the simple model), but the field should be interacting with the plasma medium around the star in a more complex way. Goldreich and Julian [74]

were the first to consider such a model — the "aligned rotator" case ($\theta = 0°$) of the rotating magnetic dipole with a circumstellar plasma. Instead of losing energy through magnetic dipole radiation, the star loses energy from magnetic torque caused by the "winding up" of the star's magnetic field as it spins. A consequence of their model is that magnetized pulsars must have dense, co-rotating magnetospheres within the light cylinder of the star. (The light cylinder is defined by the radius at which a co-rotating point would be traveling at the speed of light: $R_{light} = c/\Omega \sim 2 \times 10^8$ cm for the Crab.) Any field lines that do not close within the light cylinder are open, and charged particles from the surface of the star are accelerated along these field lines out of the polar regions (see Fig. 2.2). The particles can be accelerated to energies perhaps as high as $E_{max} \sim 2 \times 10^{14} Z$ eV for a nebula magnetic field of $B_n \sim 2 \times 10^{-4}$ G and particle charge of Z.

An attempt to synthesize Goldreich and Julian's effort with the magnetic dipole model into a self-consistent theory for the Crab came in 1974 with Rees and Gunn [148]. They noted that an oblique rotator would produce both magnetic dipole radiation and a wind of accelerated charged particles. In addition, the magnetic and electric field structure of the wind itself carries a third kind of energy: Poynting flux. They then considered the pressure of these outflows impacting the surrounding material of the nebula and predicted a shock at $R_s \sim 0.07 R_n$, where R_n is the radius of the nebula. They predicted that at the shock radius, accelerated electrons would undergo ordinary synchrotron radiation, which would lead to the high degree of linear polarization observed. They also predicted that any pulsed magnetic dipole emission would be absorbed in the shock region and the energy transferred to the relativistic charged particles, so only synchrotron emission would remain.

Kennel and Coroniti [100] sought to make the Rees and Gunn model even more self-consistent and include newer understandings of magnetized plasmas, such as the production of pairs in a hot relativistic plasma. They constructed a steady-state spherically-symmetric MHD model of the pulsar surface and nebula. The basic features they found are that the Crab should launch a very dense highly relativistic pair plasma from its surface, and this MHD wind would be decelerated approximately 0.1 pc from the pulsar in a strong MHD shock. Their calculation of the synchrotron spectrum resulting from their model fit the available X-ray and gamma-ray data well [101]. As of this writing, this model is the standard model for the acceleration of the pulsar wind and subsequent nebular emission [85].

2.3.4 The synchrotron spectrum of the nebula

Let us now explore some of the implications of a population of relativistic electrons and positrons undergoing synchrotron radiation in the Crab nebula. A typical assumption about such a population is that the particles have a power-law distribution in energy: $\frac{dN}{dE_e} \propto E_e^{-p}$, or equivalently $\frac{dN}{d\gamma} \propto \gamma^{-p}$ where $E_e = \gamma m_e c^2$. Assuming a uniform nebular magnetic field B, the population of particles will emit synchrotron

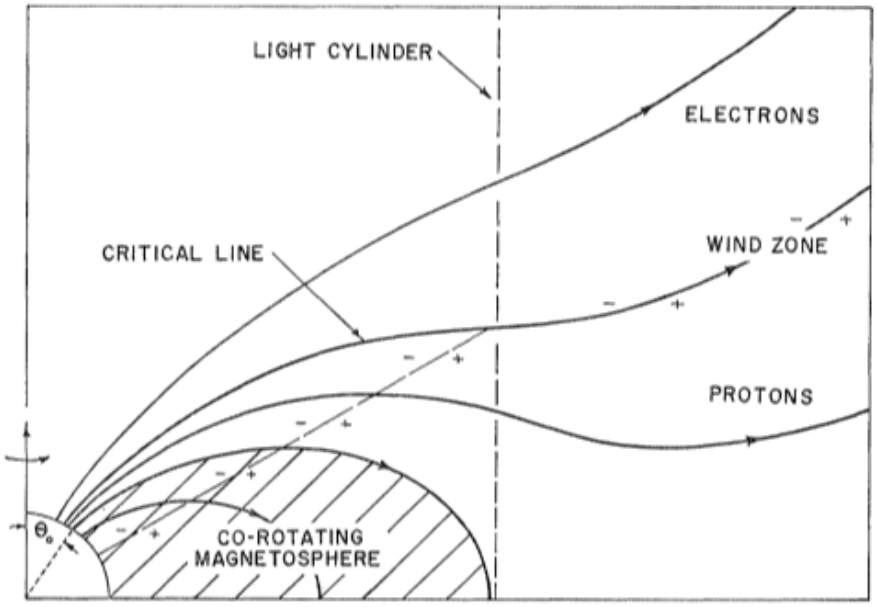

Figure 2.2: The basic picture of the magnetic field lines of the Crab, showing the co-rotating magnetosphere within the light cylinder and the open field lines along which charged particles are accelerated. Figure 1 from [74].

radiation with a power-law spectrum, and the spectral index will be $(p-1)/2$ [149]. A look at the broadband Crab spectrum (Fig. 2.3) reveals three approximately power-law regions separated by two breaks — one in the optical and one in the hard X-rays. These breaks can be understood as the results of different physical processes affecting the particle population.

2.3.4.1 The optical break

The optical break can be explained as a result of when the synchrotron cooling timescale of the particles approaches the age of the nebula. The synchrotron power emitted by a single highly relativistic electron in a magnetic field B, after averaging over pitch angle, is [149]

$$P = \frac{4q_e^4 B^2 \gamma^2}{9m_e^2 c^3}. \tag{2.10}$$

Since $E_e = \gamma m_e c^2$ and $\dot{E}_e = -P$, we find

$$\dot{\gamma} = -\frac{4q_e^4 B^2}{9m_e^3 c^5}\gamma^2 \tag{2.11}$$

which leads to the solution

$$\gamma(t) = \gamma_0(1 + t/\tau)^{-1} \tag{2.12}$$

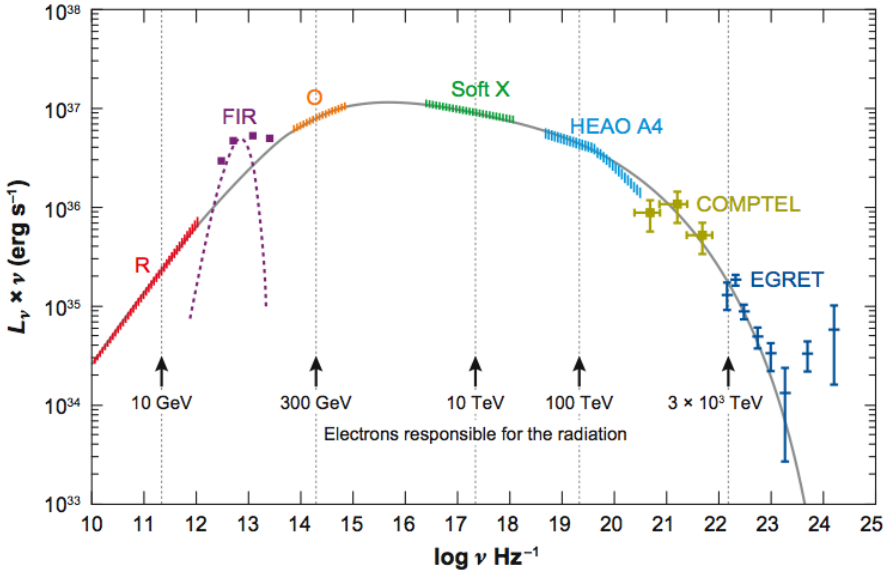

Figure 2.3: Broadband spectrum of the Crab nebula, including radio (R), far infrared (FIR), optical (O), soft X-rays, soft gamma rays (HEAO A4), medium-energy gamma rays (COMPTEL), and GeV gamma rays (EGRET). NCT's energy range is comparable to the upper part of HEAO A4's range and the lower part of COMPTEL's range. The energies of the electrons emitting the synchrotron radiation are labeled (note that $h\nu_c \propto \gamma_0^2 \propto E_e^2$ as seen in (2.15)). The spectral break in the optical is due to the short emission lifetime of the high-energy electrons, while the spectral break in the soft gamma rays is due to the electron acceleration process. Figure 2 from [85], which is based on a plot in [15].

where γ_0 is the Lorentz factor of the electron when it is initially accelerated and τ is the time it takes the electron to emit half of its energy. Using the equipartition estimate of 3×10^{-4} G for B [164], this timescale is

$$\tau = \frac{9 m_e^3 c^5}{4 q_e^4 B^2 \gamma_0} \tag{2.13}$$

$$\sim 900 \text{ yr} \left(\frac{\gamma_0}{3 \times 10^5} \right)^{-1} \left(\frac{B}{3 \times 10^{-4} \text{ G}} \right)^{-2} . \tag{2.14}$$

Since the supernova remnant is known to be only ≈ 1000 yr old, this result means that particles with energies greater than $\sim (3 \times 10^5) m_e c^2 = 150$ GeV cool rapidly, while those with lower energies cool on a timescale that is longer than the present age of the supernova remnant. This situation should lead to a break in the power-law index of the electron and positron population, with the index p softening for energies above ~ 150 GeV.

Since an electron of a given energy emits synchrotron radiation around a characteristic frequency ν_c, one should expect a spectral break in the observed emission as a

signature of the spectral break in the electron population. The characteristic energy of the synchrotron emission from a single highly-relativistic electron is [149]

$$\begin{aligned} E_c &\sim \frac{\hbar\gamma_0^2 q_e B}{m_e c} \\ &\sim 0.10 \text{ eV } \left(\frac{\gamma_0}{3\times10^5}\right)^2 \left(\frac{B}{3\times10^{-4} \text{ G}}\right) \qquad (2.15) \\ \Rightarrow \nu_c = E_c/h &\sim 2.4\times10^{13} \text{ Hz}, \qquad (2.16) \end{aligned}$$

which is in the infrared. This is within an order of magnitude of the break that is observed in the optical ($\nu_{\text{break}} \sim 2\times10^{14}$ Hz; see Fig 2.3).

2.3.4.2 The hard X-ray break

For photon energies above the optical break, the electrons and positrons producing the synchrotron emission have shorter lifetimes than the age of the nebula and therefore the photon emission is sensitive to the flow of particles in the inner nebula. In Kennel and Coroniti's model [100], electrons and positrons in the pulsar's pair plasma wind are accelerated in an MHD shock at a radius of $r_s \approx 3\times10^{17}$ cm and then undergo synchrotron radiation in the nebular magnetic field while being transported outward in an MHD flow [101]. Particles that radiate above the optical regime cool significantly before reaching the outer edge of the nebula at $r_N \approx 2$ pc. Therefore, above the optical regime, the power-law index of the spectrum will gradually steepen as less and less of the nebular volume is responsible for the radiation. This volume effect can be crudely seen in Fig. 2.1, where the X-ray region is very close to the central pulsar, while the optical and infrared emission regions are much larger. This is one effect that leads to the gradual softening through the X-ray and gamma-ray regimes.

Another prediction of the Kennel and Coroniti model that affects the high-energy spectrum is that there should be an upper limit to the allowed energies of accelerated particles. This limit is set by requiring that the Larmor radius of the particles be no greater than the size scale of the acceleration region in the MHD shock ($\sim r_s$). Since the Larmor radius is $r_L = \gamma\beta_\perp m_e c^2/q_e B \approx E_e/q_e B$ (using $\gamma \gg 1$), the upper energy limit is

$$\begin{aligned} E_{e\,max} &\sim q_e B r_s \\ &\sim 3\times10^4 \text{ TeV}. \qquad (2.17) \end{aligned}$$

The synchrotron spectrum will begin rapidly falling away as the required particle

energies approach this limit. The photon energy emitted by particles at this limit is

$$\begin{aligned} E_{c\,max} &\sim \frac{\hbar E_{e\,max}^2 q_e B}{m_e^3 c^5} \\ &\sim 10 \text{ GeV} \\ \nu_{c\,max} &\sim 2 \times 10^{24} \text{ Hz.} \end{aligned}$$

Kennel and Coroniti predict a lower value of $\nu_{c\,max} \sim 10^{22}$ Hz, or $E_{c\,max} \sim 50$ MeV, in the medium-energy gamma-ray regime. A rapid decrease in the synchrotron spectrum as the photon energy approaches $\nu_{c\,max}$ can be seen in Kennel and Coroniti's calculated model spectrum (Fig. 2.4) as well as the broadband spectrum from earlier (Fig. 2.3). Though hard X-rays ($E \sim 100$ keV, $\nu \sim 2 \times 10^{19}$ Hz) have much lower energies than $E_{c\,max}$, the break in the hard X-rays is a result of the rapidly decreasing availability of particles able to supply the emission. Since $E_{e\,max}$ and $E_{c\,max}$ depend strongly on the structure of the MHD flow in the nebula, any measurement of the rapid softening of the spectrum constrains the physics in the inner nebula.

Lastly, it should be pointed out that the persistence of emission at photon energies above $\sim$ 100 MeV can be explained by inverse Compton emission. This emission occurs when ambient photons (e.g., from synchrotron radiation) scatter with high-energy electrons. The upper limit of (2.17) is corroborated by others who try to explain the observed TeV photon emission of the nebula (e.g., [15, 80]).

2.4 Measurements of the soft gamma-ray spectrum of the Crab

Though the soft gamma-ray spectrum of the Crab nebula has been measured by many instruments over the last few decades, here we will focus on several results that are of particular relevance to this work. A full list of gamma-ray observations of the Crab nebula and pulsar can be found in [119].

The first measurement of gamma rays from the Crab was by Haymes et al. in 1968 [81]. They measured the flux in the range 35 keV$-$560 keV and noticed that their data implied a steeper power-law than prior hard X-ray spectrum measurements alone. Fitting both the hard X-ray and gamma-ray data, they reported an index of 2.19$\pm$0.08. The gamma-ray data alone implied a softer index. This was the first clue to the hard X-ray spectral break mentioned in the previous section.

Later missions confirmed these basic results. From 1977$-$1979, the HEAO A-4 instrument on board the HEAO-1 satellite measured the spectrum of the Crab nebula and pulsar in the range 10 keV$-$5 MeV [97]. They confirmed that there is a need for a spectral break around 100 keV. The break represented a softening of the spectrum, with the power-law index changing from 2.08 for 10$-$100 keV to $\approx$2.5 for energies above 150 keV. Likewise, the GRIS balloon experiment measured the Crab between

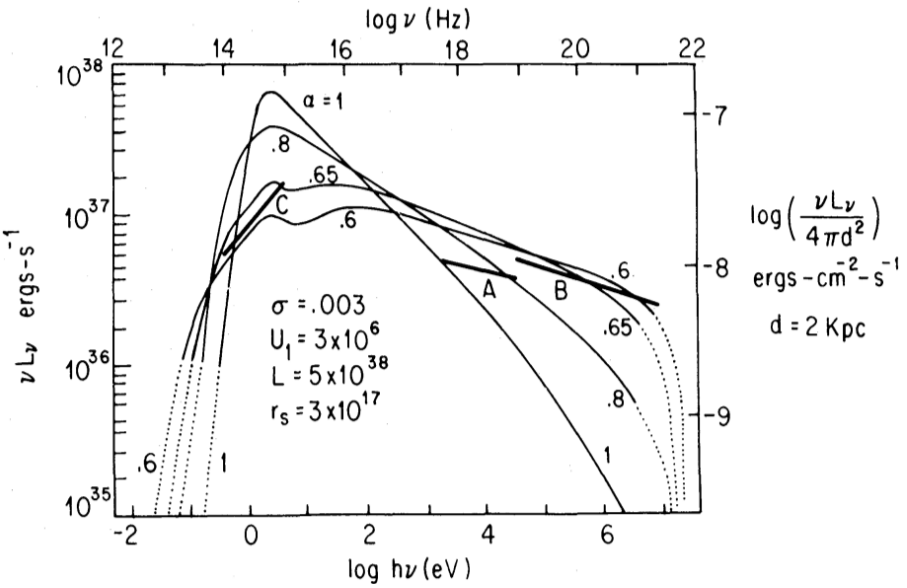

Figure 2.4: The predicted synchrotron spectrum of the Crab nebula from the MHD model of Kennel and Coroniti [100, 101]. The bold lines labeled A, B, and C are observations in the X-ray, gamma-ray, and optical-UV ranges, respectively. The thin lines are the predictions for different power-law indices of the accelerated particles. The model predicts an optical break as well as a rapid steepening in the gamma-rays, which matches the spectrum in Figure 2.3 as well. Figure 12 from [101].

20 keV and 8 MeV, also concluding that a broken power-law was needed to describe the spectrum [19]. In their case, they used a break energy of 60 keV, with power-law indices of 2.00 below the break and 2.22 above the break.

In the 1990s, the Compton Gamma Ray Observatory (CGRO) flew in low Earth orbit with four gamma-ray experiments that measured the spectrum of the Crab — the COMPTEL [150], BATSE [69], OSSE [94], and EGRET [99] experiments. Spectral measurements of the total Crab emission and the pulsar emission were used to cross-calibrate all the instruments [136]. Detailed analyses of the Crab spectrum were published by BATSE, COMPTEL, and EGRET [110, 119, 138]. EGRET's measurements [138] were made above 50 MeV and so are out of the scope of this discussion.

BATSE measured the gamma-ray spectrum of the Crab nebula and pulsar in the range 30 keV−1.7 MeV [119]. BATSE confirmed the standard spectrum — that for 35 keV−670 keV a broken power-law was needed with break energy of 112 keV, lower index of 2.10, and higher index of 2.35. However, they noticed an upturn in the spectrum from 670 keV−1.7 MeV, reporting a harder power-law with index 1.75. Another new result from BATSE was that their measured fluxes below 300 keV over the mission lifetime was not consistent with a constant flux. They estimated a timescale of days to weeks for the variability.

The COMPTEL results contradicted these two new claims by BATSE of variability

and a harder spectrum above 700 keV, but confirmed the standard spectral shape [110, 135, 167]. From 0.75 MeV to 3 MeV, photons were divided up into whether they were part of the pulsed emission (i.e., directly from the pulsar) or from the nebula emission. Separate spectra were measured, with the nebula-only spectrum having a power-law index of 2.227±0.013 and the pulsar spectrum having a softer power-law index of 2.35±0.06 (see Fig. 2.5). Because the spectra of both the nebula and pulsar were separated, COMPTEL was able to report the pulsed fraction of the total emission as a function of energy (Fig. 2.6). For NCT's energy range, the pulsed fraction is approximately 20%.

Since the end of the CGRO mission, SPI on board the INTEGRAL satellite [168] has measured the Crab spectrum in the range 23 keV to 6 MeV [96] (see Fig. 2.7). Once again, a single power-law description of the spectrum is inferior to a broken power-law with a break at 100 keV and indices of 2.07 and 2.23. As in the COMPTEL analysis, the SPI data refutes the BATSE claims of hardening above 700 keV and flux variability. In fact, SPI reports flux that is constant over the six-year timescale of the data. The authors of [168] note that the spectral break energy is sensitive to systematic errors, and to avoid this problem they fit a spectral model with a constantly-varying spectral index:

$$F(E) = 3.87 \times E^{-1.79-0.134\log_{10}(E/20)} \text{ cm}^{-2} \text{ s}^{-1} \text{ keV}^{-1} \tag{2.18}$$

where E is the energy in keV, and signs and notation have been corrected from [96]. This model fits the SPI data better than a broken power-law.

It should also be noted that SPI and others have searched for spectral features such as the positron annihilation line and cyclotron absorption lines, but no narrow line features have ever been found [96]. Such features may eventually be found — a positron annihilation line because positrons are predicted to be in the pulsar wind, and cyclotron absorption lines because the magnetic field of the pulsar is very large near the pulsar's surface.

While no gamma-ray lines or cyclotron absorption lines have been observed in the soft gamma-ray spectrum, it is clear that there is at least one feature in the spectrum at hard X-rays and soft gamma rays — a softening of the spectrum. No single power-law fit is favored, with all analyses favoring a break around 100 keV and a softening of the index above that energy. The SPI analysis has taken this modeling one step further to avoid large uncertainties on the value of the fitted break energy by using a model with a continually softening power law index. This spectral fit was adopted for the NCT Crab simulations.

2.5 Summary

The Crab nebula has been studied extensively over the past few decades. The spectrum of both the persistent and pulsed emission has been measured multiple

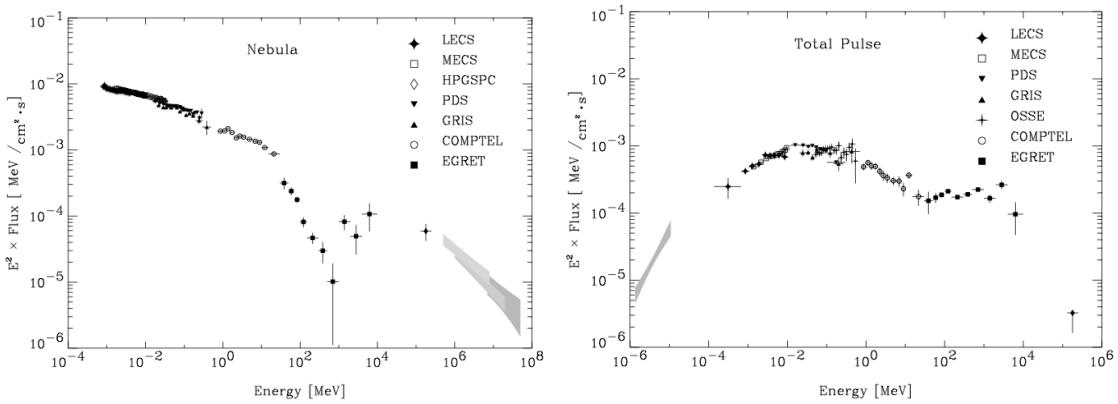

Figure 2.5: Spectra of the Crab nebula alone (left) and the pulsar (right), compiled from COMPTEL and other hard X-ray and gamma-ray instrument data. Figures 8 and 9 from [110].

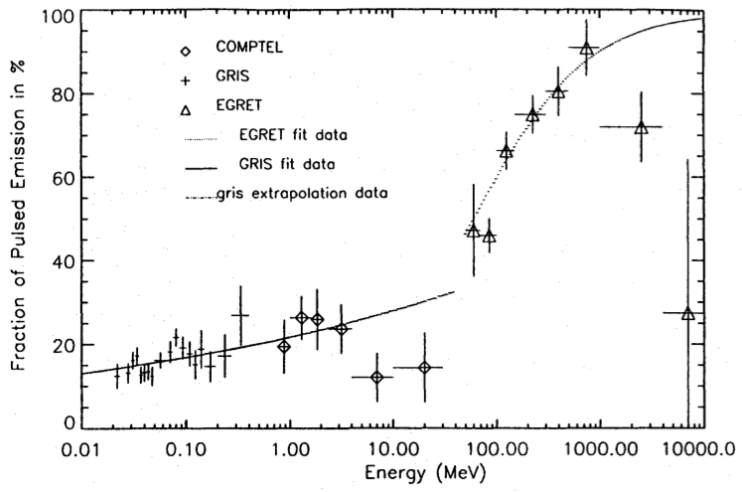

Figure 2.6: Pulsed fraction of total flux from COMPTEL measurements. For NCT's energy range, the fraction is approximately 20%. Fig. 6 from [135].

times in the soft gamma-ray regime and is found to have a constant flux over the timescale of years. The spectrum is well-fit by a broken power-law or constantly softening power-law, and no line features have been found to a high sensitivity. This break in the spectrum can be understood as a result of the short emission lifetime of the electrons radiating that those energies. The Crab is a useful calibration source in the X-ray and gamma-ray regimes because of its well-measured spectrum and constant flux, and it is an important touchstone for new instruments like NCT to observe.

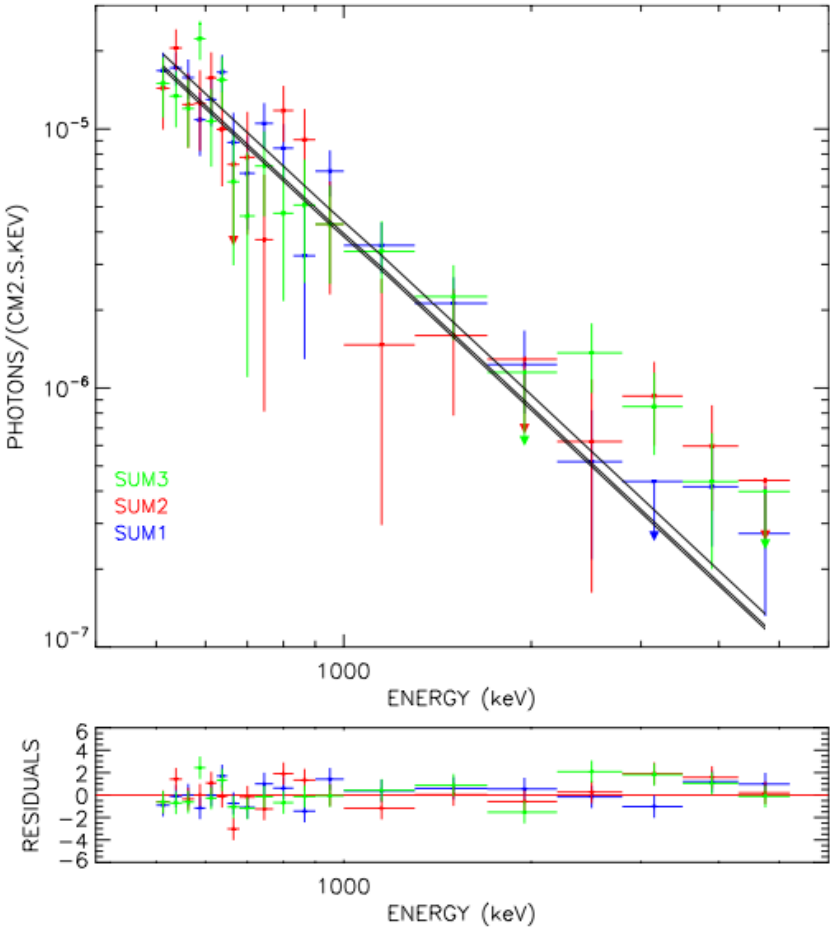

Figure 2.7: SPI spectrum over three different measurements. Fig. 2 from [96].

Part II

The NCT instrument and calibrations

Chapter 3

Overview of the Nuclear Compton Telescope[1]

3.1 Introduction

The Nuclear Compton Telescope (NCT) is a balloon-borne soft gamma-ray telescope designed to study astrophysical sources of nuclear line emission in the crucial 0.5−2 MeV range and gamma-ray polarization in the 0.2−0.5 MeV range [30,33,35,46]. NCT employs a novel compact Compton telescope design utilizing twelve high spectral resolution orthogonal strip germanium detectors (GeDs) with the ability to record in three dimensions the location of each individual photon interaction. Tracking individual interactions serves three purposes: imaging the sky using Compton imaging techniques, measuring polarization, and very effectively reducing background.

The entire set of detectors and their cryostat are enclosed inside a well of anticoincidence BGO shields to reduce the Earth albedo and atmospheric backgrounds (Fig. 3.1). The resulting overall field of view is primarily limited by the BGO shields to ≈3.2 sr. The entire instrument and readout electronics are mounted in a pointed, autonomous balloon platform (Sec. 3.4).

To date, NCT has flown on two conventional balloon flights. The first was a prototype flight in 2005 that succeeded in measuring the soft gamma-ray atmospheric background and galactic anticenter region [40, 41, 53]. The second was the flight described here of the a 10-GeD version of the instrument in May 2009.

[1]Much of the content of this chapter appeared in [18].

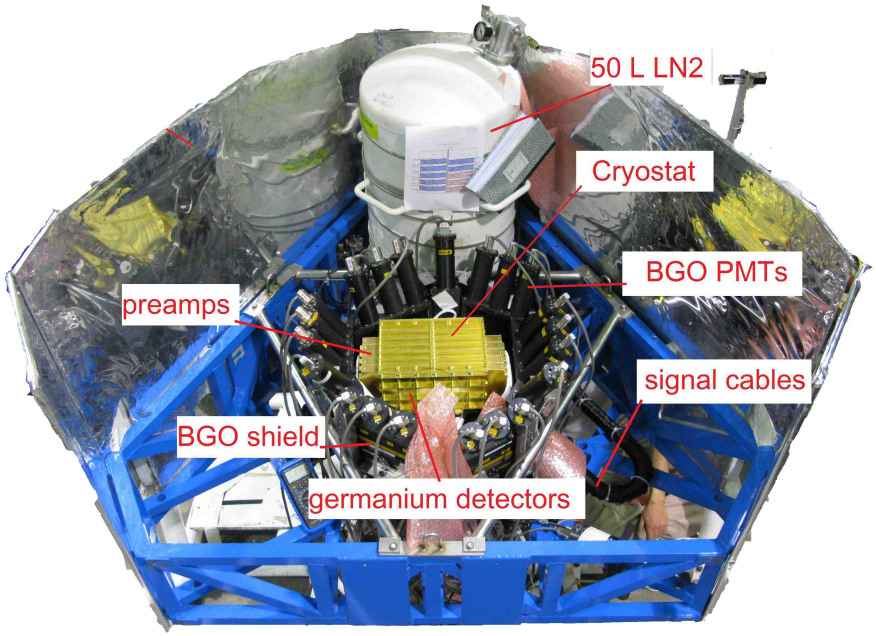

Figure 3.1: The NCT instrument cradle during the 2009 flight, showing the cryostat that houses the 10 GeDs, the liquid nitrogen dewar, and the anticoincidence BGO shields surrounding the cryostat.

3.2 Detectors and Cryostat

NCT currently consists of ten high-purity germanium cross-strip detectors (GeDs) that measure both the position and energy of gamma-ray interactions. A single GeD is shown in Fig. 3.2, and the entire array of 10 GeDs is shown in Fig. 3.3. Each GeD measures 8×8×1.5 cm, with a 2 mm strip pitch and 37 strips on each side. There is a gap of 0.25 mm between the strips to minimize the number of charge sharing events and the resulting charge loss, while maintaining high spectral resolution. A 2 mm-thick guard ring surrounds this active area on both faces of the detector, with a 1 mm gap between the ring and the edge of the crystal. The guard rings are instrumented to provide anticoincidence signals for rejection of events with interactions in these regions.

Since the GeDs are orthogonal strip detectors, the 2D position of each gamma-ray interaction is determined through which X and Y strips collect the charge. The depth inside the detector is determined using the difference in collection time between the electrons and holes. The full 3D position resolution is approximately 2 mm^3.

The NCT GeDs are operated as fully depleted p-i-n junctions. The seven p-type GeDs are operated at biases ranging from -600 to -1600 V, depending on the impurity concentration. The three n-type GeDs are operated at biases ranging from

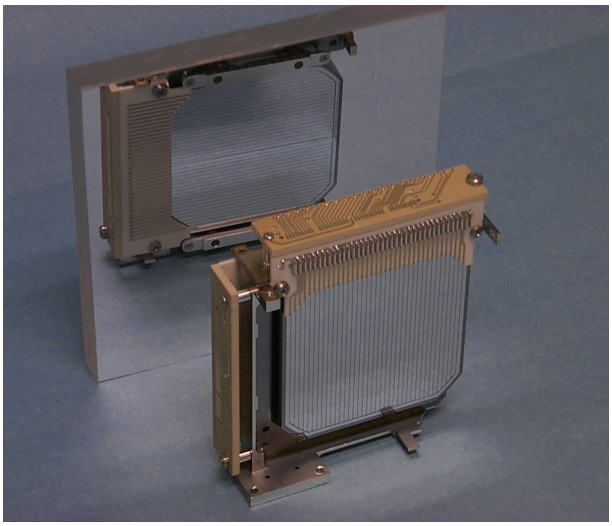

Figure 3.2: One GeD in front of a mirror, showing the vertical and horizontal metal electrodes implanted on the front and back sides of one detector.

+600 to +1000 V. The crystals were fabricated by ORTEC and processed at LBNL using amorphous germanium contact technology [5,122]. In addition, three of the ten detectors were coated with amorphous silicon on the cathode side, which has been found to increase the stability of detectors through temperature cycles [6].

The ten NCT GeDs are housed in a single cryostat that successfully flew on the prototype flight. The cryostat is attached to a single 50-liter liquid nitrogen dewar which cools the GeDs to ≈85 K for 7 days (see Fig. 3.1). The dewar is vented through a 5 psi valve keeping the liquid nitrogen under pressure at float. Each GeD is mounted in its own carrier bracket that mounts on a central copper coldfinger. The entire assembly is enclosed in a thin IR radiation shield. Figure 3.4 shows the relative placement of the detectors inside the IR shield and cryostat, and Fig. 3.5 shows a cross-section of the dewar and coldfinger.

3.3 Instrumentation

NCT uses conventional GeD-quality signal processing electronics [54]. Each detector strip has a compact, low-power signal processing chain made predominantly of conventional surface mount components. Detector signal extraction is accomplished with a low-power, high-performance charge-sensitive preamplifier [66]. The power consumption of the preamps is 25 mW/channel. A pulse-shaping amplifier, with both a fast and a slow channel, follows each preamplifier. The slow channel, with a 6 μs time-to-peak unipolar shaper, is followed by a peak detect and stretch function. The fast channel uses a bipolar shaper with a shaping time of 170 ns to timestamp each waveform at the signal zero-crossing, as a proxy for the half rise time of the signal.

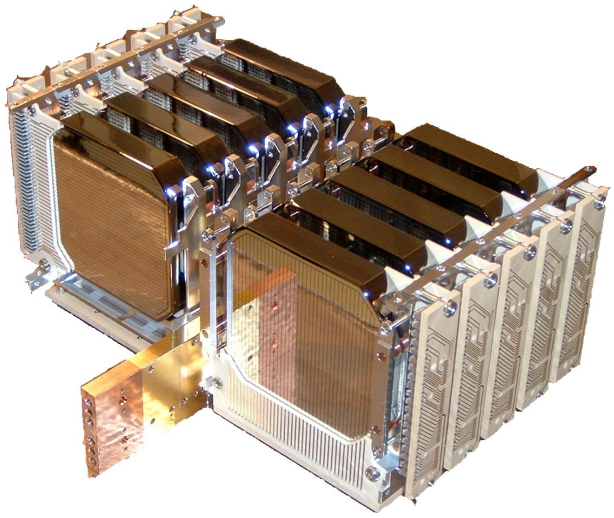

Figure 3.3: The 10 germanium cross-strip detectors of NCT that were flown in the May 2009 balloon flight.

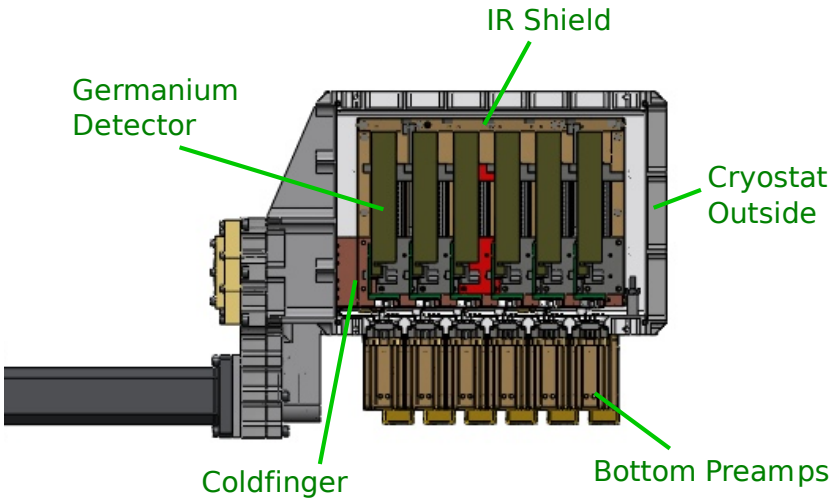

Figure 3.4: Schematic of the NCT cryostat, showing the placement of the GeDs.

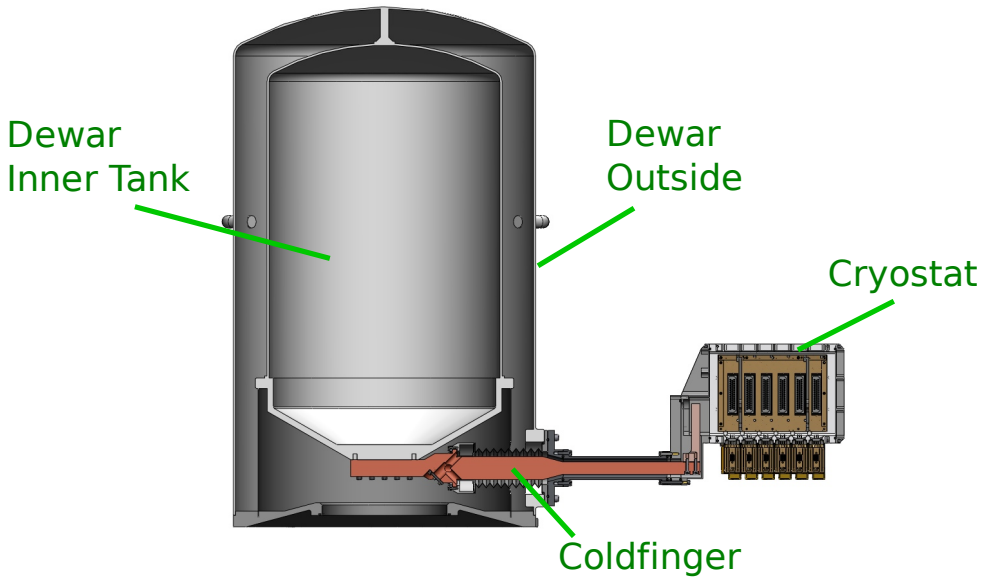

Figure 3.5: Schematic of the NCT dewar and cryostat.

The slow channel has a low-level discriminator (LLD) with a threshold of ≈20 keV to reject detector noise and an upper-level discriminator (ULD) with threshold ≈2000 keV to reject charged particle events. The fast channel discriminator (FLD) has a threshold set to ≈40 keV to reject noise (the fast channel is noisier than the slow channel).

One 10-channel signal processing cluster resides on a single printed circuit card with both the fast and slow analog signal processing electronics. Eight of these "analog boards" are required for each GeD. Each set of eight analog boards connects to a common backplane, which supplies bi-directional housekeeping communication, power, and event data channels. Low level input signals connect to the front panel, well away from the back plane to minimize noise. Each analog board has one ACTEL Field-Programmable Gate Array (FPGA). This ACTEL keeps track of trigger rates and coordinates logic between the different channels. A single Altera NIOS embedded processor board interfaces with each set of eight analog boards. This "DSP board" coordinates the logic between the eight ACTELs, compresses event data from the ACTELs, and communicates with the main flight computer via an ethernet link. For signal cabling, NCT employs a compact coaxial ribbon cable manufactured by Gore Industries. This cabling provides significant savings in mass and complexity while meeting the NCT requirement of <10 ns rise time over the 5 m of cabling needed. Fig. 3.6 shows the board enclosure for one detector and the cabling connected to the

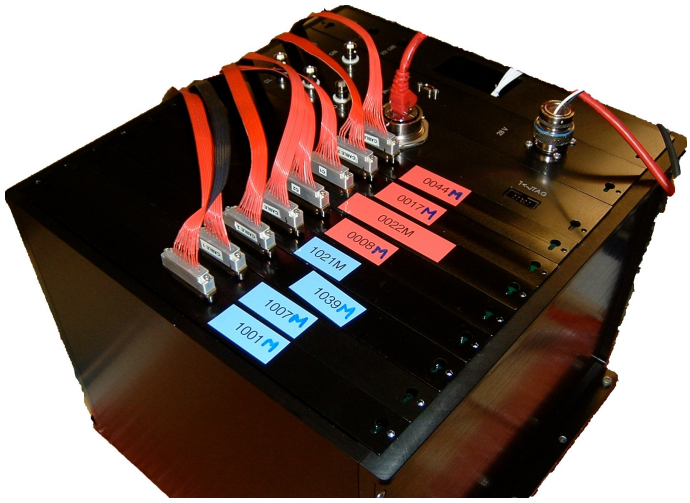

Figure 3.6: The eight analog boards needed to instrument one GeD are contained in a single enclosure along with a DSP board and low- and high-voltage power supplies. The compact coaxial ribbon cable may be seen connecting to the preamp boxes on the sides of the cryostat.

cardcage.

More details on the digital system, including flow charts of the digital logic involved in acquiring events, can be found in [88].

3.4 Balloon Gondola

The NCT balloon gondola contains systems to provide power, telemetry, aspect measurement, and autonomous pointing for the telescope. Fig. 3.8 shows the gondola used in the 2009 flight with major components labeled. The detectors and cryostat are held in a movable cradle (Fig. 3.1) which is protected by roll bars. The electronic boards, flight computer, and batteries are carried in an enclosed electronics bay 3.7. The gondola systems will be summarized here, but more details can be found in [22].

3.4.1 Power System

For the 2009 flight, the solar power system (SPS) of NCT consists of two large photovoltaic arrays, a charge control unit, and a battery system. Because this flight was intended to qualify NCT for a long duration balloon flight (LDBF), solar panels were used in addition to batteries. The panels recharge the batteries, allowing NCT to operate continually for many day-night cycles, as required for a long-duration mid-latitude flight.

3.4.2 Flight Computer

The onboard flight computer controls the operation of the detectors and readout electronics, stores and telemeters science and housekeeping data, interfaces with the CSBF command uplink, and executes the pointing plan. Data is archived inflight to two redundant flash solid-state drives with capacities of 64 GB and 8 GB. The flight computer also interfaces with the CSBF Support Instrument Package (SIP) system, which provides telemetry and remote commanding during the flight.

3.4.3 Pointing and Aspect

Because of NCT's large field of view, its pointing requirements are relatively modest at about 2° pointing accuracy. A rotor assembly allows pointing in azimuth, and a three-axis magnetometer is used to orient the gondola relative to the local magnetic field.

Since the prototype flight, we have added a Magellan ADU5 differential GPS receiver. This dGPS system provides an accurate full aspect solution in real time during the flight. The dGPS aspect solution is stored in housekeeping and telemetered. Additionally, the flight computer uses the dGPS aspect to correct for any slowly-varying biases in the magnetometer-based pointing. An aspect magnetometer and accelerometer are also retained for redundancy. The instrument's $\approx 5 - 10°$ angular resolution [17] means that aspect reconstruction is needed to only 0.5° or better.

3.5 Analysis Tools

The software analysis tools for NCT are built using the Medium Energy Gamma-ray Astronomy library (MEGAlib) [178, 181]. MEGAlib provides utilities for simulations (Cosima [180]), geometry modeling (geomega), event reconstruction (revan), and imaging reconstruction (mimrec), in addition to tools for building a custom analysis pipeline. A schematic of the NCT analysis pipeline is shown in Fig. 3.9.

3.5.1 Simulation Tools (Cosima)

Cosima [180] is a gamma-ray telescope simulation tool based on GEANT4 [2, 4]. It produces an event list of exact interaction locations for use in calculating the detector response. Cosima is capable of simulating various source spectra and geometries, along with particle backgrounds. Thus it is suitable for simulations of ground calibrations as well as balloon and space environments.

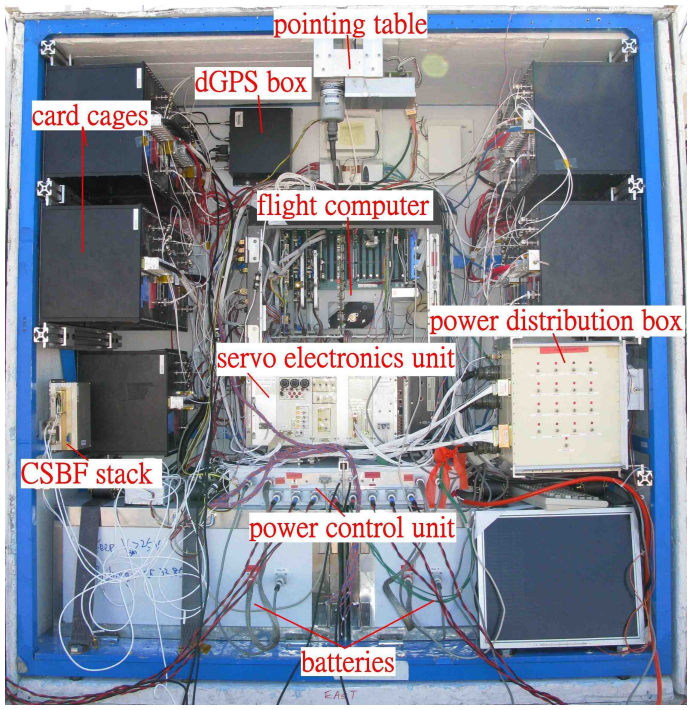

Figure 3.7: The NCT gondola electronics bay. Visible are the 10 card cages (black anodized aluminum boxes mounted on the sides of the bay), each of which contains the readout electronics for one detector (80 channels). Also visible is the gondola control unit (GCU; the brown box in the middle of the bay consisting of the flight computer and pointing system) and parts of the solar power system (SPS; the battery boxes are the large white boxes on the floor of the bay, and the power control unit is the smaller white box sitting atop them). The flatscreen monitor and keyboard were removed before flight.

3.5.2 Detector Effects Engine

The purpose of the Detector Effects Engine is to convert simulated data into realistic events. The ideal photon interaction locations from simulations are grouped into individual strip hits, and energy and timing information is calculated using the inverse of the energy and depth calibrations. The resolutions of the energy and timing channels are added to the data as noise, and thresholds are applied. After using the Engine, simulations are run through the identical analysis pipeline as the real data.

3.5.3 Event Calibration

The NCT event calibration pipeline is written in C++ using tools from MEGAlib. The input to the software is a file listing raw detector events, which is a list of the strips that were active during the event, and the slow channel ADC and fast channel

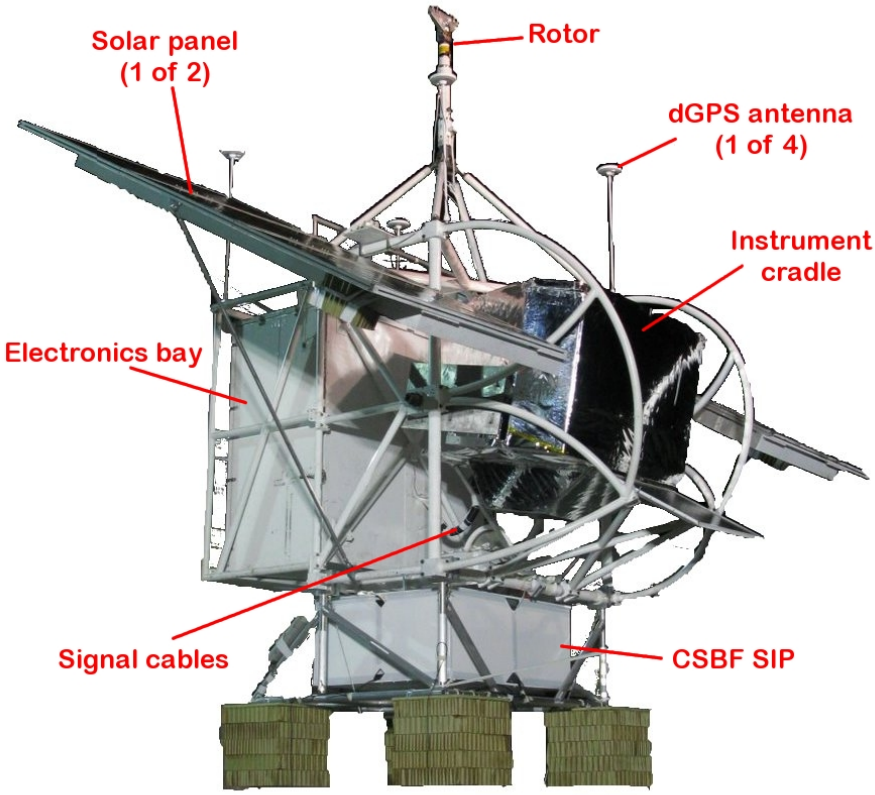

Figure 3.8: The NCT gondola with major components labeled.

timing for each strip. This raw data can come from either the detectors or simulations that have been processed by the Detector Effects Engine. The output file contains reconstructed detector events. Each event is a list of photon hits, and each hit is assigned its own energy, 3D position, energy uncertainty, and 3D position uncertainty.

The event calibration routine reads events into a buffer, and events from different detectors that are coincident are matched according to their timestamp from the readout system's 10 MHz (100 ns) clock. The events are then passed to a series of modules, each of which handles a discrete step in the calibration process. A typical order for modules is shown in Fig. 3.9. Modules are aware of what actions are performed upstream of them, and the software prohibits any conflicts or redundancy in their actions.

Since the event calibration software is written to be modular, different versions of calibrations can be swapped in and out of position to compare their performance. In addition, other improvements to the event reconstruction can be inserted into the pipeline and tested without any large changes to the software.

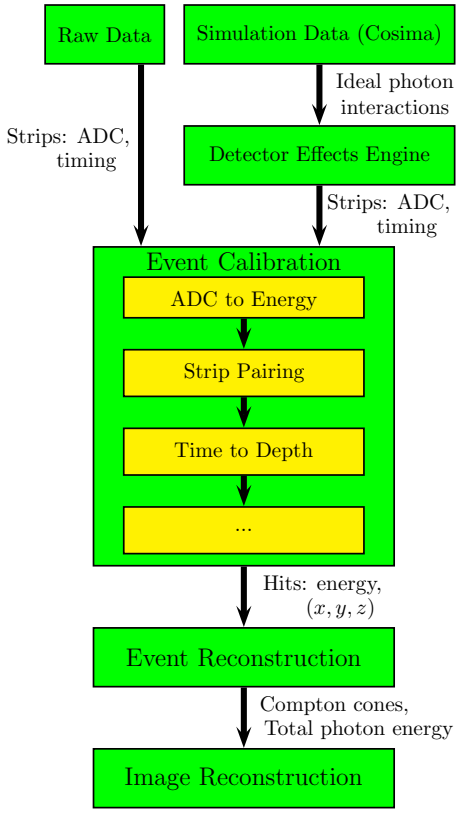

Figure 3.9: Schematic of the analysis pipeline. The analysis path is the same for real data and simulated data, allowing straightforward comparison and validation between the two.

3.5.4 Event Reconstruction (revan)

After event calibration, Compton event reconstruction is performed on the reconstructed detector events. The revan tool uses Compton Kinematic Discrimination (CKD) [31], but is also capable of other Compton reconstruction schemes. Other schemes that improve on CKD have been implemented for the analysis of the prototype NCT flight, such as neural networks [179] and Bayesian methods [177], and will soon be in place for the 10-GeD NCT.

3.5.5 Image Reconstruction and other High-level Analysis (mimrec)

Once Compton events have been reconstructed, the mimrec tool is used to create images in various coordinate systems, including 3D Cartesian, spherical, and galactic coordinates. Various imaging algorithms have been implemented to improve on sim-

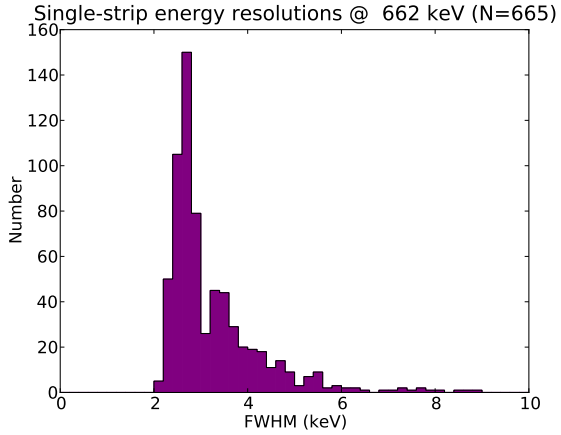

Figure 3.10: Histogram of single-strip energy resolutions at 662 keV.

ple Compton back-projection, such as List-Mode Maximum Likelihood Expectation Maximization (ML-EM) [173]. Other utilities include plots of the locations of initial photon interactions, calculation of the Angular Resolution Measure (ARM), and total photon energy spectra.

3.6 Calibrations

Various calibrations and tests were performed on the NCT instrument prior to and after the 2009 flight. Here we summarize the preliminary results of these tests, with further details found in [47] and [21].

3.6.1 Energy Calibration

For each of the 37 energy channels on each side of each detector (≈700 channels total), we need to know how to convert the ADC value into energy in keV. To do this, we took data with several calibration sources so that each of the channels has several calibration lines between 30 keV (^{129}I) and 1333 keV (^{60}Co), allowing for a complete energy calibration at all relevant energies. From the calibration curve and measured line widths, the energy resolution was also determined. A histogram of the energy resolutions for each strip at 662 keV (^{137}Cs) is shown in Fig. 3.10, which reveals that most channels have excellent energy resolution (0.3−0.9% at 662 keV). Further details on the energy calibration will be shown in Chapter 5.

3.6.2 Depth Calibration

Depth is calculated from the timing difference between X and Y strips. Since each timing channel has slightly different properties, the timing difference must be

calibrated for each of the roughly 37^2 effective pixels formed by the individual strip crossings. Data was taken with low-energy calibration sources incident on each side of the detector to measure the positions of the surfaces in timing space. This data was then used to scale a depth calibration curve derived using detector field and charge transport simulations. Validation results using high-energy sources show good agreement between the data and simulations [47]. The depth calibration of the protoype NCT instrument is detailed in Chapter 4.

3.6.3 Effective Area

The effective area is a key performance parameter for gamma-ray telescopes. Determining the effective area of NCT is complicated by the large field of view, requiring many data points to cover an azimuth range of $-180°$ to $+180°$ and zenith angle range of $0°$ to $80°$. Three different sources were used to cover the energy range of 356 keV to 1333 keV. In order for the sources to be in the far field within error, the sources were positioned 5 m away from the detectors. Approximately 1 cm position reconstruction was attained by using a theodolite and sighting points on the source mount (Fig. 3.11).

Some preliminary results for the effective are are shown in Fig. 3.12 from [21]. The results of simulations of the calibration sources are shown beside the real data, yielding good agreement thus far. Simulations and the detector effects engine are undergoing continual improvements.

3.6.4 Imaging

Data points from the effective area calibration are also being combined together and used for imaging tests. So far, this work has focused on trying to separate closely-spaced sources, such as the two ^{137}Cs sources shown in Fig. 3.13 [47].

3.6.5 Polarization

In order to determine the sensitivity of NCT to polarization, we created a partially polarized gamma-ray source by allowing a ^{137}Cs source to scatter off of a CsI crystal (Fig. 3.14). Photons that are coincident between the CsI and the detectors are expected to be partially polarized because the photons are effectively forced to scatter at a given angle, thus selecting photons with polarizations parallel to the CsI surface.

Early results show good agreement between simulations and data, and NCT's polarization modulation factor is being estimated [21]. See Fig. 3.15 for an example of data where a modulation is seen due to polarization.

Figure 3.11: Setup for the effective area calibration. The theodolite used for placement can be seen in the lower right corner, and the board used for source placement and sighting can be seen in the upper left. The sources were placed 5 m away from the detectors.

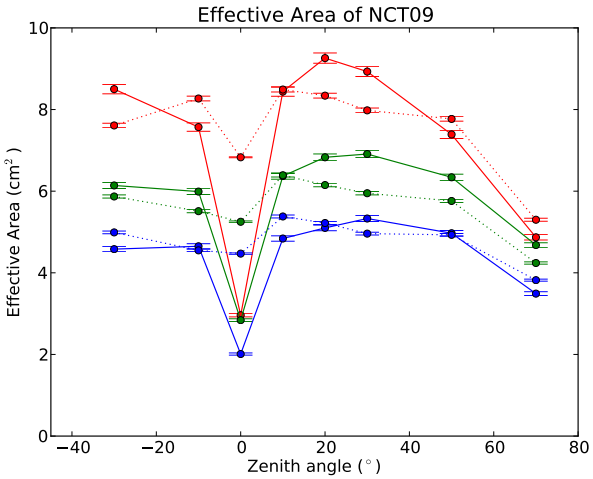

Figure 3.12: On-axis effective area at different zenith angles for 662 keV (red), 1173 keV (green), and 1333 keV (blue). Real data are connected by solid lines, while simulated data are connected by dotted lines. The dip in effective area at 0° is a geometrical effect due to the source photons being incident on the top edges of all detectors.

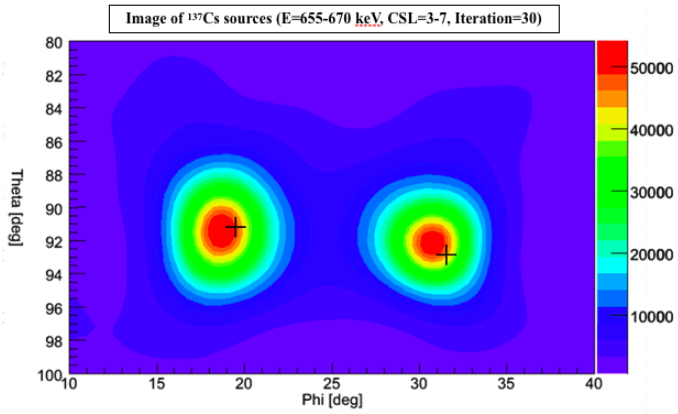

Figure 3.13: Two ^{137}Cs sources (662 keV) separated by 12°, shown after 30 iterations of the ML-EM algorithm.

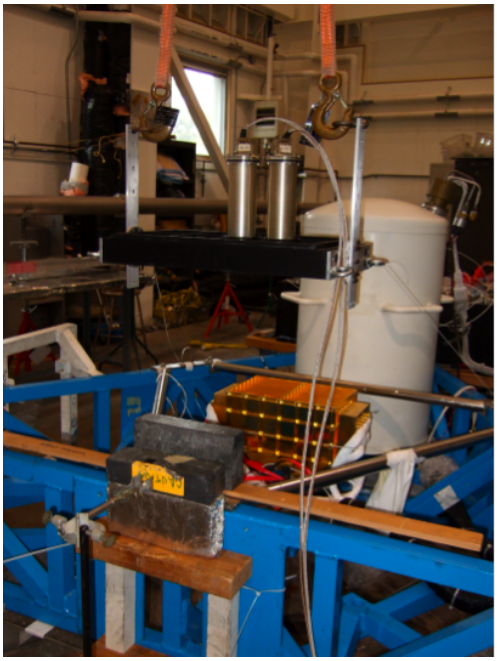

Figure 3.14: Polarization test setup. The ^{137}Cs source is located in the bottom left, shielded by Pb bricks. A CsI scintillator is suspended above the source, and source photons that are coincident between the CsI and the detectors is analyzed. Through forcing the photons to Compton scatter off of the planar surface of the CsI, a partially polarized source is created (although it is not monoenergetic).

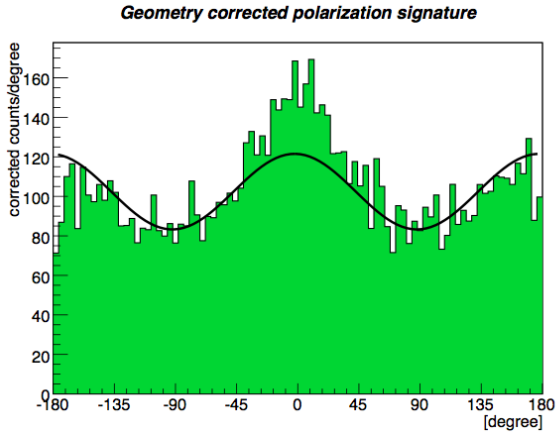

Figure 3.15: Polarization modulation data. As expected from a partially-polarized source, there is a sinusoidal signature in this histogram of the Compton scatter azimuth.

Chapter 4

Position Calibrations of the Prototype Nuclear Compton Telescope[1]

4.1 Introduction

The NCT prototype was a scaled-down, two-detector version of NCT. The NCT prototype flew on a high-altitude balloon from Fort Sumner, New Mexico, on 2005 June 1. The duration of the flight was approximately 9 hr, with approximately 5 hr at float. A summary of the prototype flight can be found in [53]. Fig. 4.1 shows a photograph of the two detectors D0 and D1, while Fig. 4.2 shows a view from above the cryostat as it was situated in the balloon gondola in 2005.

The prototype NCT energy calibrations have been presented elsewhere [42]. Here we present the detailed position calibrations.

4.2 Depth Calibration Approach

NCT, like other instruments utilizing Compton scattering of gamma-ray photons, must be able to reconstruct the positions and deposited energies of Compton scatters and photoabsorptions of gamma rays in the detector volume. Since NCT uses Ge cross-strip detectors, the full 3D position of any single gamma-ray interaction is determined by identifying the active cross-strip pair, or 'pixel,' and by determining the depth (z) of the interaction.

[1]Much of the content of this chapter appeared in [17].

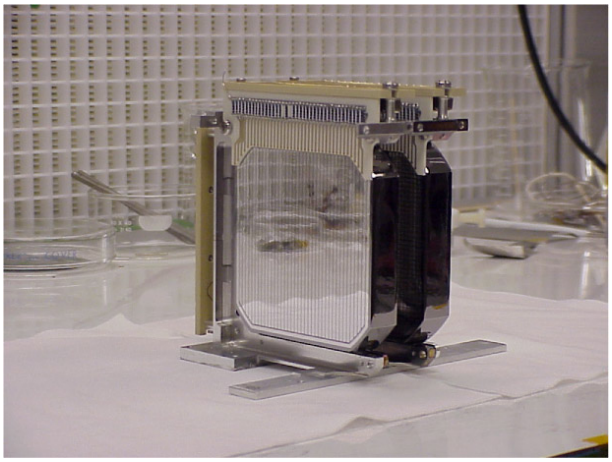

Figure 4.1: The two HPGe detectors, D0 and D1.

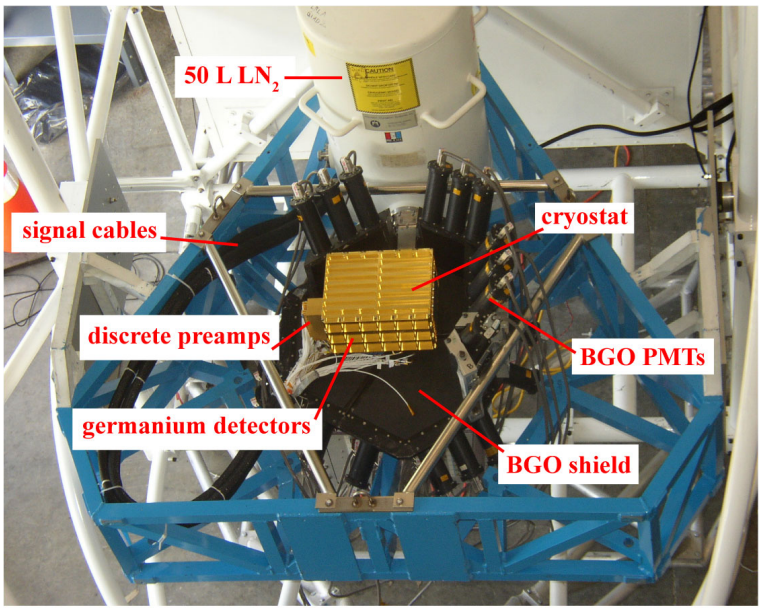

Figure 4.2: The cryostat as it was situated in the 2005 balloon gondola. The view is from above and in front of the detectors.

The z-coordinate cannot be measured directly, but is inferred from the charge collection time difference (CTD). The CTD is defined as the difference between the signal half-rise times of the DC (anode) and AC (cathode) sides of the detector, as measured using constant fraction discriminators with 10 ns resolution on each strip. For an in-depth discussion of the CTD, see [5] and [7]. Depth calibration means the determination of the relationship between the CTD and the z-coordinate of the interaction.

Calibrating the depth z in terms of the CTD presents unique challenges. We cannot accurately constrain the photons to interact at a known depth in the detectors, but we can use a known depth *distribution* of photon interactions. We have to turn to indirect methods to calibrate the depth.

4.2.1 Previous Work

Previous work has demonstrated that an accurate depth calibration is possible when both sides of a GeD are accessible [7, 50]. The relationship between CTD and the depth z was assumed to be a cubic polynomial. Data was taken with a source placed on one side, and only photopeak events were used in the calibration. Since photopeak events are exponentially distributed in depth, one can determine from the assumed z-CTD polynomial what the expected CTD histogram should be. Then one can fit the measured data and determine the mean free path (MFP) of the photons. Using illumination by 60 keV and 122 keV sources from both sides of the detector, one can check both that illumination from each side gives the same MFP and also that the MFPs agree with the predicted values. A test statistic was used to obtain a best-fit cubic z-CTD relationship. The present method builds on the experience gained in this first depth calibration.

There are several differences between the previous depth calibration and the prototype telescope calibration presented in this paper. The primary difference is that the new depth calibration had to be performed with both detectors installed in the cryostat. Since one detector was placed behind the other, illumination from both sides for each detector was impossible. Also, because the cryostat was mounted on a coldfinger right in front of the LN_2 dewar, back-illumination of the second detector was effectively impossible — leaving front-illumination of both detectors the most feasible procedure. However, the MFP of 60 keV photons in germanium is 0.9 mm, and that of 122 keV photons is 5.2 mm, so both sources will be completely attenuated in the first detector, and neither is suitable for the depth calibration of both detectors. The source chosen for this calibration was ^{137}Cs, with its 662 keV line. This source choice constitutes a compromise between a large MFP (2.7 cm) and a reasonable total cross-section.

Another major difference is that the earlier calibration was only performed for a single pixel of the detector. Now, we had to calibrate each of the 1,369 pixels of each detector. However, even though we took several days of data with our 662 keV

source, not enough photopeak events were accumulated to individually calibrate all of the pixels. We had to use less restrictive data cuts to obtain enough counts in each pixel.

Last but not least, the previous method does not require any Monte Carlo simulations, while the current method uses simulations extensively.

4.2.2 Calibration Method

The method we use for this calibration consists of three basic steps. These steps are listed here and elaborated on in the following sections.

1. Choose an event cut on the calibration data so that there is a sufficient number of counts in each pixel. Use MGEANT [158] simulations that mimic the event cut to produce the expected depth distribution of gamma-ray interactions. Do this step for each of the two detectors.

2. Use custom charge transport code with the MGEANT depth distributions as inputs and produce the expected CTD distribution. Thus, create a "CTD template" for each of the two detectors. Then allow the template two degrees of freedom (offset and stretching factors; see 4.2.2.2) and fit each pixel to relate the measured CTD in each pixel to the CTD template.

3. Use custom charge transport simulations to relate the CTD template to z.

4.2.2.1 Event Cuts

We decided to use single-site events for the depth calibration so that no Compton event reconstruction would be necessary. Event reconstruction would also require a provisional depth calibration, so using single-site events is one of the most straightforward methods. (By single-site events, we mean that only one AC strip and one DC strip collect charge.) The main features of the single-site spectrum, besides the 662 keV line and associated features, are background lines from ^{40}K, ^{60}Co, the Thorium series (^{208}Tl), and the Radium series (^{214}Bi and ^{214}Pb), and a smooth continuum. This underlying continuum is probably due to multiple Compton scatters of background gamma-ray lines. The background lines are consistent with the presence of naturally occurring radioisotopes (except for ^{60}Co, which was probably from an inadequately-shielded lab source).

Only events with energies of 200−700 keV were used. This cut was chosen for three reasons. First, it includes all of the 662 keV photoabsorptions and the Compton edge at 478 keV. Second, the background in the region follows a power-law and is free of sharp features, so we assumed that it would be easy to model. Third, this cut provides ample counts to perform the calibration (≈700 counts per pixel per detector). This

cut contains approximately 75% background and 25% events associated with the 662 keV source (see below).

In order to model the background, we first assumed the background was isotropic between zenith angles 0° to 80°. Active BGO shielding covers the bottom and sides of the detectors, blocking out the other possible incident directions (except in the front), justifying this assumption (see Fig. 4.2). We believe the background continuum to arise from background gamma-ray lines that undergo multiple Compton scatters in ambient material before entering the detectors. The exact spectral shape is determined by the geometry and composition of the detector, shielding, and ambient material. This behavior has been seen in other germanium detectors, such as those used for double-beta decay and dark matter experiments, when they are not heavily shielded (e.g., [86]). Since the background sources are diffuse and the gamma rays are multiply-scattered, we expect the semi-isotropic assumption to be a reasonable one.

To find the appropriate background power-law index, we first fit the measured spectrum with a power-law ($\frac{dN}{dE} \propto E^{\alpha}$) and found $\alpha = -3.25$. The measured power-law index will not be the *input* power-law index unless the detector has perfect response. To determine the *input* power-law index, we simulated power-law sources that were isotropic between azimuth angles of 0° and 80° using the MGEANT package [158] and an NCT mass model including the cryostat and BGO shielding. For input power-law indices of $\alpha = -2.5$ to 0.0, NCT was found to have a linear relationship between input power-law indices and measured power-law indices. From this relationship, an input power-law index of -1.6 was determined.

MGEANT was used once again to simulate two sources: the $\alpha = -1.6$ power-law semi-isotropic background and the 662 keV source. A superposition of the two resulting simulated spectra was fit to the measured spectrum in order to determine the relative contributions of each. In the energy band chosen, 75% are background events and 25% are source events. Fig. 4.3 compares the combined simulated spectrum (divided by 2 for clarity) to the measured spectrum. Using information from the simulations, we were also able to determine the intensity of the background continuum:

$$I = 2.3 \times 10^{-3} \left(\frac{E}{100 \text{ keV}} \right)^{-1.6} \frac{\text{phot}}{\text{cm}^2 \text{ s sr keV}} \tag{4.1}$$

We note that using the source and background continuum is one way of performing this calibration. It would have been more desirable to use photons from the 662 keV line only, since that would improve our ability to simulate the calibration. In this case, there was not enough data to use only the 662 keV photons. For NCT 2009, a method was used that uses only line photons.

4.2.2.2 Template Production and Pixel Fitting

Using the simulated background and 662 keV source, we can predict the expected depth distribution in each of the two detectors. These depth distributions are shown

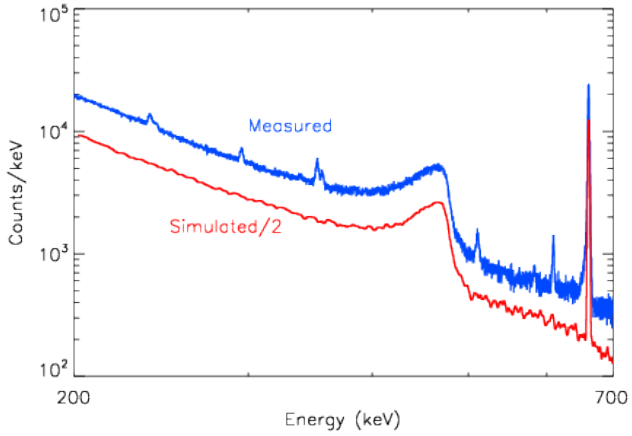

Figure 4.3: Measured single-site event spectrum compared to simulated 662 keV source plus semi-isotropic power-law background. The simulated spectrum is divided by 2 for ease of comparison. These Monte Carlo simulations are used to create templates of interaction depth.

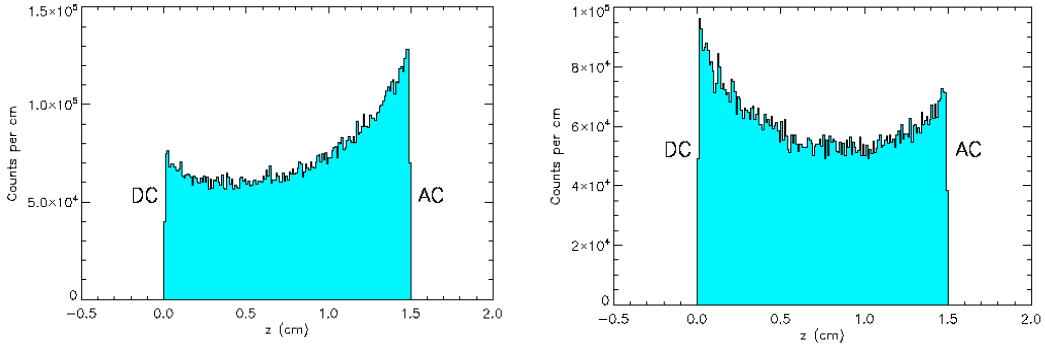

Figure 4.4: Monte Carlo depth distribution templates for D0 (left) and D1 (right).

in Fig. 4.4.

These depth distributions are used as inputs into our custom charge transport code to find the expected CTD distributions. The custom charge transport code we used has been shown to accurately reflect our GeDs [8]. We call the resulting CTD distributions our CTD templates.

The CTD templates are shown in Fig. 4.5. Notice the spikes near the edges of the otherwise flat histograms. These edge effects arise because the weighting field near the electrodes rises rapidly [8], creating a degeneracy in CTD values for a ≈1 mm deep region near each edge. The sharpness of these edges is an important tool to exploit when we fit the templates to the measured data.

These simulated CTD histograms are now used as templates to calibrate the

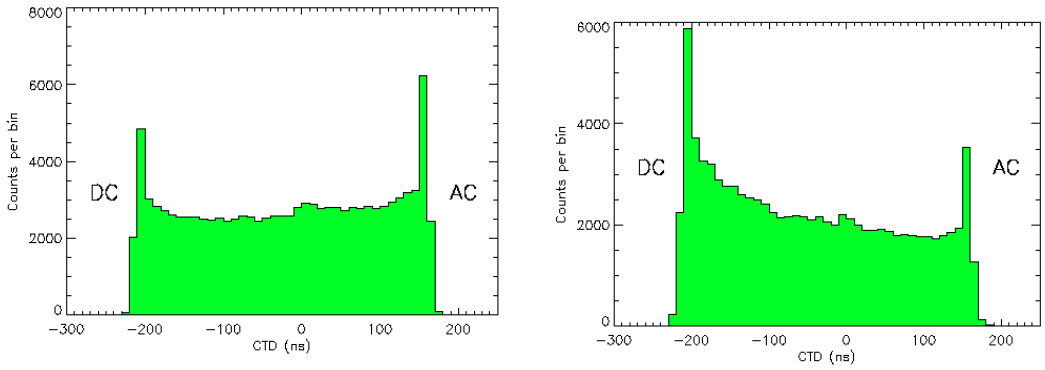

Figure 4.5: CTD template histograms for D0 (left) and D1 (right), obtained from charge transport simulations of the depth templates from Fig. 4.4. See the text for an explanation of the edge effects.

individual detector pixels, assuming a linear relationship between the measured CTD (τ) and CTD template ($\tilde{\tau}$):

$$\tau = \eta\tilde{\tau} + \Delta \tag{4.2}$$

The two parameters are the "stretching factor" η and "time offset" Δ. The CTD template $\tilde{\tau}$ represents the ideal, simulated CTD that we will use to calculate z.

The time offset Δ is included to account for electronics channel variations. Each strip has its own fast electronics channel, and each channel has its own delay line. The delay lines we used have a 200 ns delay, accurate to 20%. The time offset accounts for the difference between the the delay lines in the two crossing strips of each pixel.

The stretching factor η accounts for electric field variations in the detector. We do not expect the field in a given pixel to be exactly the same as the simulations, nor do we expect the field to be the same throughout the detector because of impurity variations. But because the same voltage is applied across the detector, the average electric field should be the same in every pixel. The local impurity concentration will determine how much the electric field varies in depth around this average value. An impurity concentration of zero would make the electric field equal to the average value at all depths, while increasing the impurity concentration would cause a sharper and sharper drop in field as a function of depth while still maintaining the average field value (see Fig. 4.6).

Since we operate at drift velocities near saturation (Fig. 4.7), if the impurity concentration is higher than in the simulation, the field in a given pixel varies more than the simulated field. This results in lower mean electron and hole drift velocities and longer collection times. Therefore, the measured distribution will be wider, and $\eta > 1$. Likewise, if the impurity concentration is less than the simulated amount, $\eta < 1$.

Examples of template fits to individual pixels are shown in Fig. 4.8, which shows

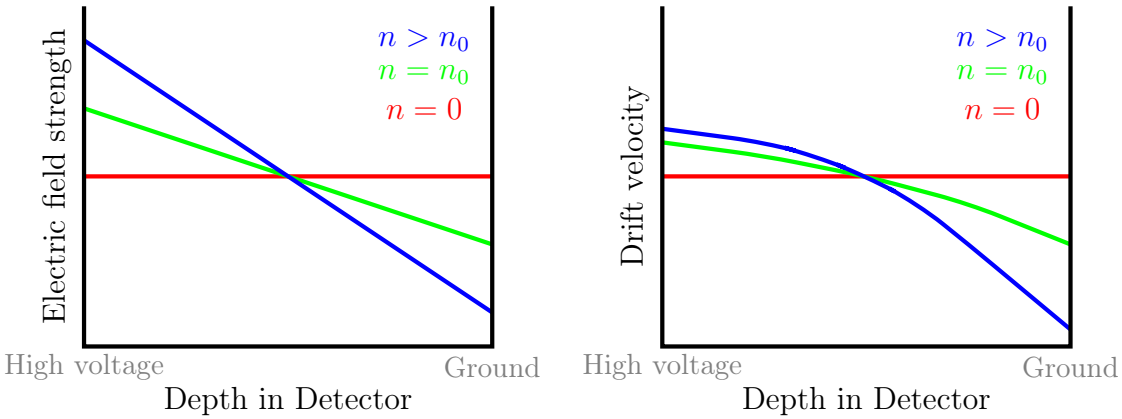

Figure 4.6: Schematic of electric field strength (left) and drift velocity (right) as a function of depth inside the detector. Three different impurity concentrations are shown: no impurities ($n = 0$), an impurity concentration equal to the value assumed in the field simulations ($n = n_0$), and an impurity concentration greater than that used in the field simulations ($n > n_0$). The drift velocity is not linear like the electric field because the NCT detectors are operated at voltages in the saturation regime. Notice that the higher the impurity concentration is, the lower the average drift velocity.

an individual pixel for D0 and D1. Qualitatively, the CTD templates fit the general shape of the pixel CTD histograms well. The normalization of the template is held fixed in all of the fits, and the templates are convolved with an assumed 15 ns FWHM electronic noise.

4.2.2.3 Calculating z

Now that η and Δ for the individual pixels have been found, we can determine the corresponding CTD template $\tilde{\tau}$ from the measured CTD τ using (4.2). The task still remains to determine z from the CTD template $\tilde{\tau}$. To do this, we once again turn to charge transport simulations. We simulate energy deposits at a grid of points 0.2 cm×0.2 cm wide (i.e., spanning the 0.175 cm-wide strip and going midway into the gaps on either side of the strip) and at 300 evenly-distributed depths. Fig. 4.9 shows the results of the simulations plotted in green.

From these simulated points, we calculate both the calibration curve to find $z(\tilde{\tau})$ and the intrinsic uncertainty in z. For a given CTD value $\tilde{\tau}$, we take all points within 5 ns of $\tilde{\tau}$ and calculate the mean z and RMS deviation Δz around the mean. We use a 10 ns window because that is the time resolution of the readout electronics. Therefore, Δz represents the intrinsic uncertainty we would expect from our detector model given this time resolution and no electronic noise. Fig. 4.10 plots Δz versus z.

We use a grid of the mean z values as our calibration curve (shown in blue in Fig.

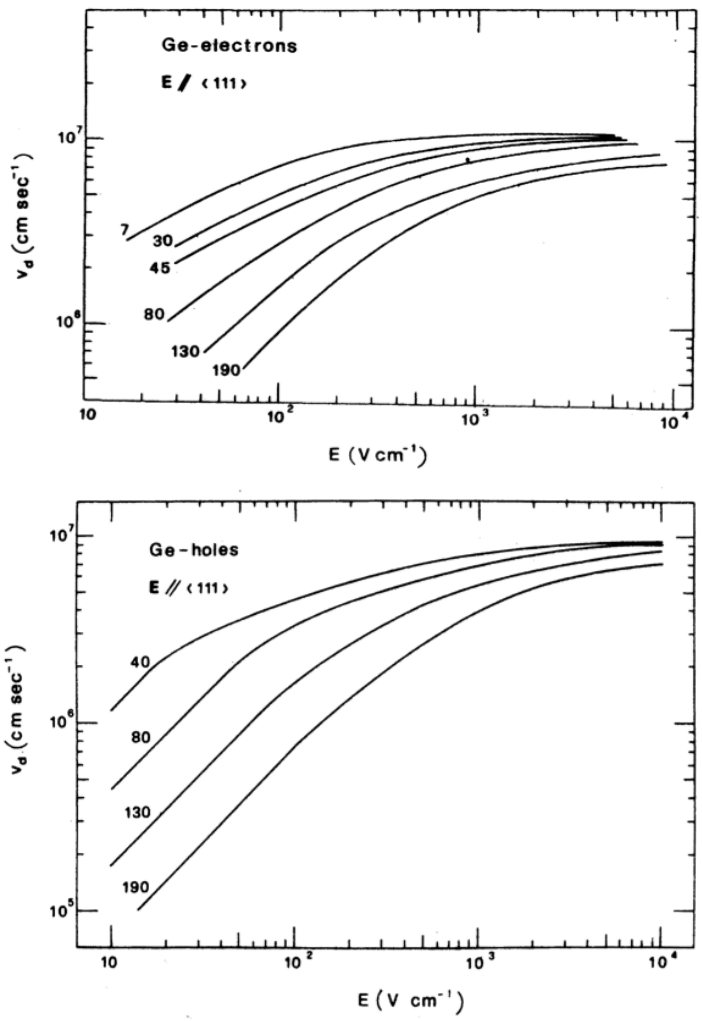

Figure 4.7: Electron (top) and hole (bottom) drift velocities as a function of electric field (from [142]). The curves are labeled by temperature. Notice that for low fields ($\sim$ 10 V/cm), drift velocity is proportional to electric field. At higher fields, the drift velocity approaches a saturation value. The NCT detectors are operated at an average electric field of $\approx$ 540 V/cm, which is in the saturation regime.

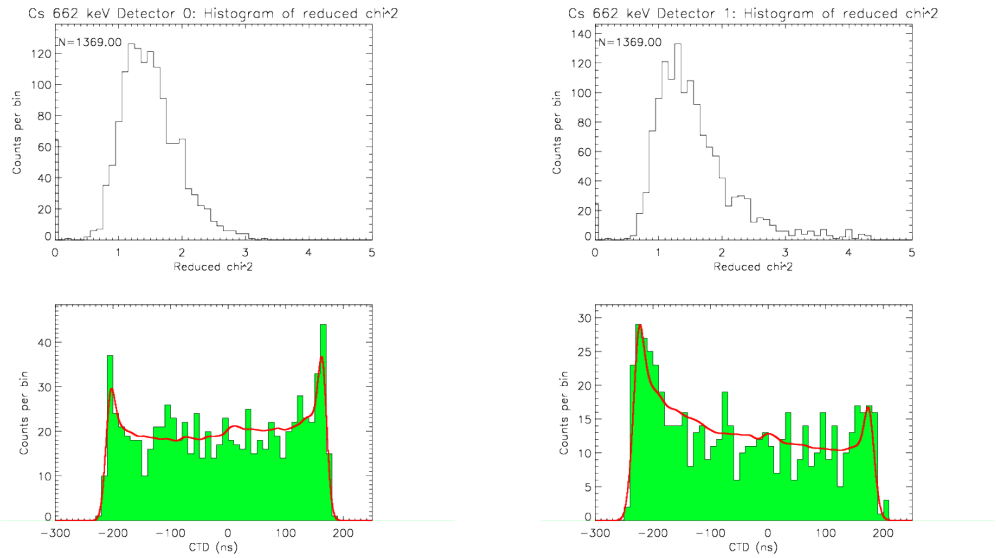

Figure 4.8: Examples of individual pixel fits: AC8×DC32 on D0 (left) and AC8×DC32 on D1 (right). In both cases, one can see that each detector's template convolved with 15 ns FWHM noise (red) reflects the general shape of the pixel's CTD distribution (green).

4.9). We obtain $z(\tilde{\tau})$ for a given $\tilde{\tau}$ from interpolation of this grid of values.

One can see from Fig. 4.10 that over most of the depth, $\Delta z \approx 0.2$ mm. This depth resolution was achieved in previous work with a prototype detector [50]. Near the edges, Δz increases. The degeneracy in CTD near the edges of the detector discussed above causes this larger uncertainty.

The charge transport simulations reveal no changes in the calibration curve for different energies deposited. The constant fraction discriminators used on NCT to measure the CTD were specifically chosen to avoid energy-dependent response [54]. Thus we assume that to first order there is no energy dependence on the calibration.

4.3 Calibration Results

The CTD templates fit both detectors reasonably well. For templates assuming 15 ns FWHM noise, the average reduced χ^2 was 1.56 for D0 and 1.63 for D1. When 10 ns noise was assumed, the average reduced χ^2 was 1.51 for D0 and 1.67 for D1. Lower and higher noise assumptions both led to higher average reduced χ^2 values. We are able to conclude that the total noise was around 10−15 ns FWHM.

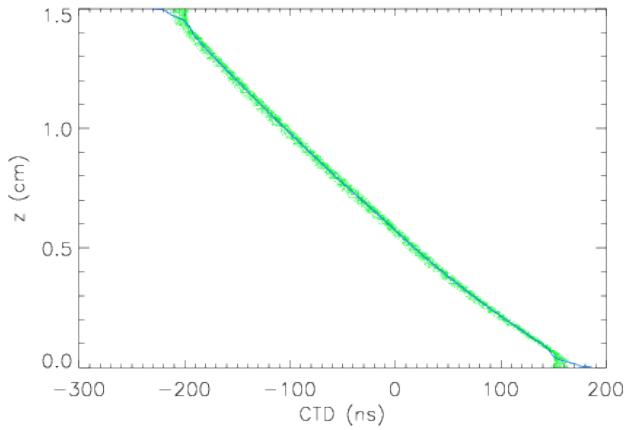

Figure 4.9: Relationship between CTD template $\tilde{\tau}$ and z. Simulated points are plotted in green. The blue curve is the calibration curve $z(\tilde{\tau})$ that we use to interpolate depth.

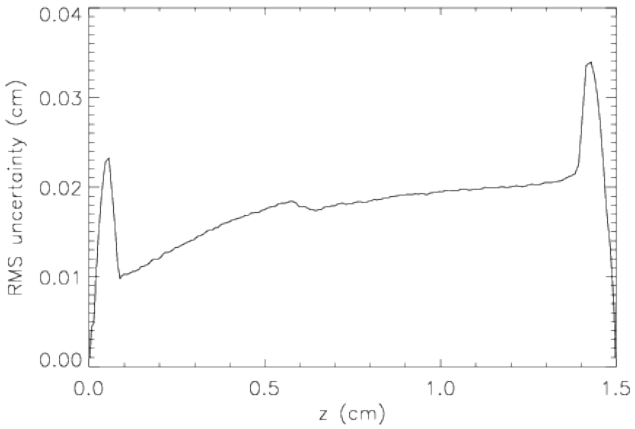

Figure 4.10: This graph shows Δz versus z. The quantity Δz is the RMS deviation of the simulated points from the calibration curve in Fig. 4.9, averaged over 10 ns intervals.

4.3.1 Parameter Correlations

In order to check if there are any parameter correlations in the fits, we examined correlations between the different properties of each pixel fit: number of counts accumulated in the pixel, reduced χ^2 of the template fit, stretching factor η, and time offset Δ. The only potential correlation is that between counts and η, although this is probably due to the fact that both of those quantities also correlate with radius from the center of the crystal.

The number of counts in a pixel increases with radius in each detector because for each one, the other detector will shield the inner pixels from an isotropic source. Also, the BGO shields the bottom of both detectors, so we would not expect the bottom outer edges of the detector to have as many in counts. This pattern is observed in both detectors — an increase in counts per pixel with radius, but a stronger increase toward the top of the detector than toward the bottom.

The radial dependence of the stretching factor η — which has a very different origin — will be discussed in Section 4.3.3.

4.3.2 Full-Detector CTD Histograms

One test of this calibration method is to examine a CTD histogram of the entire detector. In Fig. 4.11, histograms of measured CTDs for both detectors are plotted in the left column, while histograms of CTD template values (i.e., $\tilde{\tau}$ after correcting for each pixel's η and Δ) are plotted in the right column. Notice for both detectors that the templates reflect the overall shape well. After correcting the CTD, the edges of the detectors become much sharper. There is even the emergence of a small bump at $\tilde{\tau} \approx 0$ that is seen in the template but not in the measured data. The origin of this feature has not been conclusively determined, but it appears in the simulations and even more sharply in the real data.

4.3.3 Parameters across the Detector Face

Another test of this calibration method is to examine the variations of the two fit parameters across the face of the detector. Fig. 4.12 shows the time offset in each pixel for both detectors. The time offset has clear vertical and horizontal bands, showing a strong correlation with AC and DC strips. This is exactly what one would expect if Δ accounted for the difference in delay lines of the crossed strips, as already discussed.

Fig. 4.13 shows the stretching factor in each pixel. In both D0 and D1, η clearly decreases with radius from the center of the crystal. As previously discussed, a decrease in η corresponds to an increase in impurities. Thus we see in both detectors, the impurity concentration increases with radius. Since the germanium crystals are grown radially outward from the center, this data presents evidence that the impurity

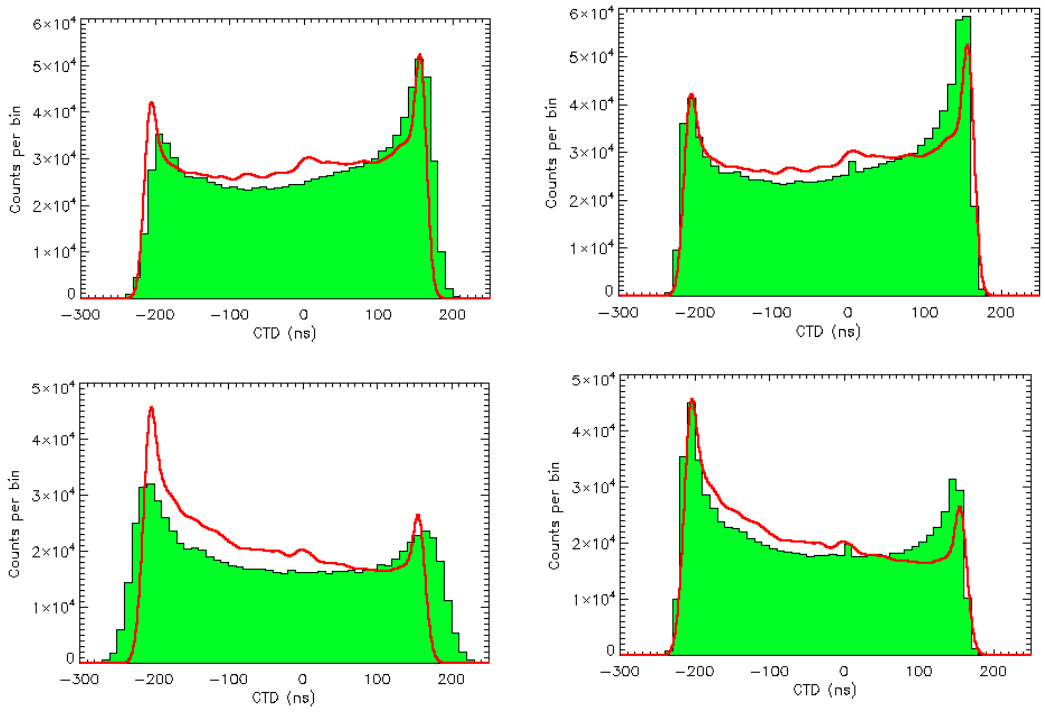

Figure 4.11: Top left: A histogram of measured CTDs (τ) for all the pixels of D0 (green) with the detector pixel template also plotted (red). Top right: A histogram of CTD templates ($\tilde{\tau}$) for all the pixels of D0, again showing the detector template. Bottom left and right: The same as the top row, but for D1. Notice both for detectors that the CTD template histograms match the simulated templates well, and sharp features emerge.

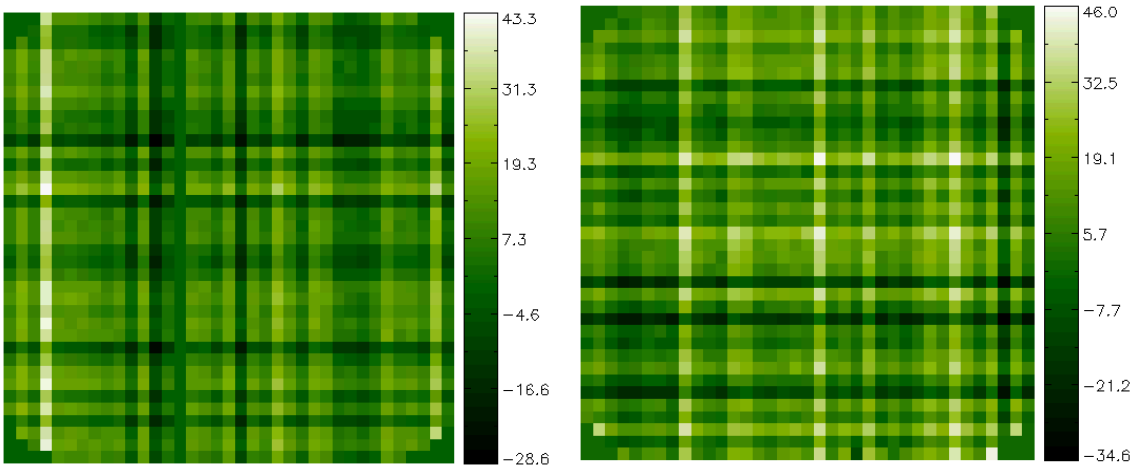

Figure 4.12: The time offset Δ of the calibration fit for D0 (left) and D1 (right). The time offset is clearly correlated to individual strips and reflects the difference in delay lines between each pair of crossing strips.

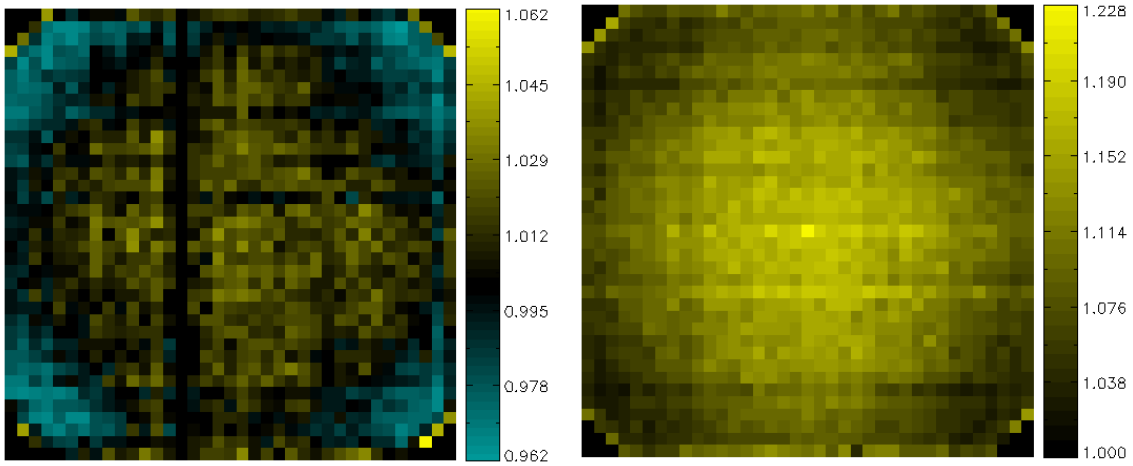

Figure 4.13: The stretching factor η of the calibration fit for D0 (left) and D1 (right). Yellow means the factor is > 1, while blue means the factor is < 1. For both detectors, the stretching factor decreases with radius from the center of the crystal. The stretching factor is used to account for electric field variation across the face of the detector, so this pattern might reflect different impurity concentrations in the crystal growth process. Investigation is ongoing.

concentration increases as the crystal is grown. This corroborates observations in the lab that the detectors deplete at lower voltages in the center than in the outer strips.

Another observation is that for D0, η crosses 1, while for D1, $\eta \geq 1$. Since η is larger on average for D1, the impurity concentration of D1 is lower than that of D0.

4.3.4 Checking Depth Distributions

As a final check of the calibration performance, we tried to recover a known depth distribution. We chose to examine photopeak events of several gamma-ray lines with the source nearly on-axis. The number of photopeak events at a given depth should be a decaying exponential with a characteristic mean free path (MFP) that depends on the line energy. The six calibration lines that we used are shown in Fig. 4.1. These lines have MFPs spanning the range 0.097 cm (^{241}Am 60 keV line) to 2.7 cm (^{137}Cs 662 keV line). The MFP values are calculated for germanium from the total cross section without coherent scattering [24].

For each calibration line, only single-site events were used, and a cut was made on energy to keep only those events within one sigma of the line center. Line widths ranged from σ=1.0−1.1 keV in D0 to σ=1.3−1.9 keV in D1. This tight cut was made to decrease the percentage of background events, which makes up 2−8% in the final cuts (except for 122 keV in D0 with 13% and 303 keV in D1 with 16%). The depth calibration procedure described earlier is applied to the CTD values of events passing the cuts — each measured CTD τ is corrected for offset and stretching factor to obtain

a CTD template value $\tilde{\tau}$, and then the depth z is obtained from the calibration curve in Fig. 4.9. A histogram is made of the resulting depth values for the entire detector. This histogram is fit with an exponential between a depth of 1 mm and 1.4 mm (or to 2 MFP is the MFP is small). The results of the MFP measurements are shown in Table 4.1.

In general, the measured MFP is close to the MFP inferred from calculations. For D0, all of the deviations are within 3σ. However, the measured MFPs were much worse for D1, presumably because of a lower source photon rate due to shielding by D0.

4.4 Conclusion

We have developed a simulation-intensive technique for calibrating the depth of interactions in our planar germanium cross-strip detectors. The depth resolution we achieve is $\approx$0.2 mm RMS for the inner volume, and slightly worse resolution in the outer $\approx$1 mm on each side of the detector.

Table 4.1: The six calibration lines used for the depth distribution check, showing calculated mean free path (MFP) along with measured values for each detector. All MFPs are measured in centimeters, and errors are one-sigma. The calculated MFPs use values for germanium and include a factor of $\cos\theta$ to account for the source position. All six lines were usable in D0, but only the last three lines (with the longest MFPs) were present in D1 due to shielding by D0.

Isotope	Energy (keV)	MFP (cm)	D0 (cm)	D1 (cm)
^{241}Am	59.54	9.416×10^{-2}	$(9.165 \pm 0.094) \times 10^{-2}$	—
^{133}Ba	80.99	2.154×10^{-1}	$(2.102 \pm 0.026) \times 10^{-1}$	—
^{57}Co	122.06	5.586×10^{-1}	$(5.846 \pm 0.120) \times 10^{-1}$	—
^{133}Ba	302.85	$1.723 \times 10^{+0}$	$(1.466 \pm 0.135) \times 10^{+0}$	$(3.165 \pm 0.875) \times 10^{+0}$
^{133}Ba	356.02	$1.909 \times 10^{+0}$	$(1.999 \pm 0.173) \times 10^{+0}$	$(5.425 \pm 1.759) \times 10^{+0}$
^{137}Cs	661.66	$2.628 \times 10^{+0}$	$(2.465 \pm 0.430) \times 10^{+0}$	$(8.937 \pm 7.316) \times 10^{+0}$

Chapter 5

The Energy Calibration of NCT 2009

5.1 Introduction

The basic goal of the energy calibration of any radiation detector is to convert a pulse-height (i.e., analog-to-digital converter, or ADC) channel reported by the readout electronics into the energy deposit that it most likely represents, in units that are useful to the experimenter — in our case, keV or MeV. Generally speaking, one does this by sampling the energy range of the detector and electronics with nuclear gamma-ray lines of known energies, noting where the corresponding peaks in ADC channels are found. A model $E(x)$ is then chosen to convert ADC channel x to energy E in keV.

Another goal of the calibration is to determine the energy resolution of the detector and electronics as a function of energy. Though the nuclear lines used for the calibration are intrinsically narrow and can be treated mathematically as delta functions for our purposes, the detector response to the nuclear lines is not a delta function and can usually be modeled as a gaussian or as a related function. The energy resolution is typically measured using the full-width at half maximum (FWHM) of the detector response distribution (e.g., the gaussian) in units of keV, and the resolution is sometimes recorded as a percentage of the total energy of the line. Once the FWHM in keV is measured at various known energies, one can fit models to estimate the FWHM at an arbitrary energy. A model $\Delta E(E)$ is adopted to calculate the FWHM ΔE in keV from the energy E in keV.

The scope of the calibration process can be enormous — any part of the detector that is governed by a different energy response function must be extensively calibrated. For our detectors, this means calibrating the energy channel for each of the 37 strips on both sides of all 10 detectors, totaling as many as $37 \times 2 \times 10 = 740$ channels. In principle, one could subdivide each strip into pixels or even voxels and calibrate each one, although this process requires even more time to accumulate enough counts in each division and significantly complicates the calibration analysis.

For the prototype NCT, significant hole and electron trapping and/or recombina-

tion was noted [41]. In this study, however, we found little evidence of peak tailing in single-site events and did not perform any subdivision by depth to account for such effects.

5.2 Calibration Procedure

The process of calibrating involves illuminating each of the detector strips with a gamma-ray source with lines of known energy. The goal is to obtain enough counts from each line to perform an adequate fit of the line, and to do so with the least possible influence and confusion from other calibration lines.

5.2.1 Asymmetric background model for line fitting

To reduce bias in fitting due to the presence of background counts near the line, and to improve the overall goodness-of-fit of the model, one can add components to the basic gaussian model to model the background in the region of the line as well. Assuming a constant background or even a polynomial background did not generally yield good χ^2 values in this work. Instead, the background is approximated as a constant immediately above the line, and a different constant in the region immediately below the line. So the line model we adopt for perfect energy resolution is

$$f(x) = N\delta(x-\mu) + \begin{cases} C_<, & x < \mu \\ C_>, & x > \mu \end{cases} \tag{5.1}$$

where N is the number of counts in the line, δ is the Dirac delta function, μ is the line energy, $C_<$ is the constant background level below the line, and $C_>$ is the constant background level above the line. The reason for treating the two background regions separately is that the line itself breaks the symmetry of the background — the background spectrum just below the line can contain the energy deposits of electrons that escape the detector material or whose charge clouds undergo charge loss in the gap between strips, but the region just above the line should not have any such enhancement. For a suitably small region around the line, a constant should be a suitable approximation to the background.

The model used to fit the data is obtained by convolving (5.1) with a Gaussian noise function of standard deviation σ. After performing the convolution, the model is calculated to be

$$h(x) = \frac{1}{2}\left(C_< + C_>\right) + \frac{1}{2}\left(C_> - C_<\right)\operatorname{erf}\left(\frac{x-\mu}{\sqrt{2}\sigma}\right) + \frac{N}{\sqrt{2\pi}\sigma}\exp\left(\frac{x-\mu}{2\sigma}\right) \tag{5.2}$$

where σ is the energy resolution of the region (in gaussian sigma, not FWHM) and

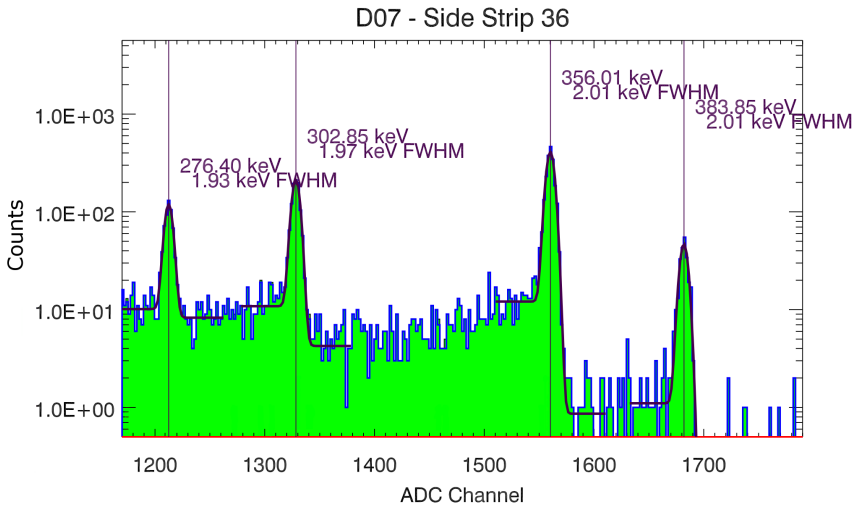

Figure 5.1: An example of fitting the model given in 5.2 to four lines from a ^{133}Ba source.

$$\mathrm{erf}(x) = \frac{2}{\sqrt{\pi}} \int_0^x \exp(-y^2) dy \tag{5.3}$$

is the error function. Figure 5.1 shows an example of fitting this function to four lines from the isotope ^{133}Ba.

5.2.2 Experimental setup

The NCT detectors are sensitive from their LLD threshold of ≈18 keV to a ULD threshold of ≈1800 keV, so this entire energy range should be sampled for the energy calibration. Table 5.1 lists the ten different line energies used in the calibration, ranging from 60 keV to 1333 keV. The calibrated energies we used are from [83].

The "toaster" arrangement of the 10 NCT detectors complicates the process of calibrating the energy (see Fig. 5.2), since the arrangement makes uniform illumination of each detector at normal incidence impossible. Instead, the following procedure was performed. For low-energy sources ($<$ 662 keV), since their mean free paths in germanium are comparable to or less than the detector thickness (15 mm), it is still necessary for those photons to be incident on the face of the detector to reach all the detector strips. Therefore, one detector was calibrated at a time, and the sources were placed above the gaps on either side of the detector. Lead shielding was placed above the detector to prevent photons from entering from the top edge of the detector because this data was also used for depth calibrations, which required photons to be incident on the side of the detector. Figure 5.2 shows the setup for low-energy sources.

Isotope	Line Energy(keV)	Half-life	Activity in Line (μCi)	Ge Mean Free Path (mm)
^{241}Am	59.5409	432.2 y	354.26	0.904
^{133}Ba	80.998	10.51 y	15.65	2.02
^{57}Co	122.061	271.79 d	1.08	4.47
^{133}Ba	276.399	10.51 y	3.29	15.0
^{133}Ba	302.851	10.51 y	8.42	16.7
^{133}Ba	356.013	10.51 y	28.50	18.4
^{133}Ba	383.848	10.51 y	4.11	19.5
^{137}Cs	661.657	30.07 y	64.38	26.3
^{60}Co	1173.228	5.27 y	22.07	35.5
^{60}Co	1332.492	5.27 y	22.08	37.9

Table 5.1: Calibration sources and lines used in the energy calibration.

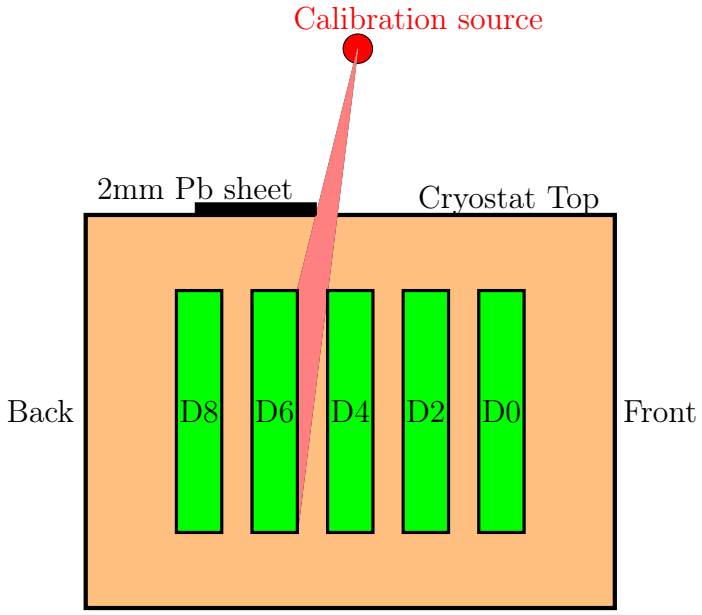

Figure 5.2: Schematic of the setup for low-energy source calibration. In this case, the lead sheet and source are arranged so that the source photons are incident on the front face of D6.

For the high-energy sources (662 keV and higher), normal incidence was not used either, because the mean free paths for these lines are comparable to the thickness of the detectors, and this would lead to very few counts in the rear detectors. Instead, the sources were placed about one meter from the detectors at about 45° elevation in both the front and the back to provide exposure to all strips of all detectors. Data was taken for all detectors at the same time.

After the raw data was collected, only events which had exactly one AC strip and

one DC strip hit ("single-site events") were selected for the energy calibration analysis. This selection was made in order to preferentially choose photopeak events (i.e., all of the gamma-ray energy is deposited in one single interaction).

The fits to each calibration line for each of the energy channels were scripted in the IDL language, and the resulting plots (e.g., Fig. 5.1) were scanned by eye. Any problems in specific fits were manually corrected. Fitting was performed using the MPFIT function [127], which performs chi-squared minimization using the Levenberg-Marquardt algorithm [114, 128]. The peaks generally appear symmetric.

5.3 Calibration Model Selection

In order to select the best model $E(x)$ to use for relating the channel x to energy E in keV, one must first decide what qualities constitute a good model. The criteria considered in this study are:

1. Goodness-of-fit (i.e., low χ^2 value)
2. Robustness
3. Good prediction of data points not in set

Typical empirical models used are the following linear combinations of polynomials and inverted powers (e.g., [61]):

$$E_{P1}(x) = a_0 + a_1 x \tag{5.4}$$
$$E_{P2}(x) = a_0 + a_1 x + a_2 x^2 \tag{5.5}$$
$$E_{P1+I1}(x) = a_0 + a_1 x + \frac{a_2}{x} \tag{5.6}$$
$$E_{P1+I1+I2}(x) = a_0 + a_1 x + \frac{a_2}{x} + \frac{a_3}{x^2} \tag{5.7}$$

Other empirical models were considered that are variants of the above models:

$$E_{P3}(x) = a_0 + a_1 x + a_2 x^2 + a_3 x^3 \tag{5.8}$$
$$E_{P4}(x) = a_0 + a_1 x + a_2 x^2 + a_3 x^3 + a_4 x^4 \tag{5.9}$$
$$E_{P1+I2}(x) = a_0 + a_1 x + \frac{a_2}{x^2} \tag{5.10}$$
$$E_{P2+I1}(x) = a_0 + a_1 x + a_2 x^2 + \frac{a_3}{x} \tag{5.11}$$
$$E_{P2+I2}(x) = a_0 + a_1 x + a_2 x^2 + \frac{a_3}{x^2} \tag{5.12}$$
$$E_{P2+I1+I2}(x) = a_0 + a_1 x + a_2 x^2 + \frac{a_3}{x} + \frac{a_4}{x^2} \tag{5.13}$$

Initial investigation revealed that most channels have an upturn in the calibration curve at lower energies. Other models introduced to account for the low-energy behavior are:

$$E_{P1+Gauss}(x) = a_0 + a_1 x + a_2 \exp\left[-\frac{1}{2}\left(\frac{x}{a_3}\right)^2\right] \quad (5.14)$$

$$E_{P1+Exp3}(x) = a_0 + a_1 x + a_2 \exp\left[-\left(\frac{x}{a_3}\right)^3\right] \quad (5.15)$$

$$E_{P2+Gauss}(x) = a_0 + a_1 x + a_2 x^2 + a_3 \exp\left[-\frac{1}{2}\left(\frac{x}{a_4}\right)^2\right] \quad (5.16)$$

$$E_{P2+Exp3}(x) = a_0 + a_1 x + +a_2 x^2 + a_3 \exp\left[-\left(\frac{x}{a_4}\right)^3\right] \quad (5.17)$$

Each model was fit to data from each energy channel of the instrument, which determines the coefficients $a_0, a_1, \ldots$ and these models were evaluated relative to each other using the criteria described below.

5.3.1 Goodness-of-fit

A first-order requirement for a good model is simply that the model fits the measured data well. For least-squares fitting, the χ^2 statistic is a measure of the goodness-of-fit, as well as the reduced χ^2 statistic (χ^2_ν), which should be ≈ 1 for a good fit to the data. Figure 5.3 shows box plots of the reduced χ^2 for each fit for all channels on the negative side of D8. A box plot shows markings for the minimum, lower quartile, median, upper quartile, and maximum of a distribution of data, along with any outliers, so we can get a sense of the distribution of fits for all the channels on one side of a detector. Similar distributions hold for the other detectors as well.

5.3.2 Characterizing model robustness with cross-validation

A good model should also be robust, in the sense that the removal of data should not greatly affect the final result. The model should also be a good predictor of data that is not in the given dataset. Both of these qualities can be quantified using cross-validation (e.g., [72, 157]).

"Leave-k-out cross validation" can be defined in the following way. Let us have N data points $\{(x_i, y_i)\}$, where $i \in I$ and I is the set of all indices (e.g., $I = [1 \ldots N]$). The data will be fit by a model $\hat{y}(x, \alpha)$, where α represents the model parameters. The number k is the number of data points to be excluded from each trial fit. Define $P(I, k)$ as the set of all unordered partitions of the index set I into groups of length $N - k$ with no repetitions.

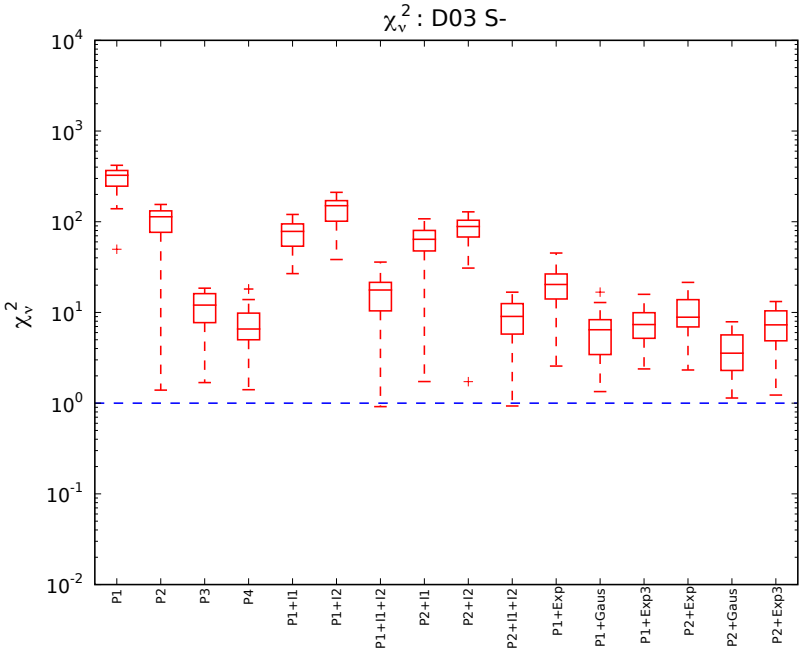

Figure 5.3: Box plots of reduced χ^2 for all of the negative strips on D3 across various models that were tested. The box plot shows markings for the minimum, lower quartile, median, upper quartile, and maximum of a distribution of data, along with any outliers (marked with + signs), so we can get a sense of the distribution of the fits. A model that describes the data well will have a reduced χ^2 of approximately 1 (dotted blue line).

For a given set of indices $S \in P(I,k)$, the model $\hat{y}$ is fit to the subset of the data $\{(x_i, y_i)\}$, $i \in S$. Fitting can be done using least-squares. Call α_S the model parameters that are derived in this way. We are interested in how close the model $\hat{y}(\alpha_S)$ comes to the *excluded* data points $\{(x_j, y_j)\}$, $j \in I \backslash S$. The excluded data is known as the *validation set*. To test the model on the validation set, we use the residual sum of squares statistic (RSS) for the validation set, which is defined as

$$RSS(S) = \sum_{j \in I \backslash S} \left(\frac{\hat{y}(x_j, \alpha_S) - y_j}{\sigma_j} \right)^2 . \tag{5.18}$$

The statistical behavior of (5.18) depends on the particular situation and data. In order to understand the behavior in a limited way, let us consider the following best-case scenario — for all sets S, the fit parameters α_S are always the same and identical to the fit parameters when using all the data (i.e., $\alpha_S = \alpha_I \ \forall S$). In general, this will not be the case. Let us assume the least squares fit to the data has a chi-squared value χ^2. So the average value over all sets $S \in P(I,k)$ is (with a prime to denote this ideal case, and using some identities from combinatorics):

$$\langle RSS' \rangle_{S \in P(I,k)} = \frac{1}{\left(\begin{array}{c} N \\ k \end{array} \right)} \sum_{S \in P(I,k)} \sum_{j \in I \setminus S} \left(\frac{\hat{y}(x_j, \alpha_I) - y_j}{\sigma_j} \right)^2 \tag{5.19}$$

$$= \frac{1}{\left(\begin{array}{c} N \\ k \end{array} \right)} \sum_{S' \in P(I,N-k)} \sum_{j \in S'} \left(\frac{\hat{y}(x_j, \alpha_I) - y_j}{\sigma_j} \right)^2 \tag{5.20}$$

$$= \frac{1}{\left(\begin{array}{c} N \\ k \end{array} \right)} \left(\begin{array}{c} N-1 \\ k-1 \end{array} \right) \sum_{i \in I} \left(\frac{\hat{y}(x_i, \alpha_I) - y_i}{\sigma_i} \right)^2 \tag{5.21}$$

$$= \frac{k}{N} \chi^2 \tag{5.22}$$

So we see that the RSS bears more than a superficial resemblance to the definition of χ^2, and by including a factor of N/k we can "normalize" the average RSS for comparison to χ^2. So we define the RSS for leave-k-out cross-validation in the following way:

$$\langle RSS \rangle_k \equiv \frac{N}{k} \frac{1}{\left(\begin{array}{c} N \\ k \end{array} \right)} \sum_{S \in P(I,k)} RSS(S)$$

$$= \frac{1}{\left(\begin{array}{c} N-1 \\ k-1 \end{array} \right)} \sum_{S \in P(I,k)} RSS(S). \tag{5.23}$$

This definition will aid the comparison between χ^2 and the RSS for different values of k.

5.3.3 Discussion of model selection

This process of data exclusion, performing a fit to the remaining data, and calculating the $\langle RSS \rangle_k$ was done for all of the models mentioned previously. The resulting values of reduced χ^2, reduced $\langle RSS \rangle_1$, and reduced $\langle RSS \rangle_2$ (i.e., all have been normalized by the degrees of freedom ν of the fit to all of the data) for one side of D3 are shown in Fig. 5.4.

The box plots in Fig. 5.4 are representative of all the other detectors. Some interesting features emerge from this analysis. First, some models are remarkably stable when performing cross-validation (e.g., P1, P2, P1+Gauss, P1+Exp3), while others are unstable to the removal of data points (e.g., P4, P1+I1+I2, P2+Gauss). We wish to avoid the latter kind of model. In general, the addition of model parameters causes a smaller reduced χ^2 for the fit but can drastically increase the reduced $\langle RSS \rangle_1$

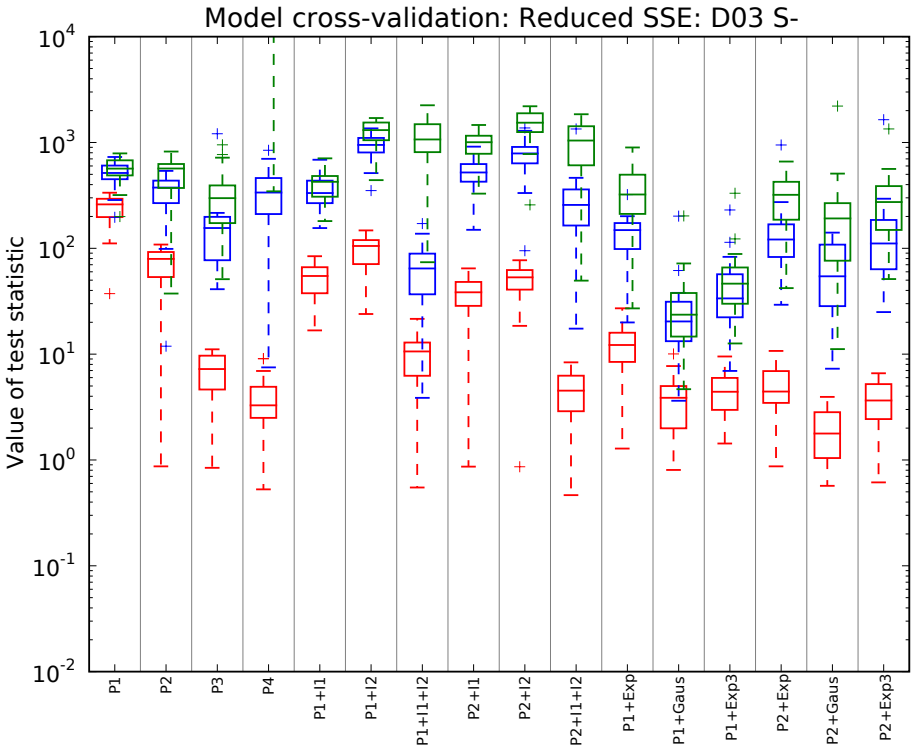

Figure 5.4: Plots of the cross-validation statistics for reduced χ^2 (red) , reduced $\langle RSS \rangle_1$ (blue), and reduced $\langle RSS \rangle_2$ (green) for all 37 strips on the negative side of D3. This plot is similar for all sides of all detectors.

and $\langle RSS \rangle_2$ (e.g., the series of models P1, P2, P3, P4). Among the models considered, the best combination of good cross-validation performance and low χ^2 is found in the P1+Gauss model:

$$E_{P1+Gauss}(x) \quad = \quad a_0 + a_1 x + a_2 \exp\left[-\frac{1}{2}\left(\frac{x}{a_3}\right)^2\right] \tag{5.24}$$

Residuals for the fits to this model and to P1 (which is a baseline standard for germanium detectors) are shown in Figs. 5.5 and 5.6. Shown alongside the fit residuals are the residuals of the validation points for leave-one-out cross-validation (i.e., the calculation of $\langle RSS \rangle_1$).

5.4 Energy Resolution Model Selection

Cross-validation was also used to select the best model for the energy resolution of each channel. The following are typical empirical models that are fit to the FWHM

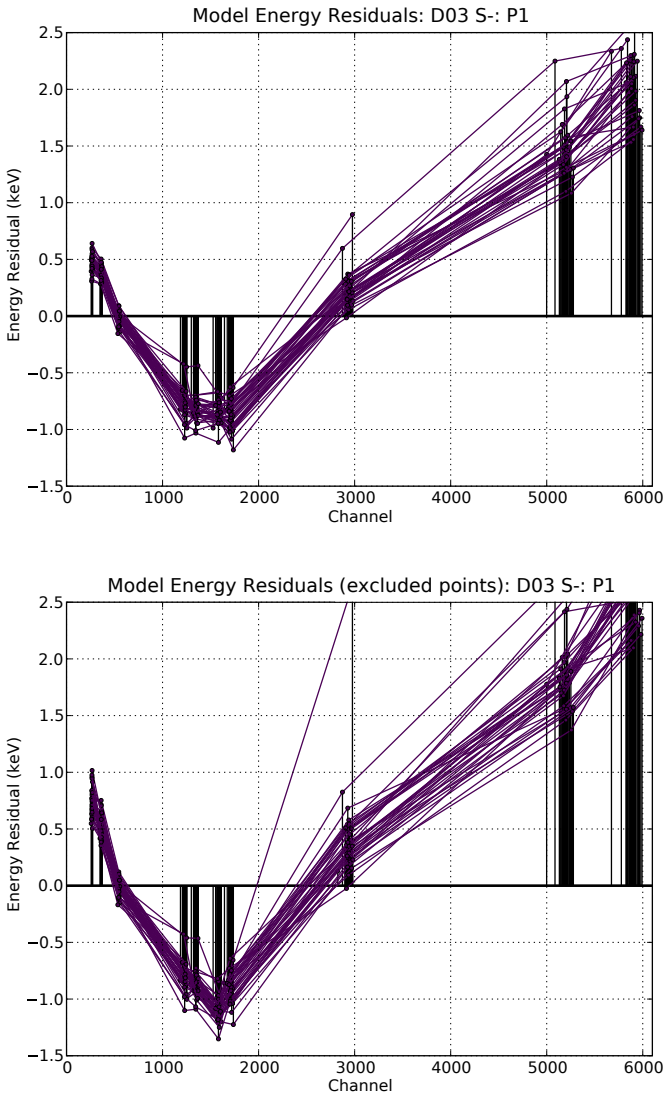

Figure 5.5: Plots of the residuals for the linear model (P1). The top plot shows residuals from the fit to all the data, while the bottom plot shows the residuals of the excluded points when using leave-one-out cross-validation. Notice that in general the residuals in the bottom plot are slightly larger than in the top plot, since these points are not included in the fit. The channels shown here are all 37 strips from the negative side of D3.

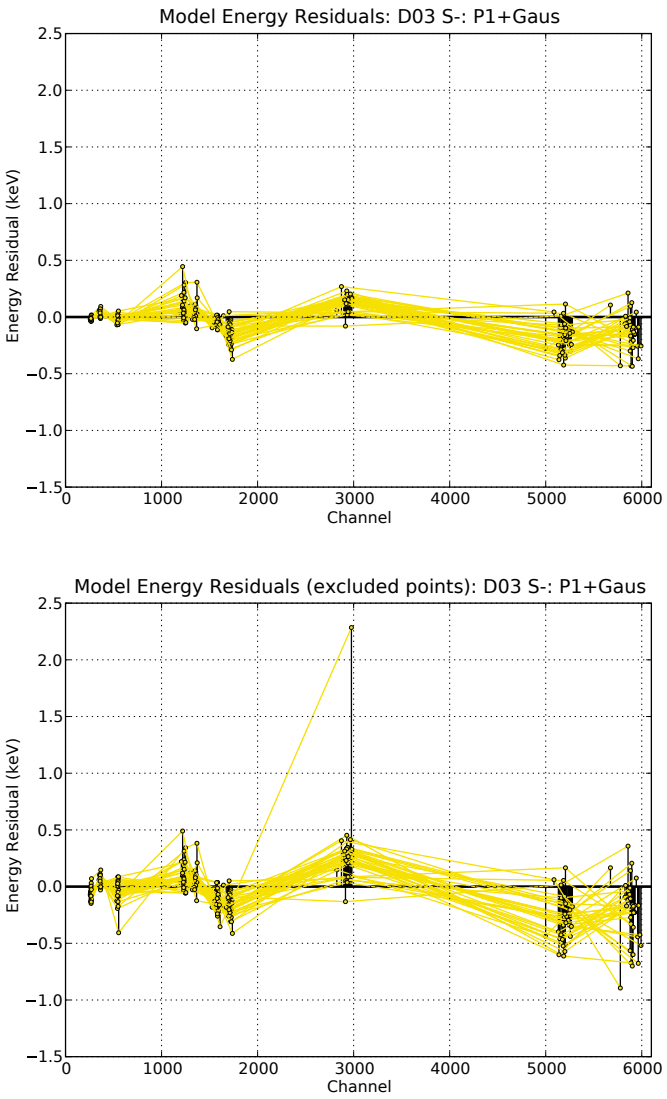

Figure 5.6: Plots of the residuals for the linear model plus gaussian (P1+Gauss). The top plot shows residuals from the fit to all the data, while the bottom plot shows the residuals of the excluded points when using leave-one-out cross-validation. Notice that in general the residuals in the bottom plot are slightly larger than in the top plot, since these points are not included in the fit. Notice also the dramatic improvement of this model over Fig. 5.5. The channels shown here are all 37 strips from the negative side of D3.

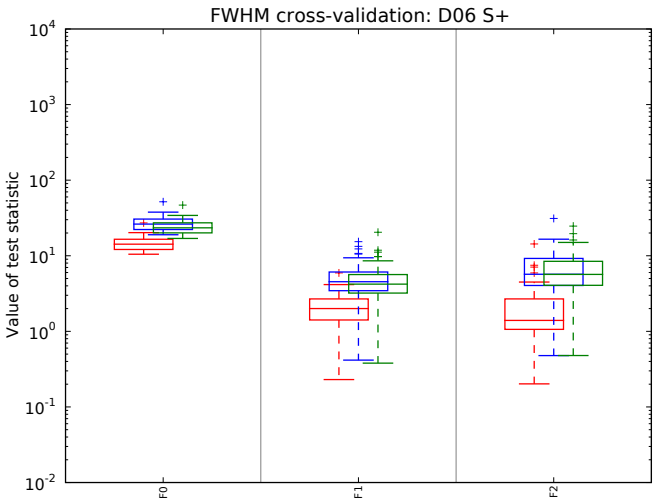

Figure 5.7: Plots of the cross-validation statistics for reduced χ^2 (red) , reduced $\langle RSS \rangle_1$ (blue), and reduced $\langle RSS \rangle_2$ (green) for all 37 strips on the positive side of D6. This plot is similar for all sides of all detectors.

in keV of each strip (e.g., [61]):

$$W_{P0}(x) = (a_0)^{1/2} \tag{5.25}$$

$$W_{P1}(x) = (a_0 + a_1 x)^{1/2} \tag{5.26}$$

$$W_{P2}(x) = \left(a_0 + a_1 x + a_2 x^2\right)^{1/2} \tag{5.27}$$

This process of data exclusion, performing a fit to the remaining data, and calculating the $\langle RSS \rangle$ was done for these three models. The resulting values of reduced χ^2, reduced $\langle RSS \rangle_1$, and reduced $\langle RSS \rangle_2$ for one side of D6 are shown in Fig. 5.7. The result is that the P1 and P2 models do comparably well. The P1 model was chosen because its RSS values were slightly better than the P2 model. Residuals of the P1 model for the same side of D6 are shown in Fig. 5.8.

5.5 Calibration Results

Nine of the ten NCT 2009 detectors were calibrated using these methods. The positive side of D0 was not functional due to very high leakage current, which did not permit the observation of any spectral lines. The positive side of D2 was similarly crippled by high leakage current, although some lines were visible on most strips. The cause of the high leakage current is not known, although it may have been caused by a combination of high impurities in the amorphous germanium surface coating and high temperatures due to their location near the end of the coldfinger.

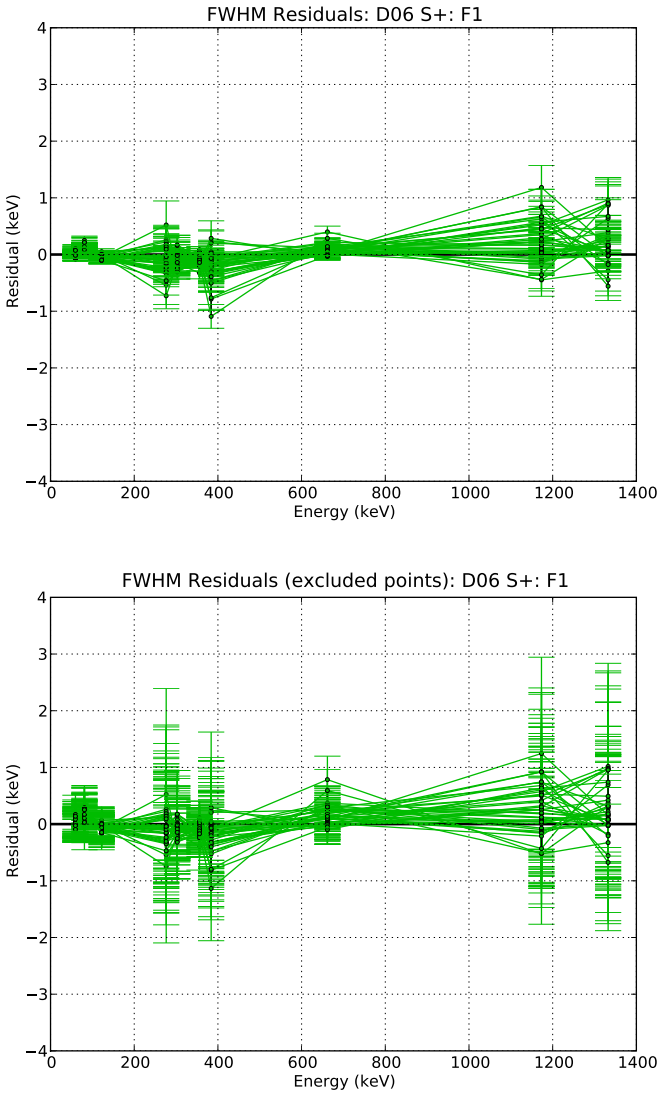

Figure 5.8: Plots of the residuals for the linear FWHM model (P1). The top plot shows residuals from the fit to all the data, while the bottom plot shows the residuals of the excluded points when using leave-one-out cross-validation. The channels shown here are all 37 strips from the positive side of D6.

Another anomaly observed was occasional high noise on several strips on the D8 negative side and D9 positive side. This elevated noise level was always seen contemporaneously on the two detectors. This noise could be microphonics from the liquid nitrogen boiling, since these two detector sides are the closest to the dewar. These data points were excluded from the model fits to the energy resolution of these channels.

5.5.1 Energy Resolution

The energy resolution of each strip was obtained from the calibration. Histograms of the single-strip resolutions at different line energies are shown in Fig. 5.9. The resolution of negative channels on all detectors increases slightly with energy, as expected due to statistical effects of electron-hole generation. The positive strips in general perform much worse at higher energies. Since three of the detectors (D1, D3, D5) are n-type germanium while the others are p-type, this may suggest that electron trapping and recombination are present in the detectors (electrons are sensed in the NCT electronics by positive-going pulses). Another possibility is that the positive channel electronics are slightly noisier than their negative counterparts.

Plots of the energy resolution for all strips are shown in Figures 5.10 and 5.11. The microphonics anomalies are seen in D8 and D9 for the ^{137}Cs and ^{60}Co data. These plots also reveal the worse performance of the positive strips.

5.5.2 Thresholds

The LLD and FLD thresholds can be obtained by fitting the low-energy continuum of the calibration data. The LLD threshold is narrow — approximately 2−3 channels wide in most cases, and so it was fit with a step function:

$$f_{LLD}(x) = \begin{cases} 0, & x < x_{LLD} \\ A, & x >= x_{LLD} \end{cases} \tag{5.28}$$

The FLD threshold was a much wider transition due to higher noise in the fast channel. In order to fit the FLD threshold, two spectra were created — one of LLD-only events (which should die away above the FLD threshold), and one of FLD events (which should die away below the FLD threshold). Two functions were simultaneously fit to the LLD-only and FLD spectra:

$$g_{LLD}(x) = \frac{1}{2} g(x) \left[1 - \mathrm{erf}\left(\frac{x - x_{FLD}}{\sqrt{2}\sigma} \right) \right] \tag{5.29}$$

$$g_{FLD}(x) = \frac{1}{2} g(x) \left[1 + \mathrm{erf}\left(\frac{x - x_{FLD}}{\sqrt{2}\sigma} \right) \right] \tag{5.30}$$

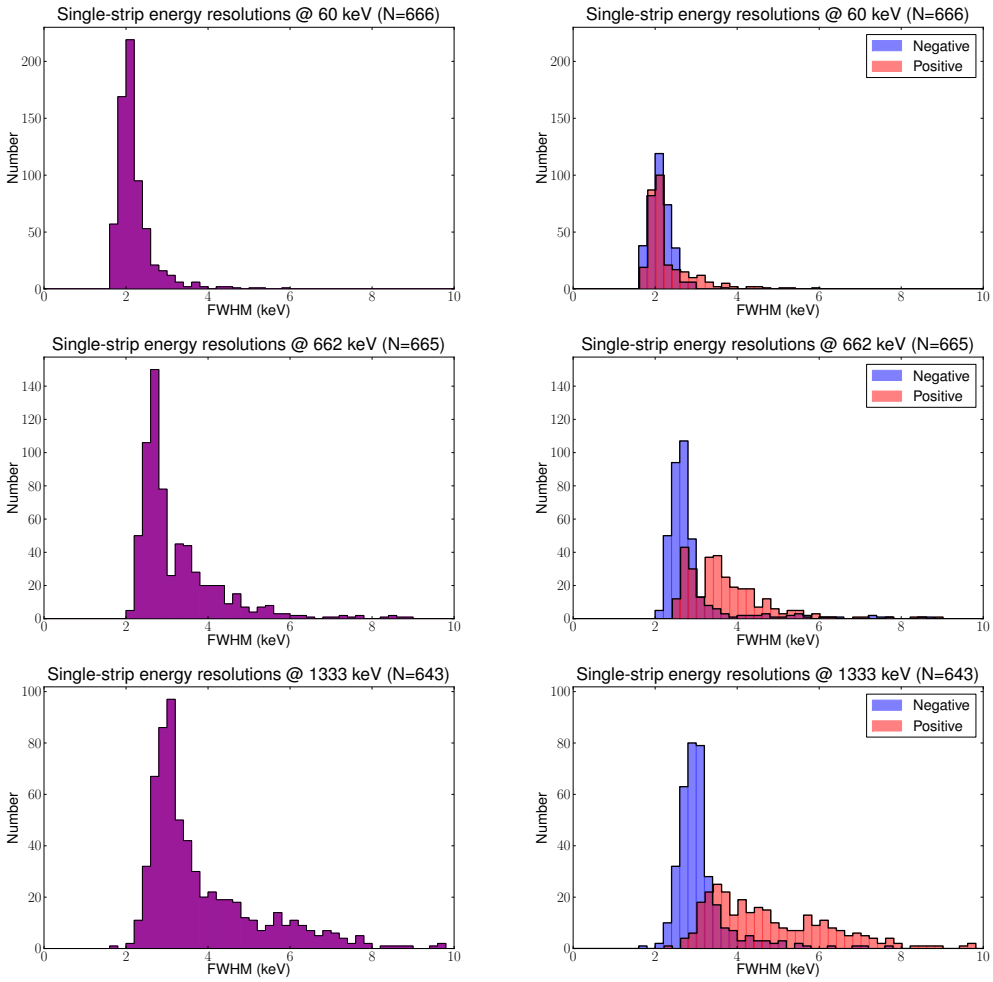

Figure 5.9: Histogram of single-strip energy resolution for all channels at 60 keV (top), 662 keV (middle), and 1333 keV (bottom). For each energy, the histogram of all strips is shown on the left hand side, while the right hand side shows histograms broken down by positive and negative strips to see how each class of strips contributes to the total. At 60 keV, both positive and negative strips contribute similarly to the total. At the higher energies, the resolution becomes worse, as is expected due to greater statistical fluctuations in the generation of electron-hole pairs. However, it also becomes clear at the higher energies that the positive strips end up with worse resolution on average than the negative strips, suggesting that electron trapping is important in the NCT detectors.

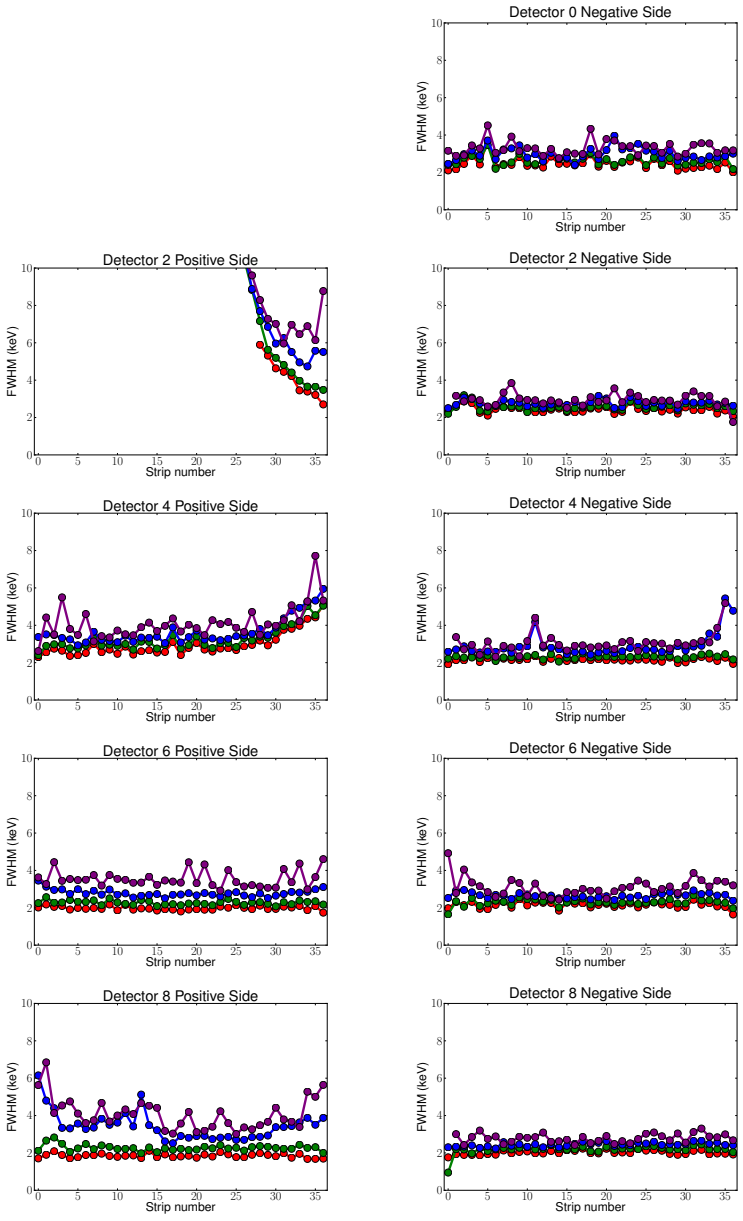

Figure 5.10: Energy resolution (FWHM in keV) for all of the strips on the positive side (left) and negative side (right) of D0, D2, D4, D6, and D8 at 60 keV (red), 356 keV (green), 662 keV (blue), and 1333 keV (purple).

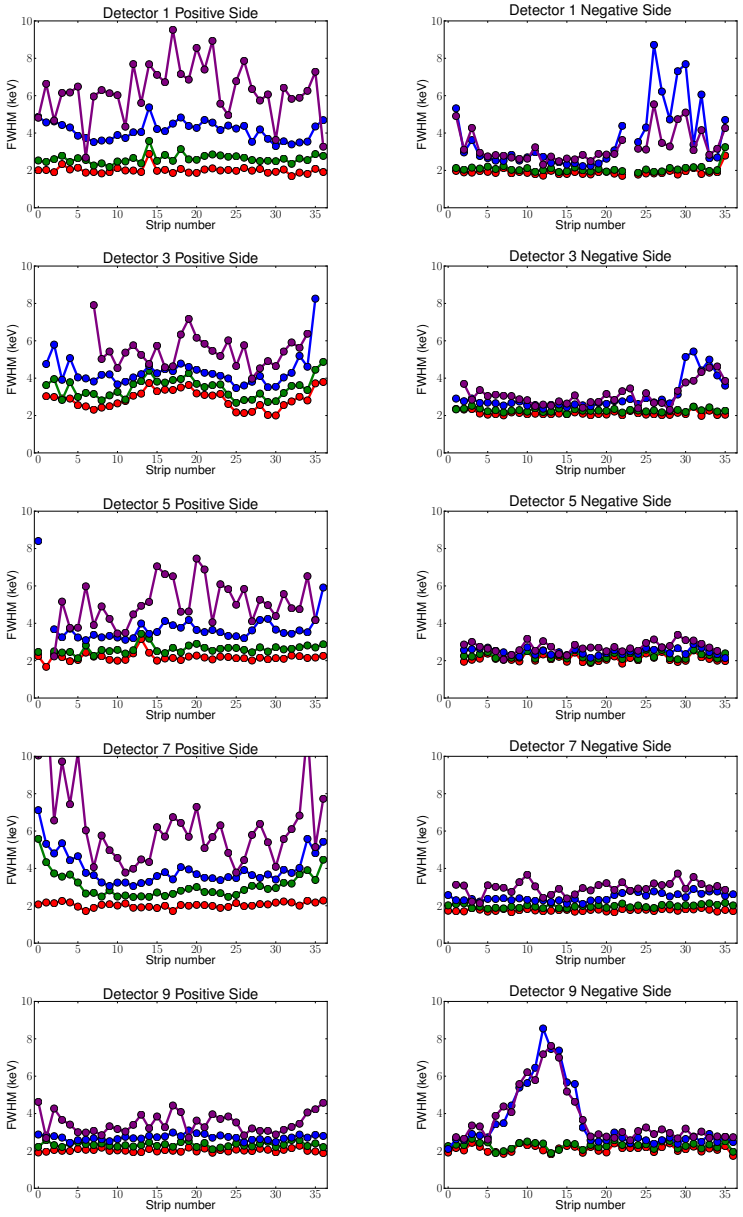

Figure 5.11: Energy resolution (FWHM in keV) for all of the strips on the positive side (left) and negative side (right) of D1, D3, D5, D7, and D9 at 60 keV (red), 356 keV (green), 662 keV (blue), and 1333 keV (purple).

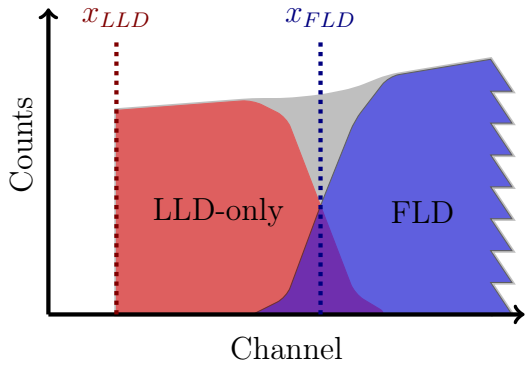

Figure 5.12: Schematic of the low end of a channel spectrum showing the LLD and FLD threshold. The LLD-only spectrum (blue) contains events that have only an energy trigger, while the FLD spectrum (red) includes events with both energy and timing triggers. The LLD threshold has a very sharp cutoff and is modeled with a step function. The FLD threshold is more gradual and occurs over a region where the spectral shape is changing, so it is modeled with a step function convolved with gaussian noise multiplied by the total spectrum ($g(x)$, shown here as the gray region).

where $g(x)$ is the sum of the LLD-only and FLD spectra. Figure 5.12 shows a schematic of the spectrum in this region. Once the functions are fit, the channel values x_{LLD} and x_{FLD} are converted to energy using the energy calibration. Figures 5.13 and 5.14 show the results for the LLD threshold and FLD threshold for all channels of all detectors. We find that in most cases, both thresholds were at their nominal value (20 keV for LLD and 40 keV for FLD).

5.5.3 Summed-strip spectra

Another measure of the performance of the energy calibration is the resolution obtained after adding multiple strip energies together, instead of only single-strip events as was used until this point. As seen in Fig. 5.15, the summed spectrum does not have the simple gaussian shape expected, but a secondary peak appears above the main line. This peak is not as sharp as the main peak and appears to have an exponential tail. The cause of these effects is cross-talk between strips and charge loss in the gap between strips, as will be handled in the next chapter.

5.6 Summary

An energy calibration for NCT 2009 was developed, where the calibration model was selected from several candidate models using cross-validation. The same model selection was performed for the energy resolution as a function of energy. The resulting

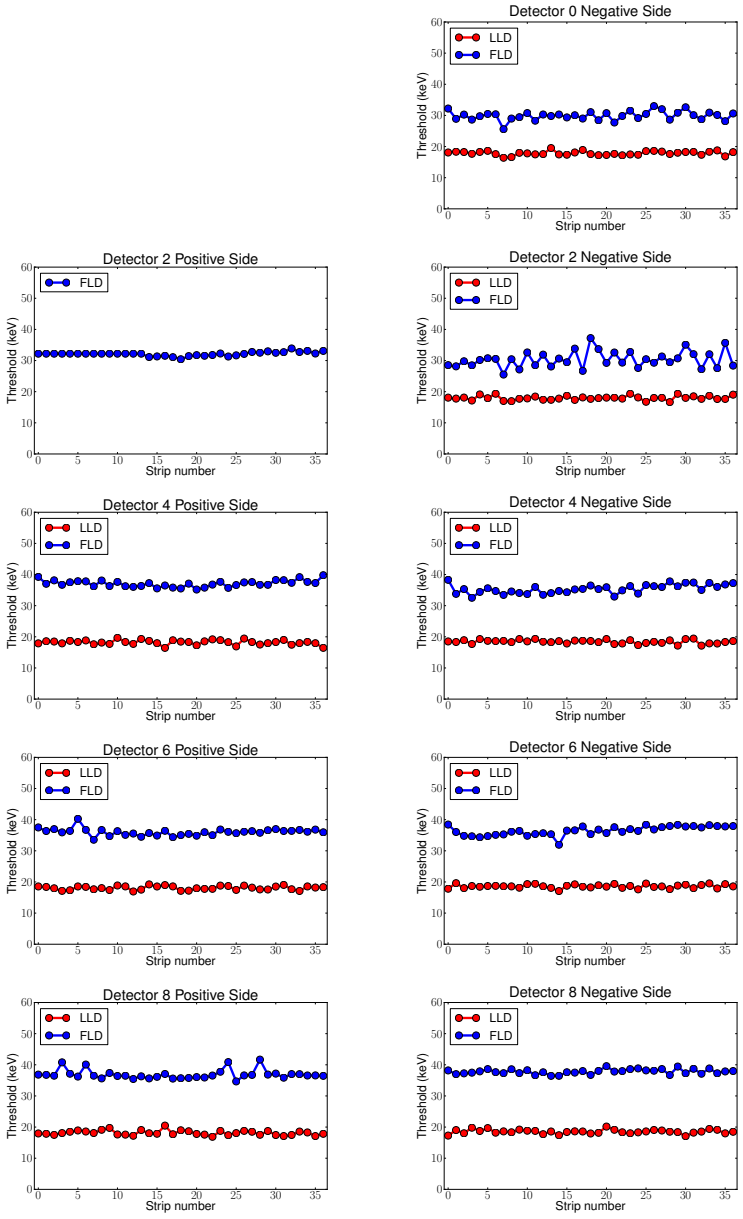

Figure 5.13: LLD and FLD energy thresholds for all of the strips on the positive side (left) and negative side (right) of D0, D2, D4, D6, and D8.

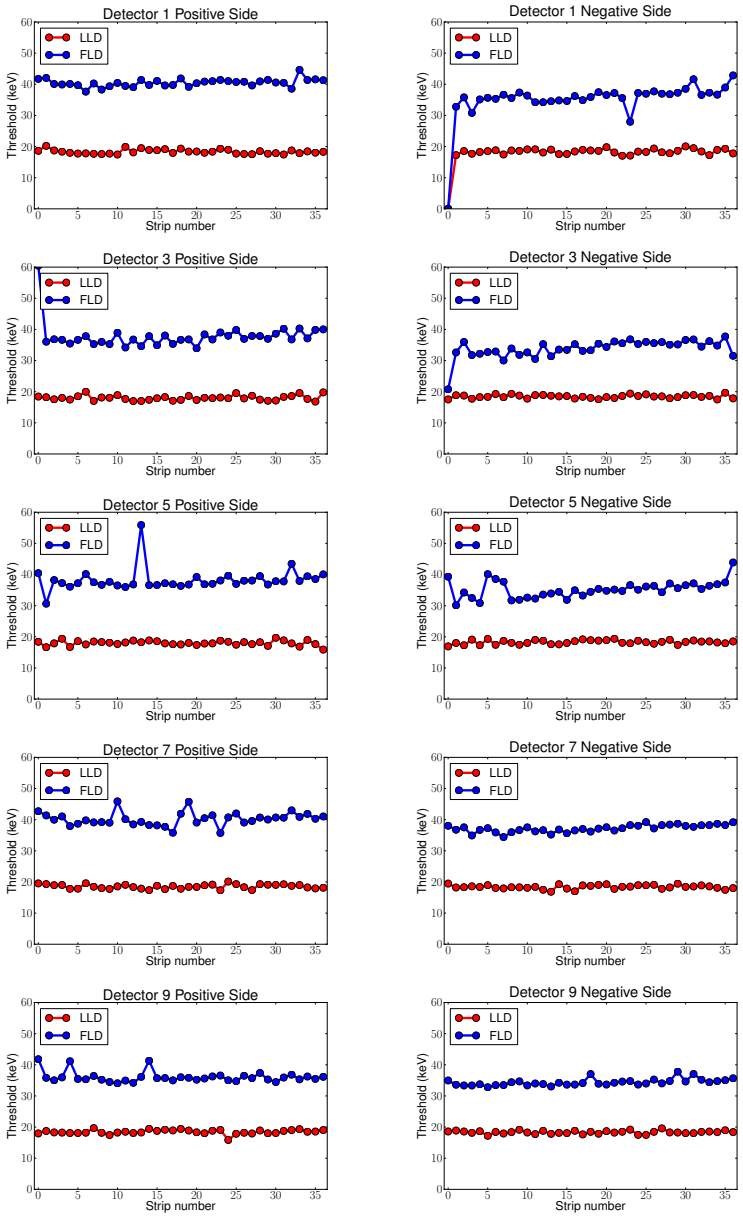

Figure 5.14: LLD and FLD energy thresholds for all of the strips on the positive side (left) and negative side (right) of D1, D3, D5, D7, and D9.

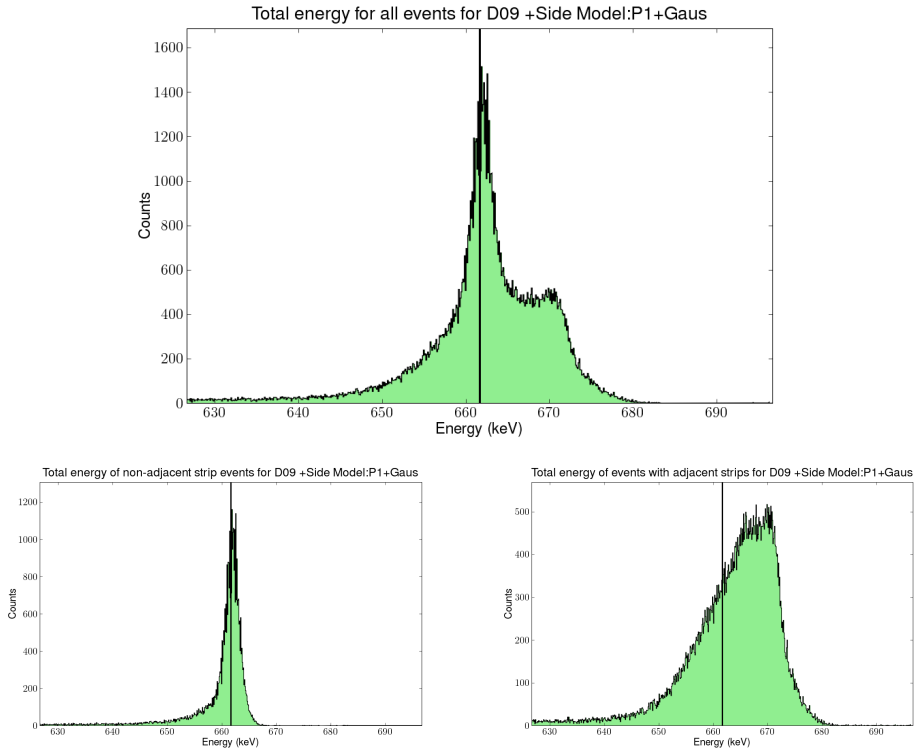

Figure 5.15: Summed-strip spectrum of 662 keV photons (top). A secondary line and an exponential tail become apparent when summing the energies. Below, the spectrum is broken down into those events with no adjacent strips (left) and events with adjacent strips (right). Clearly, the events with adjacent strips are the only contributors to the secondary line, suggesting cross-talk between adjacent strips. Data is from the positive side of D9. The expected line energy is marked with a solid black line in the center of the plot.

calibration performs well, although it is found that the positive electronics channels have worse energy resolution than the negative electronics channels, either due to electron trapping and recombination or the electronics design. Additional, when adding multiple-strip energies together, a secondary peak and exponential tail are observed. These problems will be discussed in the next chapter.

Some potential issues were not addressed in the energy calibration, such as the amount on gain drift with temperature and the source of microphonics noise on D8 and D9. These issues would be important to understand in future missions.

Chapter 6

The Cross-talk and Charge Loss Corrections for NCT 2009

6.1 Introduction

As seen in Chapter 5, the energy calibration for NCT revealed two undesired effects in the spectrum of multiple-strip events. These effects — the appearance of another peak above the photopeak, and the tailing below that peak (Fig. 6.1) — can be explained as the result of primarily two phenomena: cross-talk between adjacent channels and charge loss in the gap between strips. The correction for these two effects will be demonstrated in this chapter.

Cross-talk is the influence of one electronics channel upon another. The cause can be anywhere in the signal chain, from the detector itself, to the signal cables, to the analog and digital readout electronics [76]. Although no strong evidence for cross-talk between adjacent strips was seen in the prototype NCT instrument [42], clear evidence was seen in NCT 2009 for cross-talk once the energy calibration was performed and summed strip energies were first examined in detail. Fortunately, this has been seen in similar germanium detectors and can be corrected [56, 76].

Charge loss occurs when part of the charge cloud is not collected to the strip electrodes during the dynamic time of the energy channel electronics. Charge loss can be a result of trapping in the detector material or low electric field near the surface in the gap between strips [5]. This effect has been observed before in other germanium strip detectors [5, 51, 82], and the effect can be corrected.

6.2 Measuring the cross-talk effect

As we shall see, cross-talk occurs between any two nearby strips regardless of the underlying type of interaction, while charge loss only occurs for single-site events shared between two adjacent strips. The cross-talk effect causes an increase in the

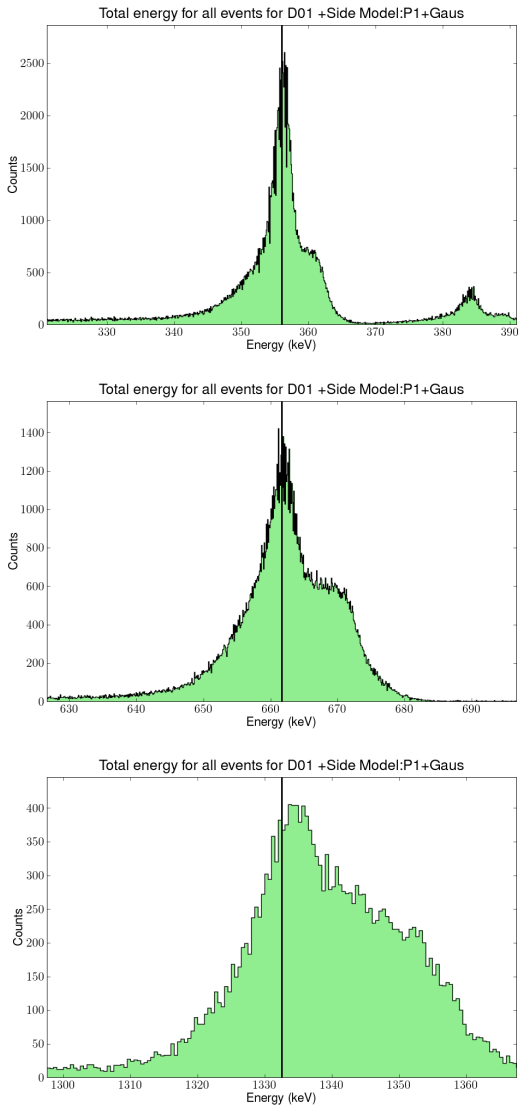

Figure 6.1: Summed-strip spectrum of photons at 356 keV (top), 662 keV (middle), and 1333 keV (bottom). The offset of the secondary line increases proportionally to the energy. Data is from the positive side of D1.

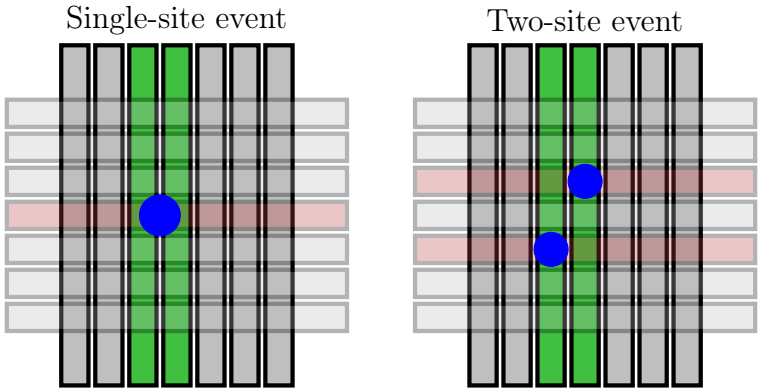

Figure 6.2: Schematic of the different underlying photon events that can be measured in adjacent strips. The blue dots mark the location of the charge cloud formed at the energy deposits. Since charge loss can occur in events that occur in the gap between strips, we need to discard events like those in the left-hand diagram. The remaining events (right-hand diagram) will have cross-talk and only a small loss of charge if the interactions are near the gap.

measured energy on neighboring strips (e.g., Fig. 6.1). In order to measure the effect of cross-talk, we will examine its effect on adjacent strips and strips that are separated from each other.

6.2.1 The effect between adjacent strips

Let us assume that we have two adjacent strips that measure energy during an event. The underlying photon event can be one of two types: a single energy deposit whose charge cloud has been collected on two adjacent strips (a "single-site event") or multiple energy deposits (a "multiple-site event") (see Fig. 6.2). Since charge loss occurs in the gap between strips, single-site events are more likely to have a maximal amount of charge loss compared to multiple-site events. So to measure the cross-talk effect by itself, we should use only adjacent strip events that are likely to have an underlying multiple-site event.

To select adjacent strips with underlying multiple-site events, events were selected that had two adjacent strips on one side and any two strips on the other side. If the two strips on the opposite side are not adjacent, then we assume that their underlying event is a multiple-site event. However, if the two strips on the opposite side are adjacent, we need to determine whether it is more likely to be a single-site event or multiple-site event. The strips were paired using their energies in the following manner. If detector side i has two adjacent strips with energies $E_{i,1}$ and $E_{i,2}$, and the other detector side j has two adjacent strips with energies $E_{j,1}$ and $E_{j,2}$, we construct

the following reduced chi-squared values:

$$\chi^2_{1-site} = \frac{(E_{i,1}+E_{i,2}-E_{j,1}-E_{j,2})^2}{\sigma^2_{i,1}+\sigma^2_{i,2}+\sigma^2_{j,1}+\sigma^2_{j,2}} \quad (6.1)$$

$$\chi^2_{2-site,1-1} = \frac{1}{2}\left[\frac{(E_{i,1}-E_{j,1})^2}{\sigma^2_{i,1}+\sigma^2_{j,1}}+\frac{(E_{i,2}-E_{j,2})^2}{\sigma^2_{i,2}+\sigma^2_{j,2}}\right] \quad (6.2)$$

$$\chi^2_{2-site,1-2} = \frac{1}{2}\left[\frac{(E_{i,1}-E_{j,2})^2}{\sigma^2_{i,1}+\sigma^2_{j,2}}+\frac{(E_{i,2}-E_{j,1})^2}{\sigma^2_{i,2}+\sigma^2_{j,1}}\right], \quad (6.3)$$

where σ is the energy resolution for each energy measurement. Note that χ^2_{1-site} is the reduced chi-squared for grouping the strips into a single site, while the χ^2_{2-site} values are the reduced chi-squared values for each of the two possible matches between the strips ($i1-j1$ and $i2-j2$, or $i1-j2$ and $i2-j1$). We select the minimum of these three reduced chi-squared values as the most likely underlying event, and thus are able to reject most single-site events.

Plots of the summed energy of multiple-site events and single-site events are shown in Fig. 6.3. The shifted lines are fitted with a phenomenological model: a delta function plus an exponential tail, convolved with gaussian noise (e.g., [146]):

$$f_{gaussian}(x;N,\mu,\sigma) = \frac{N}{\sqrt{2\pi}\sigma}\exp\left[-\frac{(x-\mu)^2}{2\sigma^2}\right] \quad (6.4)$$

$$f_{tail}(x;N,\mu,\sigma,\lambda) = \frac{N}{2\lambda}\exp\left(\frac{x-\mu}{\lambda}+\frac{\sigma^2}{2\lambda^2}\right)\left[1-\mathrm{erf}\left(\tfrac{x-\mu}{\sqrt{2}\sigma}+\tfrac{\sigma}{\sqrt{2}\lambda}\right)\right] \quad (6.5)$$

$$f_{gauss+tail}(x) = \eta f_{tail}+(1-\eta)f_{gaussian} \quad (6.6)$$

where N is the number of counts, μ is the line position, and σ is the noise. The tail is an exponential with decay constant λ (keV), and a fraction η of the counts is in the tail (with $1-\eta$ in the gaussian). This model fits the multiple-site spectrum well, and the fitted gaussian σ is comparable in all cases to the gaussian σ of the non-adjacent strip summed spectrum. The tail fraction also tends to be low ($\eta < 0.5$), suggesting that these events are not dominated by charge loss. On the other hand, the single-site spectrum is not fit very well by this function, and as expected is not useful in isolating the cross-talk effect.

6.2.2 The effect between separated strips

Let us assume that we have two non-adjacent strips that both measure energy during an event. Since these two strips are not adjacent, the underlying event must be a multiple-site event. These two strips can potentially have cross-talk between them.

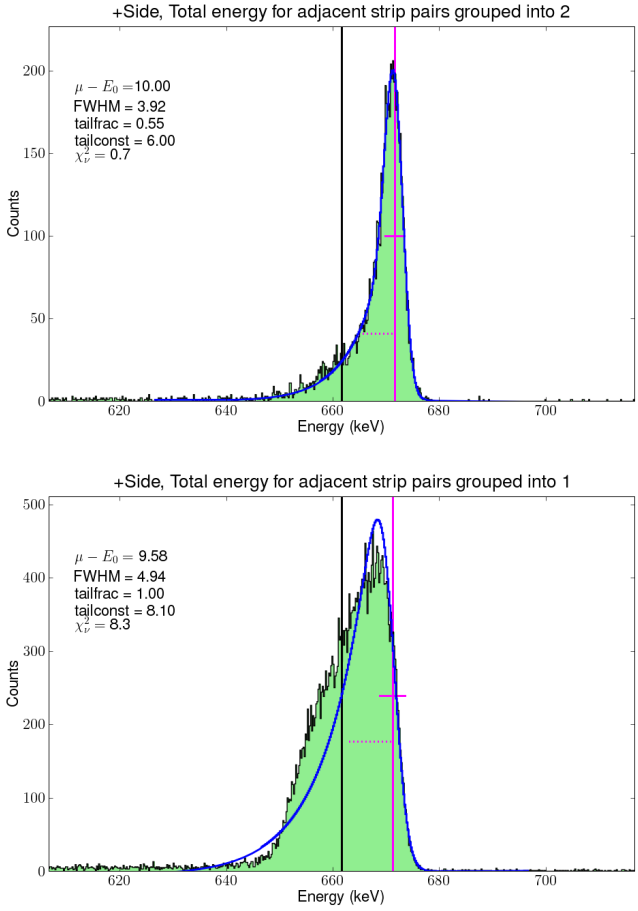

Figure 6.3: In an attempt to isolate the cross-talk effect from charge sharing, events that are likely due to two-site events (top) are separated from single-site events (bottom). A narrow gaussian with a small exponential tail fits the two-site event data well, and its mean is used to calculate the cross-talk effect. The single-site event data is not as useful in isolating the cross-talk effect. Data is at 662 keV, from the positive side of D1.

In order to isolate the cross-talk between separated strips, events were selected that had exactly two non-adjacent strips on one side of the detector and any two strips on the other side. The summed spectrum was calculated for each type of separation between strips: "skip-1 neighbors," "skip-2 neighbors," and so on (see Fig. 6.4). The result is that there is a smaller yet measurable cross-talk effect between strips, but the effect is imperceptible for skip-3 neighbors and farther (see Fig. 6.5).

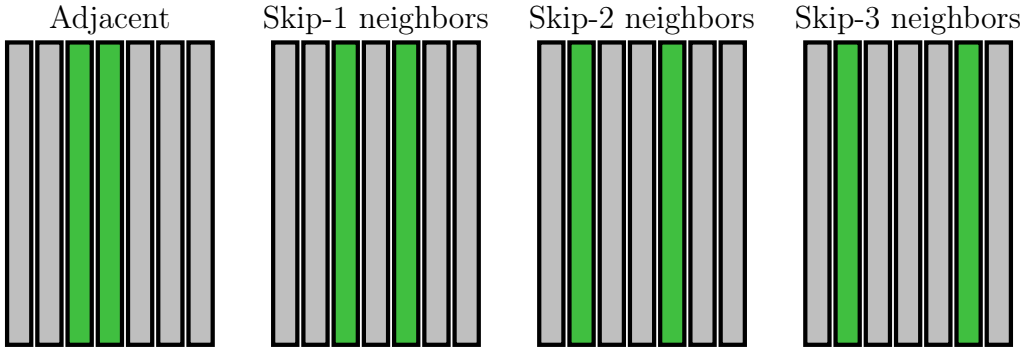

Figure 6.4: Schematic of the different configurations of neighboring strips.

6.2.3 Discussion

The offset caused by cross-talk was found to be linear with energy. This linearity held for adjacent strip pairs and skip-1 neighbors. For most detectors, the effect was imperceptible or very weak for skip-2 neighbors, skip-3 neighbors, and farther. Figure 6.6 shows linear fits to the cross-talk offsets for several energies. Fits using only a linear term (i.e., bE) return very poor fits, while linear functions (i.e., $a+bE$) fit very well. The constant a is always negative and fall in the range 0 to -3 keV.

6.3 Cross-talk correction

Since the cross-talk effect appears to be linear, it should be possible to disentangle its effects and recover the true deposited energies. Regardless of the cause of the cross-talk, a reasonable assumption is that the cross-talk effect on a neighboring strip is proportional to the energy on the original strip, and *vice versa*. In mathematical language, letting a tilde ($\sim$) denote the measured energy, this means:

$$\begin{cases} \tilde{E}_A &= E_A + \beta_1 E_A \\ \tilde{E}_B &= E_B + \beta_1 E_B \end{cases} \tag{6.7}$$

where A and B are two adjacent strips and no other energies are deposited (Fig. 6.7). Then the total measured energy is

$$\tilde{E} \;=\; (1+\beta_1)E. \tag{6.8}$$

However, if there are sub-threshold energy deposits on adjacent strips, those also

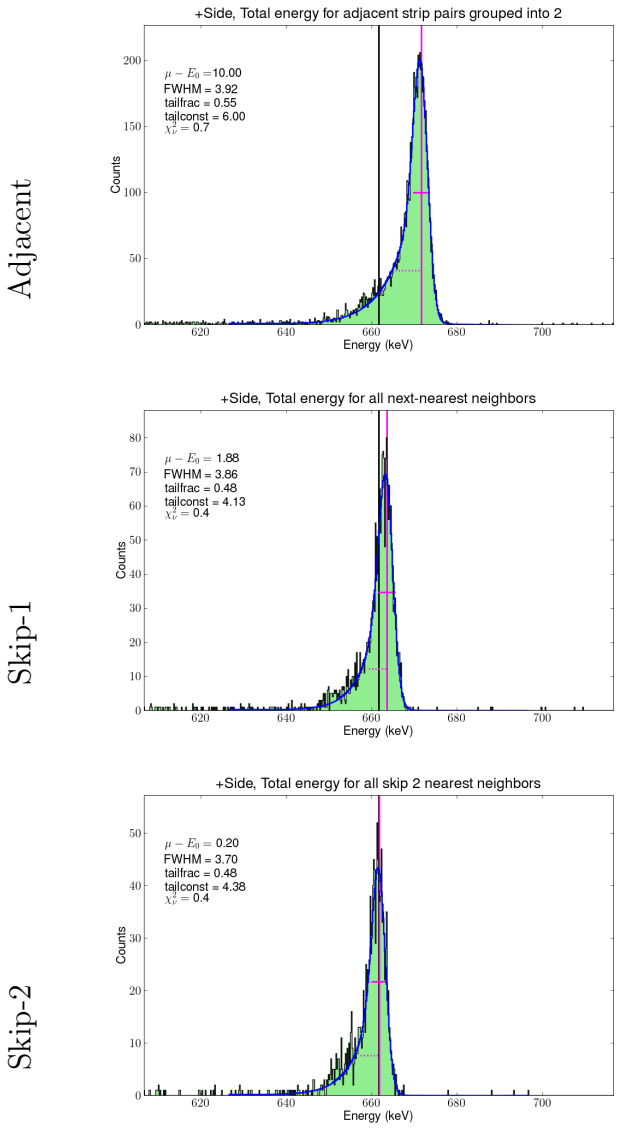

Figure 6.5: Cross-talk even affects strips that are not immediately adjacent. The top plot shows the summed spectrum of two adjacent strips for likely two-site events. The middle plot shows the summed spectrum for two strips separated by one inactive strip ("skip-1 neighbors"). The bottom plot shows the same data for two strips separated by two inactive strips ("skip-2 neighbors"). The offset from the true line energy decreases as the strips are farther apart. Data is at 662 keV, from the positive side of D1.

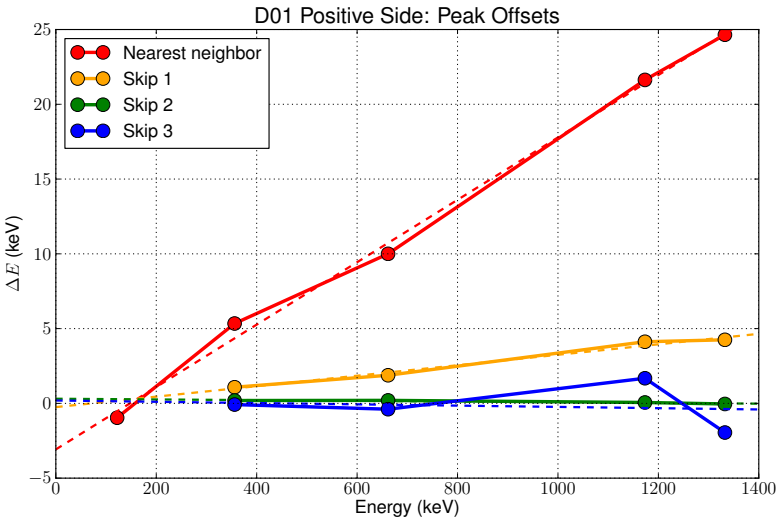

Figure 6.6: Fits of cross-talk offsets for one detector at several energies. The strongest effect is for nearest neighbors, and a weaker effect is found for skip-1 neighbors. Skip-2 and skip-3 neighbors do not have a measurable effect for most detectors and will be excluded from the cross-talk correction. Data is from the positive side of D1 but is representative of all other detectors.

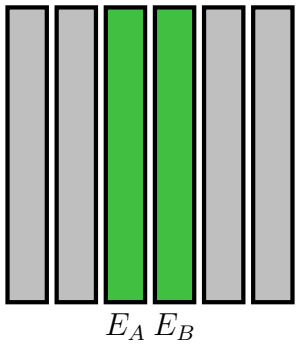

Figure 6.7: Schematic of strips A and B. The measured energy on each strip is influenced by the energy on the other strip.

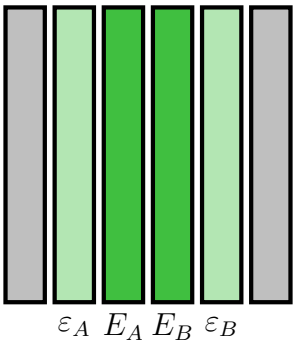

Figure 6.8: Schematic of strips A and B when there are sub-threshold energy deposits (ε_A and ε_B) on neighboring strips.

should affect the measured energy. Considering the case shown in Fig. 6.8, we obtain

$$\begin{cases} \tilde{\varepsilon}_A &= \varepsilon_A + \beta_1 E_A \\ \tilde{E}_A &= E_A + \beta_1 E_B + \beta_1 \varepsilon_A \\ \tilde{E}_B &= E_B + \beta_1 E_A + \beta_1 \varepsilon_B \\ \tilde{\varepsilon}_B &= \varepsilon_B + \beta_1 E_B. \end{cases} \tag{6.9}$$

The total energy deposited is $E_0 = E_A + E_B + \varepsilon_A + \varepsilon_B$, but only the above-threshold deposits are measured. Calling the total above-threshold energy $E = E_A + E_B$, the total measured energy is

$$\begin{aligned} \tilde{E} &= \tilde{E_A} + \tilde{E_B} && (6.10)\\ &= E_A + E_B + \beta_1(E_A + E_B + \varepsilon_A + \varepsilon_B) && (6.11)\\ &= E_0 - (\varepsilon_A + \varepsilon_B) + \beta_1 E_0 && (6.12)\\ &= (1 + \beta_1)E_0 - (\varepsilon_A + \varepsilon_B) && (6.13) \end{aligned}$$

So sub-threshold adjacent strips affect the measured line energies by introducing an offset. The presence of sub-threshold energies explains the negative constant in the linear fit to the crosstalk effect:

$$\tilde{E} = (1 + \beta_1)E_0 - \alpha_1 \tag{6.14}$$

To account for the negative constant offset in our simple model, let us split the effect of sub-threshold events between the two adjacent strips:

$$\begin{cases} \tilde{E}_A &= E_A + \beta_1 E_A - \frac{\alpha_1}{2} \\ \tilde{E}_B &= E_B + \beta_1 E_B - \frac{\alpha_1}{2} \end{cases} \tag{6.15}$$

Equation 6.15 will form the basis for our cross-talk correction method. Let us now examine some specific cases and then generalize.

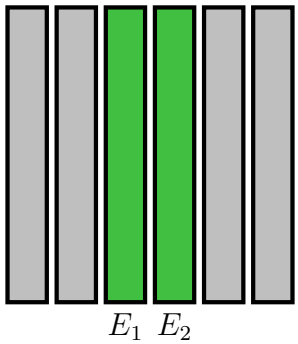

Figure 6.9: Schematic of two adjacent strips.

6.3.1 Correction for two adjacent strips

In the case of two adjacent strips (Fig. 6.9), the measured energies are:

$$\begin{cases} \tilde{E}_1 &= E_1 + \beta_1 E_2 - \frac{\alpha_1}{2} \\ \tilde{E}_2 &= E_2 + \beta_1 E_1 - \frac{\alpha_1}{2} \end{cases} \tag{6.16}$$

These equations can be written in matrix form:

$$\begin{pmatrix} \tilde{E}_1 \\ \tilde{E}_2 \end{pmatrix} = \left[\begin{pmatrix} 1 & 0 \\ 0 & 1 \end{pmatrix} + \beta_1 \begin{pmatrix} 0 & 1 \\ 1 & 0 \end{pmatrix} \right] \begin{pmatrix} E_1 \\ E_2 \end{pmatrix} - \frac{\alpha_1}{2} \begin{pmatrix} 1 \\ 1 \end{pmatrix} \tag{6.17}$$

$$\mathbf{\tilde{E}} = \mathbf{ME} - \mathbf{C} \tag{6.18}$$

Because these matrices are 2×2, a closed-form solution can be found:

$$\mathbf{E} = \mathbf{M^{-1}} \left(\mathbf{\tilde{E}} + \mathbf{C} \right) \tag{6.19}$$

$$= \frac{1}{1 - \beta_1^2} \begin{pmatrix} 1 & -\beta_1 \\ -\beta_1 & 1 \end{pmatrix} \begin{pmatrix} E_1 + \frac{\alpha_1}{2} \\ E_2 + \frac{\alpha_1}{2} \end{pmatrix} \tag{6.20}$$

This case of two adjacent strips is the simplest example of the correction method. Let us now look at a more complex case.

6.3.2 Correction for three adjacent strips

The case with three adjacent strips (Fig. 6.10) is similar to the case with two adjacent strips, but now next-nearest neighbors must also be accounted for. Accounting for the proper adjacencies of strips, the measured energies become:

$$\begin{cases} \tilde{E}_1 &= E_1 + \beta_1 E_2 - \frac{\alpha_1}{2} + \beta_2 E_3 - \frac{\alpha_2}{2} \\ \tilde{E}_2 &= E_2 + \beta_1 E_1 - \frac{\alpha_1}{2} + \beta_1 E_3 - \frac{\alpha_1}{2} \\ \tilde{E}_3 &= E_3 + \beta_1 E_2 - \frac{\alpha_1}{2} + \beta_2 E_1 - \frac{\alpha_2}{2} \end{cases} \tag{6.21}$$

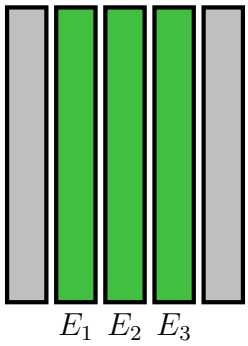

Figure 6.10: Schematic of three adjacent strips.

This can be written in with matrices in the following form, which will lead to generalization later:

$$\begin{pmatrix} \tilde{E}_1 \\ \tilde{E}_2 \\ \tilde{E}_3 \end{pmatrix} = \left[\begin{pmatrix} 1 & 0 & 0 \\ 0 & 1 & 0 \\ 0 & 0 & 1 \end{pmatrix} + \beta_1 \begin{pmatrix} 0 & 1 & 0 \\ 1 & 0 & 1 \\ 0 & 1 & 0 \end{pmatrix} + \beta_2 \begin{pmatrix} 0 & 0 & 1 \\ 0 & 0 & 0 \\ 1 & 0 & 0 \end{pmatrix} \right] \begin{pmatrix} E_1 \\ E_2 \\ E_3 \end{pmatrix} - \frac{\alpha_1}{2} \begin{pmatrix} 1 \\ 2 \\ 1 \end{pmatrix} - \frac{\alpha_2}{2} \begin{pmatrix} 1 \\ 0 \\ 1 \end{pmatrix} \tag{6.22}$$

$$\tilde{\mathbf{E}} = \mathbf{ME} - \mathbf{C} \tag{6.23}$$

Leading us to the solution for the corrected energy E:

$$\mathbf{E} = \mathbf{M^{-1}} \left(\tilde{\mathbf{E}} + \mathbf{C} \right) \tag{6.24}$$

6.3.3 Correction for the general case

Now we consider an arbitrary arrangement of strips. It was shown earlier that strips that are up to skip-1 neighbors have a measurable crosstalk effect on a given strip. Accounting for strips that are skip-1 and closer, we can write:

$$\tilde{\mathbf{E}} = \left(\mathbf{I} + \beta_1 \mathbf{M_1} + \beta_2 \mathbf{M_2} \right) \mathbf{E} - \left(\mathbf{C_1} + \mathbf{C_2} \right) \tag{6.25}$$

$$\equiv \mathbf{ME} - \mathbf{C}, \tag{6.26}$$

where the adjacency matrices are calculated as follows. Let $\mathbf{M}_\kappa$ be the matrix for strips separated by κ strips (e.g., $\kappa = 1$ for nearest-neighbors, $\kappa = 2$ for skip-1 neighbors). Then $(\mathbf{M}_\kappa)_{ij} = 1$ if strips i and j are separated by κ.

The offsets $\mathbf{C}_\kappa$ are calculated using the following rule:

$$\mathbf{C}_\kappa = \frac{\alpha_\kappa}{2}\mathbf{M}_\kappa \begin{pmatrix} 1 \\ \vdots \\ 1 \end{pmatrix}, \tag{6.27}$$

leading us to the solution for the corrected energy E:

$$\mathbf{E} = \mathbf{M^{-1}}\left(\tilde{\mathbf{E}} + \mathbf{C}\right) \tag{6.28}$$

Figure 6.11 shows the results of the full correction method on calibration data for several different energies.

6.4 Charge loss

To examine charge loss, we would like to look at adjacent strip events that are likely caused by single-site events. So we will use the events that were discarded in the cross-talk analysis. Charge loss will become apparent when plotting the energy deposited on one strip versus the energy deposited on the second (e.g., [51]). For clarity, we chose to plot the sum of the energies on adjacent strips versus their difference (as in [76]). In sum-difference plots, the sum $S = E_1 + E_2$ and difference $D = |E_1 - E_2|$ are calculated for adjacent strip energies E_1 and E_2. Events from all adjacent strip pairs on one side of a detector are accumulated together into a two-dimensional histogram. Each energy pair is plotted at (D, S) and $(-D, S)$ for clarity.

Because events that appear in sum-difference plots contain two adjacent strips on one side, they will be primarily single-site or two-site events. Besides using strip pairing to decide between event type, kinematics may also be used. The reason is that some two-site events may deposit energy in two adjacent strips on one side but only along one strip on the other side. Using strip pairing alone, such events will be considered single-site events. But in detectors like NCT's, high energy photons ($\gtrsim$500 keV) are most likely to be fully absorbed in the detectors if the first Compton interaction is a backscatter (i.e., $E_1 > E_2$) [31]. The energy difference D for two energies that are a result of a Compton scatter of a photon with energy E_0 by an angle φ is

$$\begin{aligned} D(\varphi) &= E_1 - E_2 && (6.29)\\ &= [E_0 - E_{scatter}(E_0, \varphi)] - E_{scatter}(E_0, \varphi) && (6.30)\\ &= E_0 - 2E_{scatter}(E_0, \varphi) && (6.31)\\ &= E_0 - \frac{2E_0}{1 + \frac{E_0}{m_e c^2}(1 - \cos\varphi)}. && (6.32) \end{aligned}$$

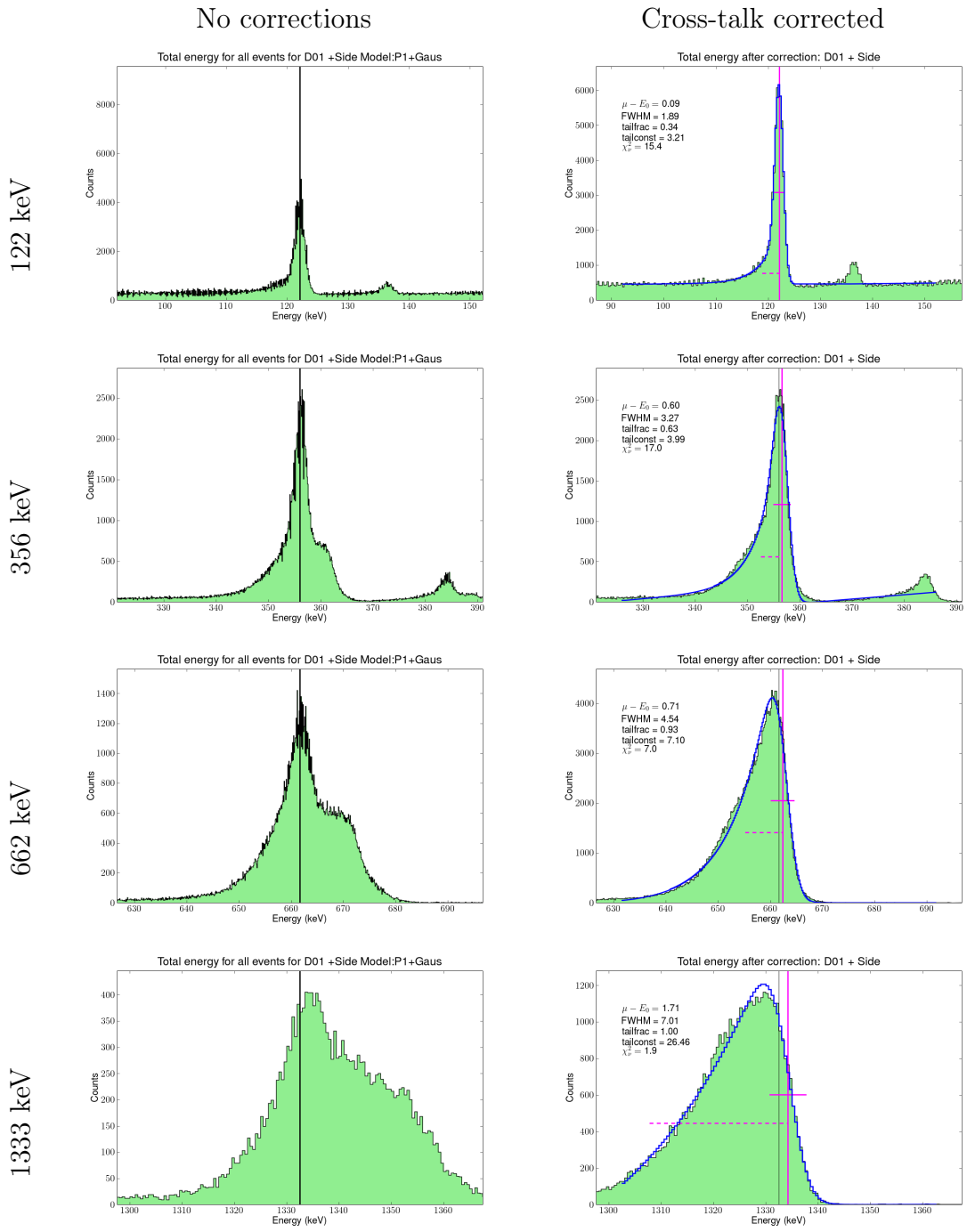

Figure 6.11: Summed-strip spectrum of photons at various energies. The effect of the cross-talk correction can be seen. The cross-talk correction removes the secondary peak, while the exponential tail still remains. Data is from the positive side of D1.

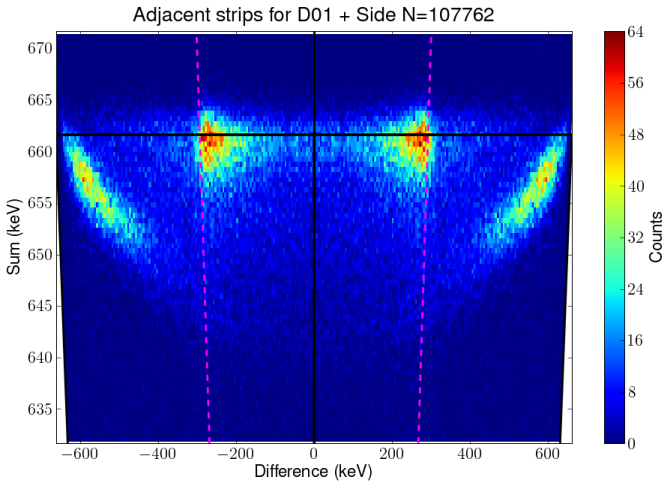

Figure 6.12: Sum-difference histogram from all adjacent strips after cross-talk correction has been applied. The line energy is marked with a horizontal black line, and the maximum difference for a two-site Compton backscatter event is shown as the dotted magenta line. Data is from the positive side of D1.

This has a maximum at $\varphi = \pi$, where the difference has the value

$$D_{max}(E_0) = E_0 \left(\frac{E_0 - \frac{m_e c^2}{2}}{E_0 + \frac{m_e c^2}{2}} \right). \tag{6.33}$$

In each of the sum-difference plots, lines will be plotted to denote $D = \pm D_{max}(S)$. For the higher-energy photons ($E_0 \gtrsim 500$ keV), events with an energy difference smaller than D_{max} are more likely to be two-site events than the events outside that region.

A sum-difference plot for 662 keV is shown in Fig. 6.12. In the plot, all adjacent strip events are used regardless of underlying event type. The clusters of events near $(\pm D_{max}, E_0)$ are Compton scatters with $\varphi \approx \pi$. Events outside of the magenta lines are more likely to be single-site events. Figure 6.13 shows the same data, broken down into those likely to be two-site events and those likely to be single-site events based on strip pairing. Charge loss effects appear in the single-site plot in the form of "wings" at large energy difference. These events in the wings are single-site events with charge loss, and they need to be corrected.

6.4.1 Correction method for charge loss

Let us consider the following phenomenological model for the charge loss:

$$S(D) = \begin{cases} E_0 - \frac{B}{2E_0}\left(E_0^2 - D^2\right), & E_0 < 300 \text{ keV} \\ E_0 - B\left(E_0 - D\right), & E_0 > 300 \text{ keV} \end{cases} \tag{6.34}$$

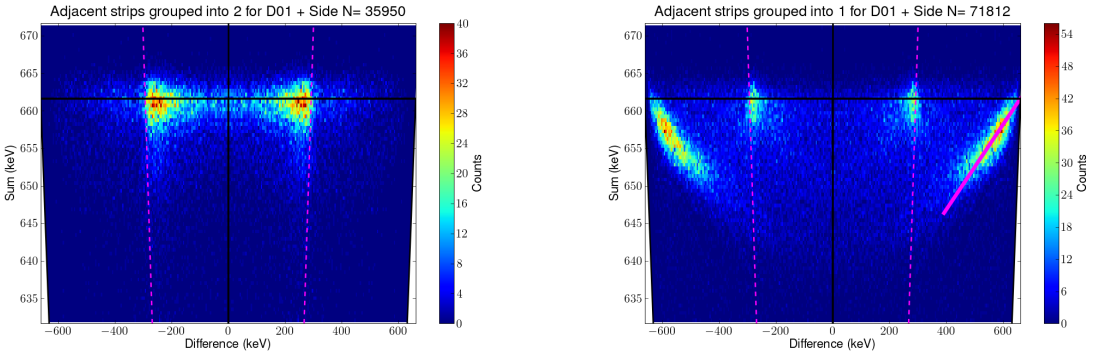

Figure 6.13: Sum-difference histograms for adjacent strip events that likely result from two-site events (left) and single-site events (right). Single-site events show the largest effects from charge loss — the appearance of wings at large energy difference. Data is from the positive side of D1.

The parameter B is the slope of the wing when it meets the line $S = E_0$. This model was chosen because both versions of it are determined only by B. At higher energies, only the outer wings are available for the fit since the inner region contains mostly two-site events, and the outer wings look largely linear. At lower energies, all energies are available for the fit, and there is a clear curved shape. Since both versions of the model are determined only by B, direct comparison may be made between the low energy fits and the high-energy fits. A schematic of the model is shown in Fig. 6.15.

The model is fit to the following region:

$$E_0 - 30 \text{ keV} \leq S \leq E_0 + 5 \text{ keV} \tag{6.35}$$

$$\begin{cases} 0 \leq D \leq E_0, & E_0 < 300 \text{ keV} \\ D_{max}(E_0) + 0.15E_0 \leq D \leq E_0, & E_0 > 300 \text{ keV} \end{cases}. \tag{6.36}$$

A least-squares fit is performed, using the counts in each bin at the weight for each term. Any bins that are below half of the maximum are excluded from the fit. Examples of fits are shown in Fig. 6.16.

The charge loss fraction B is plotted in Fig. 6.17 for all detectors at several energies. A linear fit is made to interpolate B to other energies:

$$B(E) = A_0 + A_1 E \tag{6.37}$$

Correction for charge loss is then performed by estimating the coefficient $B(E_0)$ as $\hat{B} = B(S) = A_0 + A_1 S$. Solving for E_0 in the model, we obtain the estimate $\hat{E}_0$:

$$\hat{E}_0(S, D) = \begin{cases} \frac{1}{2-\hat{B}} \left[S + \left(S^2 - \hat{B}(2-\hat{B})D^2 \right)^{1/2} \right], & E_0 < 300 \text{ keV} \\ \frac{S - \hat{B}D}{1-\hat{B}}, & E_0 > 300 \text{ keV} \end{cases} \tag{6.38}$$

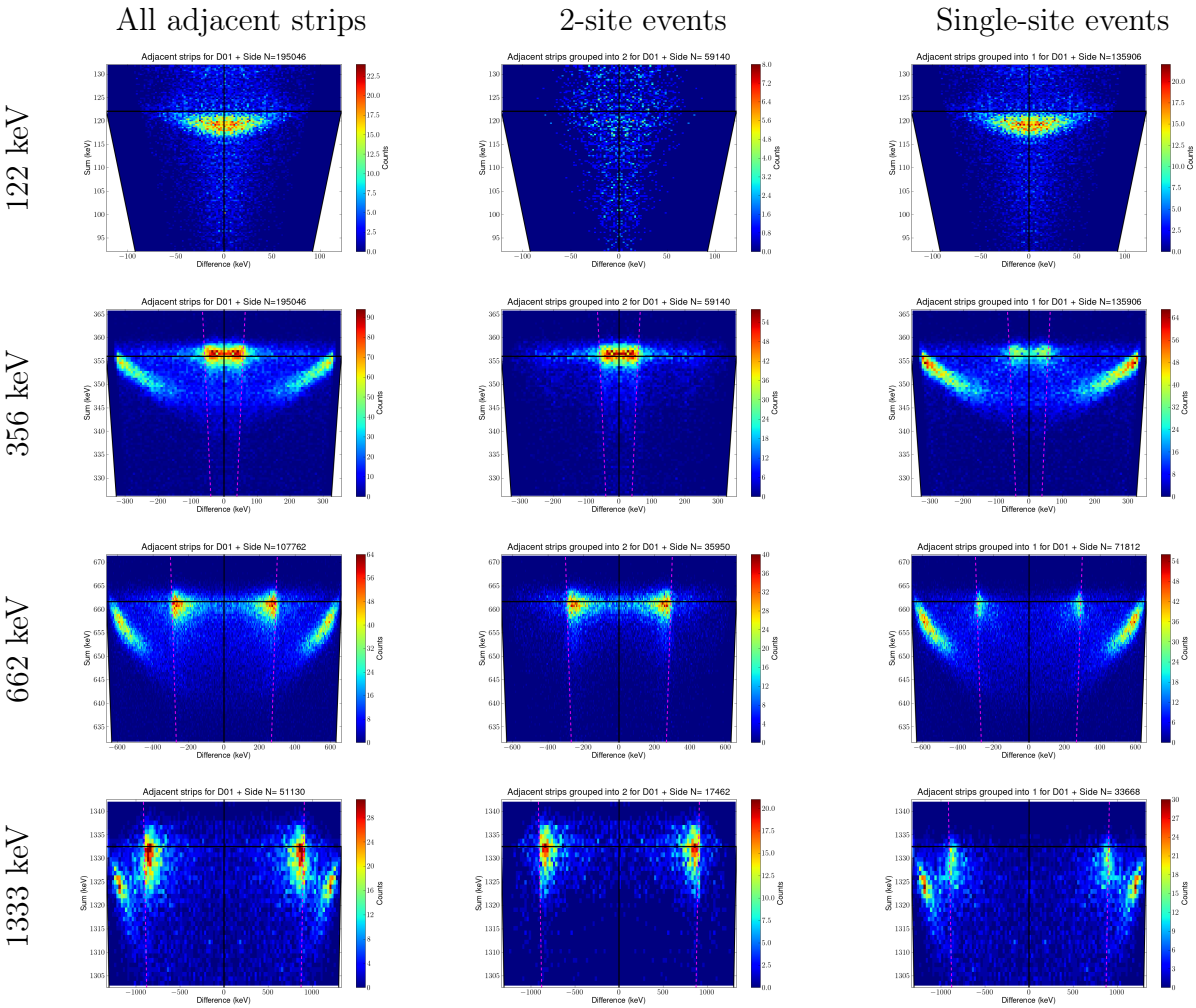

Figure 6.14: Sum-difference plots for adjacent strips at different energies. In the left column, all adjacent strip hits are shown; in the middle, only adjacent strip hits that are likely due to two-site events are shown; and in the right column, adjacent strip hits that are likely from single-site events are plotted. The "wings" in the outer portions of the single-site plots are due to charge loss in the gap between strips. Data is from the positive side of D1.

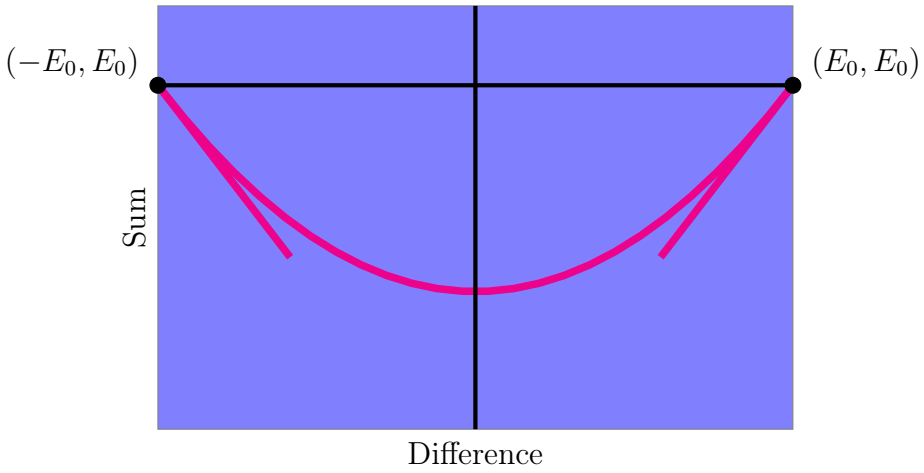

Figure 6.15: Schematic of charge loss model function. The quadratic version is used at lower energies ($E_0 < 300$ keV). The linear version is used at higher energies ($E_0 > 300$ keV) due to the exclusion of two-site backscatter events in the inner regions of the sum-difference plots. In either case, the model is specified only by the slope B at (E_0, E_0).

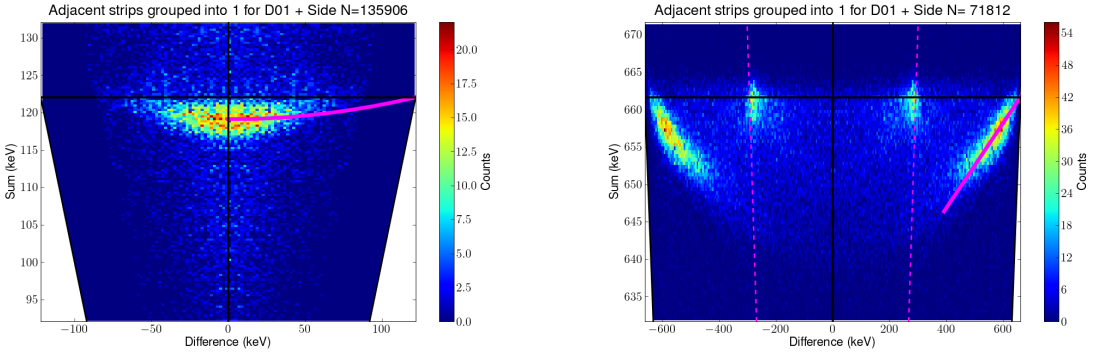

Figure 6.16: Sum-difference plot for single-site events near 122 keV (left) and 662 keV (right). The quadratic model is fit to the entire 122 keV histogram, while the linear model is fit to the "wings" of the 662 keV data. Data is from the positive side of D1.

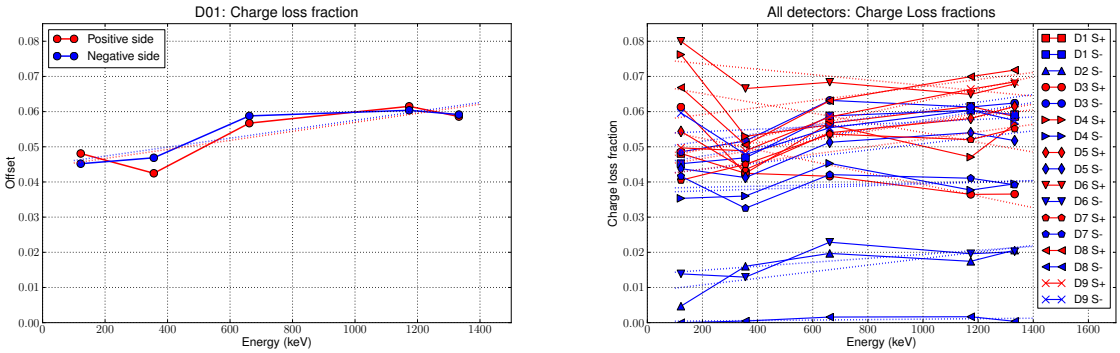

Figure 6.17: Plots of the charge loss fraction (B) for several energies for D1 (left) and all detectors (right). Note that the negative side of D8 has essentially no charge loss.

The charge loss correction using this formula was performed. The results are shown in Fig. 6.18 (sum-difference plots) and Fig. 6.19 (spectra). The charge loss correction improves the resolution and line position of adjacent strip summed spectra, though there is still a significant exponential tail.

6.4.2 Discussion

The charge loss fractions plotted in Fig. 6.17 do not seem to have any clear trend to increase, decrease, or remain constant with energy. It is not clear what if anything determines the magnitude of the charge loss — and especially what determines the near-zero charge loss on the negative side of D8. One prediction we can test is that the charge loss should be lower when there is a high electric field, which should decrease the size of the gap. The field is higher at the high-voltage electrode than at the low-voltage electrode, so the charge loss fraction should be lower at the high-voltage electrode. There may also be a dependence on bias voltage — higher bias voltage might lead to lower charge loss.

To test this, the average charge loss fraction (B) was calculated for each detector and plotted against its bias voltage (Fig. 6.20). The bias voltage has the same sign as the high-voltage electrode (i.e., positive bias means the positive side is the high-voltage side), so it is apparent that the charge loss is lower for the high-voltage side of every detector, as expected. The sole exception is D5, though the fractions from both sides are similar to each other. There seems to be no correlation with bias voltage. The rest of the charge loss magnitude is probably determined by surface conduction or other detector surface effects that influence the field at the gap. In particular, of the detectors with the most similar high-voltage and ground charge loss fractions (D1, D9, D3, and D5), the three detectors D1, D3, and D5 have different surface processing than the rest of the detectors (they are passivated with amorphous Ge

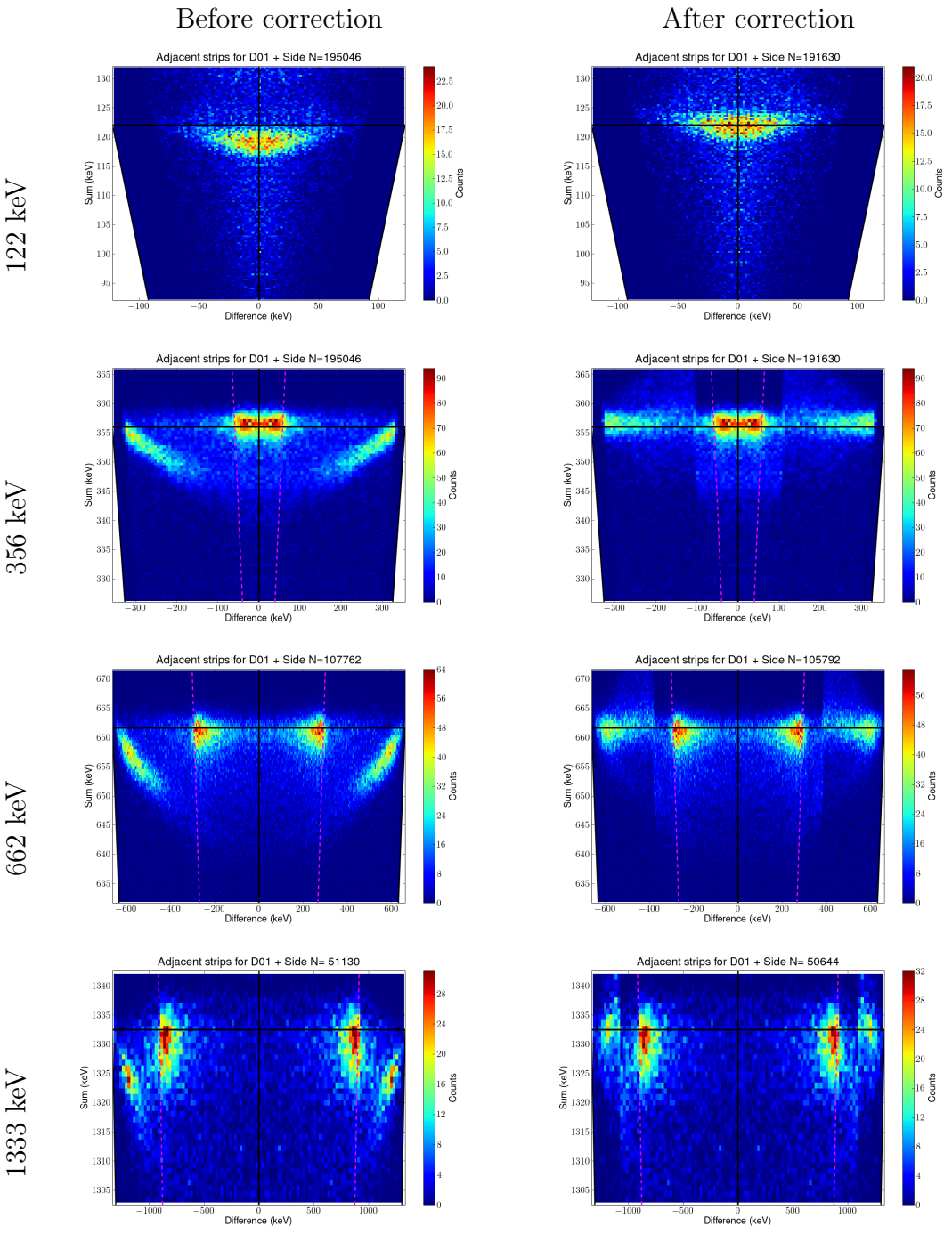

Figure 6.18: Sum-difference plot for adjacent strip events before and after charge loss correction has been applied. Data is from the positive side of D1.

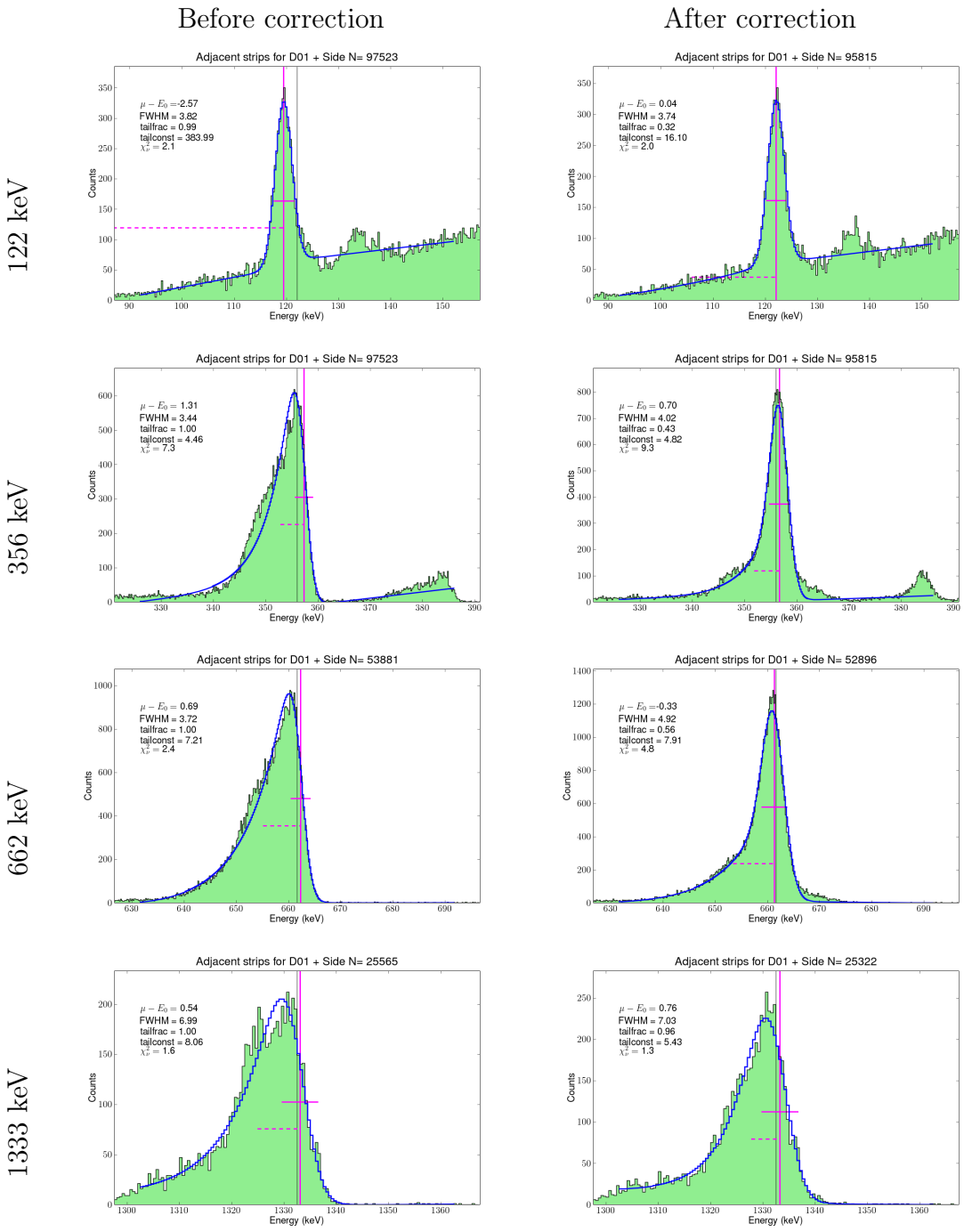

Figure 6.19: Summed strip spectrum for adjacent strip events at various energies before (left) and after (right) charge loss correction has been applied. Notice that the distribution is narrower and shifted toward the true line energy, though a tail still remains. Data is from the positive side of D1.

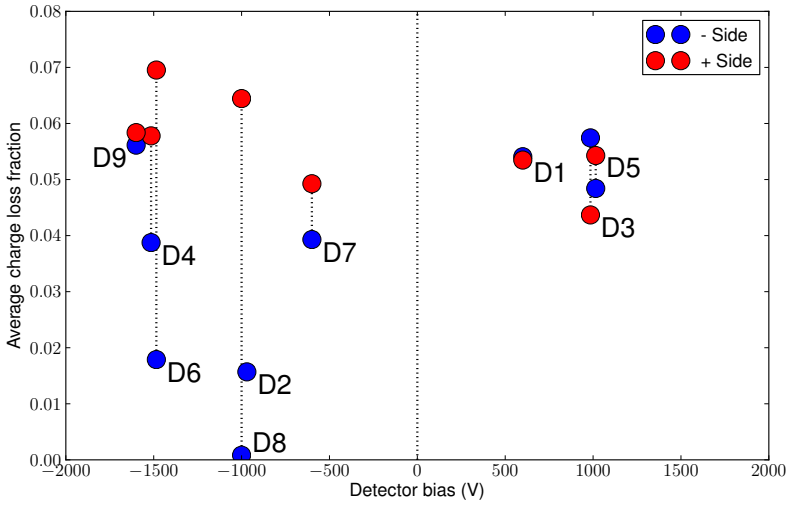

Figure 6.20: Plots of the average charge loss fraction (B) for D1 through D9 versus the bias voltage of the detector. Detector names mark the charge loss fraction for each detector's high-voltage side. Since the electric field at the high-voltage electrode is higher, less charge should be lost on that side. There is no correlation between charge loss fraction and bias voltage.

and amorphous Si, not just amorphous Ge [6]). So the different surface coating might affect the charge collection.

A major drawback to the charge loss correction method presented here is that it requires knowledge of the underlying event type (i.e., single-site or two-site), so it must be done after strip pairing. But since strip pairing is done by matching strip energies, events will often be improperly matched before they can be corrected. One possible solution to this problem is to include the charge-loss correction in the strip pairing algorithm. Some sort of iterative approach should be used. For example, the strip-pairing algorithm might examine two adjacent strips, then the charge loss correction would suggest a new energy for those combined strips. Then the pairing algorithm can determine whether that correction will lead to a single-site event or not. If so, the correction is justified; if not, the correction should be discarded.

6.5 Summary

While the cause of the inter-strip cross-talk is not known, we have seen that its effects can be corrected. Charge loss can also be partially corrected, and some detector physics clearly affects charge loss. Figure (6.21) shows the step-by-step results of applying these two additional corrections, which leads to dramatic improvements over the initial spectra.

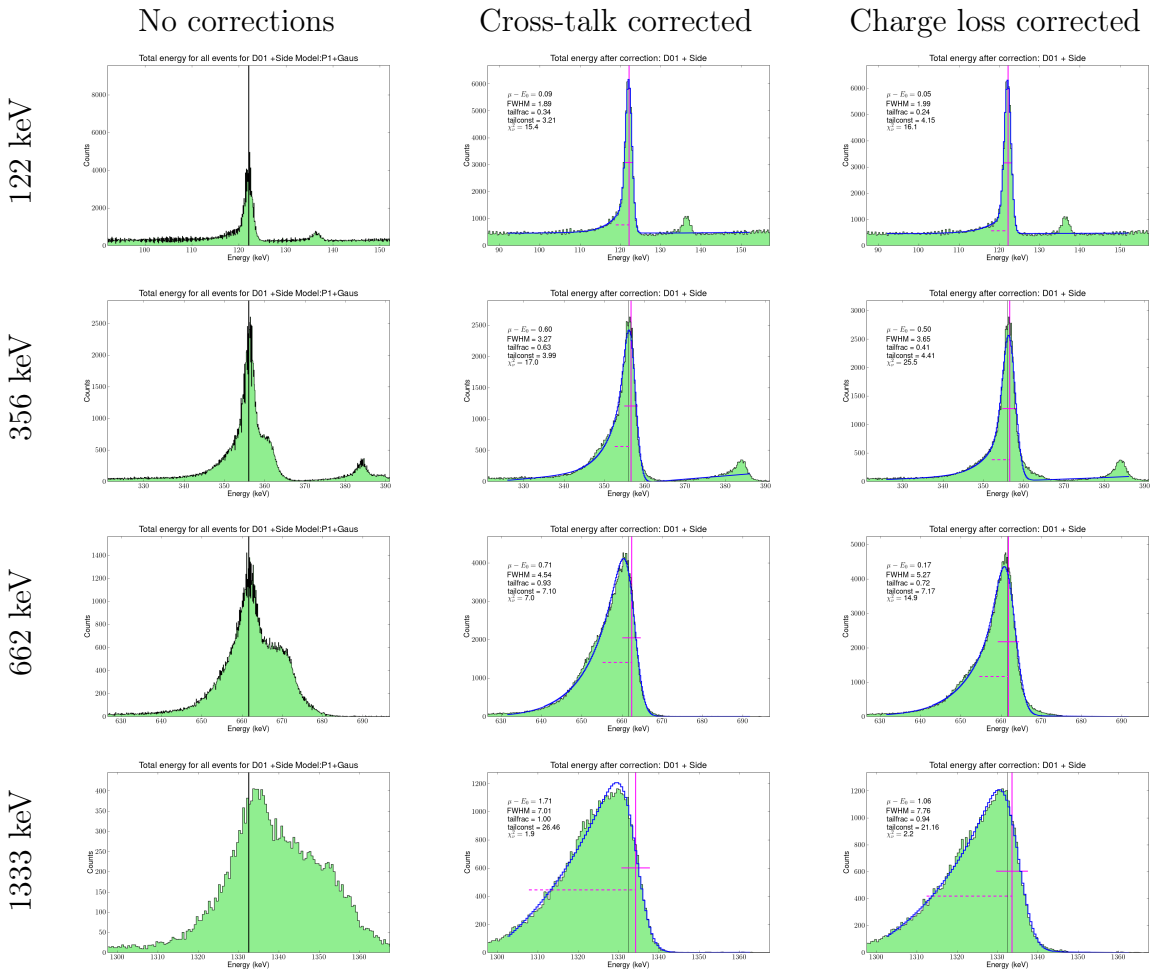

Figure 6.21: Summed-strip spectrum of photons at various energies. The effect of the two successive corrections can be seen. The cross-talk correction removes the secondary peak, and the charge loss correction removes part of the exponential tail. Data is from the positive side of D1.

Part III

The NCT balloon flight and Crab observation

Chapter 7

The Spring 2009 Balloon Flight of the NCT[1]

7.1 Introduction

The 10-GeD NCT was launched from the Columbia Scientific Balloon Facility (CSBF) in Fort Sumner, New Mexico (34.5°N, 104.2°W) at 1330 UT 5/17/2009. The flight was terminated at 0400 UT 5/19/2009 near Kingman, Arizona (34.9°N, 113.7°W). The total flight time was about 38.5 hours, with nine of the ten detectors on for a total of 22 hours at float. Fig. 7.1 shows the flight path of the balloon as it traveled from eastern New Mexico to western Arizona. Fig. 7.2 shows the altitude of the balloon during the flight. Altitude was maintained between 35 and 40 km for the entire time the detectors were operational.

The GeDs functioned nearly perfectly during the flight. The electronics for one of the ten detectors (D0) did not turn on for the second day of the flight, but earlier it had been practically unusable due to high leakage currents on the ground side. Also, the readout electronics for another detector (D4) encountered several errors during the flight, probably due to mismatches in timing between the analog boards. This cardcage had to be reset repeatedly to fix the problem.

The flight met all of our goals for preparing for an eventual week-long flight (a Long Duration Balloon Flight, or LDBF). The flight computer had no problems at all, including perfect performance of the critical pointing schedule and commanding codes. All telemetry and commanding tests were successful. The differential GPS system worked flawlessly and provided us with $<0.5°$ positioning accuracy during the entire flight, well within NCT's requirements. The length of the flight also exceeded

[1]Much of the content of this chapter appeared in [18].

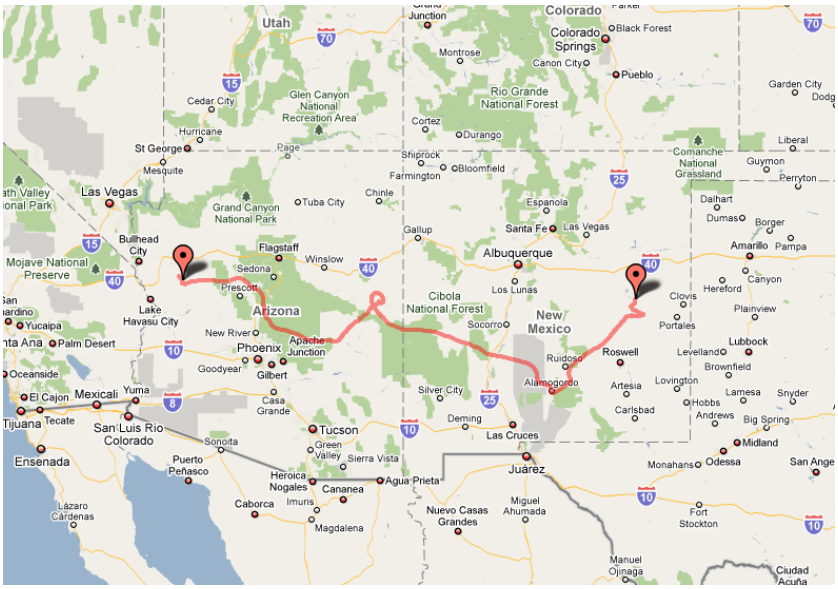

Figure 7.1: The flight path of NCT. The origin was Fort Sumner, which is the marker on the right hand side of the map. The position of the gondola at impact with the ground is denoted by the marker on the left hand side of the map. Google map courtesy of CSBF.

our required time for science observation.

While the science instrument performed well during the flight, two of the gondola systems showed anomalies. First, the azimuthal pointing system became unstable in its autonomous mode during the flight (though it eventually recovered), so that during much of the first day the gondola was pointed manually. Second, the solar power system had trouble maintaining charge on the batteries, resulting in the instrument being turned off for several hours to conserve power. This power problem was due to a failure of the solar panels, probably from overheating. The damage to the solar panels can be seen in Fig. 7.3.

7.2 Science goals

The primary science goals of the flight were to observe gamma-ray continuum emission from the Crab pulsar and the Cyg X-1 X-ray binary, both point sources visible in the northern hemisphere. Here we will discuss the prospects for observing these sources.

In considering the visibility of a gamma-ray source, it is important to understand atmospheric absorption. Figure 7.5 shows the mass column density above the telescope during the flight, which is derived from the gondola altitude and the US Standard Atmosphere [1]. Figure 7.6 shows the corresponding transmission percent

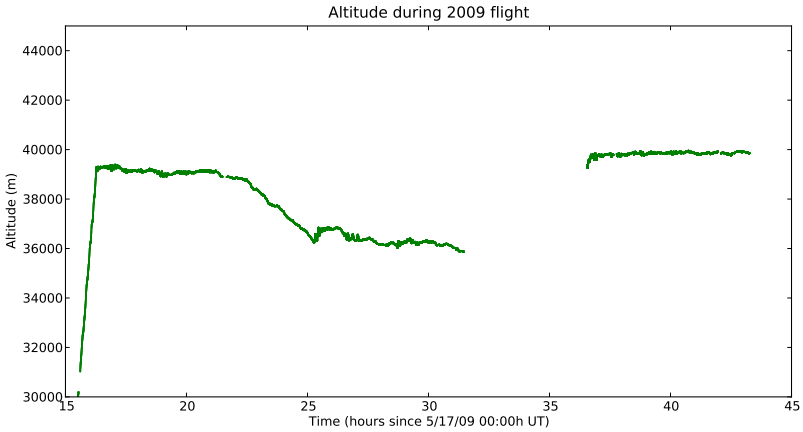

Figure 7.2: Altitude of NCT at float. The five-hour gap in the data is when the system was turned off overnight to conserve power. The flight lasted another 9 hours after the system was powered down.

Figure 7.3: The gondola on the ground after the termination of the flight. Note that the gondola landed upright, which allowed the liquid nitrogen to remain in the dewar so the detectors remained at cryogenic temperatures. Also apparent is the bubbling and cracking damage sustained by the solar panels during flight.

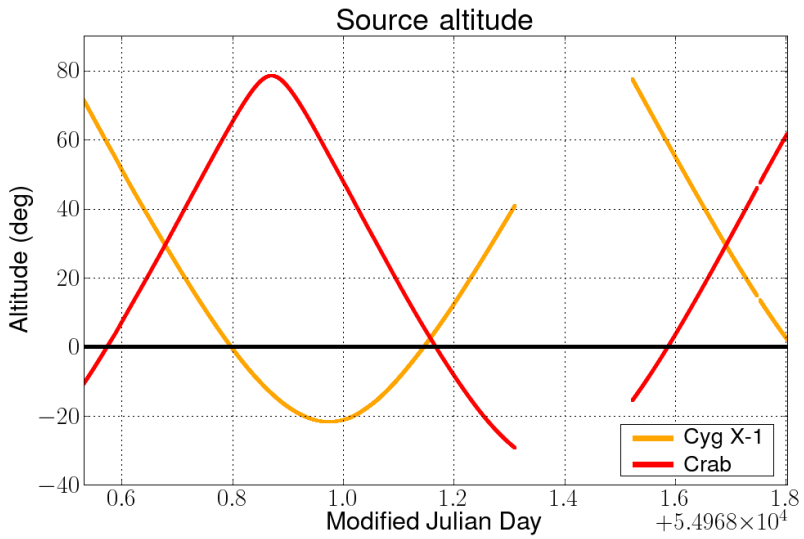

Figure 7.4: Altitude of the Crab Nebula and Cygnus X-1 during the 2009 flight. The data above 40° elevation is best for data analysis.

for several relevant photon energies. The transmission probability for photons above 250 keV is always above 55%, and above 70% during the highest altitudes achieved. The transmission probability is especially important for the Crab observation because it has much higher flux at low energies.

The elevation angles of sources will also help us to determine the appropriate data to analyze. Figure 7.4 shows the altitude of the Crab Nebula and Cygnus X-1. Approximately 33 ks of data were taken with the Crab above 40° elevation, while only 12 ks of data were taken when Cygnus X-1 was above 40°. Since the Crab is at the limit of detection and Cygnus X-1 is a weaker source, Cygnus X-1 will not be detectable in the flight data.

The main science result from the 2005 prototype NCT flight was a measurement of the gamma-ray background for the NCT instrument [41]. A spectrum of the background from this flight has been obtained, revealing the presence of a strong atmospheric background 511 keV line (Fig. 7.7), as observed in the previous flight. Further comparison of the background spectrum from the 2009 flight and the 2005 flight will be performed elsewhere.

7.3 Aspect reconstruction

The aspect of NCT during the flight was reconstructed using information from the differential GPS (dGPS) unit, which returns the pointing of the dGPS antenna plane to an accuracy of 0.1° in heading, pitch, and roll angles (θ, ϕ, ρ). The dGPS unit also gives an accurate Coordinated Universal Time (UTC), latitude, longitude, and

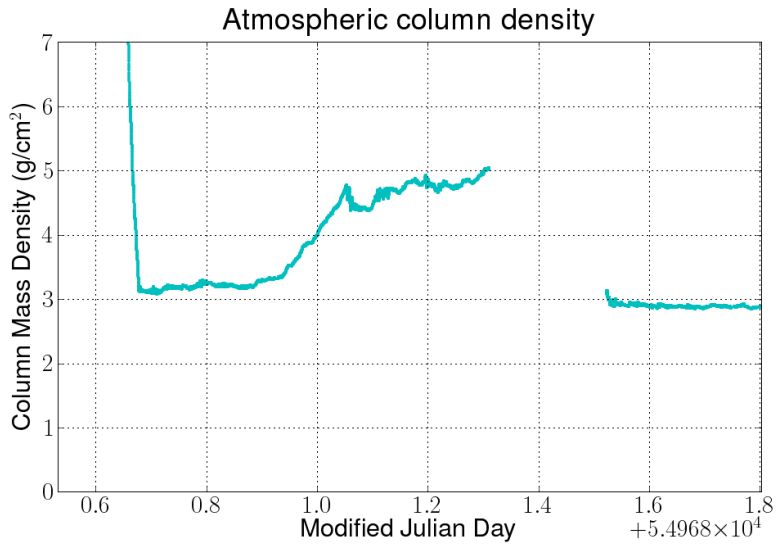

Figure 7.5: Column mass density in the vertical direction derived using the US Standard Atmosphere.

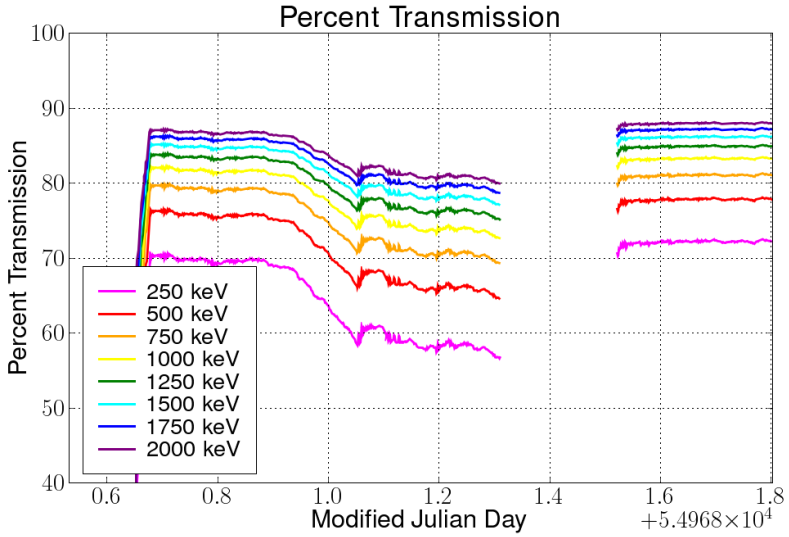

Figure 7.6: The transmission percent of photons at various energies during the flight.

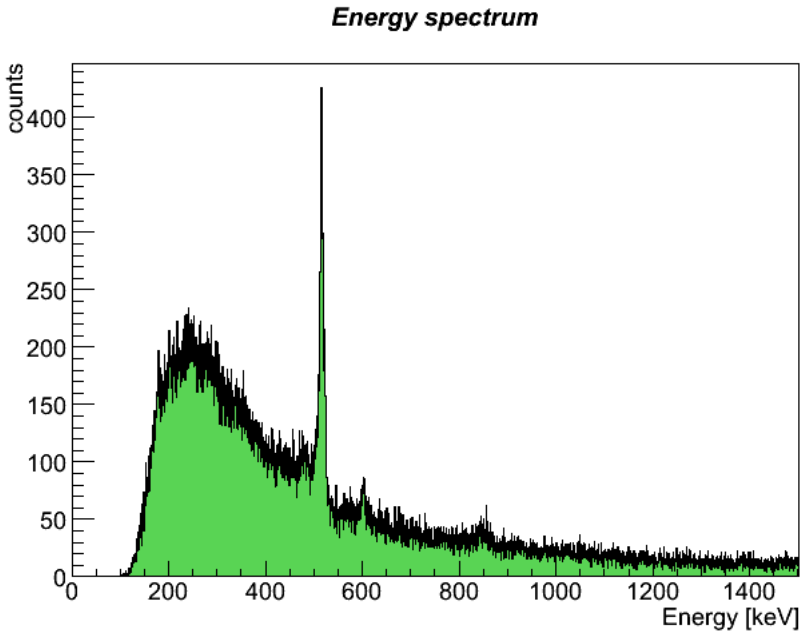

Figure 7.7: Spectrum from flight, from 0−1500 keV. The atmospheric background line at 511 keV is clearly visible.

altitude. This information is reported by the flight computer (Gondola Control Unit, or GCU) in housekeeping data every 1 or 4 seconds, depending on the type of data. A theodolite was used to measure the relative orientation of the cryostat with respect to the dGPS antennae to an accuracy of 1°. Using this information, a matrix was constructed to convert from the cryostat coordinate system to the dGPS coordinate system ($R_{cryo \to dGPS}$), which is constant during the flight. Using the dGPS aspect information, another matrix was constructed to convert from the dGPS coordinate system to the local horizon coordinate system ($R_{dGPS \to hor}(\theta, \phi, \rho)$). The interpolated UTC, latitude, and longitude of an event then can be used to convert from cryostat coordinates to equatorial or galactic coordinates.

For each event, the x-axis and z-axis of the cryostat were converted using these matrices into horizon coordinates (azimuth, elevation) and galactic coordinates (galactic longitude ℓ, galactic latitude b). This information was then used in MEGAlib [181] to perform rotations of Compton circles into galactic coordinates and make horizon cuts. The z-axis of the cryostat (the center of the field of view) is plotted in Fig. 7.8. It can be seen that the Crab is near the center of the field of view during a portion of the flight.

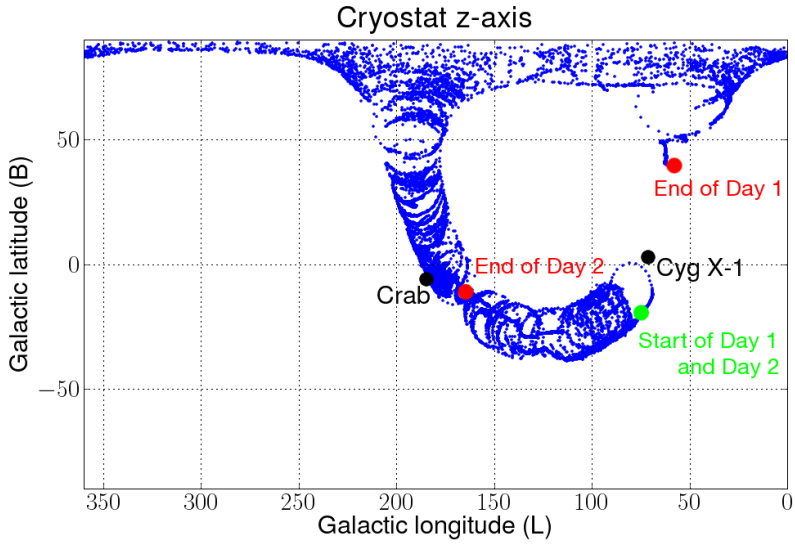

Figure 7.8: The z-axis (center of field of view) plotted in galactic coordinates for the flight. The circular patterns are due to a recurring malfunction of the pointing system that resulted in the spinning of the gondola.

7.4 Event time reconstruction

In order to properly interpolate aspect information for a given event, the event time must be known to a fraction of a second. Time information for each event is given by three different clocks: the high-precision 10 MHz 32-bit cardcage clock (T_{CL}), the low-precision Unix clock of the flight computer T_{GCU}, and the low-precision but highly accurate GPS clock from the differential GPS unit (T_{GPS}). Table (7.1) gives descriptions of each clock.

When an event is detected the cardcage assigns a T_{CL} to the event. Within a few seconds, when the data packet is processed by the flight computer to be telemetered to the ground, the T_{GCU} is assigned. So since T_{CL} is a relative clock that rolls over every 7 minutes and T_{GCU} is an absolute time but does not represent the exact second that the event occurred, a high-precision event time must be constructed from both of them.

The flight computer time T_{GCU} was reset several times during the flight due to legacy code that corrected for its significant drift. These reset points, along with power cycles of the entire system, determine several divisions of the flight data ("segments," see Fig. 7.9 and Table 7.2). The event's frame counter (FC, assigned by the GCU) and its T_{GCU} are used as indices to determine which segment the event falls in. The aspect information reported by the flight computer includes both T_{GCU} and T_{GPS} every second of the flight, so correspondence between those times is possible. Each segment has its own fitted polynomial to calculate T_{GPS} from T_{GCU} to obtain a more

Clock	Source	Time Step	Rollovers	Resets
T_{CL}	Assigned to event in cardcage, clocks are synced and incremented using an external pulse from flight computer.	100 ns	Every 429.5 sec (10 MHz, 32 bits)	When cardcage clocks are synced
T_{GCU}	Flight computer internal clock. Assigned to event by flight computer.	1 sec	None (UTC)	Occasional 30 second jumps.
T_{GPS}	Differential GPS time, available in GCU housekeeping	1 sec	None (UTC)	None, but occasional dropouts from loss of GPS fix

Table 7.1: Description of the three clocks used for event time reconstruction.

accurate UTC.

In addition, each segment was assigned a T_{GCU_0} and T_{CL_0}, which are the T_{GCU} and T_{CL} of its earliest event. The rollover correction for T_{CL} (a 10 MHz, 32-bit clock) was performed in the following way:

$$\begin{aligned} n &= \frac{T_{CL_0} + 10^7 \left(T_{GCU} - T_{GCU_0}\right)}{2^{32}} \\ n_{rollover} &= \text{integer part of } n \\ f &= \text{fractional part of } n \end{aligned}$$

The fraction since the last rollover, f, is used to adjust $n_{rollover}$ as follows:

$$\begin{aligned} &\text{if } T_{CL} < 0.3 \times 2^{32} \text{ and } f > 0.7, \qquad n_{rollover} = n_{rollover} + 1 \\ &\text{if } T_{CL} > 0.7 \times 2^{32} \text{ and } f < 0.3, \qquad n_{rollover} = n_{rollover} - 1 \end{aligned}$$

This corrects any mismatch in time between the assignment of T_{CL} in the cardcage and the assignment of T_{GCU} in the flight computer if a rollover were to occur. Any time mismatch can be as large as 0.3×2^{32} bits of the fast clock, or 128 seconds (the delay is usually <10 seconds).

The final reconstructed time is:

$$\begin{aligned} T_{CL,unrolled} &= T_{CL} + n_{rollover} 2^{32} \\ t &= T_{GCU_0} + a_0 + a_1 \left(\frac{T_{CL,unrolled} - T_{CL_0}}{10^7} \right) \end{aligned}$$

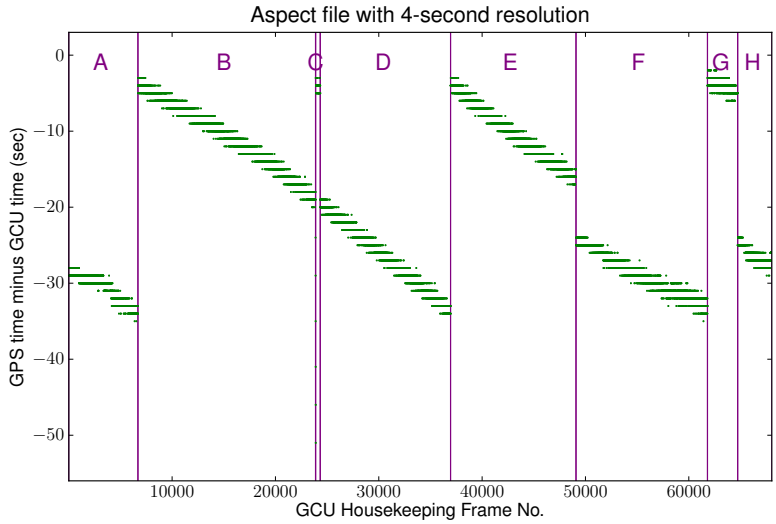

Figure 7.9: Division of GCU housekeeping data into segments based on clock resets. Shown here is the difference between T_{GPS} and T_{GCU} versus the GCU housekeeping frame number (HK). Since there are occasional resets of T_{GCU} by the flight computer, but HK increases throughout the flight, HK was used to determine which segment an event occurred in. Each segment has its own linear or quadratic fit to determine T_{GPS} from T_{GCU}.

where $a_0 \sim 1$ sec and $a_1 \approx 1$ are from a linear fit between $T_{CL,unrolled}$ and T_{GCU} during the given segment. The time t is used to interpolate the aspect over T_{GCU} to high precision. To get an accurate UTC, a polynomial is used:

$$t_{GPS} = t + b_0 + b_1 \left(t - T_{0,GPS}\right) + b_2 \left(t - T_{0,GPS}\right)^2 \tag{7.1}$$

where $T_{0,GPS}$ is a constant for each segment and the b coefficients are fit for each segment. The time t_{GPS} is used to calculate celestial coordinates.

7.5 Summary

NCT has flown successfully on a conventional balloon flight from Fort Sumner, NM. The gondola aspect reconstruction for large segments of the flight has been performed, and a method of reconstructing the event time has been presented. The data from the flight is ready for higher-level analysis.

Seg.	T_{GCU} start	T_{GCU} end	FC start	FC end	HK start	HK end	Dura -tion
Float altitude achieved at 1242577000							
B1	1242572067	1242592669	0	12896216	6693	23875	15669
B2	1242593153	1242596295	13123719	14626718	6693	23875	3142
C	1242596329	1242596936	14643589	14905309	23900	24335	607
D1	1242596937	1242600881	14920664	16777214	24336	36944	3944
D2	1242600881	1242601821	1	445677	24336	36944	940
D3	1242601859	1242605957	449801	2386199	24336	36944	4098
D4	1242605957	1242610050	2386719	4235555	24336	36944	4093
D5	1242610075	1242612559	4239273	5257640	24336	36944	2484
D6	1242612578	1242614682	5258800	6018790	24336	36944	2104
E1	1242614682	1242629778	6029166	11419972	36945	49080	15096
E2	1242629809	1242631574	11421270	12050207	36945	49080	1765
System off overnight							
F1	1242652660	1242660046	148016	3330643	49090	61807	7386
F2	1242660056	1242661841	3331053	4409981	49090	61807	1785
F3	1242661852	1242666066	4410384	6425197	49090	61807	4214
G	1242666036	1242669492	6425198	7977221	61808	64727	3456
H	1242670598	1242674163	71632	1230071	64733	68039	3565
System off and termination of flight							

Table 7.2: Data segments for the flight, which are determined by power cycles, GCU time resets, and cardcage resets. Total duration of correctable data at float is 74348 sec, or 20.65 hr.

Chapter 8

Observations of the Crab Nebula during the 2009 NCT balloon flight

8.1 Introduction

As seen in the previous chapter, approximately 33 ks of data were taken during the 2009 flight when the Crab was above an elevation of 40°. The gondola aspect and the reconstruction of Compton events has been performed, preparing the data for further treatment. In this chapter, we will discuss the selections made on the data, analysis performed on the Crab in spectrum space and angle space, and an image of the Crab as seen by NCT.

8.2 Data selections

Data from the flight was selected only when the Crab was above 40° elevation both to minimize atmospheric absorption and to sample the background (as will be discussed in sections 8.6 and 8.7). Figure 8.1 shows the z-axis of the cryostat (the center of the field-of-view) plotted during the data selection chosen. Figure 8.2 shows the atmospheric column density during the data selection. An average value of 3.2 g cm^{-2} was derived from this and used in atmospheric absorption calculations. During the chosen observation time, the average livetime for the cardcages was nearly constant with an average value of 92%. Taking into account the livetime and ≈1 ks of dead time due to cardcage and flight computer resets, this leads to an effective Crab observation time of 29.29 ks.

An energy cut of 300−495 keV and 520−1500 keV was chosen to exclude a few sources of background. The cut avoids the very strong atmospheric 511 keV background line. Also, below ≈300 keV, discrepancies were noticed between the observed background continuum and simulations, with NCT observing fewer counts by a factor of two in that region [48]. No calibration data is available to calculate the efficiency

Parameter	Allowed range
Crab elevation	>40°
Photon energy	300−495 keV, 520−1500 keV
Number of interactions	2−7
Earth horizon	Reject if >99% of Compton circle is below elevation of 0°
Compton scatter angle (φ)	no restriction (0°−180°)
Minimum distance between first two interactions	1.2 cm
Minimum distance between any two interactions	0.4 cm

Table 8.1: Data cuts used on flight data to select the best events for image analysis.

in that region of the spectrum, but the comparison of simulations and effective area calibration data at higher energies reveals a deficit of measured photons when a source is placed in the plane of the detectors, presumably because the simulations underestimate the effect of the detector guard rings. This effect is believed to affect low-energy photons more, leading to the measured deficit. This low-energy region will be excluded from the analysis.

It became clear from simulations and measured background rates that the other data cuts used for the flight data should be wide in order to attain the best signal-to-noise ratio. We chose one major constraint — to limit the distance between the first and second interactions in the detectors — in order to improve the angular resolution of the instrument and thus the signal-to-noise. Based on simulations of the Crab, setting a lower limit of 1.2 cm for the first interaction distance improves the angular width of the Crab (10° ARM FWHM to 7.4° ARM FWHM), while eliminating only 40% of the events within the central FWHM of the ARM distribution (see Section 8.4 for a discussion of the ARM). The cut is also meant to improve the likelihood that an event is properly reconstructed by ensuring that the first two interactions are separated by multiple strips.

The different cuts used in the analysis of the NCT flight data are summarized in Table 8.1.

8.3 Crab simulations

A detailed mass model for NCT has been developed, along with code that applies the detector response to the ideal simulated detector hits [18,47]. The simulation tool Cosima [180] was used, which is based on the gamma-ray telescope library MEGAlib

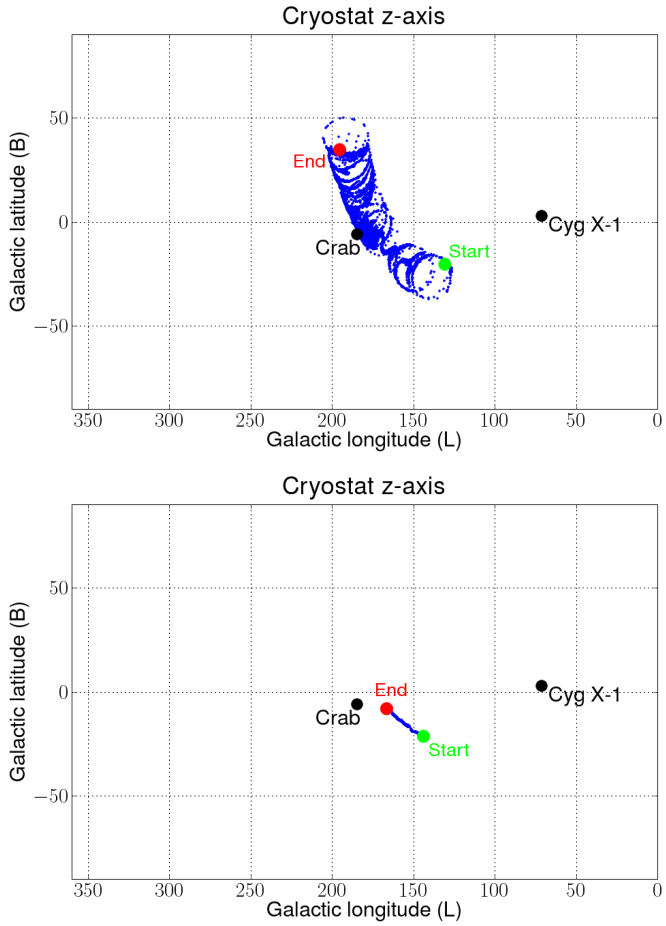

Figure 8.1: The z-axis of the detectors during the data selected for Crab analysis on Day 1 (left) and Day 2 (right). On both days, the Crab was well within the ∼90° field of view of the instrument.

[181] and the Monte Carlo framework GEANT4 [2]. A point source with a spectrum identical to the Crab spectrum measured by [96] was simulated at infinity along the z-axis of the detectors (i.e., the center of the field of view) for an equivalent real time of 100,000 seconds. The total Crab flux between 200 keV and 10 MeV was calculated to be 2.194×10^{-2} cm^{-2} s^{-1}. The total number of events between 200 keV and 10 MeV that interacted in the detectors were 219,987, with 18,622 events passing the event cuts (8.5%).

Compensation for atmospheric absorption was done after the simulation by calculating the transmission probability as a function of energy and multiplying the probability with the spectrum of events that passed the data cuts. The more accurate way of accounting for atmospheric absorption is to perform Monte Carlo simulations with a layer of air of the appropriate column density, but a brief exploration of such

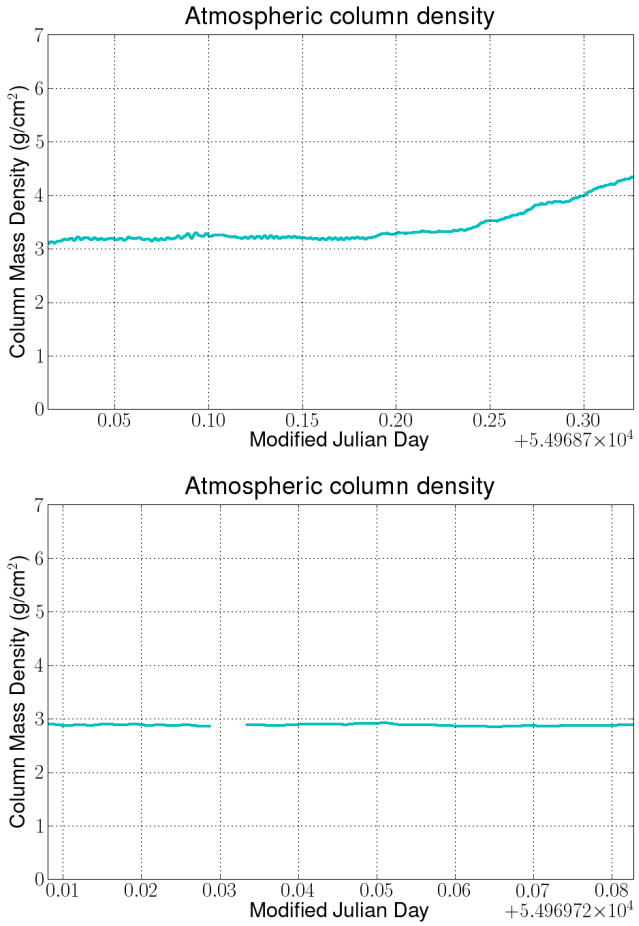

Figure 8.2: Column mass density in the vertical direction for Crab analysis data on Day 1 (left) and Day 2 (right). An average of 3.2 g cm^{-2} was assumed in absorption calculations.

simulations revealed that there was little difference. An average column density of 3.2 g cm^{-2} was assumed, and the Crab spectrum at 45°, 55°, 65°, and 75° (the Crab elevation peaks at 80° at transit) was calculated (Fig. 8.3). An average spectrum was calculated, and it contained 71% of the total counts of the original spectrum. Figure 8.4 compares this average-absorbed spectrum with the measured spectrum of the flight data.

8.4 The Angular Resolution Measure (ARM)

The Angular Resolution Measure (ARM) is a statistic that is used to measure the angular resolution of a Compton telescope (e.g., [150]). An ARM histogram can be constructed when the source's location is known. The ARM histogram is a histogram

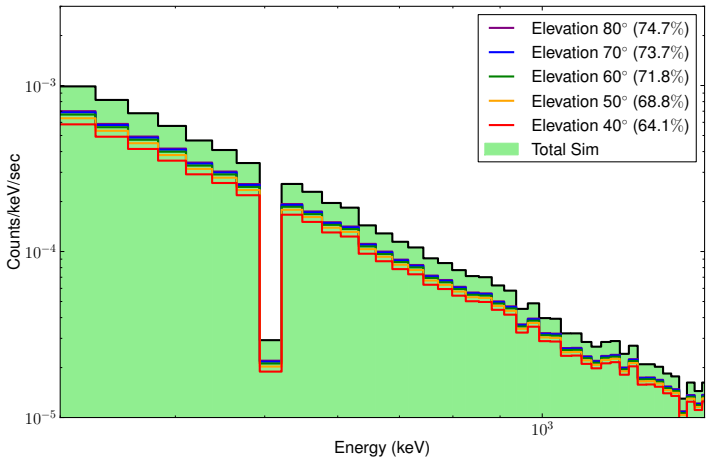

Figure 8.3: The simulated spectrum of the Crab, with absorbed spectra plotted for different elevation angles of the Crab. The gap around 511 keV is due to the energy cut that was made to exclude the atmospheric 511 keV line.

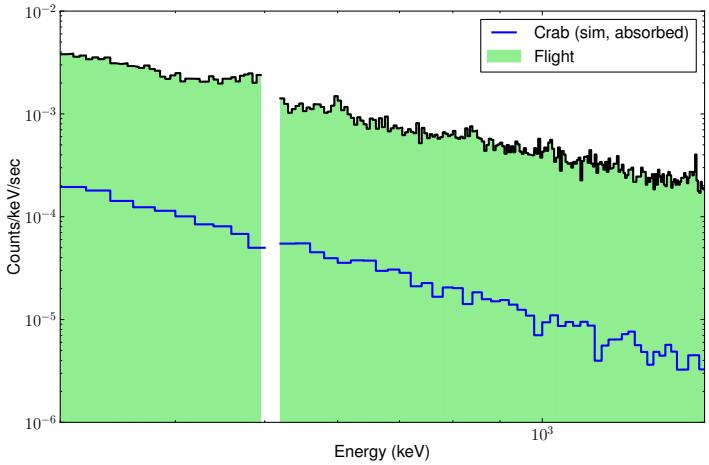

Figure 8.4: The simulated spectrum of the Crab accounting for atmospheric absorption (blue) compared to the measured spectrum during the flight for events within 5.2° of the Crab. The gap around 511 keV is due to the energy cut that was made to exclude the atmospheric 511 keV line.

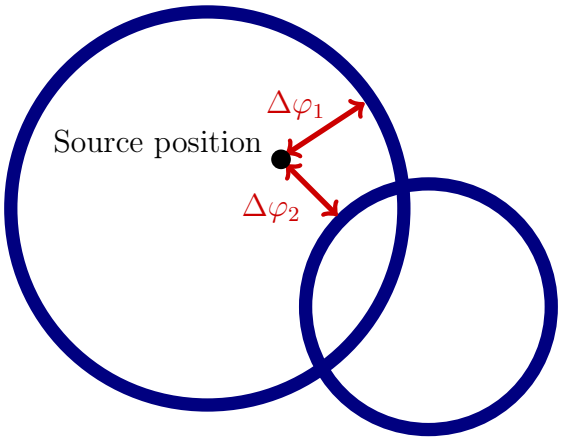

Figure 8.5: Schematic of the definition of the Angular Resolution Measure (ARM). Notice that the ARM can be positive or negative: $\Delta\varphi_1 < 0$, since its reconstructed Compton circle circumscribes the source position, while $\Delta\varphi_2 > 0$ because its Compton circle does not circumscribe the source position.

of the following quantity (e.g., [150]):

$$\Delta\varphi_{\mathrm{ARM}} \equiv \varphi_{geo} - \varphi_{recon} \tag{8.1}$$

where φ_{geo} is the scatter angle derived from the known source location and φ_{recon} is the Compton scatter angle obtained from event reconstruction (i.e., the Compton scatter formula). For a single event, $\Delta\varphi_{\mathrm{ARM}}$ measures the deviation of the event's Compton circle from the true position of the source. A graphical explanation of this definition is shown in Fig. 8.5. An ARM histogram for NCT generally has a Lorentzian shape, and the angular resolution is specified by the full-width at half maximum (FWHM).

The FWHM of the ARM histogram is affected by detector energy resolution, detector position resolution, and Doppler broadening. Doppler broadening is the deviation from the ideal Compton scatter formula caused by scattering off of bound atomic electrons (not free electrons). It is a fundamental limit to the angular resolution of a Compton telescope. This broadening has been extensively studied for different materials in [183]. Because of NCT's excellent energy resolution, the contribution from the energy resolution is not important. The position resolution of the NCT detectors (especially the 2 mm strip pitch) is the the dominant contribution to the ARM [17]. This is one reason the event cut on the first interaction distance greatly improves the ARM FWHM.

The ARM will be used to select events from the location of the Crab and test points. When the ARM distribution can be approximated by a Lorentzian distribution with some FWHM Γ, then the sensitivity of data cuts is maximized by selecting events that are within 0.7Γ of the center. For the data cuts we are using, $\Gamma = 7.4°$, so we should use an ARM cut of $\pm 5.2°$ to maximize sensitivity.

8.5 Significance of the Crab detection

To attempt to measure the significance of the Crab, events that were consistent with the Crab were extracted from the data. We selected events within the optimal ARM cut of 5.2° around the position of the Crab and extracted any photon whose Compton circle passed within that distance.

An estimate of the background counts is needed to determine the significance. Because the Crab moves through NCT's wide field of view, we can select nearby points to estimate the background at the Crab's position. An added complication is that because photons are only localized to a circle, a photon from the Crab may be consistent with an off-source point as well. For this analysis, we selected eight points that were on a circle $\delta = 20°$ away from the Crab at evenly-spaced intervals. Events were selected from within 5.2° of these points. The angular separation of $\delta = 20°$ was selected so that we could sample points that were close enough to the Crab that they have similar exposure times, and far enough away so that fewer Compton circles would be consistent with both the Crab and these points. There is a trade-off between choosing an offset angle δ so that the background estimate is reliable (i.e., δ should be small) and so that the off-axis source contribution is small (i.e., δ should be large). The value of 20° was chosen in this work as the largest angle such that the interval $(-\delta, +\delta)$ could be sampled for the later ARM analysis (due to the 40° minimum elevation of the Crab).

Table 8.2 shows total number of events that were extracted from the on-source and the off-source positions. The results of the same analysis on the Crab simulations (i.e., no background) are also shown in the table. The excess counts observed at the position of the Crab agrees with the simulations to within statistical error.

Now the significance of the excess source counts can be estimated. The naive approach is to assume that all of the measurements (off-source and on-source) are independent Poisson processes. Let the Crab point be labeled as C, and the off-source points labeled as $i = 1 \ldots 8$. Then this approach yields an approximate statistical uncertainty on the excess counts:

$$\begin{aligned} N_{excess} &= N_C - \bar{N}_{off-source} && (8.2)\\ &= N_C - \frac{1}{8}\sum_{i=1}^{8} N_i && (8.3)\\ \Rightarrow \sigma^2_{excess} &= \sigma^2_{N_C} + \frac{1}{64}\sum_{i=1}^{8} \sigma^2_{N_i} && (8.4)\\ &= N_C + \frac{1}{64}\sum_{i=1}^{8} N_i && (8.5)\\ \sigma_{excess} &= 182.9 && (8.6) \end{aligned}$$

This approach is not exact because the Compton event circles are likely to intersect

Position	Counts (flight data)	Counts (simulation of Crab alone, scaled to observation time)
(ℓ_0, b_0)	29,808	1101
Eight evenly-spaced points 20° away	29,041	481
	28,708	459
	29,453	444
	29,462	453
	29,124	482
	28,917	457
	29,093	432
	29,329	447
Average off-source	29,141	457
Excess on-source	667	644

Table 8.2: The total number of events with Compton circles within 5.2° of the Crab using the data cuts given in the text. The total number of counts is calculated at eight off-source points ($\delta = 20°$) and averaged. This is used as a background estimate. The point $(\ell_0, b_0) = (184.56°, -5.78°)$ is the position of the Crab.

multiple points, meaning N_C and N_i are not independent Poisson measurements. We identify the following independent Poisson processes that can be used to calculate a valid statistical uncertainty:

$$\begin{array}{ll} \bar{C}+k: & \text{An event intersects } k \text{ off-source points } \textbf{and not} \text{ the Crab point} \\ C+k: & \text{An event intersects } k \text{ off-source points } \textbf{and} \text{ the Crab point} \end{array} \tag{8.7}$$

where $k = 0 \ldots 8$. Let $N_{\bar{C}+k}$ and N_{C+k} be the counts measured for each Poisson process. These measurements are listed in Table 8.3. Then the number of excess Crab counts can be written in the following way:

$$N_{excess} = N_C - \bar{N}_{off-source} \tag{8.8}$$

$$= N_C - \frac{1}{8}\sum_{i=1}^{8} N_i \tag{8.9}$$

$$= \sum_{k=0}^{M} N_{C+k} - \frac{1}{8}\left(\sum_{k=1}^{8} kN_{C+k} + \sum_{k=1}^{8} kN_{\bar{C}+k}\right). \tag{8.10}$$

The factors of k in the off-source sum are needed because each event tallied by N_{C+k} or $N_{\bar{C}+k}$ is counted at k different off-source points. The statistical uncertainty for the

Number of off-source points (k)	Events at exactly k off-source points and not the Crab point ($N_{\bar{C}+k}$)	Events at exactly k off-source points and the Crab point (N_{C+k})
0	N/A	2578
1	29,209	12,801
2	61,448	14,373
3	11,752	51
4	803	5
5	88	0
6	27	0
7	8	0
8	22	0
Total	103,357	29,808
	Flight data	Simulation data
Excess on-source	667	644
Background noise (σ)	163.4	163.4 (using flight value)
Significance	$\mathbf{4.1\sigma}$	$\mathbf{3.9\sigma}$

Table 8.3: Calculation of the signal-to-noise ratio of the Crab data. The calculation is complicated by the non-independence of the off-source measurements both with each other and with the on-source measurement (see text for discussion). The Crab is detected in this manner at the 4σ level, which is consistent with simulations.

excess counts becomes

$$\sigma^2_{excess} = \sum_{k=0}^{8} N_{C+k} + \frac{1}{64}\left(\sum_{k=1}^{8} k^2 N_{C+k} + \sum_{k=1}^{8} k^2 N_{\bar{C}+k}\right) \quad (8.11)$$

$$\Rightarrow \sigma_{excess} = 163.4 \quad (8.12)$$

The result of this calculation is that the Crab was detected at the 4.1σ level, which is within statistical error of the expected 3.9σ from simulations.

8.6 Analysis of the Crab spectrum

Further analysis breaks up the total counts into different spectral bins. A spectrum is formed for the on-source data, and an average off-source spectrum is also calculated. Error bars are calculated for each spectral bin in the same manner described in Section

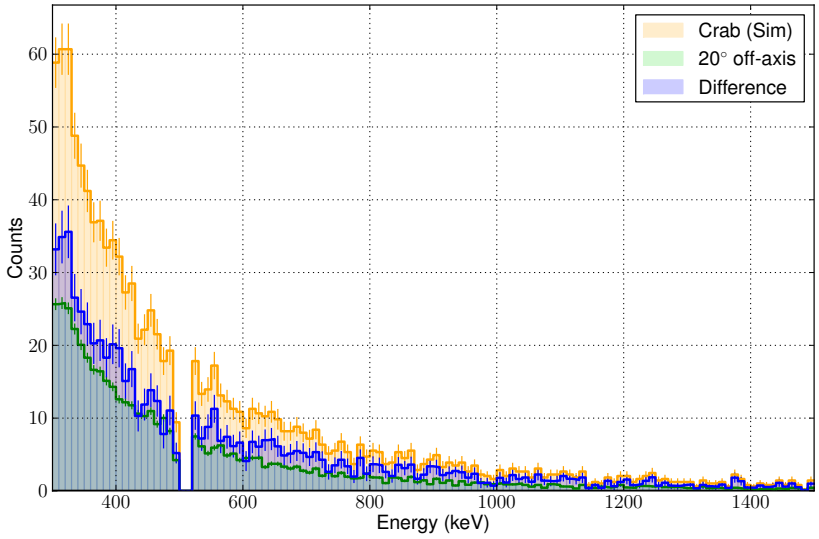

Figure 8.6: Simulated spectrum for events within 5.2° of the Crab using data cuts given in the text (orange). The averaged spectrum measured at points 20° away is plotted in green. The difference of these two distributions (blue) is the signature we expect in the flight data after estimating the spectrum at nearby points.

8.5 and Table 8.3. The results of this procedure for the simulated Crab alone are shown in Fig. 8.6.

The analysis of the flight data (Fig. 8.7) reveals a spectrum that is inconsistent with a null result with significance of 3.0σ, and the spectrum is consistent ($p = 0.78$) with the simulations. To test the spectral analysis method, three other test points were chosen that had similar exposure during the flight: (160°, -10°), (170°, +10°) and (175°, +20°). All of these points yields a spectrum that is consistent with zero. The results are shown in Fig. 8.8.

8.7 Analysis with the Angular Resolution Measure (ARM)

This analysis will focus on dividing the Crab data by the ARM measurement rather than the spectrum in order to further confirm the detection of the Crab. In order to see if there are excess counts in the ARM histogram at the location of the Crab, we must first estimate what the ARM should be in the absence of a source. To do this, we used the same eight 20° off-axis points that were used in the previous analyses. As mentioned earlier, the value of $\delta = 20°$ was chosen in this work as the largest angle such that the full interval $(-\delta, +\delta)$ could be sampled in this analysis

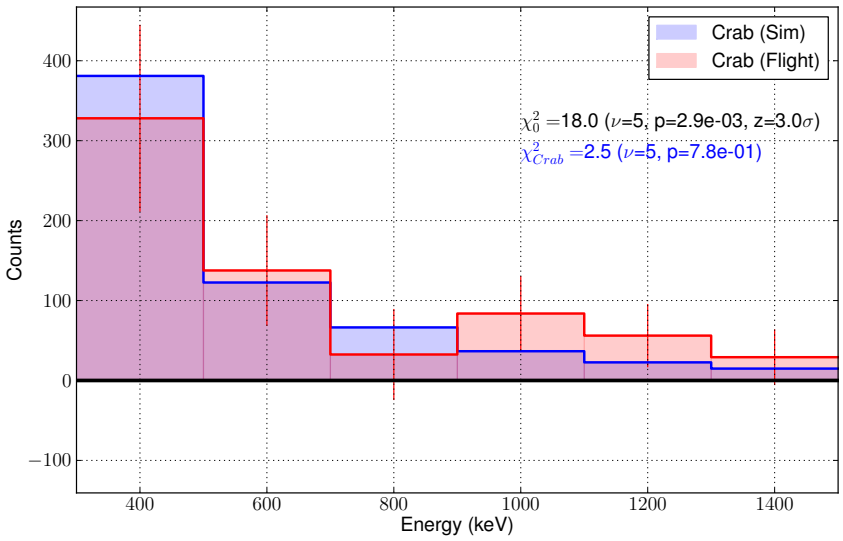

Figure 8.7: Measured spectrum for the Crab (red) plotted with the expected excess from simulations (blue). The spectrum is measured by subtracting the average spectrum from points 20° away from the Crab. Error bars are calculated using Poisson statistics. The measured spectrum is inconsistent with zero (3.0σ) but is consistent with the simulated Crab spectrum ($p = 0.78$). The bins are 200 keV wide.

(due to the 40° minimum elevation of the Crab). The ARM histogram was calculated for each of those points, and the average was constructed.

An ARM histogram that is calculated at a point separated from a point source by an angle δ (20° in this case) will have an ARM histogram that no longer looks like a Lorentzian, but it is a mostly flat distribution between $\pm\delta$ that decays away beyond that region. So the points we used to estimate the ARM have photons from the Crab in them, and not an insignificant number. We must account for the stray counts from the Crab in some way or risk underestimating the flux. An example of this off-source ARM contribution is shown in Fig. 8.9, where the on-source Crab simulation is shown with the 20° off-source Crab ARM. The difference between the on-source and off-source ARM histograms is the signature that we expect to see in the flight data when subtracting background estimates that are an angle δ away from the Crab.

The difference between the ARM histogram at the Crab position and the average ARM histogram of the off-source points was formed, and the error bars of each bin were calculated in the same manner described in Section 8.5 and Table 8.3. The result is shown in Fig. 8.10. The measured ARM excess is significant ($p = 0.00011$, or 3.9σ). The ARM distribution is also very close to the simulated expectation ($p = 0.83$). In addition, the central bin, which has the largest number of counts, has a signal-to-

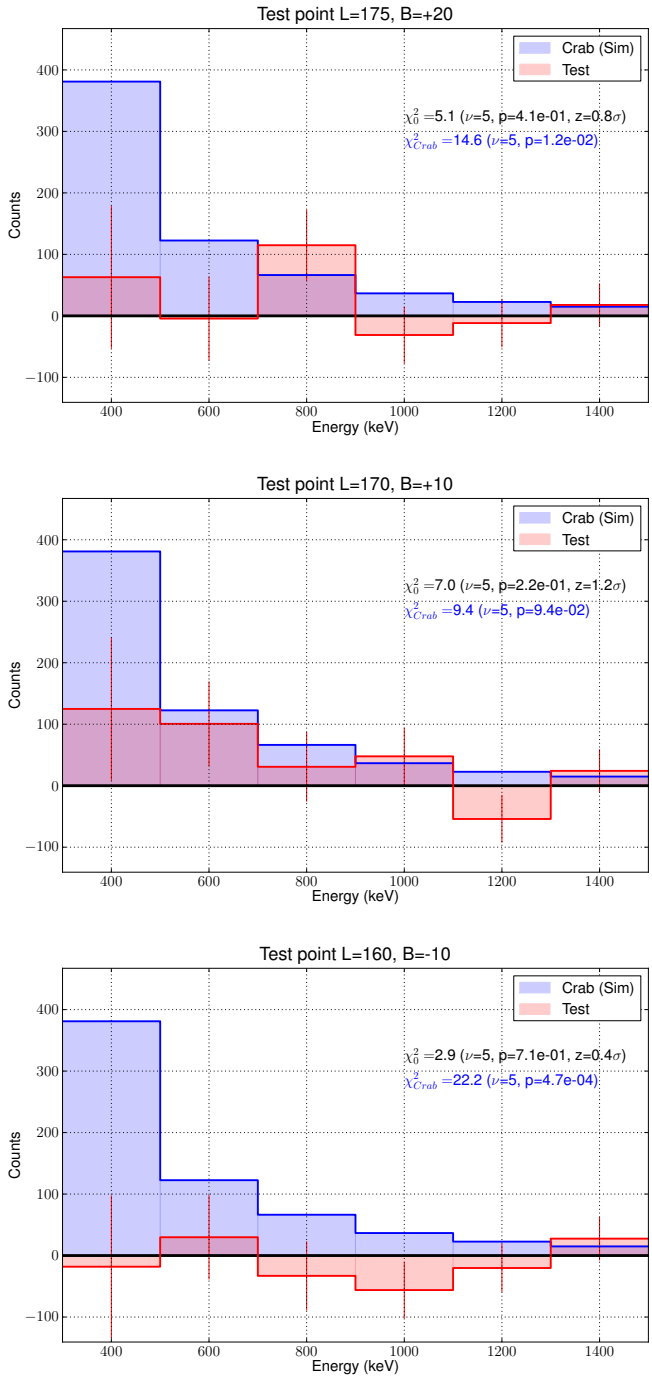

Figure 8.8: Measured spectrum at three different test points (red) plotted with the expected excess from Crab simulations (blue). The spectrum is measured by subtracting the average spectrum from eight points 20° away from the test points. The spectrum at the three test points is consistent with zero.

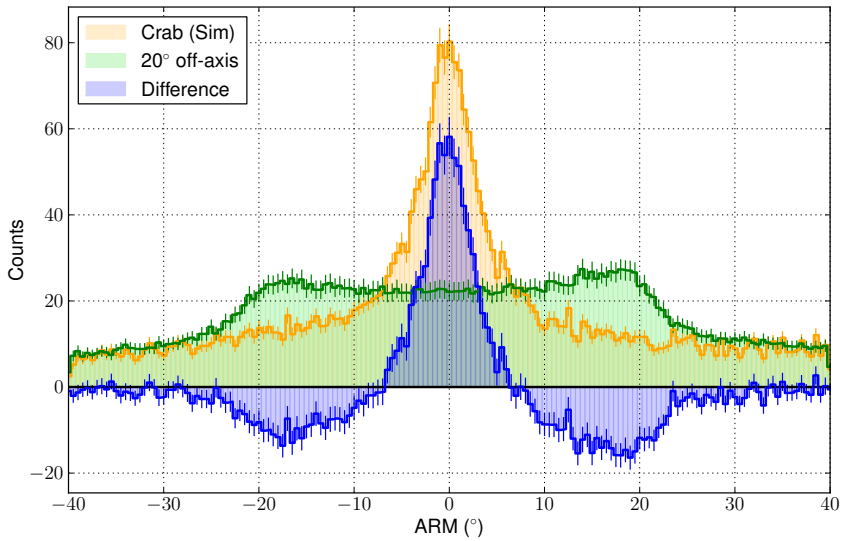

Figure 8.9: Simulated ARM distribution for the Crab using the data cuts given in the text (orange). The averaged ARM distribution at points 20° away is plotted in green. The difference of these two distributions (blue) is the signature we expect in the flight data after estimating the ARM at nearby points.

noise ratio of 4.2σ, similar to the significance derived in section 8.5. The expected simulation value for the central bin is 3.9σ, so the simulations are in close agreement with the flight data.

To test the ARM analysis method, three other test points were chosen that had similar exposure during the flight: (160°, -10°), (170°, +10°) and (175°, +20°). All of these points were consistent with null (the maximum significance is 1.8σ). The results are shown in Fig. 8.11.

8.8 Crab Image

The final confirmation of NCT's detection of the Crab nebula can be done with imaging. Compton imaging can be done through the straightforward backprojection of Compton circles onto the sky or with more sophisticated image processing. One imaging tool that has been used for NCT data in the past is List-Mode Maximum Likelihood Expectation Maximization (MLEM) [173], which has been implemented in MEGAlib. This method is iterative, and it uses a maximum likelihood statistic to determine the most likely distribution of each photon's Compton circle. The result is that point sources become clearer and other features are sharpened.

An image was constructed from the NCT flight data using the cuts mentioned previously. A total of 345,816 event circles were plotted in a 120° × 120° backpro-

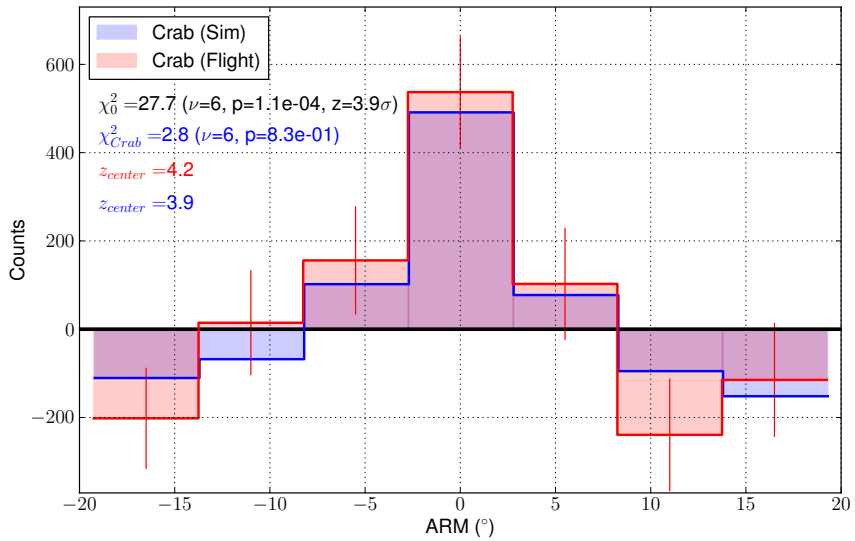

Figure 8.10: Measured ARM excess for the Crab (red) plotted with the expected excess from Crab simulations (blue). The spectrum is measured by subtracting the average spectrum from eight points 20° away from the Crab. Error bars are calculated using Poisson statistics. The measured ARM excess is significantly inconsistent with zero counts ($p = 0.00011$, or 3.9σ) and is compatible with the Crab simulation ($p = 0.83$). The signal-to-noise ratio of the central bin is 4.2σ. These results confirm the 4σ significance found in Section 8.5.

jection, of which approximately 3,600 event circles (1%) are expected from the Crab (Fig. 8.12). A total of 25 iterations of the MLEM algorithm were run on the image, producing the enhanced image seen in Fig. 8.13. The result is that the Crab appears in the image, though it was not clearly apparent in the backprojection. The Sun was in the field of view but no source appears there, as expected.

The Crab image reveals a slight offset ($\approx 2°$) in the position of the source. The significance of this offset can be evaluated in the following manner. Given the equivalent gaussian sigma of the ARM histogram for the Crab ($7.4°/2.35 = 3.1°$) and the signal-to-noise estimate of 4σ, the one-sigma uncertainty of the image position can be estimated as $\approx 3.1°/4 = 0.8°$ (e.g., [29]). This statistical uncertainty, combined with the $\approx 1°$ systematic uncertainty in the gondola aspect, means the $\approx 2°$ offset in the source position is not statistically significant.

8.9 Summary

The Crab was detected at a significance of 4σ by NCT during the 2009 balloon flight. Examination of the spectrum and ARM histograms from the source are con-

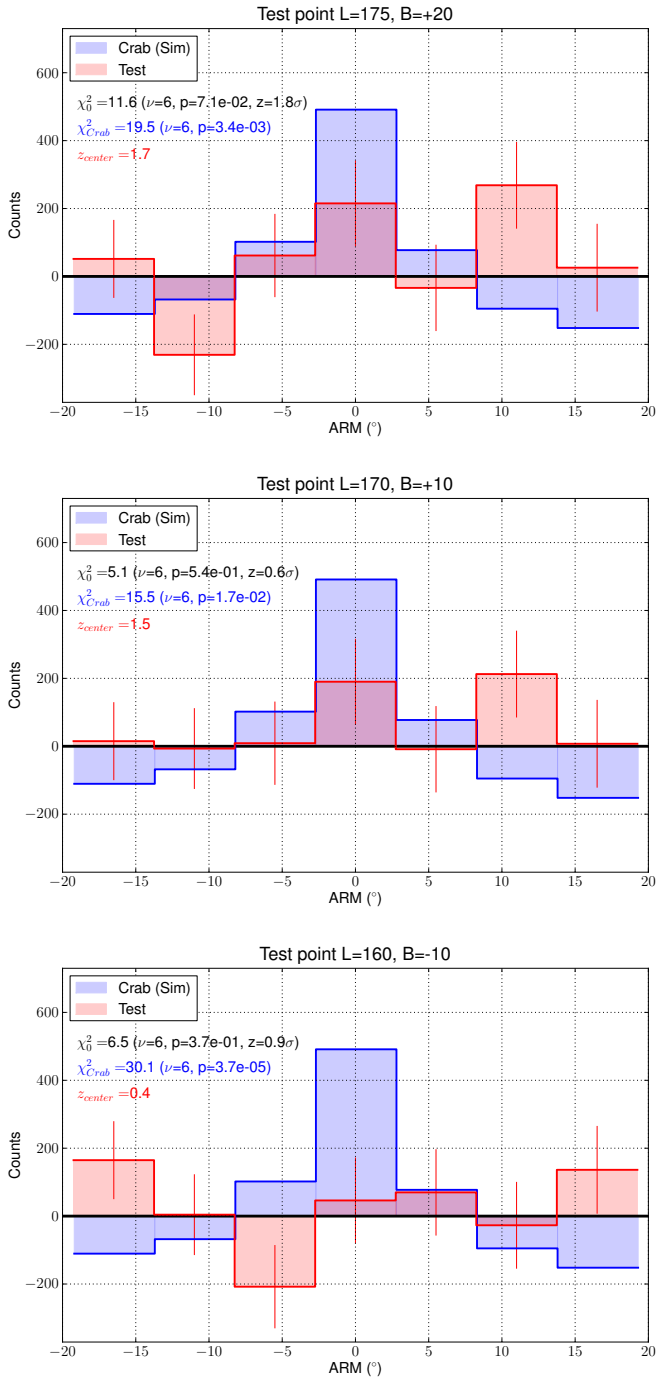

Figure 8.11: Measured ARM excess for three different test points (red) plotted with the expected excess from Crab simulations (blue). The spectrum is measured by subtracting the average spectrum from eight points 20° away from the test points. The ARM excess at the three test points is consistent with zero.

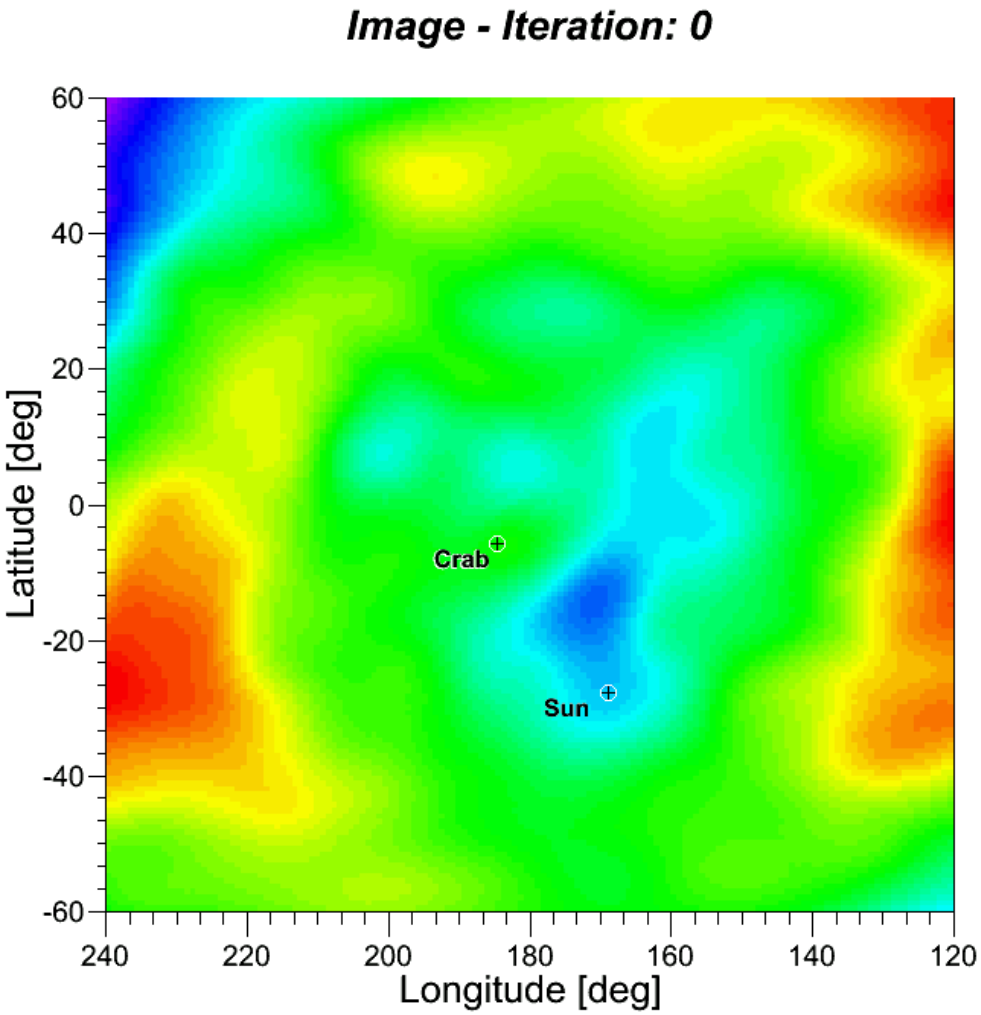

Figure 8.12: Raw Compton circle backprojection in galactic coordinates, with the position of the Crab and the Sun marked. A total of 345,816 event circles are plotted, and 1% of that number are expected to come from the Crab

sistent with the simulations of the Crab and are inconsistent with a null result. Using image processing, the Crab also appears in a Compton image made from the data. This result is the first significant detection of a celestial source by a compact Compton telescope.

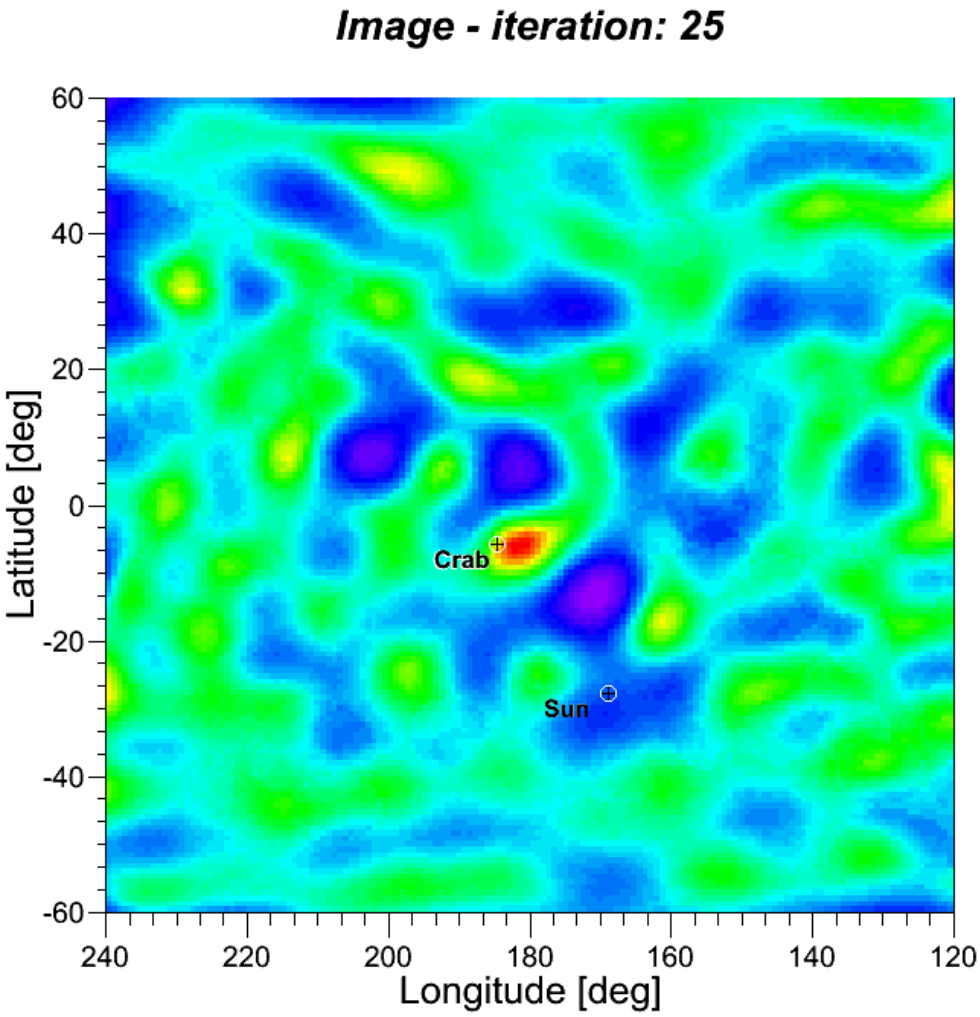

Figure 8.13: Image from Fig. 8.12 after 25 iterations of the MLEM algorithm. There is a clear excess in the vicinity of the Crab that is enhanced by the image processing, while bright diffuse areas in the background have been greatly reduced.

Bibliography

[1] *U.S. Standard Atmosphere, 1976*. U.S. Government Printing Office, Washington, D.C., 1976.

[2] S. Agostinelli, J. Allison, K. Amako, J. Apostolakis, H. Araujo, P. Arce, M. Asai, D. Axen, S. Banerjee, G. Barrand, F. Behner, L. Bellagamba, J. Boudreau, L. Broglia, A. Brunengo, H. Burkhardt, S. Chauvie, J. Chuma, R. Chytracek, G. Cooperman, et al. Geant4 – A Simulation Toolkit. *Nuclear Instruments and Methods in Physics Research Section A*, 506:250, Jul 2003.

[3] A. Akyuz, D. Bhattacharya, V. Kong, T. Miyagi, T. O. Neill, M. Polsen, J. Samimi, and A. Zych. Effect of Doppler broadening on the resolution of Compton telescopes. *34th COSPAR Scientific Assembly*, 34:1029, Jan 2002.

[4] J. Allison, K. Amako, J. Apostolakis, H. Araujo, P. Arce Dubois, M. Asai, G. Barrand, R. Capra, S. Chauvie, R. Chytracek, G. A. P. Cirrone, G. Cooperman, G. Cosmo, G. Cuttone, G. G. Daquino, M. Donszelmann, M. Dressel, G. Folger, F. Foppiano, J. Generowicz, et al. Geant4 developments and applications. *IEEE Transactions on Nuclear Science*, 53:270, Feb 2006.

[5] M. Amman and P. N. Luke. Three-dimensional position sensing and field shaping in orthogonal-strip germanium gamma-ray detectors. *Nuclear Instruments and Methods in Physics Research Section A*, 452:155, Sep 2000.

[6] M. Amman, P. N. Luke, and S. E. Boggs. Amorphous-semiconductor-contact germanium-based detectors for gamma-ray imaging and spectroscopy. *Nuclear Instruments and Methods in Physics Research Section A*, 579:886, Sep 2007.

[7] S. Amrose, S. E. Boggs, W. Coburn, R. P. Lin, and D. M. Smith. Calibration of 3D positioning in a Ge cross-strip detector. *Nuclear Instruments and Methods in Physics Research Section A*, 505:170, Jun 2003.

[8] S. Amrose, SE Boggs, W. Coburn, G. Holland, RP Lin, and DM Smith. Numerical simulations of 3D positioning in cross-strip Ge detectors. *2001 IEEE Nuclear Science Symposium Conference Record*, 1, 2001.

[9] E. Aprile, A. Bolotnikov, D. Chen, and R. Mukherjee. A Monte Carlo analysis of the liquid xenon TPC as gamma-ray telescope. *Nuclear Instruments and Methods in Physics Research Section A*, 327:216, Mar 1993.

[10] E. Aprile, A. Curioni, K. L. Giboni, M. Kobayashi, U. G. Oberlack, S. Ventura, E. L. Chupp, P. P. Dunphy, T. Doke, and J. Kikuchi. Calibration and in-flight performance of the Compton telescope prototype LXeGRIT. *New Astronomy Reviews*, 48:257, Feb 2004.

[11] E. Aprile, A. Curioni, K. L. Giboni, M. Kobayashi, U. G. Oberlack, and S. Zhang. Compton imaging of MeV gamma-rays with the Liquid Xenon Gamma-Ray Imaging Telescope (LXeGRIT). *Nuclear Instruments and Methods in Physics Research Section A*, 593:414, Aug 2008.

[12] Elena Aprile, Alessandro Curioni, Valeri Egorov, Karl-Ludwig Giboni, Uwe G. Oberlack, Sandro Ventura, Tadayoshi Doke, Jun Kikuchi, Kyoko Takizawa, Edward L. Chupp, and Philip P. Dunphy. Spectroscopy and imaging performance of the Liquid Xenon Gamma-Ray Imaging Telescope (LXeGRIT). *Proc. SPIE Vol. 4140*, 4140:333, Dec 2000.

[13] Elena Aprile, Reshmi Mukherjee, and Masayo Suzuki. A liquid xenon imaging telescope for 1-30 MeV gamma-ray astrophysics. *IN: EUV*, 1159:295, Nov 1989.

[14] Elena Aprile, Uwe G. Oberlack, Alessandro Curioni, Valeri Egorov, Karl-Ludwig Giboni, Sandro Ventura, Tadayoshi Doke, Jun Kikuchi, Kyoko Takizawa, Edward L. Chupp, and Philip P. Dunphy. Preliminary results from the 1999 balloon flight of the Liquid Xenon Gamma-Ray Imaging Telescope (LXeGRIT). *Proc. SPIE Vol. 4140*, 4140:344, Dec 2000.

[15] A. M. Atoyan and F. A. Aharonian. On the mechanisms of gamma radiation in the Crab Nebula. *Monthly Notices RAS*, 278:525, Jan 1996.

[16] R. E. Baker, R. R. Lovett, K. J. Orford, and D. Ramsden. Gamma ray of 1 to 10 MeV from the Crab and Cygnus regions. *Nature Physical Science*, 245:18, Sep 1973.

[17] M. E. Bandstra, J. D. Bowen, A. Zoglauer, S. E. Boggs, W. Coburn, C. B. Wunderer, M. Amman, and P. N. Luke. Position Calibrations and Preliminary Angular Resolution of the Prototype Nuclear Compton Telescope. *IEEE Nuclear Science Symposium Conference Record*, pages 770–777, Jan 2006.

[18] M.S. Bandstra, E.C. Bellm, J.-L. Chiu, J.-S. Liang, Z.-K. Liu, D. Perez-Becker, A. Zoglauer, S. E. Boggs, H.-K. Chang, Y.-H. Chang, M. A. Huang, M. Amman, S.J. Chiang, W.-C. Hung, P. Jean, C.-H. Lin, P. N. Luke, R.-S. Run, and C. B.

Wunderer. The Spring 2009 Balloon Flight of the Nuclear Compton Telescope. *IEEE Nuclear Science Symposium Conference Record*, 2009.

[19] Lyle Monroe Bartlett. High Resolution Gamma-Ray Spectroscopy of the Crab. *Thesis (Ph.D.)–University of Maryland College Park*, page 55, Jan 1994.

[20] M. Bejger and P. Haensel. Accelerated expansion of the crab nebula and evaluation of its neutron-star parameters. *Astronomy and Astrophysics*.

[21] E.C. Bellm, J.-L. Chiu, D. Perez-Becker, J.-S. Liang, A. Zoglauer, M. S. Bandstra, Z.-K. Liu, S. E. Boggs, H.-K. Chang, Y.-H. Chang, M. A. Huang, M. Amman, W.-C. Hung, P. Jean, C.-H. Lin, P. N. Luke, R.-S. Run, and C. B. Wunderer. Efficiency and Polarimetric Calibrations of the Nuclear Compton Telescope. *IEEE Nuclear Science Symposium Conference Record*, 2009.

[22] Eric C. Bellm, Steven E. Boggs, Mark S. Bandstra, Jason D. Bowen, Daniel Perez-Becker, Cornelia B. Wunderer, Andreas Zoglauer, Mark Amman, Paul N. Luke, Hsiang-Kuang Chang, Jeng-Lun Chiu, Jau-Shian Liang, Yuan-Hann Chang, Zong-Kai Liu, Wei-Che Hung, Chih-Hsun Lin, Minghuey A. Huang, and Pierre Jean. Overview of the Nuclear Compton Telescope. *IEEE Transactions on Nuclear Science*, 56:1250, Jun 2009.

[23] Eric C. Bellm, Kevin Hurley, Valentin Pal'shin, Kazutaka Yamaoka, Mark S. Bandstra, Steven E. Boggs, Soojing Hong, Natsuki Kodaka, A. S. Kozyrev, M. L. Litvak, I. G. Mitrofanov, Yujin E. Nakagawa, Masanori Ohno, Kaori Onda, A. B. Sanin, Satoshi Sugita, Makoto Tashiro, V. I. Tretyakov, Yuji Urata, and Claudia Wigger. Observations of the Prompt Gamma-Ray Emission of GRB 070125. *The Astrophysical Journal*, 688:491, Nov 2008.

[24] M. Berger, J. Hubbell, and S. Seltzer. XCOM: Photon cross sections database. *NIST Standard Reference Database 8 (XGAM)*, Jan 1998.

[25] Lars Bildsten, Edwin E. Salpeter, and Ira Wasserman. The fate of accreted CNO elements in neutron star atmospheres – X-ray bursts and gamma-ray lines. *Astrophysical Journal*, 384:143, Jan 1992.

[26] Lars Bildsten, Edwin E. Salpeter, and Ira Wasserman. Helium destruction and gamma-ray line emission in accreting neutron stars. *Astrophysical Journal*, 408:615, May 1993.

[27] H. Bloemen, R. Wijnands, K. Bennett, R. Diehl, W. Hermsen, G. Lichti, D. Morris, J. Ryan, V. Schönfelder, A. W. Strong, B. N. Swanenburg, C. de Vries, and C. Winkler. COMPTEL observations of the Orion complex: Evidence for cosmic-ray induced gamma-ray lines. *Astronomy and Astrophysics (ISSN 0004-6361)*, 281:L5, Jan 1994.

[28] P. F. Bloser, R. Andritschke, G. Kanbach, V. Schönfelder, F. Schopper, and A. Zoglauer. The MEGA advanced Compton telescope project. *New Astronomy Reviews*, 46:611, Jul 2002.

[29] Norman Bobroff. Position measurement with a resolution and noise-limited instrument. *Review of Scientific Instruments*, 57:1152, Jun 1986.

[30] S. E. Boggs, W. Coburn, D. M. Smith, J. D. Bowen, P. Jean, J. M. Kregenow, R. P. Lin, and P. von Ballmoos. Overview of the Nuclear Compton Telescope. *New Astronomy Reviews*, 48:251, Feb 2004.

[31] S. E. Boggs and P. Jean. Event reconstruction in high resolution Compton telescopes. *Astronomy and Astrophysics Supplement*, 145:311, Aug 2000.

[32] S. E. Boggs and P. Jean. Performance characteristics of high resolution Compton telescopes. *Astronomy and Astrophysics*, 376:1126, Aug 2001.

[33] S. E. Boggs, P. Jean, R. P. Lin, D. M. Smith, P. von Ballmoos, N. W. Madden, P. N. Luke, M. Amman, M. T. Burks, E. L. Hull, W. Craig, and K. Ziock. The Nuclear Compton Telescope: A balloon-borne soft gamma-ray spectrometer, polarimeter, and imager. *GAMMA 2001: Gamma-Ray Astrophysics 2001. AIP Conference Proceedings*, 587:877, Sep 2001.

[34] Steven Boggs, James Kurfess, James Ryan, Elena Aprile, Neil Gehrels, Marc Kippen, Marc Leising, Uwe Oberlack, Cornelia Wunderer, Allen Zych, Peter Bloser, Michael Harris, Andrew Hoover, Alexei Klimenk, Dan Kocevski, Mark McConnell, Peter Milne, Elena I. Novikova, Bernard Phlips, Mark Polsen, et al. The Advanced Compton Telescope. *Space Telescopes and Instrumentation II: Ultraviolet to Gamma Ray. Edited by Turner*, 6266:62, Jul 2006.

[35] Steven E. Boggs, Mark S. Amman, Pierre Jean, Susan Amrose, Wayne Coburn, Robert P. Lin, David M. Smith, Paul N. Luke, Norman W. Madden, Morgan Burks, Ethan L. Hull, Peter von Ballmoos, William W. Craig, and Klaus Ziock. Upcoming balloon flight of the Nuclear Compton Telescope. *X-Ray and Gamma-Ray Telescopes and Instruments for Astronomy. Edited by Joachim E. Truemper*, 4851:1221, Mar 2003.

[36] Steven E. Boggs and David M. Smith. Search for Neutron-Capture Gamma-Ray Lines from A0535+26 in Outburst. *The Astrophysical Journal*, 637:L121, Feb 2006.

[37] Steven E. Boggs, A. Zoglauer, E. Bellm, K. Hurley, R. P. Lin, D. M. Smith, C. Wigger, and W. Hajdas. The Giant Flare of 2004 December 27 from SGR 1806-20. *The Astrophysical Journal*, 661:458, May 2007.

[38] J. G. Bolton and G. J. Stanley. The Position and Probable Identification of the Source of the Galactic Radio-Frequency Radiation Taurus-A. *Australian Journal of Scientific Research A*, 2:139, Jun 1949.

[39] J. G. Bolton, G. J. Stanley, and O. B. Slee. Positions of Three Discrete Sources of Galactic Radio-Frequency Radiation. *Nature*, 164:101, Jul 1949.

[40] J. Bowen, M. Bandstra, SE Boggs, A. Zoglauer, C. Wunderer, M. Amman, and P. Luke. Depth dependent background measurements with NCT. *Nuclear Science Symposium Conference Record, 2007. NSS '07. IEEE*, 1:436 – 444, Jan 2007.

[41] J. D. Bowen. *The Prototype Nuclear Compton Telescope: Observations of the Galactic Anticenter Region.* PhD thesis, U.C. Berkeley, 2009.

[42] Jason D. Bowen, Mark E. Bandstra, Steven E. Boggs, Wayne Coburn, Cornelia B. Wunderer, Robert P. Lin, Mark Amman, Paul N. Luke, Morgan T. Burks, William Craig, Norman W. Madden, David M. Smith, Peter von Ballmoos, and Pierre Jean. Pre-flight calibration of the prototype Nuclear Compton Telescope. *Proc. of SPIE*, 6266:63, Jul 2006.

[43] S. Bowyer, E. T. Byram, T. A. Chubb, and H. Friedman. Lunar Occulation of X-ray Emission from the Crab Nebula. *Science*, 146:912, Nov 1964.

[44] S. Bowyer, E. T. Byram, T. A. Chubb, and H. Friedman. X-ray Sources in the Galaxy. *Nature*, 201:1307, Mar 1964.

[45] Şirin Çalişkan, Emrah Kalemci, Matthew G. Baring, Steven E. Boggs, and Peter Kretschmar. Search for a Redshifted 2.2 MeV Neutron Capture Line from A0535+262 in Outburst. *The Astrophysical Journal*, 694:593, Mar 2009.

[46] Hsiang-Kuang Chang, Steven Boggs, and Yuan-Hann Chang. The Nuclear Compton Telescope (NCT): Scientific goals and expected sensitivity. *Adv Space Res*, 40(8):1281–1287, Jan 2007.

[47] J.-L. Chiu, Z.-K. Liu, M. S. Bandstra, D. Perez-Becker, E. C. Bellm, A. Zoglauer, S. E. Boggs, H.-K. Chang, Y.-H. Chang, M. A. Huang, M. Amman, W.-C. Hung, J.-S. Liang, C.-H. Lin, P. N. Luke, R.-S. Run, and C. B. Wunderer. Energy, Depth Calibration, and Imaging Capability of the Nuclear Compton Telescope. *IEEE Nuclear Science Symposium Conference Record*, 2009.

[48] Jeng-Lun Chiu. *The Nuclear Compton Telescope (NCT): The Mission and the Crab-Nebula Detection.* PhD thesis, National Tsing-Hua University, 2010.

[49] George W. Clark. Balloon Observation of the X-Ray Spectrum of the Crab Nebula Above 15 keV. *Physical Review Letters*, 14:91, Jan 1965.

[50] W. Coburn, S. Amrose, S. E. Boggs, R. P. Lin, M. S. Amman, M. Burks, E. L. Hull, P. N. Luke, and N. W. Madden. 3D positioning germanium detectors for gamma-ray astronomy. *Proceedings of SPIE*, 4784:54, 2003.

[51] W. Coburn, SE Boggs, S. Amrose, RP Lin, MT Burks, M. Amman, PN Luke, NW Madden, and EL Hull. Results of charge sharing tests in a Ge-strip detector. *2001 IEEE Nuclear Science Symposium Conference Record*, 1, 2001.

[52] Wayne Coburn and Steven E. Boggs. Polarization of the prompt γ-ray emission from the γ-ray burst of 6 December 2002. *Nature*, 423(6938):415–417, May 2003.

[53] Wayne Coburn, Steven E. Boggs, Jason D. Bowen, Mark E. Bandstra, Mark S. Amman, Morgan T. Burks, William Craig, Pierre Jean, Robert P. Lin, Paul N. Luke, Norman W. Madden, David M. Smith, and Peter von Ballmoos. First results from the balloon flight of the NCT prototype. *Proc. of SPIE*, 5898:13, Aug 2005.

[54] Wayne Coburn, Steven E. Boggs, Julia M. Kregenow, Jason D. Bowen, Mark S. Amman, Morgan T. Burkes, William W. Craig, Pierre Jean, Robert P. Lin, Paul N. Luke, Norman W. Madden, David M. Smith, Peter von Ballmoos, and Klaus Ziock. Preliminary laboratory performance of the NCT prototype flight electronics. *X-Ray and Gamma-Ray Instrumentation for Astronomy XIII. Edited by Flanagan*, 5165:131, Feb 2004.

[55] P. A. Connors and R. F. Stark. Observable gravitational effects on polarised radiation coming from near a black hole. *Nature*, 269:128, Sep 1977.

[56] R. J. Cooper, A. J. Boston, H. C. Boston, J. R. Cresswell, A. N. Grint, L. J. Harkness, P. J. Nolan, D. C. Oxley, D. P. Scraggs, I. Lazarus, J. Simpson, and J. Dobson. Charge collection performance of a segmented planar high-purity germanium detector. *Nuclear Instruments and Methods in Physics Research Section A*, 595:401, Oct 2008.

[57] A. Curioni, E. Aprile, T. Doke, K. Giboni, M. Kobayashi, and U. G. Oberlack. A study of the LXeGRIT detection efficiency for MeV gamma-rays during the 2000 balloon flight campaign. *Nuclear Inst. and Methods in Physics Research*, Jan 2007.

[58] Alessandro Curioni, Elena Aprile, Karl-Ludwig Giboni, Masanori Kobayashi, Uwe G. Oberlack, Edward L. Chupp, Philip P. Dunphy, Tadayoshi Doke, Jun Kikuchi, and Sandro Ventura. On the background rate in the LXeGRIT Instrument during the 2000 Balloon Flight. *X-Ray and Gamma-Ray Telescopes and Instruments for Astronomy. Edited by Joachim E. Truemper*, 4851:1281, Mar 2003.

[59] S. Daju, R. R. Hillier, A. F. Janes, and R. M. Redfern. The X-ray Spectrum of the Crab Nebula between 20 keV and 3 MeV. *Astrophysical Letters*, 6:225, Jul 1970.

[60] P. M. Dauber and L. H. Smith. The Liquid-Xenon Compton Telescope: A New Technique for Gamma-Ray Astronomy. *Proceedings of the 13th International Conference on Cosmic Rays*, 4:2716, Jan 1973.

[61] K. Debertin and R.G. Helmer. *Gamma- and X-ray spectrometry with semiconductor detectors*. Elsevier, 2001.

[62] Defense Department, Navy, and Nautical Almanac Office. Astronomical Almanac for the Year 2009. Jan 2008.

[63] Roland Diehl and F. X. Timmes. Gamma-Ray Line Emission from Radioactive Isotopes in Stars and Galaxies. *The Publications of the Astronomical Society of the Pacific*, 110:637, Jun 1998.

[64] J. J. L. Duyvendak. Further Data Bearing on the Identification of the Crab Nebula with the Supernova of 1054 A.D. Part I. The Ancient Oriental Chronicles. *Publications of the Astronomical Society of the Pacific*, 54:91, Apr 1942.

[65] Robley D. Evans. *The Atomic Nucleus*. McGraw-Hill, 1965.

[66] L. Fabris, N. W. Madden, and H. Yaver. A fast, compact solution for low noise charge preamplifiers. *Nuclear Instruments and Methods in Physics Research Section A*, 424:545, Mar 1999.

[67] A. Finzi and R. A. Wolf. Possible Conversion of Rotational Energy of the Neutron Star in the Crab Nebula Into Energy of Relativistic Electrons. *Astrophysical Journal*, 155:L107, Feb 1969.

[68] G. J. Fishman. The gamma-ray burst capabilities of BATSE and the Gamma Ray Observatory. *10.1063/1.37235. AIP Conference Proceedings*, 170:378, Sep 1988.

[69] G. J. Fishman, C. A. Meegan, T. A. Parnell, R. B. Wilson, W. Paciesas, J. L. Mateson, T. L. Cline, and B. J. Teegarden. Burst and Transient Source Experiment (BATSE) for the Gamma Ray Observatory (GRO). *In NASA. Goddard Space Flight Center 19th Intern. Cosmic Ray Conf.*, 3:343, Aug 1985.

[70] M. Forot, P. Laurent, I. A. Grenier, C. Gouiffès, and F. Lebrun. Polarization of the Crab Pulsar and Nebula as Observed by the INTEGRAL/IBIS Telescope. *The Astrophysical Journal*, 688:L29, Nov 2008.

[71] N. Gehrels, S. D. Barthelmy, B. J. Teegarden, J. Tueller, M. Leventhal, and C. J. MacCallum. GRIS observations of positron annihilation radiation from the Galactic center. *Astrophysical Journal*, 375:L13, Jul 1991.

[72] S. Geisser. The predictive sample reuse method with applications. *Journal of the American Statistical Association*, 70(350):320–328, Jan 1975.

[73] T. Gold. Rotating Neutron Stars as the Origin of the Pulsating Radio Sources. *Nature*, 218:731, May 1968.

[74] Peter Goldreich and William H. Julian. Pulsar Electrodynamics. *Astrophysical Journal*, 157:869, Aug 1969.

[75] R. J. Grader, R. W. Hill, F. D. Seward, and A. Toor. X-Ray Spectra from Three Cosmic Sources. *Science*, 152:1499, Jun 1966.

[76] S. Gros, N. J. Hammond, C. J. Lister, P. Chowdhury, S. M. Fischer, and S. J. Freeman. Performance tests of large area position-sensitive planar germanium detectors with conventional and amorphous contacts. *Nuclear Instruments and Methods in Physics Research Section A*, 602:467, Apr 2009.

[77] D. E. Gruber, R. E. Rothschild, J. L. Matteson, and R. L. Kinzer. The HEAO-1 diffuse component spectrum from 15 to above 500 keV. *MPE Rep.*, 184:129, Jan 1984.

[78] James E. Gunn and Jeremiah P. Ostriker. Magnetic Dipole Radiation from Pulsars. *Nature*, 221:454, Feb 1969.

[79] H. Halloin, P. von Ballmoos, J. Evrard, G. K. Skinner, N. Abrosimov, P. Bastie, G. di Cocco, M. George, B. Hamelin, P. Jean, J. Knödlseder, P. Laporte, C. Badenes, P. Laurent, and R. K. Smither. Performance of CLAIRE, the first balloon-borne gamma-ray lens telescope. *Nuclear Instruments and Methods in Physics Research Section A*, 504:120, Apr 2003.

[80] A. K. Harding and O. C. De Jager. Constraints on electron acceleration in the Crab nebula. *In: Particle acceleration in cosmic plasmas; Proceedings of the Workshop*, 264:471, Jan 1992.

[81] R. C. Haymes, D. V. Ellis, G. J. Fishman, J. D. Kurfess, and W. H. Tucker. Observation of Gamma Radiation from the Crab Nebula. *Astrophysical Journal*, 151:L9, Jan 1968.

[82] Jason P. Hayward and David K. Wehe. Charge Loss Correction in a High-Purity Germanium Double-Sided Strip Detector. *IEEE Transactions on Nuclear Science*, 55:2789, Oct 2008.

[83] R. G. Helmer and C. van der Leun. Recommended standards for γ-ray energy calibration (1999). *Nuclear Instruments and Methods in Physics Research Section A*, 450:35, Aug 2000.

[84] D. Herzo. A large double scatter telescope for gamma rays and neutrons. *Nuclear Instruments and Methods*, 123:583, Feb 1975.

[85] J. Jeff Hester. The Crab Nebula: An Astrophysical Chimera. *Annual Review of Astronomy & Astrophysics*, 46:127, Sep 2008.

[86] G. Heusser. Low-radioactivity background techniques. *Annual Review of Nuclear and Particle Science*, Jan 1995.

[87] A. Hewish, S. J. Bell, J. D. H. Pilkington, P. F. Scott, and R. A. Collins. Observation of a Rapidly Pulsating Radio Source. *Nature*, 217:709, Feb 1968.

[88] Wei-Che Hung, Yuan-Hann Chang, Chih-Hsun Lin, Steven E. Boggs, Hsiang-Kuang Chang, Mark S. Bandstra, Eric C. Bellm, Jeng-Lun Chiu, Jau-Shian Liang, Zong-Kai Liu, Daniel Perez-Becker, Cornelia B. Wunderer, Andreas Zoglauer, Ming-Huey Huang, Mark Amman, and Paul N. Luke. The Data Readout System of the Nuclear Compton Telescope (NCT). *IEEE Transactions on Nuclear Science*, 56:2303–2308, Aug 2009.

[89] S. D. Hunter, L. M. Barbier, P. F. Bloser, and et al. Astrophysics with the 3-DTI Gamma-Ray Telescope. *Proceedings of the 30th International Cosmic Ray Conference. July 3 - 11*, 3:1389, Jan 2008.

[90] G. J. Hurford, E. J. Schmahl, R. A. Schwartz, A. J. Conway, M. J. Aschwanden, A. Csillaghy, B. R. Dennis, C. Johns-Krull, S. Krucker, R. P. Lin, J. McTiernan, T. R. Metcalf, J. Sato, and D. M. Smith. The RHESSI Imaging Concept. *Solar Physics*, 210:61, Nov 2002.

[91] A. F. Iyudin, R. Diehl, H. Bloemen, W. Hermsen, G. G. Lichti, D. Morris, J. Ryan, V. Schönfelder, H. Steinle, M. Varendorff, C. de Vries, and C. Winkler. COMPTEL observations of Ti-44 gamma-ray line emission from CAS A. *Astronomy and Astrophysics (ISSN 0004-6361)*, 284:L1, Apr 1994.

[92] P. Jean and N. Guessoum. Neutron-capture and 2.22 MeV emission in the atmosphere of the secondary of an X-ray binary. *Astronomy and Astrophysics*, 378(2):509–521, Nov 2001.

[93] P. Jean, G. Vedrenne, J. P. Roques, V. Schönfelder, B. J. Teegarden, A. von Kienlin, J. Knödlseder, C. Wunderer, G. K. Skinner, G. Weidenspointner, D. Attié, S. Boggs, P. Caraveo, B. Cordier, R. Diehl, M. Gros, P. Leleux, G. G. Lichti, E. Kalemci, J. Kiener, et al. SPI instrumental background characteristics. *Astronomy and Astrophysics*, 411:L107, Nov 2003.

[94] W. N. Johnson, J. D. Kurfess, W. R. Purcell, S. M. Matz, M. P. Ulmer, M. S. Strickman, R. J. Murphy, D. A. Grabelsky, R. L. Kinzer, G. H. Share, R. A. Cameron, R. A. Kroeger, M. Maisack, G. V. Jung, C. M. Jensen, D. D. Clayton, M. D. Leising, J. E. Grove, and C. S. Dyer. Initial results from OSSE on the Compton Observatory. *Astronomy and Astrophysics Supplement Series (ISSN 0365-0138)*, 97:21, Jan 1993.

[95] E. Jourdain, D. Götz, N. J. Westergaard, L. Natalucci, and J. P. Roques. INTEGRAL Cross-calibration Status: Crab observations between 3 keV and 1 MeV. *Proceedings of the 7th INTEGRAL Workshop. 8 - 11 September 2008 Copenhagen*, page 144, Jan 2008.

[96] E. Jourdain and J. P. Roques. The High-Energy Emission of the Crab Nebula from 20 keV TO 6 MeV with Integral SPI. *The Astrophysical Journal*, 704:17, Oct 2009.

[97] G. V. Jung. The hard X-ray to low-energy gamma-ray spectrum of the Crab Nebula. *Astrophysical Journal*, 338:972, Mar 1989.

[98] G. Kanbach, R. Andritschke, F. Schopper, V. Schönfelder, A. Zoglauer, P. F. Bloser, S. D. Hunter, J. A. Ryan, M. McConnell, V. Reglero, G. DiCocco, and J. Knödlseder. The MEGA project. *New Astronomy Reviews*, 48:275, Feb 2004.

[99] G. Kanbach, D. L. Bertsch, A. Favale, C. E. Fichtel, R. C. Hartman, R. Hofstadter, E. B. Hughes, S. D. Hunter, B. W. Hughlock, D. A. Kniffen, Y. C. Lin, H. A. Mayer-Hasselwander, P. L. Nolan, K. Pinkau, H. Rothermel, E. Schneid, M. Sommer, and D. J. Thompson. The project EGRET (energetic gamma-ray experiment telescope) on NASA's Gamma-Ray Observatory GRO. *Space Science Reviews*, 49:69, Jan 1989.

[100] C. F. Kennel and F. V. Coroniti. Confinement of the Crab pulsar's wind by its supernova remnant. *Astrophysical Journal*, 283:694, Aug 1984.

[101] C. F. Kennel and F. V. Coroniti. Magnetohydrodynamic model of Crab nebula radiation. *Astrophysical Journal*, 283:710, Aug 1984.

[102] M. G. F. Kirsch, W. Becker, S. Larsson, S. Brandt, C. Budtz-Jørgensen, N. J. Westergaard, and R. Much. Cross Calibration of Instruments on Board XMM-Newton and INTEGRAL with the Crab. *Proceedings of the 5th INTEGRAL Workshop on the INTEGRAL Universe (ESA SP-552). 16-20 February 2004*, 552:863, Oct 2004.

[103] Ray W. Klebesadel, Ian B. Strong, and Roy A. Olson. Observations of Gamma-Ray Bursts of Cosmic Origin. *Astrophysical Journal*, 182:L85, Jun 1973.

[104] O. Klein and T. Nishina. Über die streuung von strahlung durch freie elektronen nach der neuen relativistischen quantendynamik von dirac. *Zeitschrift für Physik*, 52:853, Nov 1929.

[105] Jürgen Knödlseder, Peter von Ballmoos, Filippo Frontera, Angela Bazzano, Finn Christensen, Margarida Hernanz, and Cornelia Wunderer. GRI: focusing on the evolving violent universe. *Experimental Astronomy*, 23:121, Feb 2009.

[106] Stefanie Komossa. X-ray and Gamma-ray properties of AGN: Results from XMM-Newton, Chandra and INTEGRAL. *Adv Space Res*, 38:1382, Jan 2006.

[107] R. A. Kroeger, S. E. Inderhees, W. N. Johnson, R. L. Kinzer, J. D. Kurfess, and N. Gehrels. Charge division readout of a two-dimensional germanium strip detector. *Nuclear Instruments and Methods in Physics Research Section A*, 348:507, Sep 1994.

[108] R. A. Kroeger, W. N. Johnson, J. D. Kurfess, B. F. Phlips, and E. A. Wulf. Three-Compton telescope: theory, simulations, and performance. *IEEE Transactions on Nuclear Science*, 49:1887, Aug 2002.

[109] Richard A. Kroeger, W. Neil Johnson, Robert L. Kinzer, James D. Kurfess, Sue E. Inderhees, Bernard Phlips, Neil A. Gehrels, and Brad Graham. Spatial resolution and imaging of gamma rays with germanium strip detectors. *Proc. SPIE Vol. 2518*, 2518:236, Sep 1995.

[110] L. Kuiper, W. Hermsen, G. Cusumano, R. Diehl, V. Schönfelder, A. Strong, K. Bennett, and M. L. McConnell. The Crab pulsar in the 0.75-30 MeV range as seen by CGRO COMPTEL. A coherent high-energy picture from soft X-rays up to high-energy gamma-rays. *Astronomy and Astrophysics*, 378:918, Nov 2001.

[111] J. D. Kurfess, W. N. Johnson, R. L. Kinzer, R. A. Kroeger, M. S. Strickman, J. E. Grove, M. D. Leising, D. D. Clayton, D. A. Grabelsky, W. R. Purcell, M. P. Ulmer, R. A. Cameron, and G. V. Jung. Oriented Scintillation Spectrometer Experiment observations of Co-57 in SN 1987A. *Astrophysical Journal*, 399:L137, Nov 1992.

[112] J. D. Kurfess, W. N. Johnson, R. A. Kroeger, B. F. Phlips, and E. A. Wulf. Development and applications of position-sensitive solid-state gamma ray detectors. *Nuclear Instruments and Methods in Physics Research Section A*, 505:256, Jun 2003.

[113] J. M. Lattimer and M. Prakash. The Physics of Neutron Stars. *Science*, 304:536, Apr 2004.

[114] Kenneth Levenberg. A method for the solution of certain non-linear problems in least squares. *Quart. Appl. Math.*, 2:164–168, 1944.

[115] A. M. Levine, F. L. Lang, W. H. G. Lewin, F. A. Primini, C. A. Dobson, J. P. Doty, J. A. Hoffman, S. K. Howe, A. Scheepmaker, W. A. Wheaton, J. L. Matteson, W. A. Baity, D. E. Gruber, F. K. Knight, P. L. Nolan, R. M. Pelling, R. E. Rothschild, and L. E. Peterson. The HEAO 1 A-4 catalog of high-energy X-ray sources. *Astrophysical Journal Supplement Series (ISSN 0067-0049)*, 54:581, Apr 1984.

[116] G. Lichti and V. Schönfelder. Measurement of the spectrum of diffuse gamma quanta in the energy range from 1 to 10 MeV with the aid of a double-Compton telescope. *(Astronomische Gesellschaft and Arbeitsgemeinschaft fuer extraterrestrische Physik*, 35:228, Jan 1974.

[117] R. P. Lin, B. R. Dennis, G. J. Hurford, D. M. Smith, A. Zehnder, P. R. Harvey, D. W. Curtis, D. Pankow, P. Turin, M. Bester, A. Csillaghy, M. Lewis, N. Madden, H. F. van Beek, M. Appleby, T. Raudorf, J. McTiernan, R. Ramaty, E. Schmahl, R. Schwartz, et al. The Reuven Ramaty High-Energy Solar Spectroscopic Imager (RHESSI). *Solar Physics*, 210:3, Nov 2002.

[118] R. P. Lin, S. Krucker, G. J. Hurford, D. M. Smith, H. S. Hudson, G. D. Holman, R. A. Schwartz, B. R. Dennis, G. H. Share, R. J. Murphy, A. G. Emslie, C. Johns-Krull, and N. Vilmer. RHESSI Observations of Particle Acceleration and Energy Release in an Intense Solar Gamma-Ray Line Flare. *The Astrophysical Journal*, 595:L69, Oct 2003.

[119] J. C. Ling and Wm. A. Wheaton. Gamma-Ray Spectra and Variability of the Crab Nebula Emission Observed by BATSE. *The Astrophysical Journal*, 598:334, Nov 2003.

[120] J. A. Lockwood, L. Hsieh, L. Friling, C. Chen, and D. Swartz. Atmospheric neutron and gamma ray fluxes and energy spectra. *Journal of Geophysical Research*, 84:1402, Apr 1979.

[121] J. A. Lockwood, W. R. Webber, L. A. Friling, J. Macri, and L. Hsieh. Observations of gamma radiation between 0.4 MeV and 7 MeV at balloon altitudes using a Compton telescope. *Astrophysical Journal*, 248:1194, Sep 1981.

[122] PN Luke, CP Cork, NW Madden, CS Rossington, and MF Wesela. Amorphous Ge bipolar blocking contacts on Ge detectors. *Nuclear Science Symposium and Medical Imaging Conference, 1991., Conference Record of the 1991 IEEE*, pages 85–89, 1991.

[123] A. G. Lyne, R. S. Pritchard, and F. Graham-Smith. Twenty-Three Years of Crab Pulsar Rotational History. *R.A.S. Monthly Notices V.265*, 265:1003, Dec 1993.

[124] W. A. Mahoney, J. C. Ling, A. S. Jacobson, and R. E. Lingenfelter. Diffuse galactic gamma-ray line emission from nucleosynthetic Fe-60, Al-26, and Na-22 – Preliminary limits from HEAO 3. *Astrophysical Journal*, 262:742, Nov 1982.

[125] W. A. Mahoney, J. C. Ling, A. S. Jacobson, and R. M. Tapphorn. The HEAO 3 gamma-ray spectrometer. *Nuclear Instruments and Methods*, 178:363, Jan 1980.

[126] W. A. Mahoney, J. C. Ling, W. A. Wheaton, and A. S. Jacobson. HEAO 3 discovery of Al-26 in the interstellar medium. *Astrophysical Journal*, 286:578, Nov 1984.

[127] C. B. Markwardt. Non-linear Least-squares Fitting in IDL with MPFIT. *Astronomical Data Analysis Software and Systems XVIII ASP Conference Series*, 411:251, Sep 2009.

[128] D. Marquardt. An algorithm for least-squares estimation of nonlinear parameters. *Journal of the Society for Industrial and Applied Mathematics*, 11:431–441, Jan 1963.

[129] J. L. Matteson. The UCSD/MIT hard X-ray and low energy gamma-ray experiment for HEAO-1 – Design and early results. *American Institute of Aeronautics and Astronautics*, Jan 1978.

[130] N. U. Mayall and J. H. Oort. Further Data Bearing on the Identification of the Crab Nebula with the Supernova of 1054 A.D. Part II. The Astronomical Aspects. *Publications of the Astronomical Society of the Pacific*, 54:95, Apr 1942.

[131] M. McConnell, J. Ryan, R. Diehl, V. Schönfelder, A. Strong, H. Bloemen, W. Hermsen, K. Bennett, R. van Dijk, and S. Fletcher. A Possible Point Source of 2.2 MeV Gamma-Rays. *American Astronomical Society*, 191:1370, Dec 1997.

[132] B. Y. Mills. The Positions of Six Discrete Sources of Cosmic Radio Radiation. *Australian Journal of Scientific Research*, 5:456, Jan 1952.

[133] D. J. Morris, G. Lichti, V. Schönfelder, H. Blomen, W. Hermsen, M. L. McConnell, J. M. Ryan, and K. Bennett. Evidence for 56Co γ-ray line emission from the type Ia SN 1991T using COMPTEL. *American Astronomical Society*, 185:762, Dec 1994.

[134] Igor V. Moskalenko, Werner Collmar, and Volker Schönfelder. A Combined Model for the X-Ray to Gamma-Ray Emission of Cygnus X-1. *Astrophysical Journal v.502*, 502:428, Jul 1998.

[135] R. Much, K. Bennett, R. Buccheri, M. Busetta, R. Diehl, D. Forrest, W. Hermsen, L. Kuiper, G. G. Lichti, M. McConnell, J. Ryan, V. Schönfelder, H. Steinle, A. Strong, and M. Varendorff. COMPTEL observations of the Crab during the CGRO sky survey. *Astronomy and Astrophysics*, 299:435, Jul 1995.

[136] R. Much, B. A. Harmon, P. Nolan, M. S. Strickman, K. Bennett, R. Buccheri, R. Diehl, J. M. Fierro, G. J. Fishman, D. A. Grabelsky, J. E. Grove, W. Hermsen, W. N. Johnson, G. V. Jung, R. L. Kinzer, R. A. Kroeger, L. Kuiper, J. D. Kurfess, G. G. Lichti, S. M. Matz, et al. The Crab total gamma-ray emission as seen by CGRO. *Astronomy and Astrophysics Supplement*, 120:703, Dec 1996.

[137] R. E. Nather, B. Warner, and M. Macfarlane. Optical Pulsations in the Crab Nebula Pulsar. *Nature*, 221:527, Feb 1969.

[138] P. L. Nolan, Z. Arzoumanian, D. L. Bertsch, J. Chiang, C. E. Fichtel, J. M. Fierro, R. C. Hartman, S. D. Hunter, G. Kanbach, D. A. Kniffen, P. W. Kwok, Y. C. Lin, J. R. Mattox, H. A. Mayer-Hasselwander, P. F. Michelson, C. von Montigny, H. I. Nel, D. Nice, K. Pinkau, H. Rothermel, et al. Observations of the Crab pulsar and nebula by the EGRET telescope on the Compton Gamma-Ray Observatory. *Astrophysical Journal*, 409:697, Jun 1993.

[139] U. Oberlack, K. Bennett, H. Bloemen, R. Diehl, C. Dupraz, W. Hermsen, J. Knödlseder, D. Morris, V. Schönfelder, A. Strong, and C. Winkler. The COMPTEL 1.809MeV all-sky image. *Astronomy and Astrophysics Supplement*, 120:311, Dec 1996.

[140] Uwe G. Oberlack, Elena Aprile, Alessandro Curioni, Valeri Egorov, and Karl-Ludwig Giboni. Compton scattering sequence reconstruction algorithm for the liquid xenon gamma-ray imaging telescope (LXeGRIT). *Proc. SPIE Vol. 4141*, 4141:168, Nov 2000.

[141] T. J. O'Neill, D. Bhattacharya, M. Polsen, A. D. Zych, J. Samimi, and A. Akyuz. Development of the TIGRE compton telescope for intermediate-energy gamma-ray astronomy. *IEEE Transactions on Nuclear Science*, 50:251, Apr 2003.

[142] G. Ottaviani, C. Canali, and AA Quaranta. Charge carrier transport properties of semiconductor materials suitable for nuclear radiation detectors. *IEEE Transactions on Nuclear Science*, 22:192–204, 1975.

[143] F. Pacini. Energy Emission from a Neutron Star. *Nature*, 216:567, Nov 1967.

[144] F. Pacini. Rotating Neutron Stars, Pulsars and Supernova Remnants. *Nature*, 219:145, Jul 1968.

[145] Laurence E. Peterson, Allan S. Jacobson, R. M. Pelling, and Daniel A. Schwartz. Observations of cosmic X-ray sources in the 10-250 keV range. *Canadian Journal of Physics. Vol. 46*, 46:437, Jan 1968.

[146] G. Phillips and K. Marlow. Automatic analysis of gamma-ray spectra from germanium detectors. *Nucl. Instrum. Methods*, Jan 1976.

[147] Tsvi Piran. The physics of gamma-ray bursts. *Reviews of Modern Physics*, 76:1143, Jan 2005.

[148] M. J. Rees and J. E. Gunn. The origin of the magnetic field and relativistic particles in the Crab Nebula. *Monthly Notices RAS*, 167:1, Apr 1974.

[149] George B. Rybicki and Alan P. Lightman. *Radiative Processes in Astrophysics*. John Wiley & Sons, 1979.

[150] V. Schönfelder, H. Aarts, K. Bennett, H. de Boer, J. Clear, W. Collmar, A. Connors, A. Deerenberg, R. Diehl, A. von Dordrecht, J. W. den Herder, W. Hermsen, M. Kippen, L. Kuiper, G. Lichti, J. Lockwood, J. Macri, M. McConnell, D. Morris, R. Much, et al. Instrument description and performance of the Imaging Gamma-Ray Telescope COMPTEL aboard the Compton Gamma-Ray Observatory. *Astrophysical Journal Supplement Series (ISSN 0067-0049)*, 86:657, Jun 1993.

[151] V. Schönfelder, K. Bennett, J. J. Blom, H. Bloemen, W. Collmar, A. Connors, R. Diehl, W. Hermsen, A. Iyudin, R. M. Kippen, J. Knödlseder, L. Kuiper, G. G. Lichti, M. McConnell, D. Morris, R. Much, U. Oberlack, J. Ryan, G. Stacy, H. Steinle, et al. The first COMPTEL source catalogue. *Astronomy and Astrophysics Supplement*, 143:145, Apr 2000.

[152] V. Schönfelder, A. Hirner, and K. Schneider. A telescope for soft gamma-ray astronomy. *Nuclear Instruments and Methods*, 107(385), 1973.

[153] I. S. Shklovsky. Optical Emission from the Crab Nebula in the Continuous Spectrum. *Electromagnetic Phenomena in Cosmical Physics*, 6:520, Jan 1958.

[154] D. M. Smith. RHESSI results on γ-ray lines from diffuse radioactivity. *New Astronomy Reviews*, 48:87, Feb 2004.

[155] F. G. Smith. An Accurate Determination of the Positions of Four Radio Stars. *Nature*, 168:555, Sep 1951.

[156] David H. Staelin and Edward C. Reifenstein. Pulsating Radio Sources near the Crab Nebula. *Science*, 162:1481, Dec 1968.

[157] M. Stone. Cross-validation and multinomial prediction. *Biometrika*, Jan 1974.

[158] S. J. Sturner, H. Seifert, C. Shrader, and B. J. Teegarden. MGEANT-A GEANT-based multi-purpose simulation package for gamma-ray astronomy missions. *The Fifth Compton Symposium. AIP Conference Proceedings*, 510:814, Apr 2000.

[159] A. Takada, T. Tanimori, H. Kubo, K. Miuchi, K. Tsuchiya, S. Kabuki, H. Nishimura, K. Hattori, K. Ueno, S. Kurosawa, N. Nonaka, E. Mizuta, R. Orito, and T. Nagayoshi. Observation of diffuse gamma-ray with Electron-Tracking Compton imaging camera loaded on balloon. *IEEE Nuclear Science Symposium Conference Record, 2007.*, 4:2558 – 2563, 2007.

[160] Shin'Ichiro Takeda, Shin Watanabe, Takaaki Tanaka, Kazuhiro Nakazawa, Tadayuki Takahashi, Yasushi Fukazawa, Hajimu Yasuda, Hiroyasu Tajima, Yoshikatsu Kuroda, Mitsunobu Onishi, and Kei Genba. Development of double-sided silicon strip detectors (DSSD) for a Compton telescope. *Nuclear Instruments and Methods in Physics Research Section A*, 579:859, Sep 2007.

[161] B. J. Teegarden, S. D. Barthelmy, N. Gehrels, J. Tueller, M. Leventhal, and C. J. MacCallum. GRIS observations of Al-26 gamma-ray line emission from two points in the Galactic plane. *Astrophysical Journal*, 375:L9, Jul 1991.

[162] B. J. Teegarden, T. L. Cline, N. Gehrels, G. Porreca, J. Tueller, M. Leventhal, A. F. Huters, C. J. MacCallum, and P. D. Stang. The Gamma-Ray Imaging Spectrometer (GRIS): A new balloon-borne experiment for gamma-ray line astronomy. *In its 19th Intern. Cosmic Ray Conf.*, 3:307, Aug 1985.

[163] A. Toor and F. D. Seward. The Crab Nebula as a calibration source for X-ray astronomy. *Astronomical Journal*, 79:995, Oct 1974.

[164] Virginia Trimble. Motions and Structure of the Filamentary Envelope of the Crab Nebula. *Astronomical Journal*, 73:535, Sep 1968.

[165] P. Ubertini, F. Lebrun, G. Di Cocco, A. Bazzano, A. J. Bird, K. Broenstad, A. Goldwurm, G. La Rosa, C. Labanti, P. Laurent, I. F. Mirabel, E. M. Quadrini, B. Ramsey, V. Reglero, L. Sabau, B. Sacco, R. Staubert, L. Vigroux, M. C. Weisskopf, and A. A. Zdziarski. IBIS: The Imager on-board INTEGRAL. *Astronomy and Astrophysics*, 411:L131, Nov 2003.

[166] Kazuki Ueno, Toru Tanimori, Hidetoshi Kubo, Kentaro Miuchi, Shigeto Kabuki, Atsushi Takada, Hironobu Nishimura, Kaori Hattori, Shunsuke Kurosawa, Chihiro Ida, and Satoru Iwaki. Development of an electron-tracking Compton camera based on a gaseous TPC and a scintillation camera for a balloon-borne experiment. *Space Telescopes and Instrumentation 2008: Ultraviolet to Gamma Ray. Edited by Turner*, 7011:96, Aug 2008.

[167] R. D. van der Meulen, H. Bloemen, K. Bennett, W. Hermsen, L. Kuiper, R. P. Much, J. Ryan, V. Schönfelder, and A. Strong. COMPTEL gamma-ray study of the Crab nebula. *Astronomy and Astrophysics*, 330:321, Feb 1998.

[168] G. Vedrenne, J.-P. Roques, V. Schönfelder, P. Mandrou, GG Lichti, A. von Kienlin, B. Cordier, S. Schanne, J. Knödlseder, G. Skinner, P. Jean, F. Sanchez, P. Caraveo, B. Teegarden, P. von Ballmoos, L. Bouchet, P. Paul, J. Matteson, S. Boggs, C. Wunderer, et al. SPI: The spectrometer aboard INTEGRAL. *Astron Astrophys*, 411(1):L63–L70, Jan 2003.

[169] T. C. Weekes, M. F. Cawley, D. J. Fegan, K. G. Gibbs, A. M. Hillas, P. W. Kowk, R. C. Lamb, D. A. Lewis, D. Macomb, N. A. Porter, P. T. Reynolds, and G. Vacanti. Observation of TeV gamma rays from the Crab nebula using the atmospheric Cerenkov imaging technique. *Astrophysical Journal*, 342:379, Jul 1989.

[170] G. Weidenspointner, G. Skinner, P. Jean, J. Knödlseder, P. von Ballmoos, G. Bignami, R. Diehl, AW Strong, B. Cordier, and S. Schanne. An asymmetric distribution of positrons in the Galactic disk revealed by gamma-rays. *Nature*, 451(7175):159–162, 2008.

[171] John Archibald Wheeler. Superdense Stars. *Annu. Rev. Astro. Astrophys.*, 4:393, Jan 1966.

[172] C. Wigger, W. Hajdas, K. Arzner, M. Güdel, and A. Zehnder. Gamma-Ray Burst Polarization: Limits from RHESSI Measurements. *The Astrophysical Journal*, 613:1088, Oct 2004.

[173] S. Wilderman, N. Clinthorne, J. Fessler, and W. Rogers. List-mode maximum likelihood reconstruction of Compton scatter camera images in nuclear medicine. *Nuclear Science Symposium, 1998. Conference Record. 1998 IEEE*, 3:1716 – 1720 vol.3, Nov 1998.

[174] R. V. Willstrop. Optical Flashes from the Crab Nebula M1. *Nature*, 221:1023, Mar 1969.

[175] C. Winkler, T. J.-L. Courvoisier, G. Di Cocco, N. Gehrels, A. Giménez, S. Grebenev, W. Hermsen, J. M. Mas-Hesse, F. Lebrun, N. Lund, G. G. C. Palumbo, J. Paul, J.-P. Roques, H. Schnopper, V. Schönfelder, R. Sunyaev, B. Teegarden, P. Ubertini, G. Vedrenne, and A. J. Dean. The INTEGRAL mission. *Astronomy and Astrophysics*, 411:L1, Nov 2003.

[176] L. Woltjer. X-Rays and Type i Supernova Remnants. *Astrophysical Journal*, 140:1309, Oct 1964.

[177] A. Zoglauer, R. Andritschke, G. Kanbach, and S. Boggs. A Bayesian-based Method for Particle Track Identification in Low-energy Pair-creation Telescopes. *AIP Conference Proceedings*, Jan 2007.

[178] A. Zoglauer, R. Andritschke, and F. Schopper. MEGAlib The Medium Energy Gamma-ray Astronomy Library. *New Astronomy Reviews*, 50:629, Sep 2006.

[179] A. Zoglauer and S. Boggs. Application of Neural Networks to the Identification of the Compton Interaction Sequence in Compton Imagers. *IEEE Nuclear Science Symposium Conference Record*, Jan 2007.

[180] A. Zoglauer, G. Weidenspointner, M. Galloway, S. E. Boggs, and C. B. Wunderer. Cosima – the Cosmic Simulator of MEGAlib. *IEEE Nuclear Science Symposium Conference Record*, 2009.

[181] Andreas Zoglauer, Robert Andritschke, Steven E. Boggs, Florian Schopper, Georg Weidenspointner, and Cornelia B. Wunderer. MEGAlib: simulation and data analysis for low-to-medium-energy gamma-ray telescopes. *Space Telescopes and Instrumentation 2008: Ultraviolet to Gamma Ray. Edited by Turner*, 7011:101, Jul 2008.

[182] Andreas Zoglauer, Steven E. Boggs, Robert Andritschke, and Gottfried Kanbach. Recognition of Compton scattering patterns in advanced Compton telescopes. *Mathematics of Data/Image Pattern Recognition*, 6700:15, Oct 2007.

[183] Andreas Zoglauer and Gottfried Kanbach. Doppler broadening as a lower limit to the angular resolution of next-generation Compton telescopes. *X-Ray and Gamma-Ray Telescopes and Instruments for Astronomy. Edited by Joachim E. Truemper*, 4851:1302, Mar 2003.

[184] Andreas Christian Zoglauer. First Light for the Next Generation of Compton and Pair Telescopes. *Ph.D. Thesis*, pages 1–174, Dec 2005.

[185] A. D. Zych, T. J. O'Neill, D. Bhattacharya, C. Trojanowski, S. Wijeratne, C. Teichegaeber, and M. Mathews. TIGRE prototype gamma-ray balloon instrument. *Hard X-Ray and Gamma-Ray Detector Physics and Penetrating Radiation Systems VIII. Edited by Franks*, 6319:37, Aug 2006.

[186] Allen D. Zych, T. J. O'Neill, D. Bhattacharya, E. Harris, K. Kamiya, and C. Trojanowski. Balloon Flight Performance and Preliminary Results of the Prototype Tracking and Imaging Gamma-Ray Experiment (TIGRE). *American Astronomical Society*, 213:439, Jan 2009.

[187] Allen D. Zych, T. J. O'Neill, D. Bhattacharya, E. J. Harris, K. Kamiya, C. Trojanowski, and S. Wijeratne. Preliminary Balloon Flight Results with Prototype TIGRE Gamma-Ray Instrument. *American Astronomical Society*, 10, Mar 2008.